Light-Flow Characterization and Manipulation in 1 and 2 Dimensional Photonic Crystals

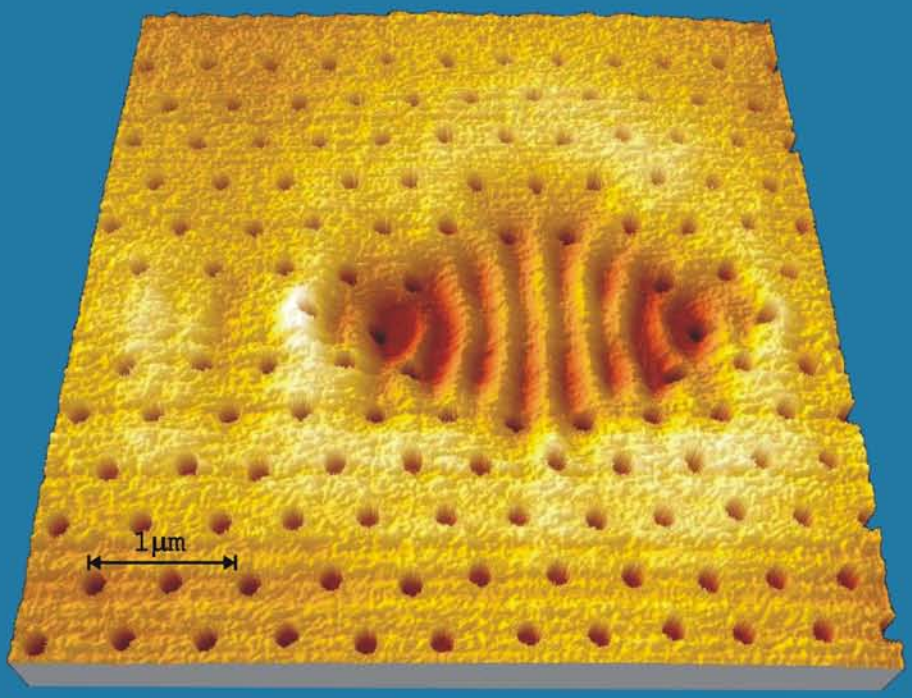

Wico Hopman

LIGHT-FLOW CHARACTERIZATION AND MANIPULATION IN 1 AND 2 DIMENSIONAL PHOTONIC CRYSTALS

Wico Hopman

Graduation committee:

Chairman and secretary:	Prof. dr. ir. A.J. Mouthaan	University of Twente
Promotor:	Prof. dr. M. Pollnau	University of Twente
Promotor:	Prof. dr. A. Driessen	University of Twente
Assistant promotor:	Dr. ir. R.M. de Ridder	University of Twente
Members:	Dr. H.J.W.M. Hoekstra	University of Twente
	Prof. dr. V. Subramaniam	University of Twente
	Prof. dr. L. Kuipers	Amolf
	Prof. dr. R.M. De La Rue	University of Glasgow
	Prof. dr. H.W.M. Salemink	TU Delft

The research described in this thesis was carried out at the Integrated Optical Microsystems (IOMS) group, Faculty of Electrical Engineering, Mathematics and Computer Science, Mesa$^+$ Institute for Nanotechnology, University of Twente, P.O. Box 217, 7500 AE Enschede, The Netherlands.

This work was financially supported by the Mesa$^+$ Advanced Photonic Structures SRO for the first two years and the last two years by NanoNed, a national nanotechnology program coordinated by the Dutch ministry of Economic Affairs.

Cover design: The illustration on the *front cover* is obtained using the T-SNOM method presented in this thesis. It shows an enhanced AFM height image overlaying the associated optical transmission data, which results in a precise map of the locations of maximum probe-field interaction. In this thesis it is shown that these interaction maxima, in the investigated configurations, correspond to amplitude peaks of the resonance pattern within the cavity. The *back cover* shows the interaction patterns found for three different wavelengths around the resonance wavelength of the undisturbed resonator, see section 4.5 for more details.

Printed by PrintPartners IPSKAMP, Enschede, The Netherlands

ISBN: 978-90-365-2492-6

LIGHT-FLOW CHARACTERIZATION AND MANIPULATION IN 1 AND 2 DIMENSIONAL PHOTONIC CRYSTALS

PROEFSCHRIFT

ter verkrijging van
de graad doctor aan de Universiteit Twente,
op gezag van de rector magnificus,
prof. dr. W. H. M. Zijm,
volgens besluit van het College voor Promoties
in het openbaar te verdedigen
op vrijdag 20 april 2007 om 13.15 uur

door

Willem Cornelis Lambert Hopman (Wico)

geboren op 16 augustus 1977
te Assen

Dit proefschrift is goedgekeurd door:

promotor: prof. dr. M. Pollnau

promotor: prof. dr. A. Driessen

assistent promotor: dr. ir. R. M. de Ridder

CONTENTS

CHAPTER 1

1 INTRODUCTION & OUTLINE

Abstract—This chapter presents a general introduction to this thesis. The motivation for this PhD research is presented as well as a description of the sponsors that have supported the work. Furthermore, this chapter contains the outline of this thesis.

1.1 Preface

High index-contrast integrated photonics is a good candidate for future densely integrated photonic microchips, because a high-index contrast allows for small bend radii and small resonators. It can play a predominant role in telecommunications systems (e.g. fiber-to-the-home [1,2]) and, for example, sensing applications for medical purposes [3-7]. This thesis focuses on an important class of optical structures: photonic crystals.

Photonic crystals are composite materials which can have (generally strong) periodic variations of the dielectric function in 1, 2 or 3 dimensions [8]. They form a powerful class of nanophotonic structures that can exert a huge influence on light propagation and emission. Recently, planar photonic crystal slabs (PCS) have been used to dramatically slow down the propagation of light [9,10] and greatly affect the properties of embedded emitters [11-13].
The number of publications related to photonic crystals has shown an exponential growth in the last 15 years [14], see the figure below.

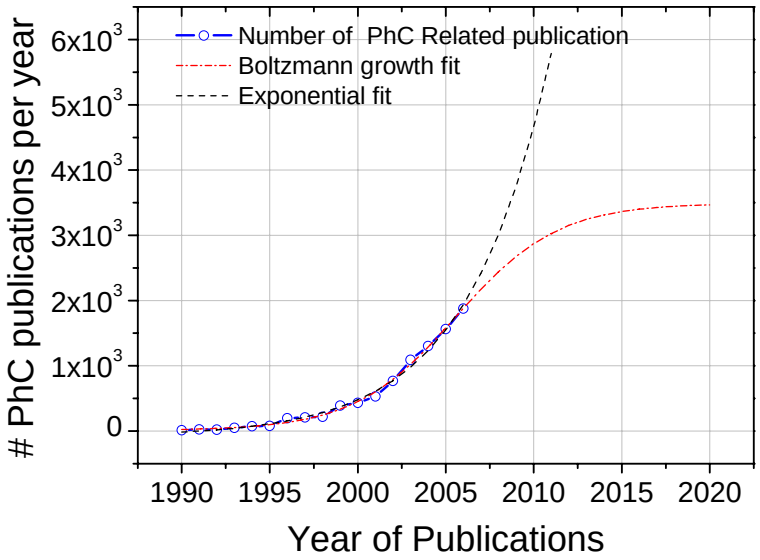

Figure 1.1-1: Number of photonic crystal (PhC) related publications during the last 15 years. Two scenarios are extrapolated from the data: an exponential growth fit, and a Boltzmann (natural) growth fit [14].

As photonic crystals are expected to form the basis for complex, integrated photonic architectures, this exponential growth may continue for a quasi-indefinite period of time, analogous to Moore's law in electronics. On the other hand, a more natural growth trend like the Boltzmann growth curve is more likely to apply. Figure 1.1-1 shows both growth scenarios. According to the Boltzmann growth fit, the number of PhC related publications is likely to be saturated around the year 2020. After 2020 the curve could show a decline, if, for example, another technology outdates and/or replaces the photonic crystal technology.
However, the fits may not take into account the current developments in the worlds market, in which India and China are strong growth centers with respect to their economics and scientific publications. Therefore, the actual shape of the curve for the coming years remains to be seen.
This thesis focuses on both future and directly exploitable applications of photonic crystals. The direct applications are: compact, highly sensitive refractometric cladding index sensors based on waveguide gratings (WGGs), and wave pattern mapping in resonator devices using near-field

interaction. A future application is a nano-electro-mechanical (NEMS) switch based on two-dimensional photonic crystals. Not coincidently, this application is the main and final goal in the research project described in section 1.2.2.

1.2 Projects

In the following sub-sections the projects, networks or actions are described, which have financially supported this work.

1.2.1 SRO advanced photonic structures

In the first 2 years of my PhD period, I worked part time for about 70%, the other part of my time was invested in a top sport career in triathlon competition. During these 2 years I worked on a project termed LIECE: Light induced electrochemical etching of silicon. However, preliminary results on this subject are not included in this thesis. The LIECE project was part of the Mesa+ strategic research orientation: advanced photonic structures (SRO-APS). The project was terminated after 2 years and an opportunity was offered to me to work on the project described in the next paragraph.

1.2.2 NanoNed nano-photonics

The next two years I switched to a full time PhD job. The research presented in this thesis was for the major part funded by the nanotechnology investment program NanoNed, by the Dutch ministry of economic affairs. Within the Nanoned program there are flagships, which comprise the main research orientations. Our project (TOE.7145: Optics), which is part of the Nanophotonics flagship, has started officially in fall 2005.

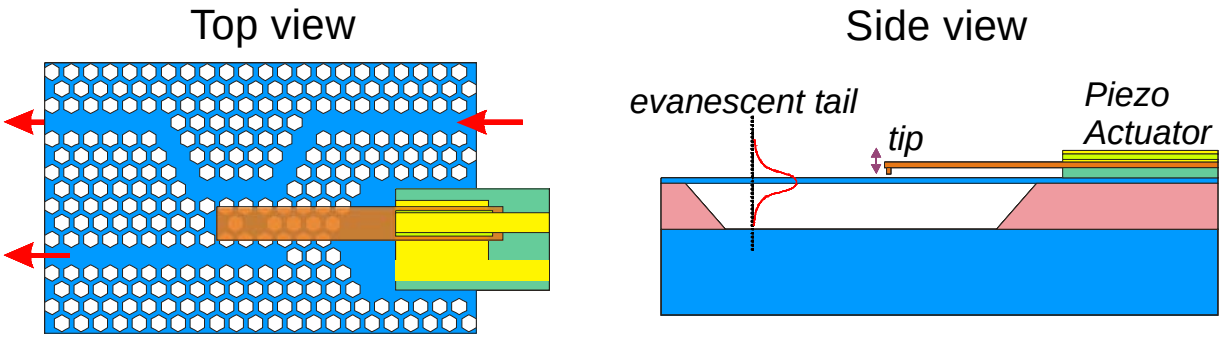

Figure 1.2-1: (a) An illustration of a nanomechanically actuated switch based on photonic crystals. (b) A side view showing a small tip that can be moved in and out the evanescent field of a resonator configuration.

The title of the project is: Optical switching by NEMS-actuated resonator arrays. The idea is to realize an optical switch based on photonic crystals, which can be actuated by mechano-optical interaction with the field inside the photonic crystal.
An illustration of a 3-port switch is shown in Figure 1.2-1. The principle of operation could, for example, be based on an optical resonator configuration, similar to [15] (as depicted in Figure 1.2-1a) by leaving a number of holes un-etched. The resonator(s) should then be designed such that a small actuator moving in the evanescent field of the cavity can be used to switch light from the input port either to the upper or lower output port, see Figure 1.2-1a. A small, piezo-driven actuator, can be used to achieve high switching speeds, if desired, see Figure 1.2-1b.

The first major milestone for the first 2 years of the project was to demonstrate tuning or interaction of an AFM with a PhC resonance. This target has been met after 1.5 years and is reported in detail in this thesis, the highlights can be found in section 4.5. My contribution to the project ends 15 August 2007, therefore my successor will continue together with the TST-group to reach the final goal in the coming 2.5 years: a fully integrated NEMS PhC switch.

1.2.3 ePIXnet: mask sharing, and FIB for photonics

The ePIXnet is a network of excellence funded by the EU to stimulate the cooperation between the best labs and scientists in Europe. Before the ePIXnet was restructured into platforms ([16]), the facility access activity 3 (FAA3), directed by Dr. Wim Bogaerts (university of Ghent, Belgium), offered the opportunity to take part in a DUV mask sharing activity. A start of this type of technology sharing was initiated already in the European PICCO project. The full title of FAA3 was: Nanophotonic circuits in SOI with CMOS-compatible technology. The principle of mask-sharing works as follows: users of the platform could contribute to a mask, which was used to fabricate the structures in SOI taking advantage of the CMOS-compatible silicon technology from IMEC (Leuven, Belgium). Because the users share the space of 1 mask, they also share the costs. An additional subsidy from the ePIXnet lead to prices for high-quality SOI devices, that are affordable for researchers in the academic community. The mask sharing facility, based on the mature DUV technology, was exploited for the results presented in this thesis. The results presented in this thesis are from the second mask sharing round: ePIXmask2.

However, in parallel, an alternative fabrication method for photonic crystals was investigated in the Mesa+ cleanroom, namely focused ion beam processing. The research partially overlapped with the joint research activity FIB (JRA-FIB) in which we also participated. Some issues of the focused ion beam processing method are addressed in section 3.1, 3.2, 3.3 and 5.2.

1.2.4 Cost P11

Finally, the last project, which had a minor contribution to this thesis, is the COST P11 action, which is a cooperation of many (mostly European) institutes. It was initiated to stimulate collaborations on the physics of linear, non-linear, and active photonic crystals. The COST P11 action is funded by the European science foundation (ESF). The photonic wire analyses have, for example, been studied in a joint numerical modeling study [17]; some of the results are presented in section 2.3.1.1.

1.3 Outline of the thesis

This thesis presents the design, realization and characterization results of gratings (1-D PhCs) and 2-D slab-type PhCs. Devices based on both configurations can exhibit high field enhancements and they consequently have potentially high sensitivities to changes in their environment. differences in geometry and size determine the applications they are best suited for. Some physical concepts, such as, field enhancement and the quality factor have been investigated using 1-D PhCs. These results can be generalized to 2-D in order to design and realize 2-D PhCs functions.

The thesis is organized as follows. In chapter 2, a general introduction on photonic crystals is presented. Some derivations are included to support the work presented in the next chapters. Furthermore, the main design choices for the results presented in this thesis are also addressed in this chapter.

An overview of the strengths and weaknesses of the exploited fabrication methods is presented firstly in chapter 3. The chapter continues in section 3.2 with a detailed example of controlling the focused ion beam machine (FIB) in order to generate nanostructured devices. Next, FIB processing is investigated to achieve nanosmooth surfaces in section 3.3. The important parameters which can influence, for example, the sidewall angle in fabricating PhCs in Si, are discussed in section 3.4. The last section (3.5) of the chapter presents a method for realizing highly uniform and apodized gratings in Si_3N_4 using a combination of conventional lithography and laser interference lithography.

Similar to the overview of fabrication processes in chapter 3, an overview of the exploited characterization setups is presented in chapter 4. In section 4.2, we show experimentally that a strong waveguide gratings (WGG) can be used as a compact building block for highly sensitive refractometric cladding sensors. Such a slow-light based sensor can be characterized using the novel method that uses Rayleigh scattering for estimating the group velocities in a WGG, which is presented in section 4.3.
To visualize the wave-patterns in resonant device like, for example, a PhC microcavity (MC), a novel method has been developed and tested by rigorous modeling, as described in section 4.4, and tested experimentally in section 4.5. The latter section also shows that the nanomechanical interaction can be used as well for tuning the important properties of a PhC MC, the resonance wavelength and the quality factor. The last section (4.6) contains a model which can be exploited to predict the interaction of a nanosized AFM tip in tapping mode operation.

Finally, chapter 5 presents an outlook, which contains the status of on-going research related to the work presented in this thesis.

1.4 References

[1] D. H. Geuzebroek, PhD thesis, "Flexible optical network components based on densely integrated microring resonators", ISBN: 90-365-2258-7, University of Twente, Enschede, 2005.

[2] E. J. Klein, PhD thesis, "Densely integrated Microring-Resonator based components for Fiber-to-the-Home applications", University of Twente, Enschede, 2007.

[3] E. Krioukov, J. Greve, and C. Otto, “Performance of integrated optical microcavities for refractive index and fluorescence sensing”, *Sensors and Actuators, B: Chemical*, vol. **90**, pp. 58-67, 2003.

[4] P. V. Lambeck, “Remote opto-chemical sensing with extreme sensitivity: Design, fabrication and performance of a pigtailed integrated optical phase-modulated Mach-Zehnder interferometer system”, *Sensors and Actuators, B: Chemical*, vol. **61**, pp. 100-127, 1999.

[5] A. K. Sheridan, R. D. Harris, P. N. Bartlett, and J. S. Wilkinson, “Phase interrogation of an integrated optical SPR sensor”, *Sensors and Actuators, B: Chemical*, vol. **97**, pp. 114-121, 2004.

[6] P. V. Lambeck, “Integrated optical sensors for the chemical domain”, *Measurement Science and Technology*, vol. **17**, pp. R93-R116, 2006.

[7] W. C. L. Hopman, P. Pottier, D. Yudistira, J. van Lith, P. V. Lambeck, R. M. De La Rue, A. Driessen, H. J. W. M. Hoekstra, and R. M. de Ridder, “Quasi-one-dimensional photonic crystal as a compact building-block for refractometric optical sensors”, *IEEE Journal Of Selected Topics In Quantum Electronics*, vol. **11**, pp. 11-16, 2005.

[8] J. D. Joannopoulos, R. D. Meade, and J. N. Winn, "Photonic crystals: Molding the flow of light", ISBN: 0-691-03744-2, Princeton University Press, 1995.

[9] R. S. Jacobsen, A. V. Lavrinenko, L. H. Frandsen, C. Peucheret, B. Zsigri, G. Moulin, J. Fage-Pedersen, and P. I. Borel, “Direct experimental and numerical determination of extremely high group indices in photonic crystal waveguides”, *Optics Express*, vol. **13**, pp. 7861-7871, 2005.

[10] L. H. Frandsen, A. V. Lavrinenko, J. Fage-Pedersen, and P. I. Borel, “Photonic crystal waveguides with semi-slow light and tailored dispersion properties”, *Optics Express*, vol. **14**, pp. 9444-9450, 2006.

[11] O. Painter, R. K. Lee, A. Scherer, A. Yariv, J. D. O'Brien, P. D. Dapkus, and I. Kim, “Two-dimensional photonic band-gap defect mode laser”, *Science*, vol. **284**, pp. 1819-1821, 1999.

[12] A. Blanco, E. Chomski, S. Grabtchak, M. Ibisate, S. John, S. W. Leonard, C. Lopez, F. Meseguer, H. Miguez, J. P. Mondla, G. A. Ozin, O. Toader, and H. M. Van Driel, "Large-scale synthesis of a silicon photonic crystal with a complete three-dimensional bandgap near 1.5 micrometres", *Nature*, vol. **405**, pp. 437-440, 2000.

[13] J. S. Foresi, P. R. Villeneuve, J. Ferrera, E. R. Thoen, G. Steinmeyer, S. Fan, J. D. Joannopoulos, L. C. Kimerling, H. I. Smith, and E. P. Ippen, "Photonic-bandgap microcavities in optical waveguides", *Nature*, vol. **390**, pp. 143-145, 1997.

[14] J. M. Bendickson, "Photonic & Sonic Band-Gap Bibliography", http://phys.lsu.edu/~jdowling/pbgbib.html.

[15] S. H. Fan, P. R. Villeneuve, and J. D. Joannopoulos, "Channel drop tunneling through localized states", *Physical Review Letters*, vol. **80**, pp. 960-963, 1998.

[16] ePIXnet, http://www.epixnet.org.

[17] P. Bienstman, S. Selleri, L. Rosa, H. P. Uranus, W. C. L. Hopman, R. Costa, A. Melloni, L. C. Andreani, J. P. Hugonin, P. Lalanne, D. Pinto, S. S. A. Obayya, M. Dems, and K. Panajotov, "Modelling leaky photonic wires: A mode solver comparison", *Optical and Quantum Electronics*, vol. **38**, pp. 731-759, 2006.

CHAPTER 2

2 PHOTONIC CRYSTALS & RESONATORS

Abstract—The aim of this chapter is to present a brief review on the theory of one and two dimensional slab photonic crystals and resonators. Some derivations of often used concepts such as group velocity and quality factor and free spectral range are given. The topics described in this chapter can be seen as background information for the remaining chapters. Furthermore, some of the design issues and design choices for waveguide gratings, photonic crystal resonators and microring resonators are also addressed in this chapter.

2.1 Introduction

Resonators play an import role in the realization of integrated optical functions. They allow, for example, for a local enhancement in power density. The associated increase in light-matter interaction has been exploited for sensing [1], non-linear applications [2] and nanomechanical applications [3]. In addition, resonators can also be used for wavelength filtering [4,5]. In this thesis three types of resonators are discussed, which can exhibit high quality factors (*Qs*): uniform (defect free) waveguide gratings (WGGs) [6], photonic crystal (PhC) microcavities (MCs) [7,8] and microring resonators (MRRs) [9]. Although these three types of resonators are all based on constructive interference at the resonance wavelength, there are quite some differences in their photonic and geometrical properties. In this chapter a basic description of the working principle of these three resonator types is given, together with some of the design considerations.

2.2 Waveguide gratings

An optical waveguide forms the most basic building block in integrated optics. It is used to transport light on chip from one location to the other. To give another functionality to the waveguide, a periodic array of slits (a grating) can be etched into it [10] to form a WGG. If these periodic corrugations are small, i.e. a few nm etch-depth, the WGG shows close resemblance to existing fiber-gratings. However, the large length of such gratings needed to obtain sufficient reflectivity, makes them unsuited for achieving a dense integration of photonic functions. By implementing stronger gratings, shorter WGG lengths can be used, which can be realized by etching the grooves deeper or possibly completely through the core layer. This configuration is referred to as a quasi-one-dimensional photonic crystal (Q1D PhC) [11]. The term “quasi” is added because the WGG is not a true 1-D PhC: the WGGs fabricated using thin film technology do not only have a periodic variation of the dielectric constant in one direction, but, in addition, also show a non-constant dielectric function in the direction perpendicular to the periodicity. The transition in this direction can lead to out–of–plane loss. Finally, we note that the term quasi-1-D should *not* be mixed up with the term quasi-periodic [12], which is a different subject and not part of this thesis.

2.2.1 One-dimensional photonic crystal

A 1-D PhC or Bragg stack, can be realized by periodically alternating layers of high and lower dielectric constant [13-16]. The layers are assumed to extend to infinity in the *x* & *y* directions perpendicular to the axis of translational symmetry, see Figure 2.2-1a. A maximum in reflection can be established by satisfying the Bragg condition,

$$m\lambda_B \approx 2\left(d_1 n_1 + d_2 n_2\right), \qquad m \in \mathbb{N}, \tag{1}$$

with d_1, n_1 and d_2, n_2 the thickness and refractive index of layer 1 and layer 2 and λ_B the Bragg wavelength, respectively. A Bragg stack or quarter-wave stack can than be formed by choosing a thickness for d_1 of $\lambda_B/4n_1$ and a value for d_2 of $\lambda_B/4n_2$.

The transmission of such a stack can be efficiently calculated using the well-known transfer matrix method (TMM). The transmission result through a 70-period Bragg stack is shown in Figure 2.2-1b. The characteristic features of the spectrum are: a range of wavelengths where the transmission is close to zero termed the stopband, and narrow fringes outside the stopband. These and other properties of periodic layered media will be described in the next sections.

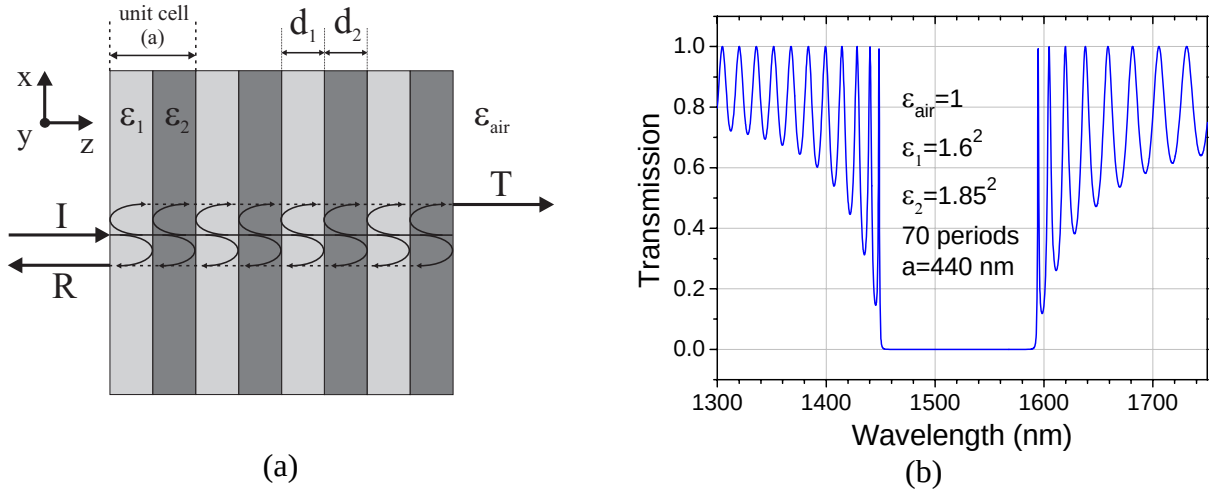

Figure 2.2-1: (a) A Bragg stack consisting of alternating layers of high and low dielectric constants. (b)Transmission (T) for a 70 period Bragg stack calculated using the transfer matrix method [17].

2.2.1.1 Bloch modes

To find optical modes that can propagate through photonic crystals it is needed to solve Maxwell's equations. In this section, a method is described for finding solution to Maxwell's equations in a PhC with discrete translational symmetry: a Bragg stack with periodicity *a*, see Figure 2.2-1. First the dielectric permittivity is written of the lossless PhC as a periodic function along the axes of translational symmetry, $\varepsilon(z)$.

$$\varepsilon(z) = \varepsilon(z + a\,l), \qquad l \in \mathbb{Z}. \tag{2}$$

Next, the Maxwell's equation for the magnetic field vector **H** can be rewritten as a Hermitian eigenvalue problem [13,18]:

$$\nabla \times \frac{1}{\varepsilon(\mathrm{z})} \nabla \times \mathbf{H}(\mathrm{z}) = \left(\frac{\omega}{c}\right)^2 \mathbf{H}(\mathrm{z}), \tag{3}$$

were ω denotes the angular frequency and *c* the speed of light in vacuum. With the constraint that there are no sources in the medium, it follows that,

$$\nabla \cdot \mathbf{H}(z) = 0. \tag{4}$$

Solutions to (3) give all –orthogonal– eigenstates of the system. The eigen-operator $\nabla \times {}^{1}\!/\!_{\varepsilon(\mathrm{z})} \nabla \times$ is periodic for the Bragg stack under study, hence the Bloch-Floquet theorem applies and the solutions to (3) for a 1-D PhC can be written as,

$$H\left(z,t\right) = e^{j\left(\omega t - kz\right)} H_k\left(z\right), \tag{5}$$

where $H(z,t)$ denotes the amplitude of the magnetic field vector **H.** Note that (3) and (4) are written in vector format, whereas the solution for a 1-D PhC can be written in scalar format. The solution in (5) is termed a Bloch wave which is a product of a plane wave expression $e^{j(\omega t - kz)}$ propagating along the *z*-axis and a periodic amplitude (the eigen-state) $H_k(z)$. An important property of this solution is that the wave number *k* is conserved, i.e. there is no scattering of the Bloch wave. The periodic function $H_k(z)$ is defined by a *finite* unit cell (applying Bloch boundary conditions), see Figure 2.2-1. Therefore the solution shown in (5) gives discrete pairs for ω and *k*, i.e. for each *k* an infinite number of discretely separated angular frequencies can be found [13]. The Bloch theorem yields that periodic media have periodic solutions, therefore different *k* numbers don't necessarily lead to different modes, i.e. the Bloch wave with wave number *k* may be identical to the Bloch wave with wave number $k + 2\pi/a$ [13]:

$$H_k(z) = H_{k+2\pi/a}(z). \tag{6}$$

These solutions separated by $2\pi/a$ are sometimes referred to as Bloch harmonics [19], see also Figure 2.2-2. Therefore, Bloch modes contain more than one of these spatial Fourier components. For some frequencies there are no eigenstates, i.e. solutions to (3). This frequency (or free space wavelength) region is referred to as stopband or stop gap for a 1-D PhC.

2.2.1.2 Dispersion graph

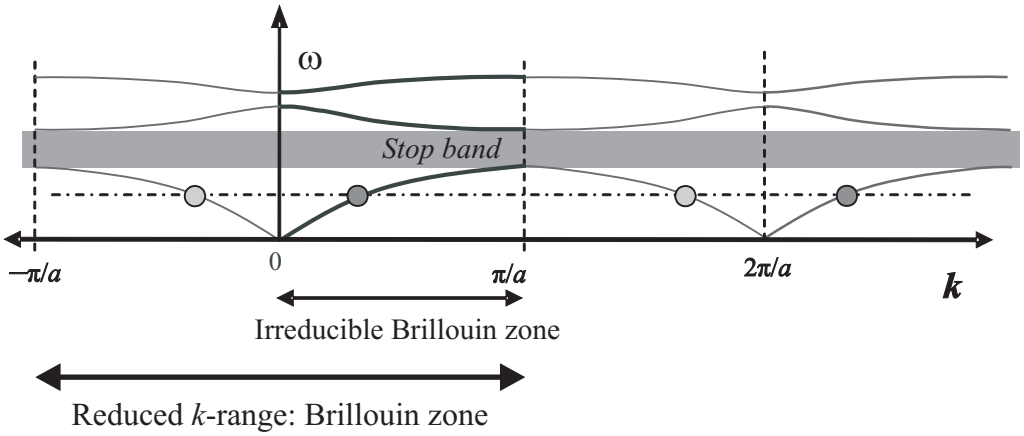

Figure 2.2-2: Dispersion graph of a Bragg stack.

The primitive cell of the reciprocal lattice $2\pi/a$ (obtained by Fourier analysis of the crystal [13,20]) is termed the first Brillouin zone: $k = -\pi/a$ to $k = \pi/a$ [13]. This zone can be reduced further for a Bragg stack, by using symmetry. A range of k-values is formed which cannot be reduced further, the irreducible Brillouin zone: $k = 0$ to $k = \pi/a$. The dispersion curve can be folded back- and forward within the irreducible Brillouin zone, due to the discrete translational symmetry, see Figure 2.2-2. The resulting dispersion diagram of this folding action can be seen in Figure 2.2-3. This figure has been calculated using a plane wave expansion technique (PWE) [18]. The Bragg stack consists of alternating layers of silicon and silicon dioxide SiO_2, i.e., refractive indices of 3.4 and 1.44, respectively, for $\lambda = 1550$ nm. The figure shows that flat regions ($d\omega/dk \rightarrow 0$) exist at $k = \pi/a$, resulting in Bloch modes having a zero group velocity.

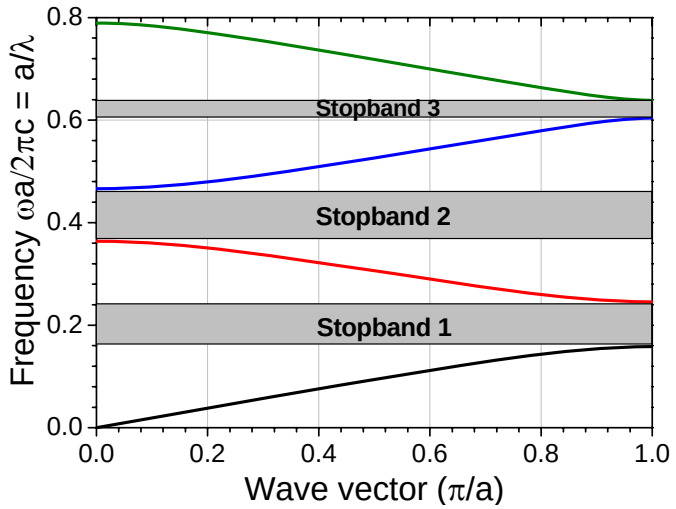

Figure 2.2-3: Dispersion graph of a Bragg stack with $\varepsilon_1=1.44^2$ (SiO_2), $\varepsilon_2=3.4^2$ calculated using a plane wave expansion method. The angular frequency is normalized by $a/2\pi c$ and the wave vector is normalized by π/a.

2.2.2 Waveguide gratings

In integrated optical devices the requirements of waveguiding imply that the refractive index (or dielectric permittivity) distribution is not invariant in all transversal directions, e.g. the refractive index n is a function of x: $n(x)$. A three-layer system consisting of a region with a high refractive index sandwiched between two layers of lower refractive index can form an optical waveguide [21]. A waveguide grating (WGG) also denoted as a quasi-one-dimensional photonic crystal (Q1D PhC), can be made by periodically modulating the refractive index along the propagating direction. In the work presented in this thesis, this periodic function $n(z)$ is realized by etching slits (grooves) perpendicular to the propagation direction into a high index Si_3N_4 (n = 1.98) guiding layer which is separated from the Si substrate by an SiO_2 (n = 1.44) buffer layer. The response of a WGG having a small indentation (or corrugation) can be approximated by substituting the effective index values of the tooth and groove of the grating for n_1 and n_2 in the TMM model to form a Bragg stack similar to that in section 2.2.1. For larger etch-depths this approach will not yield accurate results due to the out-of-plane loss (and problems of solving for a guided mode in the groove region). Therefore, the main difference between a Bragg stack and a WGG is the presence of out-of-plane loss, i.e. radiation into the substrate and the air cladding [11].

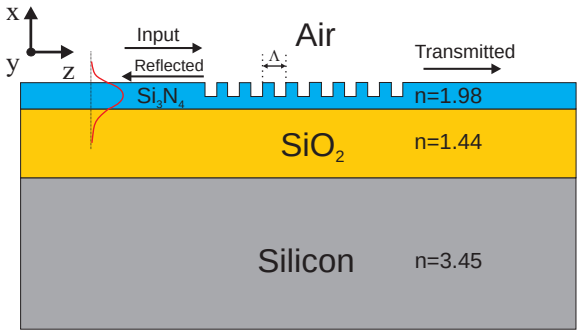

Figure 2.2-4: A cross-section of a waveguide grating.

The Bloch modes of a WGG, can be found by solving the eigenvalue problem presented in (3). The criteria for true guided modes with evanescent tails in the cladding layers is that the effective index of the Bloch mode ($n = kc/\omega$) should have a value higher than the substrate index, here n = 1.44. Solutions with an effective index below this value are extended in the cladding. They are referred to as radiation modes: their solutions (ω-k combinations) appear above the so-called light line in the dispersion diagram. The light line for the substrate is defined by $\omega = kc/n_{substrate} = kc/1.44$, see Figure 2.2-5.

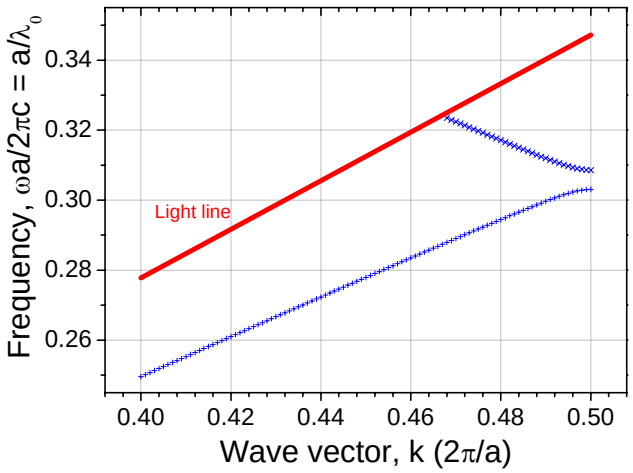

Figure 2.2-5: Normalized dispersion curve of a WGG (same as the one studied in section 4.3). Guided modes can be found below the light line with slope 1/1.44.

A more fundamental approach explaining the details of light lines in dispersion graphs or their equivalent, light cones in band diagrams, can be found in [22] or [18].

2.2.3 Phase and group velocity

In this section, expressions for the phase and group velocity are derived and it is shown how they can be obtained from the dispersion curve [21,23,24]. These expressions are used for other derivations presented in the next sections. To obtain an expression for the phase velocity, first the solution of the wave equation is written as a plane wave traveling along the *z*-axis,

$$E = E_0 e^{j(\omega t - kz)}, \tag{7}$$

were ω denotes the angular frequency and k the wave vector. The traveling speed of such a wave front is termed the phase velocity, i.e. the speed of constant phase,

$$e^{j(\omega t - kz)} = \text{constant}. \tag{8}$$

The position along the z-axis of constant phase can now be written as,

$$z(t) = \frac{\omega t}{k} + \text{constant}. \tag{9}$$

The speed of the wave front, the phase velocity, can be found by taking the time-derivative,

$$v_p = \frac{z(t)}{dt} = \frac{\omega}{k}. \tag{10}$$

The phase velocity in non-magnetic media with refractive index n is defined as,

$$v_p = \frac{c}{n}. \tag{11}$$

Modulating the amplitude of a plane wave, leads to an envelope traveling at a velocity termed the group velocity v_g. To obtain an expression for v_g, a similar derivation can be made as shown above for the phase velocity, but now the phase of the envelope is chosen to be constant. Let's consider the sum of two waves with slightly different angular frequency, $\omega_1 = \omega + \Delta\omega$ and $\omega_2 = \omega - \Delta\omega$. The corresponding wave vectors can be written as, $k_1 = k + \Delta k$ and $k_2 = k - \Delta k$. The total electric field can be written as the sum of both waves,

$$E = E_0 (e^{j((\omega+\Delta\omega)t-(k+\Delta k)z)} + e^{j((\omega-\Delta\omega)t-(k-\Delta k)z)}). \tag{12}$$

Rewriting this equation leads to,

$$E = E_0 e^{j(\omega t - kz)} (e^{j(\Delta\omega t - \Delta kz)} + e^{-j(\Delta\omega t - \Delta kz)}). \tag{13}$$

Substituting the complex notation of a cosine ($\cos(x) = 0.5(e^{jx} + e^{-jx})$), the following expression is obtained,

$$E = 2E_0 e^{j(\omega t - kz)} \cos(\Delta\omega t - \Delta kz). \tag{14}$$

Since a relatively small $\Delta\omega$ is chosen, i.e. $\Delta\omega << \omega$, it can immediately be seen that the amplitude is modulated along the propagation axes: a beating pattern moving along the propagation direction *z*. To find the velocity of the beating, we follow the same procedure as for the phase velocity, the phase of the cosine function should be taken constant, leading to the following expression for the group velocity,

$$v_g = \frac{dz}{dt} = \frac{\Delta\omega}{\Delta k}. \tag{15}$$

As the phase velocity could be found by taking the ratio of an (ω, k) pair obtained from the dispersion curve, the group velocity can be obtained by taking the tangent line to the curve in the (ω, k) point.

$$v_g = \lim_{\Delta\omega \to 0} \frac{\Delta\omega}{\Delta k} = \frac{d\omega}{dk}. \tag{16}$$

A group index n_g can be defined similar to the phase index n in (11),

$$n_g = \frac{c}{v_g}. \tag{17}$$

Since n, and consequently k and v_g are functions of frequency, also n_g is a function of frequency, which can be found by substituting (17) in (15) and applying the chain rule to obtain the derivative,

$$n_g = c\frac{dk}{d\omega} = c\frac{d(\omega n/c)}{d\omega} = c\left(\frac{n}{c} + \frac{\omega}{c}\frac{dn}{d\omega}\right) = n + \frac{1}{\lambda}\frac{dn}{d\lambda^{-1}}. \tag{18}$$

Using the mathematical identity $\frac{dy}{dx^{-1}} = -x^2\frac{dy}{dx}$, we find the following expression for the group index,

$$n_g = n - \lambda\frac{dn}{d\lambda}. \tag{19}$$

Finally, we remark that the velocity of an arbitrary pulse is not always simply the group velocity as it is sometimes stated. Equation (15) shows that the group velocity is defined in a small range close to zero around an (ω, k) pair. The spectral width of a Fourier transformed pulse, reaches a single value when the duration of the pulse goes to infinity. In many dispersion related experiments, however, the pulse bandwidth is far from zero, which in dispersive media can lead to strongly deformed pulses. In order to probe the dispersion curve using pulses, it is therefore necessary to make pulse bandwidth much smaller than the bandwidth of the probed system, as will be further described in section 4.3.

2.2.4 Fringes

The transmission spectrum of a finite periodic medium always shows fringes outside the stopband, if losses are not considered [25]. The fringes are caused by resonances of forward and backwards propagating (Bloch) waves [26,27], which are coupled by reflections from the end-facets, analogous to the waves in a Fabry-Perot resonator. These fringes may in some applications be unwanted, for example, in wavelength filters, because the fringes have a limited bandwidth making high speed operation at wavelengths near the stopband impossible. On the other hand, the fringes can be used to enhance the light matter interaction using the increased local energy density. A detailed study, discussing both experimental and theoretical results, can be found along with the references in section 4.3. In addition to the theory presented in that section, the number of fringes to be expected for a periodic medium is derived here; a first order Taylor approximation for the free spectral range formula; and an expression for the quality factor as a function of frequency and bandwidth.

2.2.4.1 Number of fringes

In this section, a value for the number of fringes N_F is derived in the frequency range between 2 stop gaps, see Figure 2.2-2. The number of fringes in a 1-D photonic crystal, or in a grating, can be found by applying the resonance condition [28]; the roundtrip phase φ is equal to an even multiple of π,

$$\varphi = 2kL = 2\pi m,\ \ m \in \mathbb{N}, \tag{20}$$

where L is the length of grating defined as the number of periods N, times the periodicity a. The difference in k between two adjacent resonances can written as,

$$\Delta k_{fringe} = \frac{\pi}{L}, \tag{21}$$

The first stopband is found at a free space wavelength where k equals π/a, see Figure 2.2-3. The next stopband is found at a wavelength where $k = 2\pi/a$. Therefore, the difference in wave number is equal to the irreducible brillouin zone,

$$\Delta k_{gaps} = \frac{\pi}{a}. \tag{22}$$

The total number of fringes due to the Fabry-Perot type oscillations can now easily be found by dividing (22) by (21),

$$N_F = \frac{\Delta k_{gaps}}{\Delta k_{fringe}} = \frac{\pi}{a}\frac{aN}{\pi} = N. \tag{23}$$

For a linear dispersion relation one would find a fixed $\Delta\omega$ for the Δk obtained from (21). However, the dispersion curve (ω, k) of a 1-D periodic medium can be better approximated by a quadratic function [26,29,30]. Therefore, in the experiments reported in this thesis we find that the fringes are closer stacked near the region of flat-curvature, where the change in effective index will be large, see equation (17) and (19).

2.2.4.2 Free spectral range

The wavelength spacing between two neighboring fringes is termed the free spectral range λ_{FSR}. An expression for λ_{FSR} can be found by applying the resonance condition (20) for two neighboring resonances, a procedure which is also outlined in [21]. The following relation is derived for a Fabry-Perot cavity consisting of 2 mirrors and an air-cavity,

$$\lambda_{FSR} = \frac{\lambda^2}{2nL}, \tag{24}$$

provided $\lambda_{FSR} << \lambda$. However, the equation cannot be applied to dispersive structures without errors. Therefore, a new expression needs to be derived, which takes into account the dispersion of waveguiding structures: the effective index n, is a function of wavelength. An expression for λ_{FSR} can be derived by using a linear approximation of the dispersion. To derive the $\lambda_{FSR,}$ the reference wavelength is defined exactly in the middle between two fringes. The resonance condition for two neighboring resonances can be written as,

$$2k_1L = 2\pi m, \quad 2k_2L = 2\pi(m+1), \quad m \in \mathbb{N}. \tag{25}$$

The phase constants k_1 and k_2 can substituted by first order Taylor approximations for $n(\lambda)$, using $n(\lambda+\Delta\lambda) - n(\lambda) = n(\lambda) - n(\lambda-\Delta\lambda) = \Delta n$.

$$k_1 = \frac{2\pi}{\lambda+\Delta\lambda}\left(n+\Delta n\right), \quad k_2 = \frac{2\pi}{\lambda-\Delta\lambda}\left(n-\Delta n\right). \tag{26}$$

A new expression for the resonance condition can be obtained by subtracting the expressions in (25) and substituting the expressions in (26) for k_2 and k_1, which leads to the following expression,

$$2L\left(2n\Delta\lambda - 2\Delta n\lambda\right) = \lambda^2 - \Delta\lambda^2. \tag{27}$$

This equation can be further simplified by rewriting expression (19) for small a small $\Delta\lambda$ region as,

$$n = n_g + \lambda\frac{\Delta n}{\Delta\lambda}, \tag{28}$$

and inserting it into (27). A new expression for λ_{FSR} (= $2\Delta\lambda$) is found for $\lambda >> \Delta\lambda$,

$$\lambda_{FSR} = \frac{\lambda^2}{2Ln_g}, \quad \lambda >> \lambda_{FSR}. \tag{29}$$

It shows that for a linear dispersive medium, λ_{FSR} can be written as a function of the group index. The expression can be used to find approximations for the group indices in dispersive media using the measured wavelength-dependent free spectral range [31-33]. The dispersion curve of a 1-D-PhC is often approximated by a quadratic curve as mentioned in the introduction of this section, but higher order dispersion terms [34] can also be expected, which may lead to even less accurate estimations for the group index.
To conclude it is expected that applying (29) may lead to inaccuracies in determining the group indices from the spectral measurement performed on, for example, a WGG. The largest differences between the estimated and actual values of the group indices may be found at the band edge, where the dispersion shows a strong curvature. A detailed experimental verification of this assumption is presented in section 4.3.

2.2.4.3 Quality factor

In this section, it is shown that the quality factor of a single (Lorentz type) resonance can be derived from its spectrum. The quality factor Q is defined as,

$$Q = -\omega_0 \frac{U}{dU/dt}, \tag{30}$$

where U is the energy stored in a resonator at the resonant angular frequency ω_0, and ($-T_0\, dU/dt$) is the energy loss in one period T_0 (= $2\pi/\omega_0$) of this frequency, see also section 4.3. Assuming an exponential decay of the total energy stored in a resonator, with decay time,

$$\tau_c = -\frac{U}{dU/dt}, \tag{31}$$

it follows that,

$$Q = \omega_0 \tau_c. \tag{32}$$

Solving the differential equation in (30) gives an expression for the envelope of time dependent energy stored in the resonator,

$$U(t) = U_0 e^{\frac{-\omega_0 t}{Q}}, \tag{33}$$

with U_0 the energy stored in the resonator at resonance at t = 0. Taking into account the field oscillations, the magnitude of the electric field, can be written as,

$$E(t) = E_0 e^{\frac{-\omega_0 t}{2Q}} e^{j\omega_0 t}, \tag{34}$$

with E_0 the electric field at t = 0. The spectral properties of the electric field can be found by Fourier transforming (34) multiplied with a Heaviside step function $u(t)$ (to avoid exponents with positive signs),

$$E(\omega) = \frac{1}{\sqrt{2\pi}} \int_{-\infty}^{\infty} E_0 e^{\frac{-\omega_0 t}{2Q}} e^{j\omega_0 t} u(t) e^{-j\omega t} dt, \tag{35}$$

The following expression can now be found for the electric field,

$$E(\omega) = \frac{A}{j(\omega - \omega_0) + \omega_0/2Q}, \tag{36}$$

with A as a constant. The energy U can now be obtained by taking the square of the absolute value of $E(\omega)$,

$$\left|E(\omega)\right|^2 = \frac{B}{(\omega - \omega_0)^2 + \left(\omega_0/2Q\right)^2}. \tag{37}$$

The full width at half maximum (FWHM=$\Delta\omega_{\text{-3dB}}$) of this function can be found by solving the quadratic equation for $|E(\omega)|^2 = 0.5\ |E(\omega_0)|^2$. The following expression for the FWHM is now derived,

$$\Delta\omega_{\text{-3dB}} = \frac{\omega_0}{Q}, \tag{38}$$

which can be rewritten as the following expression for Q,

$$Q = \frac{\omega_0}{\Delta\omega_{\text{-3dB}}}. \tag{39}$$

This well-known expression is often used to obtain the Q in practice from the spectrum of the resonator. However for the fringes near the stopband of the grating, the actual Q may differ from the Q obtained from (39), due to the large dispersion at these wavelengths, i.e. the response curve may not strictly be a Lorentz curve anymore. From the experimental results presented in section 4.3, we observed that the difference in Q is apparently small. In appendix A, a similar expression as (37) is derived for the transmission of a Fabry-Perot resonator [35].

2.2.4.4 Slow light and time-bandwidth product.

The slow-light phenomenon in photonic crystals is a popular topic. It has, for example, been proposed for time-delay applications [25,36]. However, ultra slow-light comes at the cost of a small bandwidth and high losses. Time-bandwidth products exceeding unity have been reported in e.g. [37,38]. The time-bandwidth product TB is defined as,

$$TB = \tau_{delay}\Delta\omega_{\text{-3dB}}, \tag{40}$$

with $\Delta\omega_{\text{-3dB}}$ as the bandwidth defined as the full width at half the maximum. Can we achieve slow light and a large bandwidth for a WGG? To answer that question, we refer to section 4.3 and the references therein. In that section we show, that the group delay τ_{delay} is equal to the decay time of the resonance τ_c, assuming a Lorentzian shaped resonance. This is a relatively good approximation, also for resonances in photonic crystal waveguides – compare the fringes in the results in [33,36], for example. In section 2.2.4.3 it is also derived that the Q for a Lorentz curve is equal to,

$$Q = \omega_0\tau_{res} = \omega_0\tau_{delay} = \frac{\omega_0}{\Delta\omega_{\text{-3dB}}}. \tag{41}$$

Therefore, the TB product can be written as,

$$TB = \Delta\omega_{\text{-3dB}}\tau_{delay} = \frac{\omega_0}{\omega_0} = 1. \tag{42}$$

A value for the TB product of 1 is found for the WGG which can be qualified as a minimum phase system (MFS), see for more details [24,39]. Furthermore, in general, MFSs allow for large delays, but these large delays are expected near the wavelengths where the amplitude also shows large changes [39]. Another promising method for achieving high TB products is by adding multiple non-MFS all-pass resonators with slightly shifted resonance wavelengths, although at the cost of

small ripples on the transmission. An example can be found in [39] or more recently in [40] in which a *TB* product of 3 was experimentally shown by combining 8 microring resonators (in 2-port configuration = all pass). The same principle could possibly be exploited for photonic crystals. Another alternative to create a larger *TB* is by perturbing holes adjacent to a photonic crystal waveguide which is shown in [41].
In [42] it is suggested that PhC waveguides can be modeled as waveguide gratings. Therefore, equation (21) may also apply to photonic crystal waveguides like in [37] [31], hence fringes will occur in the transmission spectrum due to de distributed Bragg effect [42]. These fringes could restrict the bandwidth in a similar way, resulting in a much lower *TB* product close to 1.
In that respect, the bandwidth from any finite linear time invariant system derived from its transfer function (impulse response), may yield different results than the bandwidth obtained from its dispersion diagram obtained from an infinite equivalent structure.

2.2.5 Waveguide grating designs

The design of the grating used for the cladding sensor measurement in section 4.2, can be found partially in this section and a detailed description can be found in the following M.Sc. thesis [43]. The design details for the gratings used in section 3.4 and 4.3 other than mentioned in the specified sections can be found in [44,45].

2.3 Photonic crystal waveguides

The section presents simulations and theory applicable to the specific (ePIXmask 2) design of the PhC waveguides used for the experiments presented in this thesis. For a more general theoretical description of other PhC waveguides we refer to [13,18].

2.3.1 Two-dimensional slab photonic crystals

The research presented in this sub-section focuses on 2-D photonic crystal slabs. Two-dimensional PhCs can be realized by combining, for example, two gratings at an angle of 90 degrees to form a square lattice or at an angle of 60 degrees to form a triangular lattice. The slab is used to confine light in its plane, similar as for the WGGs in section 2.2.2. However for the 2-D slab PhCs, the term quasi is omitted here.

2.3.1.1 Layer configuration

A silicon on insulator (SOI) [46] layer stack is used as a material system for realizing the photonic devices. The guiding layer is formed by a 220 nm Si (n = 3.45) layer on top of a 1 μm SiO_2 (n = 1.45) buffer layer. Since Si has an electronic bandgap, it is only transparent for photon energies smaller than the bandgap energy of 1.12 eV, i.e. the wavelength should be larger than 1.1 μm. The devices presented here were designed to operate around 1550 nm to ensure compatibility with telecom equipment and possible future telecom applications. All waveguides on the ePIXmask2 (see chapter 1) were designed to support only the fundamental mode. The cut-off width of the first order lateral mode for the rib waveguides, here referred to as photonic wires, was about 675 nm, therefore a 600 nm wide waveguide was chosen, see the figures below. This photonic wire supports only 1 mode and 1 polarization, namely the TE_{00} mode. The SOI wire doesn't support low loss propagation of the fundamental TM mode, because the TM_{00} suffers from high propagation loss ≈ 130 dB/cm due to substrate leakage [47].

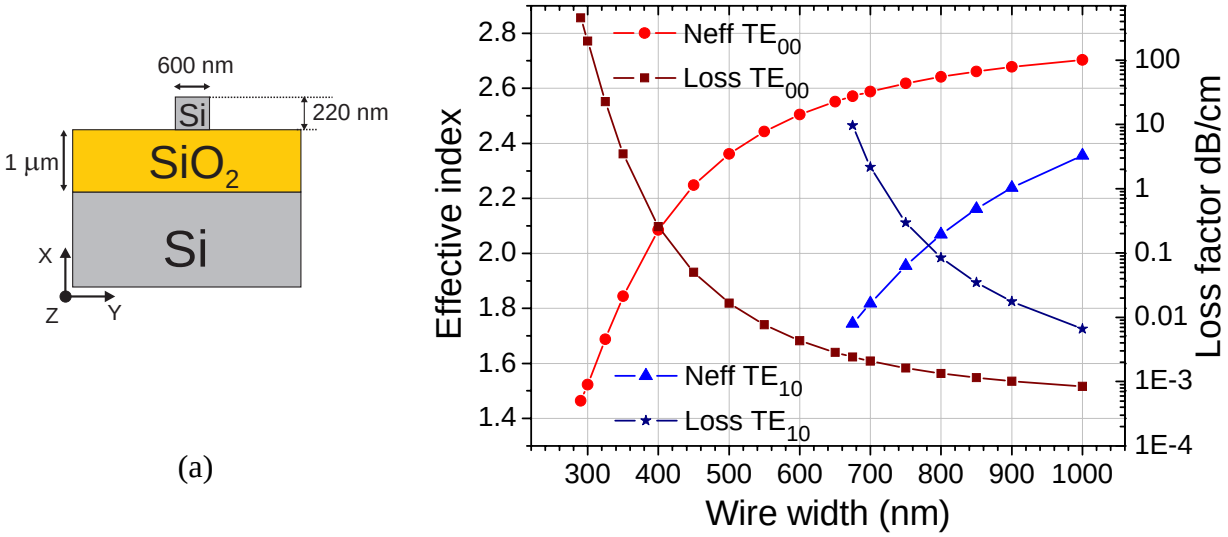

Figure 2.3-1: (a) Schematic drawing of the cross-section of a photonic SOI wire. (b)The effective index and propagation loss as function of the wire width for the fundamental (TE_{00}) and first order later mode (TE_{10}).

However, since the deep ultraviolet (DUV) exposure [48] was varied across the wafer, as a result, the wire-widths, (microring resonator) gaps and (photonic crystal) hole widths showed a variation of about 25 % around 600, 200 and 250 nm, respectively. Some of the wires discussed in section 2.5 could therefore also guide the first lateral TE mode, the TE_{10}.

The real and imaginary part of the effective index of the quasi-TE (q-TE) modes of the photonic wire shown in Figure 2.3-1b were calculated using a commercially available finite difference mode solver: Olympios from C2V [49]. Their so-called "FD Generic" solver is based on the well-known finite difference method, initially solving Maxwell's equations in terms of the transversal magnetic field **H**(x,y), using a staggered grid. This full vectorial complex mode solver uses perfectly matched layers (PMLs) as boundary conditions. The strength of the PMLs can be adjusted. These settings have been optimized for convergence before performing the final calculations presented in Figure 2.3-1b. The settings were chosen as follows:

Table 2.1. Mode solver settings.

Parameter	value
PML Reflectivity	$1*10^{-100}$
Number of PML points	15
Maximum number of iterations	10
Maximum iteration depth	$1*10^{-10}$
Number of Grid points (x,y)	250×250
Wavelength	1550 nm

The number of grid points used within the PMLs is reduced by the number of grid points in each PML, i.e. a grid of 100 x 100 results in an effective grid of 70 x 70, with 15 grid points in each PML layer. Further details on the accuracy of the loss calculation can be found in [47] and further details about the dispersion of photonic Si wires can be found in [44].

2.3.1.2 Lattice configuration & band diagram

A triangular lattice was chosen for its large bandgap and its potential for integration of high-*Q* cavities [2,7]. The PhC lattice consists of round air holes in a high dielectric material. Since the thickness of the Si top layer was fixed by our partners (Ghent University), the only parameters that

could be tuned were the hole diameter and the lattice constant within the range of the available DUV lithography. A graphical representation of the triangular PhC slab omitting the SiO_2 buffer layer is shown in Figure 2.3-2a. The two main crystal orientations are denoted by ΓK and ΓM. The *Band diagram* can be obtained by plotting the frequency as function of wave vector ($k_{||}$) in the in (yz-) plane. The edges of the bands can be found by sweeping ($k_{||}$) over the contour of the irreducible Brillouin zone. The photonic bandgap (BPG) is the frequency range in which no wave vector solutions are found (in any direction within the *zy*-plane), i.e. light is not extended within the photonic crystal. However a non-propagating evanescent field can build up at a boundary inside a PhC.

The band diagram, shown in Figure 2.3-2b. was obtained using a plane wave expansion (PWE) technique [18], first in 3 dimensions, taking into account a good approximation of the geometry using a 25 nm grid size. As we are interested in TE polarization, we only focus on even modes (the H_x-field having an antinode exactly in the middle of the slab), which are sometimes referred to as H-like modes [18]. After performing the time-consuming 3-D simulation we reduced the number of dimensions from 3 to 2 by an iterative process minimizing the differences in PBGs by changing the (effective) index of the holes and the slab. An initial guess for the slab index was obtained using a mode solver [17] resulting in an index of 2.805 for a wavelength of 1550 nm.

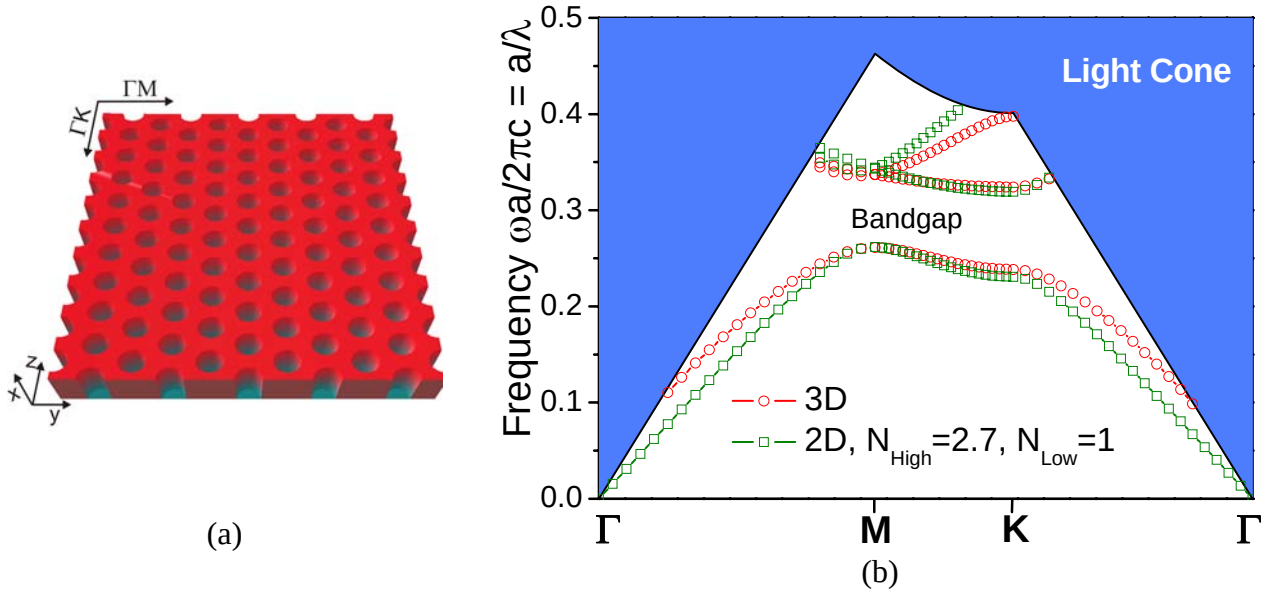

Figure 2.3-2: (a) PhC slab, the substrate has been omitted for visualization (b) Band diagram of the SOI slab PhC showing the normalized frequency as function of $k_{||}$.

In section 2.3.1.1 it was shown that the effective index of the channel mode varies as a function of the channel width, therefore the slab effective index approximation is not likely to yield very accurate results. The holes were best represented by a region of a refractive index equal to 1. The resulting band diagram, after scanning the two index parameters, is also shown in Figure 2.3-2b. The best fit was found for a slab index of 2.7 and a hole index of 1, taking the size and position of the first PBG as the fit criterion. Therefore, the two band diagrams show a reasonable agreement regarding the size and frequency position of the first PBG. The 2-D curve deviates from the 3-D curve at the lower frequencies where the Bloch modes decrease in confinement within the thin slab leading to lower effective refractive indices, which is obviously not accounted for by the 2-D model. Based on the PBG in the band diagram we expect for the 440 nm lattice a stopband in the ΓK direction between ~1290 and 1690 nm (a/λ = 0.34, a/λ = 0.26).

2.3.1.3 Transmission spectrum

Although the band diagram in Figure 2.3-2b shows that there are no guided modes within the PBG, the transmission will not be zero for a finite PhC due to evanescent waves that can couple light through the PhC slab. To find the transmitted power (transmission) as a function of wavelength we modeled a 12-layer (5.5-period) long and 29 layer wide PhC slab in the ΓK direction. A 2-D finite difference time domain (FDTD) method was used to calculate the transmission and reflection. The same refractive index parameters and calculation grid size were used as in simulation mentioned in the previous section. Figure 2.3-3a shows the model that was used to calculate the transmission and reflection. A fundamental mode is launched in the PhC direction and the power is monitored at two positions to obtain both the reflected and transmitted power. Because we use waveguides to feed and collect the light to and from the crystal, some of the transmitted and/or reflected light may be lost, because it can not couple to the waveguides, hence it is absorbed by the PMLs. It is important to make the calculation window a little bit smaller than the structure dimensions. In this way the absorbing PML-layers prevent reflections at the end-faces. However, it is obvious that for comparison with measured transmission the exact structure should be contained within the PMLs.

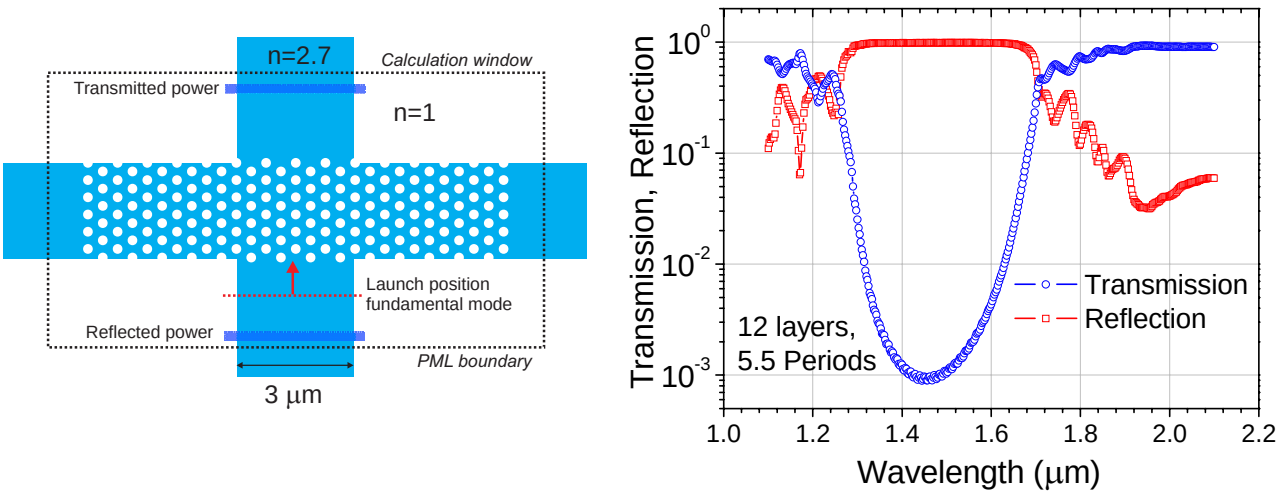

(a) (b)

Figure 2.3-3: (a) FDTD model for simulating the transmission through a ΓK oriented PhC slab of 29 by 12 layers. (b) Transmission, reflection of the PhC slab.

For only 12 layers of holes (5.5 periods) we find a maximum transmission dip of 3 orders of magnitude. In this low transmission range, almost all the light is reflected back into the feeding waveguide. The transmission dip is found exactly at the position were we would expect it based on the band diagram in Figure 2.3-2b. We also observe fringes next to the stopband, which are caused by standing waves within the crystal region; the Fabry-Perot like resonances.

2.3.2 Photonic crystal waveguides

In principle PhCs without defects can, for example, be used for negative refraction lenses [50,51], lasers [52,53] (exploiting the Γ-point) and polarization filters [54-56]. However, even a larger variety of functions may be realized by adding defects to the PhC. These defects can introduce local states within the forbidden band of energies. A line defect can be made by removing 1 layer of holes. This line defect can serve as a waveguide for optical modes. Figure 2.3-4a shows a typical configuration of a ΓK oriented line defect in a photonic crystal slab (the SiO_2 buffer layer has been omitted for visualization). A line defect consisting of a single removed row of holes is termed a W1 waveguide and removing two rows of holes will result in a W2 waveguide. It is also

possible to make smaller waveguide widths by shifting the two photonic crystal blocks closer together (for optimizing bandwidth [57]), making, for example, a 0.7W waveguide. A PhC waveguide can guide light by effective index guiding and also by gap guiding exploiting the PBG properties. The index guiding principle is similar to normal waveguides when the effective index of the optical mode is higher than the effective medium at both sides of the line waveguide. At larger wavelengths, were the light doesn't see the individual holes, we expect only effective index guiding. The dispersion curve of a line defect waveguide can be found using the projected band diagram approach [18].
The projected band diagram of the W1 line defect shown in Figure 2.3-4b is calculated defining a 9 holes wide supercell and a grid size of 25 nm using a PWE technique. Within the PBG, we now find, depending on the frequency, either two, one or zero guided mode solutions. In general, the nearly flat curve belongs to a gap-guided mode, see, for example [57], whereas linear curves, in general, belong to index guided modes.

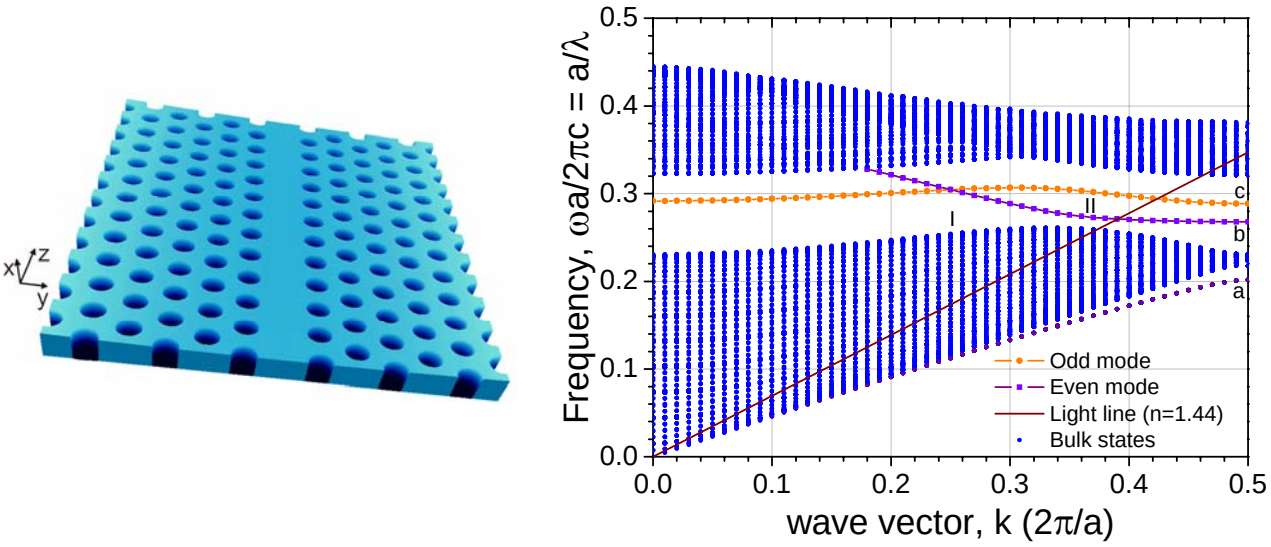

(a) (b)

Figure 2.3-4: (a) A perspective view on a photonic crystal slab W1 waveguide (visualized without SiO_2 buffer). (b) The projected band diagram of a W1 line defect. A crossing of the even and odd mode takes place at point I and an anti-crossing between the even guided mode and bulk states takes place at point II. The distributions of the field profiles (H_x^2) associated with the modes labeled by a, b and c are displayed in Figure 2.3-5.

We can distinguish two modes within the PBG, an even and an odd mode, see the corresponding field distributions in Figure 2.3-5. The dispersion curve of the even mode is a superposition of an index guided and gap guided mode, therefore it is sometimes referred to as a super mode. At point II in Figure 2.3-4b the gap-guided even mode has an *anti-crossing* [31,32,58,59] with the index guided even mode; they have equal group velocities with opposite signs within this folded representation. At point I the even and odd mode cross each other: a *crossing*; they do not interact. Furthermore, there is small *mode-gap* within the PBG between a/λ =0.262 and a/λ=0.267 (1648 to 1679 nm), which is caused by the anti crossing of the even mode. Although in 2-D calculations there can be no leaking to the top and bottom substrate, because the method produces solutions that are invariant perpendicular to the plane of calculation, we do include the light line because the structure is a representation of a 3-D PhC slab where leakage to the substrate is a physical possibility. Solutions found above this line are leaky modes; they can, however, be measured using near field techniques [19,60]. The further such a mode is above the light line, the lossier it becomes. Therefore, low loss guided modes should be designed to operate at frequencies below the light line.

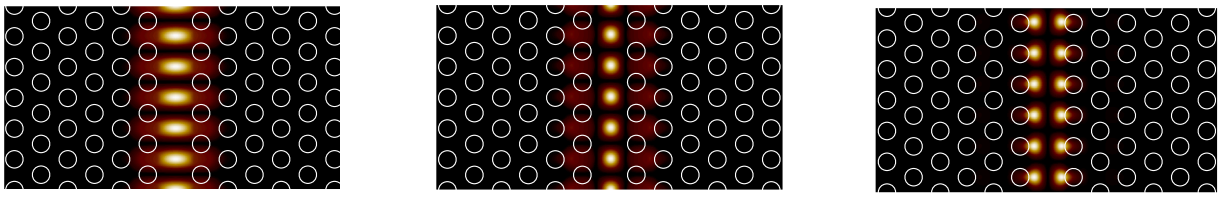

(a) (b) (c)

Figure 2.3-5: Visualization of the squared H-field distribution (H_x^2) of guided modes in a W1 line defect, see Figure 2.3-4. (a) index guided (even) mode a/λ=0.2, the effective index (n) at this frequency is n=2.4796 (b) Even mode at a/λ=0.27, n=1.8671. (c) Odd mode at a/λ=0.29, n= 1.7347.

2.3.2.1 Transmission simulation

Since it is impossible to design optical functions based on 3-D slab PhCs using analytic solutions, numerical methods are essential for predicting the device behavior. Here we use again an FDTD method to model a 20-period long W1 waveguide with 15 layers at each side of the line defect and similar settings as mentioned in the previous sections. Light was coupled into the line defect by a 600 nm wide photonic wire, similar to the ePIXmask2 design. The advantage of the FDTD method was fully exploited by launching a short pulse and Fourier transforming the monitored transmitted and reflected power to save computation time. Despite the fact that the calculation is 2-D, it can still be time consuming on the current PCs. The result shown in Figure 2.3-6 was obtained after 5 hours of calculations on a Pentium 4, 2.8 GHz machine.

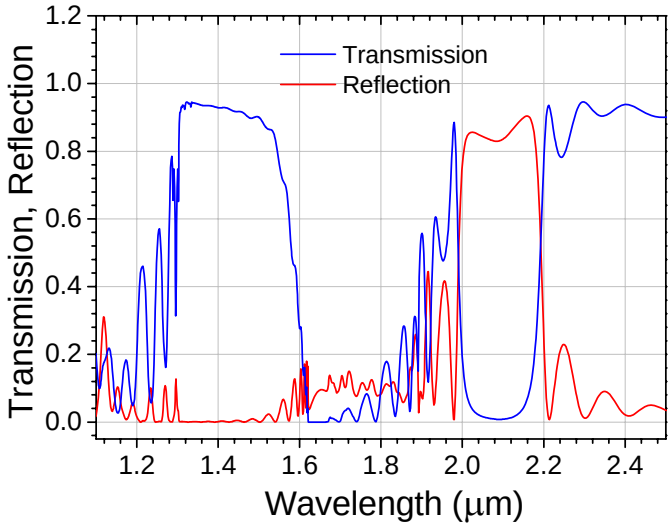

Figure 2.3-6: Simulated transmission and reflection of a 20-period long W1 waveguide.

An even mode is mainly excited, because we use a single mode input, hence the overlap with the odd modes is negligible due to symmetry reasons. In Figure 2.3-6 we find (almost) full transmission within the PBG. At the edges of the PBG we observe fringes indicating the presence of resonances. At higher wavelengths there is another stop gap due to the DBR effect.

2.4 Photonic crystal resonators

Photonic crystals are *the* building blocks for small–sized high–*Q* dielectric optical resonators. The small modal volume (*V*) of the microcavity MC can result in a high *Q*/*V* [61] ratio compared to, for example, the microring resonators discussed in section 2.5 The advantage of high *Q* over *V* ratios

is that high *Q*s in small volumes result in high energy densities which, for example, can be exploited for sensing and non-linear processes [2]. The ratio *Q*/*V* is often used a number of merit for a PhC MC. The advantage of this ratio is that it gives a measure for the expected spontaneous emission enhancement [62]. However, the drawback of the definition for *V* is that the actual modal volume may differ from the calculated volume, due to the influence of fabrication errors. The modal volume is often approximated by the physical volume of the resonator. Simulations show that the resonances can extend (as evanescent fields) far into the crystal, see Figure 2.4-3a. Therefore it remains to be seen how well the modal volume can be approximated by the physical volume of the resonator.
An alternative figure of merit for quantifying a PhC MC resonance could the finesse (*F*), which is a measure for the wavelength selectivity,

$$F = \frac{FSR}{FWHM} = Q\frac{\lambda_{FSR}}{\lambda}. \tag{43}$$

However, we should note that the FSR can be large in PhC MCs, resulting sometimes in only 1 resonance order located in the PBG, making it difficult predicting *F*.

For telecom-related applications it is often required that the available bandwidth is large enough to support Gbit/s data transmission. Therefore, it is not desired to have ultra high *Q*s, see equation (32). On the other hand, high field intensities are required to enable switching using a nanosized probe, see section 4.4 and 4.5. For these reasons, PhC MCs (high *Q*/*V* ratios) may be viable candidates to provide a good trade-off between speed and sensitivity, if the trend of loss reduction is continued. A maximum allowed *Q*-factor can be estimated if we assume a preferred data transfer speed of for example 50 Gb/s. The delay time of the resonator should at least be smaller than the duration of a single bit [63]. The maximum *Q* can be calculated from (43) resulting in an upper limit for the *Q* of $\approx 2.5\times10^4$.

2.4.1 ePIXmask2 design

The goal of the research project described in chapter 1 is to realize switching functionality in a PhC slab. Such a switching function may require complicated designs that demand high resolution fabrication processes. To explore the nanomechanical tuning experimentally, we designed a straightforward resonator inspired by the results published in [64]. Successful integration of various photonic crystal resonators design can be found in [2,8,61,64-67]. The principle of the here presented PhC MC is analogous to the well-known Fabry-Perot resonator. The original design is shown in Figure 2.4-1a. W1 waveguides are used for feeding light into and out of the cavity. At resonance a standing wave pattern can build up inside the resonator. The holes terminating the cavity at both sides act as reflectors; adding more holes will increase the *Q* if the fabrication induced losses are kept low.

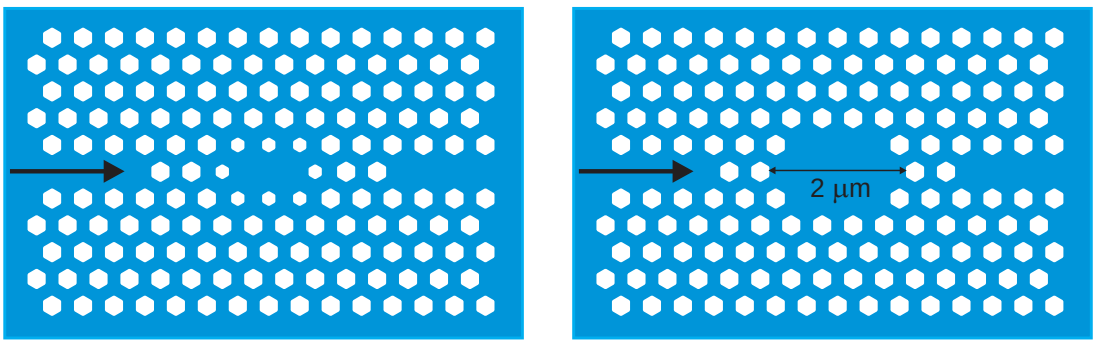

Figure 2.4-1: (a) PhC resonator design, incorporating smaller holes with a diameter of 180 nm at the (inner) circumference of the cavity. (b) The resulting cavity configuration after processing, the small holes were underexposed, hence not etched.

In the ePIXmask design, the holes are defined as hexagons because these polygons require only 6 coordinates which helps to keep the mask file size within the machine limits. The DUV exposure [68] will average out the sharp corners, resulting in round holes. The initial design had smaller holes inside the cavity which has been shown to increase the *Q* [69]. A hole diameter of 180 nm was chosen for these smaller holes inspired by the results published in [2]. After fabrication, we observed by SEM and microscope inspection (see appendix B), that these holes were not etched into the silicon. The resulting PhC MC is shown in Figure 2.4-1b.
Both resonators were also modeled using an FDTD scheme, but now with increased grid spacing set to 40 nm to speed up the simulations. Of course, the higher the *Q*, the larger the simulation time needs to be. Both resonators were integrated in a relatively large PhC array of 41 by 21 layers, to minimize the possible absorption by the PMLs. The effective indices chosen for these simulations were $n = 2.9$ and $n = 1$. The lattice period (440 nm) and the holes sizes (250 nm), were unmodified except for the holes inside the cavity (diameter = 180 nm), see Figure 2.4-1a. In section 2.3.1.2 it was shown that the PBG of a planar PhC slab obtained using a 2-D model could reasonably be matched with the 3-D results. However, for the resonators this may be different: each resonator has it own geometry and consequently particular modal distribution, leading to different representation in terms of effective indices. The *Q* values obtained from the 2-D simulations may differ from the actual *Q*s, due to the fact that the out-of-plane loss is not accounted for in 2-D simulations.

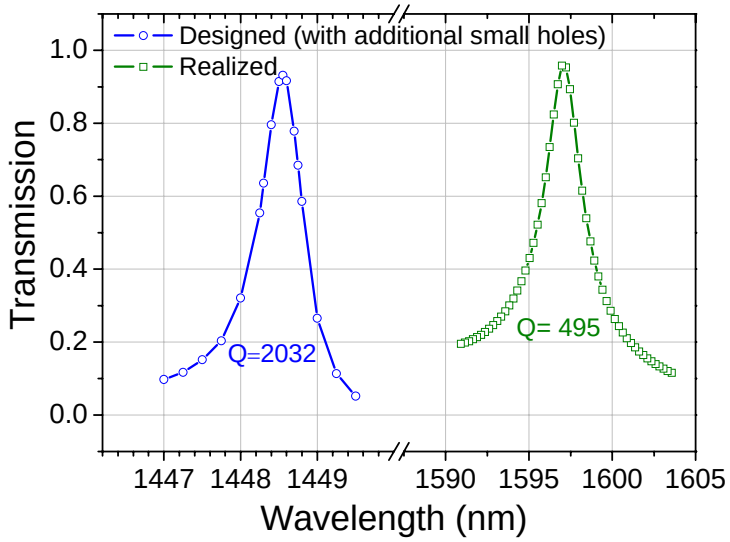

Figure 2.4-2: Transmission simulation of the cavities shown in Figure 2.4-1. The original cavity has (for the refractive indices used in the 2-D model) a Q of 2032, whereas the realized cavity has a Q of 495. However, the Qs are highly dependent on the spectral position within the PBG and thus on the refractive indices used in the 2-D simulation.

Using a 2-D FDTD method we found for the original PhC MC configuration a *Q* of 2032 at a resonance wavelength of 1488.55 nm. For the realized configuration shown in Figure 2.4-1b, we found a smaller *Q* of 495 at a resonance wavelength of 1597 nm, which is even lower than the measured *Q*, as is shown in section 4.5. However, in section 4.4, it is shown that similar *Q* values are found both in the simulations and in the measurements, when a refractive index of 2.9 for the slab is used and the ratio *R*/*a* is slightly detuned. Clearly, the *Q*s are highly dependent on the spectral position within the PBG (the reflectivity is wavelength dependent) and thus on the refractive indices used in the 2-D simulation. For a full agreement, it is obvious that 3-D simulations are required.

The field distributions of both simulated modes are quite different as can be observed in Figure 2.4-3. To visualize the resonance pattern, we performed a FDTD simulation at the resonance

wavelengths of both cavities. Next, the square of the *H*-field component perpendicular to the periodicity (along the air-holes) is plotted using a clipped scale: the maximum of the scale was fixed to the squared magnitude of the launched mode. The convenience of this type of plotting is that is shows how the field extends into the crystal. Figure 2.4-3a shows a quadrupole type pattern (neglecting the inputs and outputs), the resonance "extends" into the weakly confined ΓM direction, similar as in [67]. The light outside the cavities shows an exponential decay, therefore most of the light is still confined within the cavity. However, the exponential tails are even larger for higher-*Q* cavities, therefore this field should be taken into account when calculating the *Q* over *V* ratio. Another conclusion can be drawn from the modal distribution: it is important for these high-*Q* cavities to over-design the photonic crystal region for realization, because the evanescent tail can be converted into radiation at the crystal borders, ergo lowering the *Q*. Figure 2.4-3b shows the pattern obtained from the larger MC. A more detailed representation of the optical resonance within the cavity can be found in section 4.4.

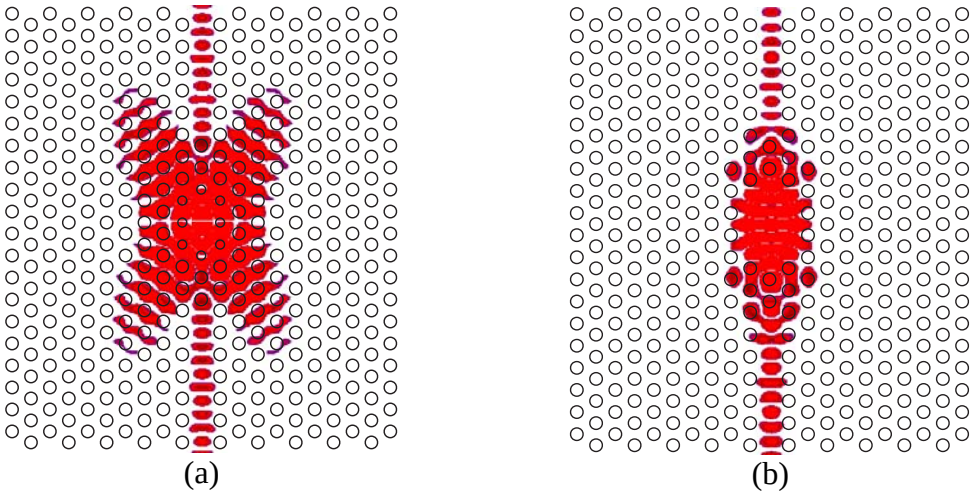

Figure 2.4-3: (a) Field pattern calculated at the resonance wavelength of the MC in Figure 2.4-1a. The type of scaling is explained in the text. (b) The Field pattern obtained for the cavity in Figure 2.4-1b.

2.5 Microring resonator

Microring resonators (MRRs) can be more easily realized than cavities in a PhC slab, as they are based on conventional waveguiding optics. These devices are perfectly suitable for switching applications [70,71]. The MRR has shown its value in, for example, sensing [72,73] and telecom applications [4,5]. In this thesis we investigate a 4-port configuration consisting of a ring and two waveguides separated by a small gap to allow evanescent coupling, as is depicted in Figure 2.5-1. The "microring" under study is actually a racetrack design to increase the power coupling constant (K) to the ring by increasing the coupling length L_c. Light is launched into port I towards port II (the through-port). Some of the light will couple to the ring at the coupling section. If the resonator mode is in phase with the light coupled in from the waveguide after a roundtrip, the power inside the MRR will build up due to constructive interference. The energy density in the MRR then increases until an equilibrium state has been reached between the power coupled to the MRR and the power loss per roundtrip. The latter loss in power is caused by propagation loss and power coupling back from the MRR to the waveguides. At resonance, depending on the coupling conditions, power from port I can be dropped to port IV. The general resonance condition in equation (20) can be rewritten for a "circular" MRR as,

$$\varphi = 2\beta\pi R = 2\pi m, \quad m \in \mathbb{N}, \tag{44}$$

with *R* defined as the radius of the ring waveguide. The free spectral range can also be derived using the procedure described in section 2.2.4.2 leading to a similar expression as in (29),

$$FSR = \frac{\lambda^2}{2\pi R n_g}, \quad \lambda >> \Delta\lambda. \tag{45}$$

The wavelength selectivity of the filter, the finesse, can be expressed as the ratio between the FSR multiplied with the *Q* and the resonance wavelength of the Lorentzian shaped drop response [24] as mentioned also in the previous section,

$$F = \frac{FSR}{FWHM} = Q\frac{\lambda_{FSR}}{\lambda} = Q\frac{\lambda}{2\pi R n_g}. \tag{46}$$

It can directly be seen that F can be increased by decreasing the roundtrip length by reducing R. The MRR can not be made as small as the PhC MCs, because of the presence of high bending loss for small radii. The maximum Q factor that can be reached by optimizing K (by tuning the gap) is determined by the roundtrip loss α (in dB/cm), which is the sum of the bend loss and the material loss [9].
Since we used the DUV at different exposure doses, we obtained a variety of waveguides and gap widths. A small gap is needed to have sufficient coupling between the ring and the waveguide. However, in our case, selecting a MRR with a small gap may unwontedly introduce wider, possibly, multi moded waveguides. The selected MRR had a gap of 200 nm, which was estimated from the SEM images. This is approximately the smallest gap that can be realized using DUV at λ = 248 nm. The widths of the waveguides and microring waveguides were approximately 700 nm. Therefore, it supports two modes, the TE_{00} and TE_{10} mode, see Figure 2.3-1b. The racetrack design, by Edwin Klein [74], has two curved sections of 20 μm radius and 2 coupling sections of 5 μm length, leading to a total path length of ≈ 136 μm, see Figure 2.5-1.

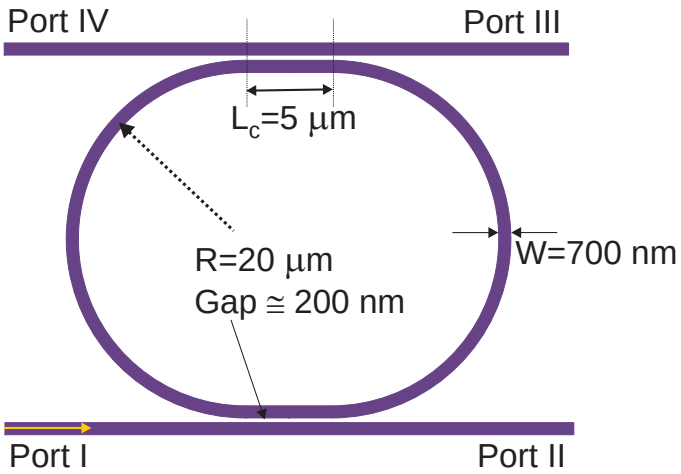

Figure 2.5-1: The microring resonator design used for the mechano-optical experiments reported in this thesis.

The MRR was also modeled using a 2-D FDTD method. The real part of the refractive index of the MRR and waveguides was obtained from Figure 2.3-1b: n_{real} = 2.6. The propagation loss can be modeled via the imaginary part of the refractive index n_{im}.

$$n = n_{real} + in_{im}. \tag{47}$$

It is quite common to express the guiding loss α in dB/cm. The imaginary part (*k*) of the refractive index can then be expressed as function of α,

$$n_{im}(\alpha,\lambda) = \frac{\alpha\lambda}{4\pi\log_{10}(e)}. \tag{48}$$

The MRR structure in Figure 2.5-1 was simulated for α = 10 dB/cm, which might be slightly larger than the actual optical loss in the fabricated structure. However, higher loss helps to reduce computing time due to the faster convergence; the simulation (obtained via the pulse response) in Figure 2.5-2 took already 4 days on a 2.8 GHz Pentium 4 PC. The simulation was smoothened using a moving average over 3 points. The 2-D FDTD simulation of our design shows that the optimal working range is around λ = 2.1 μm, which should have been around λ = 1.55 μm, because the wavelength range of our tunable laser (HP 6168c) is 1460-1600 nm. The optimal working range is defined as the wavelength (here λ = 2.1 μm) where the drop-response equals the through response, allowing symmetric switching between both ports, see Figure 2.5-2a. In the tunable wavelength range of our laser, see Figure 2.5-2b for a zoom in on a resonance, we find a reasonable on/off ratio in the drop response but only a small ratio in the through response, which is obviously not ideal for switching. The ideal working point can be shifted to shorter wavelengths by increasing the coupling constant *K*, either by decreasing the gap or increasing the coupling length. Since the gap has already been designed near the smallest feasible gap for the DUV lithography at 248 nm, it is preferable to increase the length of the coupling region. This strategy has been applied in a new design, which is not described further in this thesis.

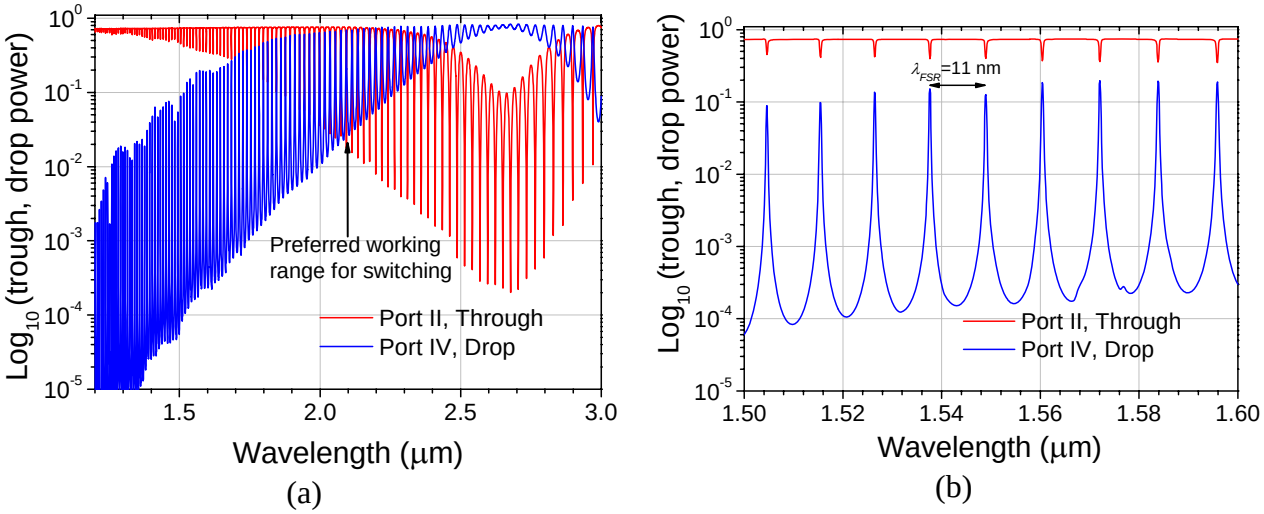

Figure 2.5-2: (a) The results of a 2-D FDTD simulation on the racetrack MRR shown in Figure 2.5-1. The graph has been smoothed (adjacent averaging over 3 points), because the number of data points was not high enough to show the trends clearly. (b) A zoom-in on the wavelength region of interest.

Switching between the through and drop ports of the MRR can be achieved by detuning the resonance wavelength. A nanomechanical tuning mechanism has been presented for a PhC MC in [3]. In chapter 5, we will show the preliminary nanomechanical tuning and interaction results of the here described MRR.
More details about MRR theory and specially design issues can be found in [74].

2.6 References

[1] W. C. L. Hopman, P. Pottier, D. Yudistira, J. van Lith, P. V. Lambeck, R. M. De La Rue, A. Driessen, H. J. W. M. Hoekstra, and R. M. de Ridder, "Quasi-one-dimensional photonic crystal as a compact building-block for refractometric optical sensors", *IEEE Journal Of Selected Topics In Quantum Electronics*, vol. **11**, pp. 11-16, 2005.

[2] M. Notomi, A. Shinya, S. Mitsugi, G. Kira, E. Kuramochi, and T. Tanabe, "Optical bistable switching action of Si high-Q photonic-crystal nanocavities", *Optics Express*, vol. **13**, pp. 2678-2687, 2005.

[3] W. C. L. Hopman, K. O. Van Der Werf, A. J. F. Hollink, W. Bogaerts, V. Subramaniam, and R. M. De Ridder, "Nano-mechanical tuning and imaging of a photonic crystal microcavity resonance", *Optics Express*, vol. **14**, pp. 8745-8752, 2006.

[4] D. H. Geuzebroek, E. Klein, H. Kelderman, N. Baker, and A. Driessen, "Compact wavelength-selective switch for gigabit filtering in access networks", *IEEE Photonics Technology Letters*, vol. **17**, pp. 336-338, 2005.

[5] E. J. Klein, D. H. Geuzebroek, H. Kelderman, G. Sengo, N. Baker, and A. Driessen, "Reconfigurable optical add-drop multiplexer using microring resonators", *IEEE Photonics Technology Letters*, vol. **17**, pp. 2358-2360, 2005.

[6] W. C. L. Hopman, R. Dekker, D. Yudistira, W. F. A. Engbers, H. Hoekstra, and R. M. de Ridder, "Fabrication and characterization of high-quality uniform and apodized Si_3N_4 waveguide gratings using laser interference lithography", *IEEE Photonics Technology Letters*, vol. **18**, pp. 1855-1857, 2006.

[7] Y. Akahane, T. Asano, B. S. Song, and S. Noda, "High-Q photonic nanocavity in a two-dimensional photonic crystal", *Nature*, vol. **425**, pp. 944-947, 2003.

[8] E. Kuramochi, M. Notomi, S. Mitsugi, A. Shinya, T. Tanabe, and T. Watanabe, "Ultrahigh- Q photonic crystal nanocavities realized by the local width modulation of a line defect", *Applied Physics Letters*, vol. **88**, pp. 041112/1-3, 2006.

[9] J. Niehusmann, A. Vörckel, P. H. Bolivar, T. Wahlbrink, W. Henschel, and H. Kurz, "Ultrahigh-quality-factor silicon-on-insulator microring resonator", *Optics Letters*, vol. **29**, pp. 2861-2863, 2004.

[10] J. H. Berends, PhD thesis, "Integrated optical Bragg reflectors as narrowband wavelength filters", ISBN: 90-9010241-8, University of Twente, Enschede, 1997.

[11] J. Ctyroky, S. Helfert, R. Pregla, P. Bienstman, R. Baets, R. De Ridder, R. Stoffer, G. Klaasse, J. Petracek, P. Lalanne, J. P. Hugonin, and R. M. De La Rue, "Bragg waveguide grating as a 1D photonic band gap structure: COST 268 modelling task", *Optical and Quantum Electronics*, vol. **34**, pp. 455-470, 2002.

[12] D. Lusk, I. Abdulhalim, and F. Placido, "Omnidirectional reflection from Fibonacci quasi-periodic one-dimensional photonic crystal", *Optics Communications*, vol. **198**, pp. 273-279, 2001.

[13] J. D. Joannopoulos, R. D. Meade, and J. N. Winn, "Photonic crystals: Molding the flow of light", ISBN: 0-691-03744-2, Princeton University Press, 1995.

[14] A. V. Vinogradov & B. Y. Zeldovich, "X-Ray and far UV multilayer mirrors: principles and possiblities", *Applied Optics*, vol. **16**, pp. 89-93, 1977.

[15] A. Yariv & H. W. Yen, "Bragg amplification and oscillation in periodic optical media", *Optics Communications*, vol. **10**, pp. 120-122, 1974.

[16] P. Yeh & A. Yariv, "Bragg Reflection Waveguides", *Optics Communications*, vol. **19**, pp. 427-430, 1976.

[17] Simulayer, version **1.09**, by R. Dekker, www.daglain.com.

[18] C. G. Bostan, PhD thesis, "Design and fabrication of quasi-2D photonic crystal components based on silicon-on-insulator technology", ISBN: 90-365-2155-6, University of Twente, Enschede, 2005.

[19] H. Gersen, T. J. Karle, R. J. P. Engelen, W. Bogaerts, J. P. Korterik, N. F. van Hulst, T. F. Krauss, and L. Kuipers, "Direct observation of Bloch harmonics and negative phase velocity in photonic crystal waveguides", *Physical Review Letters*, vol. **94**, pp. 123901/1-4, 2005.

[20] C. Kittel, "Introduction to Solid State Physics", ISBN: 0-471-49024-5, Wiley, New York, 1953.

[21] P. V. Lambeck & R. M. de Ridder, "Optical basic functions and microsystems", Integrated optical microsystems group, University of Twente, Enschede, 2006.

[22] S. G. Johnson, S. H. Fan, P. R. Villeneuve, J. D. Joannopoulos, and L. A. Kolodziejski, "Guided modes in photonic crystal slabs", *Physical Review B*, vol. **60**, pp. 5751-5758, 1999.

[23] D. K. Cheng, "Field and wave electromagnetics", (ed. Rifkind, B.), ISBN: 0-201-52820-7, Addison-Wesley, 1989.

[24] C. K. Madsen & J. H. Zhao, "Optical filter design and analysis: a signal processing approach ", (ed. Chang, K.), ISBN: 0-471-18373-3, John Wiley & Sons, New York, 1999.

[25] A. Figotin & I. Vitebskiy, "Slow light in photonic crystals", *Waves in Random and Complex Media*, vol. **16**, pp. 293-382, 2006.

[26] H. J. W. M. Hoekstra, W. C. L. Hopman, J. Kautz, R. Dekker, and R. M. de Ridder, "A simple coupled mode model for near band-edge phenomena in grated waveguides", *Optical and Quantum Electronics*, vol. **38**, pp. 799-813, 2006.

[27] D. W. L. Sprung, H. Wu, and J. Martorell, "Scattering by a finite periodic potential", *American Journal of Physics*, vol. **61**, pp. 1118-1124, 1993.

2.6 References

[28] J. M. Bendickson, J. P. Dowling, and M. Scalora, "Analytic expressions for the electromagnetic mode density in finite, one-dimensional, photonic band-gap structures", *Physical Review E - Statistical Physics, Plasmas, Fluids, and Related Interdisciplinary Topics*, vol. **53**, pp. 4107-4121, 1996.

[29] M. L. Povinelli, S. G. Johnson, and J. D. Joannopoulos, "Slow-light, band-edge waveguides for tunable time delays", *Optics Express*, vol. **13**, pp. 7145-7159, 2005.

[30] A. Sentenac, J. J. Greffet, and F. Pincemin, "Structure of the electromagnetic held in a slab of photonic crystal", *Journal Of The Optical Society Of America B-Optical Physics*, vol. **14**, pp. 339-347, 1997.

[31] X. Letartre, C. Seassal, C. Grillet, P. Rojo-Romeo, P. Viktorovitch, M. Le Vassor D'Yerville, D. Cassagne, and C. Jouanin, "Group velocity and propagation losses measurement in a single-line photonic-crystal waveguide on InP membranes", *Applied Physics Letters*, vol. **79**, pp. 2312-2314, 2001.

[32] M. Notomi, K. Yamada, A. Shinya, J. Takahashi, C. Takahashi, and I. Yokohama, "Extremely large group-velocity dispersion of line-defect waveguides in photonic crystal slabs", *Physical Review Letters*, vol. **87**, pp. 253902/1-4, 2001.

[33] Y. A. Vlasov & S. J. McNab, "Coupling into the slow light mode in slab-type photonic crystal waveguides", *Optics Letters*, vol. **31**, pp. 50-52, 2006.

[34] R. J. P. Engelen, Y. Sugimoto, Y. Watanabe, J. P. Korterik, N. Ikeda, N. F. Van Hulst, K. Asakawa, and L. Kuipers, "The effect of higher-order dispersion on slow light propagation in photonic crystal waveguides", *Optics Express*, vol. **14**, pp. 1658-1672, 2006.

[35] by R. M. de Ridder, University of Twente, Enschede, 2007.

[36] Y. A. Vlasov, M. O'Boyle, H. F. Hamann, and S. J. McNab, "Active control of slow light on a chip with photonic crystal waveguides", *Nature*, vol. **438**, pp. 65-69, 2005.

[37] M. D. Settle, R. J. P. Engelen, M. Salib, A. Michaeli, L. Kuipers, and T. F. Krauss, "Flatband slow light in photonic crystals featuring spatial pulse compression and terahertz bandwidth", *Optics Express*, vol. **15**, pp. 219-226, 2007.

[38] D. Mori & T. Baba, "Wideband and low dispersion slow light by chirped photonic crystal coupled waveguide", *Optics Express*, vol. **13**, pp. 9398-9408, 2005.

[39] G. Lenz, B. J. Eggleton, C. K. Madsen, and R. E. Slusher, "Optical delay lines based on optical filters", *IEEE Journal of Quantum Electronics*, vol. **37**, pp. 525-532, 2001.

[40] L. Zhuang, C. G. H. Roeloffzen, R. G. Heideman, A. Borreman, A. Meijerink, and W. van Etten, "Ring resonator-based single-chip 1x8 optical beam forming network in LPCVD waveguide technology", Proc. Annual symposium of the IEEE LEOS Benelux Chapter (Eindhoven), pp. 45-48 (2006).

[41] L. H. Frandsen, A. V. Lavrinenko, J. Fage-Pedersen, and P. I. Borel, "Photonic crystal waveguides with semi-slow light and tailored dispersion properties", *Optics Express*, vol. **14**, pp. 9444-9450, 2006.

[42] A. Adibi, Y. Xu, R. K. Lee, M. Loncar, A. Yariv, and A. Scherer, "Role of distributed Bragg reflection in photonic-crystal optical waveguides", *Physical Review B*, vol. **64**, pp. 041102/1-4, 2001.

[43] W. C. L. Hopman, MSc thesis, "The Visible challenge of 1-D Photonic Crystals", University of Twente, Enschede, 2002.

[44] R. Dekker, PhD thesis, "All-optical processes in integrated optical devices using materials with large third-order nonlinearities and gain", ISBN-13: 978-90-9021436-8, University of Twente, Enschede, 2006.

[45] W. F. A. Engbers, MSc thesis, "Adiabatic slow light excitation in grated channel waveguides", University of Twente, Enschede, 2005.

[46] S.O.I.TEC, Silicon on Insulator technologies, http://www.soitec.com.

[47] P. Bienstman, S. Selleri, L. Rosa, H. P. Uranus, W. C. L. Hopman, R. Costa, A. Melloni, L. C. Andreani, J. P. Hugonin, P. Lalanne, D. Pinto, S. S. A. Obayya, M. Dems, and K. Panajotov, "Modelling leaky photonic wires: A mode solver comparison", *Optical and Quantum Electronics*, vol. **38**, pp. 731-759, 2006.

[48] W. Bogaerts, P. Dumon, D. Taillaert, V. Wiaux, S. Beckx, B. Luyssaert, J. Van Campenhout, D. Van Thourhout, and R. Baets, "SOI nanophotonic waveguide structures fabricated with deep UV lithography", *Photonics and Nanostructures - Fundamentals and Applications*, vol. **2**, pp. 81-86, 2004.

[49] Olympios, "OlympIOs Integrated Optics Software", C2V, http://www.c2v.nl/software/.

[50] K. Guven, K. Aydin, K. B. Alici, C. M. Soukoulis, and E. Ozbay, "Spectral negative refraction and focusing analysis of a two-dimensional left-handed photonic crystal lens", *Physical Review B - Condensed Matter and Materials Physics*, vol. **70**, pp. 205125/1-5, 2004.

[51] E. Cubukcu, K. Aydin, E. Ozbay, S. Foteinopolou, and C. M. Soukoulis, "Subwavelength resolution in a two-dimensional photonic-crystal-based superlens", *Physical Review Letters*, vol. **91**, 2003.

[52] S. Noda, M. Yokoyama, M. Imada, A. Chutinan, and M. Mochizuki, "Polarization mode control of two-dimensional photonic crystal laser by unit cell structure design", *Science*, vol. **293**, pp. 1123-1125, 2001.

[53] C. O. Cho, J. Jeong, J. Lee, H. Jeon, I. Kim, D. H. Jang, Y. S. Park, and J. C. Woo, "Photonic crystal band edge laser array with a holographically generated square-lattice pattern", *Applied Physics Letters*, vol. **87**, pp. 161102/1-3, 2005.

[54] L. Wu, M. Mazilu, J. F. Gallet, T. F. Krauss, A. Jugessur, and R. M. De La Rue, "Planar photonic crystal polarization splitter", *Optics Letters*, vol. **29**, pp. 1620-1622, 2004.

[55] P. Pottier, S. Mastroiacovo, and R. M. De La Rue, "Power and polarization beam-splitters, mirrors, and integrated interferometers based on air-hole photonic crystals and lateral large index-contrast waveguides", *Optics Express*, vol. **14**, pp. 5617-5633, 2006.

[56] S. Shi, A. Sharkawy, C. Chen, D. M. Pustai, and D. W. Prather, "Dispersion-based beam splitter in photonic crystals", *Optics Letters*, vol. **29**, pp. 617-619, 2004.

[57] K. Aoki, T. Baba, T. Hasegawa, H. Kosaka, M. Koshiba, H. Masuda, H. Misawa, H. T. Miyazaki, S. Noda, M. Notomi, T. Sato, and M. W. Takeda, "Roadmap on Photonic Crystals", (eds. Noda, S. & Baba, T.), ISBN: 1-4020-7464-6, Kluwer, Dordrecht/ Boston/ London, 2003.

[58] S. Olivier, M. Rattier, H. Benisty, C. Weisbuch, C. J. M. Smith, R. M. De La Rue, T. F. Krauss, U. Oesterle, and R. Houdré, "Mini-stopbands of a one-dimensional system: The channel waveguide in a two-dimensional photonic crystal", *Physical Review B*, vol. **63**, pp. 113311/1-4, 2001.

[59] A. Y. Petrov & M. Eich, "Zero dispersion at small group velocities in photonic crystal waveguides", *Applied Physics Letters*, vol. **85**, pp. 4866-4868, 2004.

[60] R. J. P. Engelen, T. J. Karle, H. Gersen, J. P. Korterik, T. F. Krauss, L. Kuipers, and N. F. van Hulst, "Local probing of Bloch mode dispersion in a photonic crystal waveguide", *Optics Express*, vol. **13**, pp. 4457-4464, 2005.

[61] Y. Akahane, T. Asano, B. S. Song, and S. Noda, "Fine-tuned high-Q photonic-crystal nanocavity", *Optics Express*, vol. **13**, pp. 1202-1214, 2005.

[62] J. S. Foresi, P. R. Villeneuve, J. Ferrera, E. R. Thoen, G. Steinmeyer, S. Fan, J. D. Joannopoulos, L. C. Kimerling, H. I. Smith, and E. P. Ippen, "Photonic-bandgap microcavities in optical waveguides", *Nature*, vol. **390**, pp. 143-145, 1997.

[63] D. H. Geuzebroek, PhD thesis, "Flexible optical network components based on densely integrated microring resonators", ISBN: 90-365-2258-7, University of Twente, Enschede, 2005.

[64] H. M. H. Chong & R. M. De La Rue, "Tuning of photonic crystal waveguide microcavity by thermooptic effect", *IEEE Photonics Technology Letters*, vol. **16**, pp. 1528-1530, 2004.

[65] H. Benisty, C. Weisbuch, D. Labilloy, M. Rattier, C. J. M. Smith, T. F. Krauss, R. M. De La Rue, R. Houdre, U. Oesterle, C. Jouanin, and D. Cassagne, "Optical and confinement properties of two-dimensional photonic crystals", *Journal of Lightwave Technology*, vol. **17**, pp. 2063-2077, 1999.

[66] S. Noda, A. Chutinan, and M. Imada, "Trapping and emission of photons by a single defect in a photonic bandgap structure", *Nature*, vol. **407**, pp. 608-610, 2000.

[67] M. Notomi, A. Shinya, S. Mitsugi, E. Kuramochi, and H. Y. Ryu, "Waveguides, resonators and their coupled elements in photonic crystal slabs", *Optics Express*, vol. **12**, pp. 1551-1561, 2004.

[68] W. Bogaerts, R. Baets, P. Dumon, V. Wiaux, S. Beckx, D. Taillaert, B. Luyssaert, J. Van Campenhout, P. Bienstman, and D. Van Thourhout, "Nanophotonic waveguides in silicon-on-insulator fabricated with CMOS technology", *Journal of Lightwave Technology*, vol. **23**, pp. 401-412, 2005.

[69] C. Sauvan, G. Lecamp, P. Lalanne, and J. P. Hugonin, "Modal-reflectivity enhancement by geometry tuning in photonic crystal microcavities", *Optics Express*, vol. **13**, pp. 245-255, 2005.

[70] R. Dekker, A. Driessen, T. Wahlbrink, C. Moormann, J. Niehusmann, and M. Först, "Ultrafast Kerr-induced all-optical wavelength conversion in silicon waveguides using 1.55 μm femtosecond pulses ", *Optics Express*, vol. **14**, pp. 8336-8346, 2006.

[71] V. Van, T. A. Ibrahim, P. P. Absil, F. G. Johnson, R. Grover, and P. T. Ho, "Optical signal processing using nonlinear semiconductor microring resonators", *IEEE Journal on Selected Topics in Quantum Electronics*, vol. **8**, pp. 705-713, 2002.

[72] C. Y. Chao & L. J. Guo, "Biochemical sensors based on polymer microrings with sharp asymmetrical resonance", *Applied Physics Letters*, vol. **83**, pp. 1527-1529, 2003.

[73] E. Krioukov, D. J. W. Klunder, A. Driessen, J. Greve, and C. Otto, "Integrated optical microcavities for enhanced evanescent-wave spectroscopy", *Optics Letters*, vol. **27**, pp. 1504-1506, 2002.

[74] E. J. Klein, PhD thesis, "Densely integrated Microring-Resonator based components for Fiber-to-the-Home applications", University of Twente, Enschede, 2007.

CHAPTER 3

3 FABRICATION

Abstract—The devices presented in this thesis were fabricated using various technologies in different cleanrooms. An overview is presented first in this chapter. Then, an example stream file for focused ion beam (FIB) milling is described in detail. Furthermore, it is shown that FIB milling can also be used to smoothen a patterned surface and a study on sidewall verticality of the FIB milling process of submicrometer holes is presented. Finally, it is shown how a combination of laser interference lithography and conventional lithography can be used to realize high quality uniform and apodized gratings.

3.1 Introduction

Four different lithographic processes suitable for submicrometer structures were deployed for the research presented in this thesis. All of them have their specific strengths and weaknesses, depending on the application they are used for. In section 3.1.1, we will give an overview of the strengths and weaknesses of the four lithographic technologies. Next, an example of a PhC design of a focused ion beam (FIB) stream is presented in section 3.1.2.
First, we present a brief overview of the photonic devices reported in this thesis realized using various technologies in three different cleanrooms:

- The waveguide gratings used for the cladding sensor measurement in section 4.2 was fabricated partly in the MESA+ cleanroom and partly in the cleanroom of the University of Glasgow using their direct e-beam facilities to generate sub-200-nm period waveguide gratings (WGGs) for the visible. A detailed process description can be found in [1].
- The waveguide gratings suitable for infrared wavelengths were fabricated using laser interference lithography (LIL) in the MESA+ cleanroom. A process description is presented in section 3.4 and can also be found in [2]. A detailed description of the LIL process used in MESA+ cleanroom can be found in [3,4]. These LIL defined gratings were used for the characterization of resonances in WGGs, see section 4.3.
- The photonic crystals and the microring resonator used for the nanomechanical interaction measurements presented in section 4.5 and 4.6, were fabricated by Ghent University using the IMEC cleanroom facilities in Leuven. The main lithography tool used was their deep UV (DUV) lithography process, which is well described in the following papers [5-7]. The resulting halved 200-mm wafer was post processed in the MESA+ cleanroom: dicing, FIB milling, annealing, etc.
- The FIB milling experiments of various geometries in different materials were performed at the MESA+ institute. A description of some of the important aspects of the milling process will be given in the example presented in section 3.1.2. In section 3.3, we present an in-depth study of the FIB process for fabricating PhC slabs for mould applications in combination with imprint technologies or possibly for SOI photonic applications. More details about the spiral scan routine (explained in section 3.3 can be found in [8]). An example for FIB processing of low-loss structures using a hard mask is later presented in section5.2.

3.1.1 Strengths and weaknesses of fabrication methods

The fabrication methods mentioned in the previous section have all their specific strengths and weaknesses opportunities and threats [9] with respect to the research they are exploited for. Below we present a table with various aspects related to processing of photonic devices using FIB milling or

- LIL, using a deep UV laser at a wavelength (λ) of 266 nm,
- DUV lithography, using an exposure wavelength of λ = 248 nm,
- Direct e-beam lithography,

in combination with (proper) reactive ion etching.
The here described properties of the fabrication processes are based on experiences gained in the research presented in this thesis. The perceptions strongly depend on the environment they are used in and the applications they are used for.

FIB
From this work we conclude that the advantages of the FIB-milling processing are: the ability to structure almost any material, good for prototyping due to extremely short turn-around time, no need for separate etching processes, and the possibility of fabricating a large variety of nanostructures. On the downside of FIB milling for photonics we find the difficulty to align submicron features with previously defined structures and extremely high losses due to (surface) modification of the substrate.

LIL
The main advantage of the LIL is that it provides a technique to pattern large areas many cm^2 with periodic structures at a low cost. The disadvantage is the lack of flexibility of the method; creating other than planar periodic structures is a serious challenge, see for example [4]. However, in combination with conventional lithography, gratings can be LIL-defined with smooth transitions that realize apodizing functions, as shown in [10].

DUV lithography
Deep UV lithography is a well documented mature technology, which has been exploited for many different photonic structures. The main disadvantage is the long turn-around time in most fabrication facilities, between the design and the fabricated structure. Within the ePIXnet collaboration mentioned in chapter 1, it took about ¾ of a year, but many efforts are being made to reduce this time to half a year or less in the next mask-sharing rounds. Since the DUV masks were subsidized by the ePIXnet and shared by several partners, the costs per partner were relatively low compared to commercial rates.

E-beam lithography
E-beam lithography is at the moment the best tool for realizing low-loss nanophotonic devices. Direct e-beam writing is exploited at the frontiers of the integrated optics research, especially regarding photonic crystal and nanophotonic fabrication. However, as many groups found out, turning on the machine doesn't automatically give the expected resolutions. Although the technology is advancing rapidly, achieving appealing results using e-beam often requires the strong support of dedicated skilled technicians, who may be harder to find than the scientist who in principle "only" pulls the strings.
The best choice of lithography for the project described in section 1.2.2, depends on which aspects are regarded as most relevant. In externally funded projects, the possibility of filing a patent is of increasing importance, which may conflict with the interest of research groups as they in general strive for the output of many high quality papers [11].

Table 3.1-1: Properties of the lithographic methods used in this thesis.

Property	**FIB**	**LIL**	**DUV**	**E-beam**
Economic:				
Short turn-around times	+	+	-	+
Yield	-	+/ -	+	+
Low cost	+/ -	+	-	-
Structuring aspects:				
Minimum resolution	+	+/ -	+/ -	+
Many geometrical shapes	++	-	+/ -	+
Well documented	-	+/ -	+	+
Low mask complexity	+/ -	+	+/ -	-
Local deposition of materials	+	-	-	+
Verticality of sidewalls	+/ -	+/ -	+	+
Parameter tuning	+/ -	-	+	+
Low process complexity	+	+	-	-
No charging effects	-	+	+	-
No proximity effects	-	+	-	-
Mask aligning possibilities[b]	-	-	+	-
Structuring of hard-to-etch materials	+	-	-	-
No additional RIE process needed	+	-	-	-
No modification of substrate properties	-	+	+	+
Low-loss optical devices	-,[a]	+	+	+
Imaging by internal SEM	+	-	-	+
Fabrication of:				
Planar 2-D PhC slabs	+	+	+	+
Defect integration in a PhC	+	-	+	+
Photonic wires (< 1 μm wide, < 50 μm long)	+	-	+	+
Photonic wires (< 1 μm wide, > 50 μm long)	-	-	+	+/ -
Gratings, pitch > 350 nm	+	+	+	+
Gratings, pitch < 350 nm	+	+/ -	-	+
Apodization (by chirped periodicities)	+	+/ -	+	+
Microring resonators, R<15 μm	+	-	+	+
Microring resonators, R>15 μm	-	-	+	+
Related aspects:				
Accessibility (In this research)	+	+	+	+/ -
Accessibility (In Mesa+ cleanroom ?)	+	+	-	-[c]

Legend: + **Positive**; +/ - **Neutral**; - **Negative**

[a] High losses are observed for direct milling of Si. Lower losses can be obtained by: gas-assisted milling [12] and/or annealing or a hard mask in combination with dry etching, see chapter 5.
[b] High mask alignment accuracies have been shown feasible for all methods.
[c] The e-beam facility has recently become operational.

3.1.2 Introduction to focused ion beam processing

The number of Focused Ion Beam (FIB) related publications has shown a strong increase in the last few decades. For many years FIB processing has served mainly the semiconductor/transistor driven industries, but lately the unique capabilities for microfabrication and nanofabrication have attracted a revived interest of researchers in several research fields. These include, for example, the capabilities of 3-D structuring by deposition [13] or milling [14]. Especially in the field of

photonics, FIB processing has shown an increase in interest, examples can be found in section 3.2 and 3.3. But still, the ion-induced losses are still at a (too) high level [12] exceeding most device criteria. As mentioned in the previous section, the loss issue is currently being investigated within the ePIXnet FIB-JRA (see section 1.2.3), some preliminary results and two possible routes for lowering the losses are presented in chapter 5.
However, as mentioned in the previous section FIB processing ha some unique capabilities: FIB milling can be applied to many solid state materials including hard-to-etch materials like Al_2O_3 [15] or it can be used for fast prototyping of masks or moulds [16] which can be used in combination with imprint technologies for low-loss photonic devices.
In the following section, we provide some details about our FIB machine. Furthermore, a basic description of the strategy for fabrication various patterns using FIB micromachining or nanomachining (milling) is presented.

3.1.2.1 FIB machine

The FIB machine used in this thesis is the NOVA 600 from FEI Company. It is termed a dual-beam FIB, because it has two beam columns: one for ions and one for electrons. Therefore, it can be used for milling, imaging and direct e-beam patterning within a single vacuum. The Ga+ ions are generated by a liquid metal source. The acceleration voltage is kept constant at 30 kV in our experiments. The milling principle is based on physical "etching": high energy focused Ga+ ions (atomic number 31) knock out the Si substrate atoms (atomic number 14). During this process some Ga+ ions will be implanted into the substrate, which may alter the material properties. The suitability for nanofabrication is illustrated by the beam position control having one nanometer resolution and the 1/*e* spot size of around 10-20 nm [17]. The beam can be controlled using a so-called stream file [18], which contains the coordinates, the associated dwell times and the loop number of the desired milling pattern. In the next section we will present an example of the design and milling strategy for milling an array of holes.

3.1.2.2 Preparation of a stream file, an example

A method for generating a stream file for milling without stitching errors is presented in this section. The flowchart of the process is depicted in Figure 3.1-1 and will be explained further in this section.

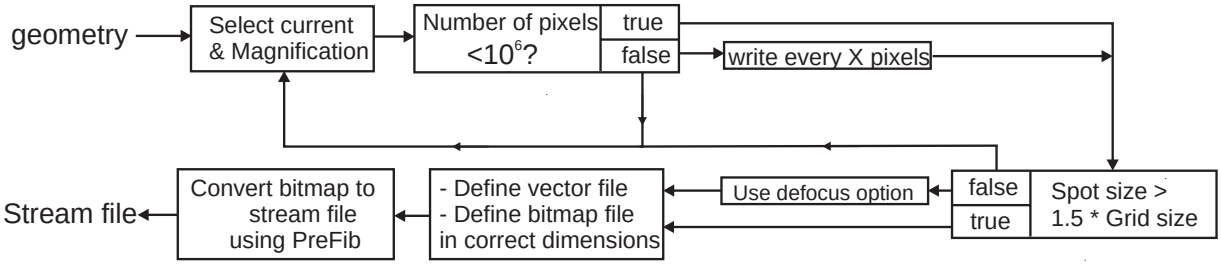

Figure 3.1-1: Flowchart for generating stream files for milling without stitching errors.

The example consists of an array of holes representing a 5 by 5 layers photonic crystal. The crystal is oriented in the ΓK direction. The lattice constant and hole radius have similar values as in 2.3, leading to a total size of the pattern of 1774 by 1130 nm. The file is created in a vector format (dxf, autocad) in which each hole is represented as a polygon defined by ≈ 100 (*x*,*y*) coordinates, see Figure 3.1-2.

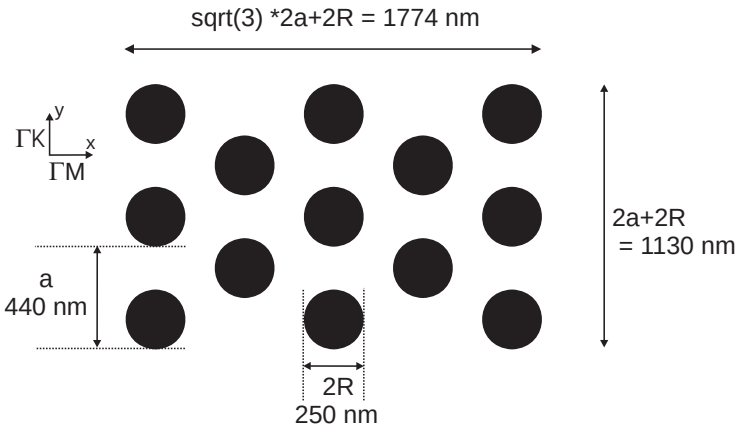

Figure 3.1-2: The example consisting of an arrangement of holes in a triangular lattice.

Current & magnification

Now that the structure dimensions are known, the Field of View FoV (the stitching free writing field of the FIB, displayed on the monitor) [18], should be determined. The FoV can not be set to arbitrary values. Therefore, a suitable combination of FoV and magnification should be chosen from Table 2.1 in order to ensure strict dimensional control of the device. The magnification is defined as the ratio of the FoV on the display screen of the FIB control console, divided by the actual FoV size on the specimen. In this research, we have worked mainly in the preset state termed Quad view, where the FoV covers ¼ of the screen area. It is just a matter of multiplying the dimensions by 2 to find the "full screen-view". The FoV is mapped onto two 12-bit analogue-to-digital (AD) converters dividing the FoV in 4096 by 4096 pixels. The size of 1 pixel can be calculated by dividing the FoV size in one direction by 4096, as is shown in the table below.

Table 3.1-2: Magnification in Quad view and the associated FoVs and grid sizes.

Magnification (Quad-view)	FoV-size (x×y) (μm)	Grid size (nm)
40k	3.175×3.175	0.78
20k	6.35×6.35	1.55
10k	12.7×12.7	3.1
5k	25.4×25.4	6.2
2.5k	50.8×50.8	12.4
1k	127×127	31.0
0.5k	254×254	62.0

Number of pixels & spot size

The number of pixels needed for the PhC design can be calculated using the filling factor (or duty cycle for gratings). This area should be divided by the area of 1 pixel to estimate the total number of pixels. If we want to mill at each pixel, this number should be smaller than 10^6: the maximum number of (*x*,*y*) coordinates allowed in a stream file. The choice whether we should mill all pixels or if it is sufficient to mill for example only one in every 2 pixels is dependent on the current we plan to use, because each current has it own 1/*e* spot size, see Table 3.1-3. As a rule of thumb the minimum grid size should be smaller than $^2/_3$ of the 1/*e* spot size (or the spot size should be at least 1.5 times the grid size). The FEI software allows for an option termed defocusing, which can be used to increase the spot size at the cost of resolution. However, this option is not used in the research reported in this section.

Table 3.1-3: Beam current versus 1/e spot sizes [17], at 30 kV

Current (pA)	1/e spot size (nm)
1.5 pA	7.5
9.7 pA	11.9
28 pA	15.5
48 pA	18.6
93 pA	22.4
0.28 nA	31.8
0.92 nA	48.8
2.8 nA	77.5

The higher the current the faster the milling will be; a relation between the milling time and the milling depth is given in section 3.3. For photonic crystal structures (~ 20 μm by 20 μm) a current of 48 pA gives a good compromise between total milling time en resolution. If we choose a magnification of 10.000 times (10 kX), we will need $(1774\times1130 - 13\times\pi R^2) / 3.1^2 =)$ 142.194 pixels for the design displayed in Figure 3.1-2. However, if we choose to use a magnification of 40 kX time, we will need 2.246.029 pixel which exceeds the limit of 10^6 pixels. Depending on the desired alignment accuracy, we can either mill at a magnification of 10 kX or mill at 40 kX but only mill one in every 2 pixels in both *x* and *y* direction. This factor of 2 is termed the *X*-factor in the Labview software PreFib [19], which can be set to any positive non-zero integer. An edge detection option is under development; it may offer the possibility to write every 1 pixel at the edge of a pattern (a hole) while the rest of the hole is written at every *X* pixels. For this example, we choose a magnification of 10 kX.

Conversion bitmap to stream file

Next, we convert the vector file to a "bmp" file, with dimensions 1774/3.1 × 1130/3.1 pixels. Rounding to the nearest integer values gives 572 × 365 pixels. A pixel depth of 8 bit is chosen, although in principle any bit depth can be used. The file can now be converted to a stream file using the PreFib program; the result of the conversion is plotted in Figure 3.1-3. The left graph shows a plot of all coordinates. The shape of the holes is well preserved compared to the designed array of holes in Figure 3.1-2.

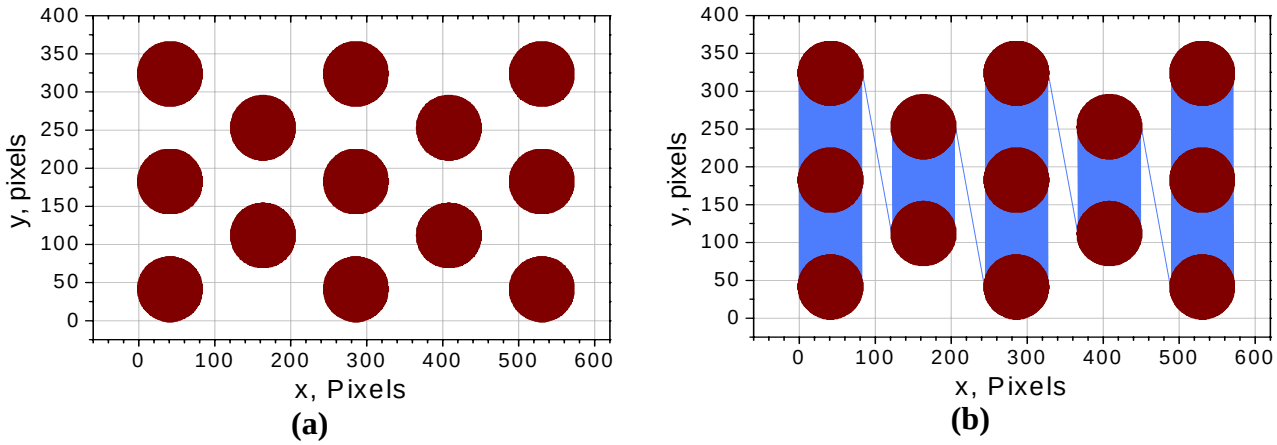

Figure 3.1-3: (a) A plot of the coordinates specified in the stream file. (b) The same file as displayed in the left graph, but the coordinates are now connected by lines. Typically for a raster scan, the interhole region is milled when the beam sweeps over the region. A spiral scan as presented in section 3.3 can minimize the interhole milling.

Figure 3.1-3b shows the same file but the coordinates are now connected by lines. The beam is directed back and forth over the interhole area. Unfortunately the Nova 600 is not equipped with a fast shutter, resulting in interhole milling. The conversion method is based on raster scanning, which leads to this interhole milling. In section 3.3 we present a spiral scanning method [8], which can be used to minimize the interhole milling.

Mounting
After preparing the stream file, the sample has to be mounted on a holder before the structure can be milled. There are two main options available for mounting at this moment: double sided conductive carbon tape and silver paint/glue. The latter is preferred, because it provides the best electrical contact and working with carbon tape is not convenient because it sticks to anything: tweezers, gloves etc. and it may be mechanically instable. Furthermore, experiments showed that the charging was less for the silver paint/glue than for the carbon tape mounting method.

Milling
After loading the sample into the machine an initial alignment procedure has to be performed. The stream file can be loaded into the machine's memory: it is displayed in the FoV on the monitor. The milling time can be predefined in the stream file, or it can be directly controlled by the operator if a long milling time (loop number) is selected. The required milling time can be estimated by either end point detection or by examining snap-shots made during the milling (the ion beam scans the whole FoV one time and the secondary electrons are imaged onto the screen). However, snapshots will induce extra implantation of Ga+ and milling in the whole FoV, which may be unwanted for some applications. A recently attached oscilloscope (described in the text below) can be used to monitor the milling process by detecting the secondary electrons generated in during the milling process.

Drift control
When long milling times are required, it is wise to mill an alignment marker at a high current before milling the final pattern. This marker can be used for the drift control option, which compares the images of snap-shots automatically made every selected time-interval. Next, the drift obtained from automatic image processing is corrected for. For nanostructures, this drift control is usually not an option, due to the milling by the snap-shots.

End point detection
Two other monitors can be used to determine the required milling time:
1) End-point detection: The current flowing through the substrate holder is monitored. Milling different layers results in different currents, caused by, for example, sputtering of charged particles, reflection of the Ga+ ion beam, and different emission rates of secondary electrons. Figure 3.1-2 shows the data obtained from the end-point-monitor (EPM). A layer stack of about 30 nm Cr on 50 nm Si_3N_4 on SOI was milled at a current of 93 pA. The milling depth is estimated by the FEI software (the method is not described in their manual). The figure shows that the estimated milling depth is approximately correct when comparing the changes in EPM detection with the fabricated layer stack. The advantage of the EPM is that transitions which are hard to observe by secondary electron (SE) emissions can be estimated quite accurately from the EPM.
2) If the transitions are well "visible" by the SE detector, then the external oscilloscope attached to this detector can be used for visually monitoring the transitions.

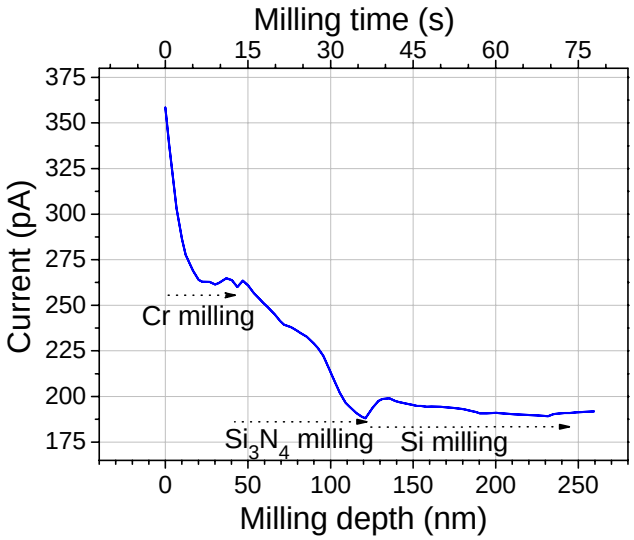

Figure 3.1-4: Graph obtained from the end-point-monitor by milling a Cr/Si_3N_4/SOI layer stack, see also section 5.2.

Post processing

A cross-sectioning method, described in section 3.3, can be used to make SEM images of the cross-section. These images can be used for process calibration by determining the time required for reaching a predefined milling depth.

Finally, the finished sample can be unloaded and cleaned, and further characterized if needed.

3.1.3 References

[1] W. C. L. Hopman, MSc thesis, "The Visible challenge of 1-D Photonic Crystals", University of Twente, Enschede, 2002.

[2] W. F. A. Engbers, MSc thesis, "Adiabatic slow light excitation in grated channel waveguides", University of Twente, Enschede, 2005.

[3] C. G. Bostan, PhD thesis, "Design and fabrication of quasi-2-D photonic crystal components based on silicon-on-insulator technology", ISBN: 90-365-2155-6, University of Twente, Enschede, 2005.

[4] L. Vogelaar, W. Nijdam, H. A. G. M. van Wolferen, R. M. de Ridder, F. B. Segerink, E. Fluck, L. Kuipers, and N. F. van Hulst, "Large area photonic crystal slabs for visible light with waveguiding defect structures: Fabrication with focused ion beam assisted laser interference lithography", *Advanced Materials*, vol. **13**, pp. 1551-1554, 2001.

[5] W. Bogaerts, R. Baets, P. Dumon, V. Wiaux, S. Beckx, D. Taillaert, B. Luyssaert, J. Van Campenhout, P. Bienstman, and D. Van Thourhout, "Nanophotonic waveguides in silicon-on-insulator fabricated with CMOS technology", *Journal of Lightwave Technology*, vol. **23**, pp. 401-412, 2005.

[6] W. Bogaerts, P. Dumon, D. Taillaert, V. Wiaux, S. Beckx, B. Luyssaert, J. Van Campenhout, D. Van Thourhout, and R. Baets, "SOI nanophotonic waveguide structures fabricated with deep UV lithography", *Photonics and Nanostructures - Fundamentals and Applications*, vol. **2**, pp. 81-86, 2004.

[7] P. Dumon, W. Bogaerts, V. Wiaux, J. Wouters, S. Beckx, J. Van Campenhout, D. Taillaert, B. Luyssaert, P. Bienstman, D. Van Thourhout, and R. Baets, "Low-loss SOI photonic wires and ring resonators fabricated with deep UV lithography", *IEEE Photonics Technology Letters*, vol. **16**, pp. 1328-1330, 2004.

[8] W. Hu, MSc thesis, "Focused Ion Beam Milling of Photonic Crystal Structures in Silicon on Insulator (SOI) and Silicon", University of Twente, Enschede, 2006.

[9] A. M. M. Blommaert, J. M. J. Blommaert, and H. C. Wytzes, "Bedrijfeconomische analyses: Bedrijfs economie vanuit managementperspectief", ISBN: 90-207-3287-0, Wolters-Noordhoff bv Groningen/Houten, 2004.

[10] W. C. L. Hopman, R. Dekker, D. Yudistira, W. F. A. Engbers, H. Hoekstra, and R. M. de Ridder, "Fabrication and characterization of high-quality uniform and apodized Si_3N_4 waveguide gratings using laser interference lithography", *IEEE Photonics Technology Letters*, vol. **18**, pp. 1855-1857, 2006.

[11] B. Jongbloed & C. Salerno, “De Bekostiging van het Universitaire Onderwijs en Onderzoek in Nederland: Modellen, Thema’s en Trends”, *Cheps, Achtergrondstudie voor de AWT*, vol. **kenmerk: C3BJ452**, 2003.

[12] J. Schrauwen, D. Van Thourhout, and R. Baets, “Focused-ion-beam fabricated vertical fiber couplers on silicon-on-insulator waveguides”, *Applied Physics Letters*, vol. **89**, pp. 141102/1-3, 2006.

[13] S. Reyntjens & R. Puers, “Focused ion beam induced deposition: fabrication of three-dimensional microstructures and Young's modulus of the deposited material”, *Journal of Micromechanics and Microengineering*, vol. **10**, pp. 181-188, 2000.

[14] C. Khan Malek, F. T. Hartley, and J. Neogi, “Fast prototyping of high-aspect ratio, high-resolution X-ray masks by gas-assisted focused ion beam”, *Microsystem Technologies*, vol. **9**, pp. 409-412, 2003.

[15] M. K. Lee & K. K. Kuo, “Microlens array on sapphire substrate prepared by FIB to enhance electroluminescence of GaN/sapphire blue LED”, *Electrochemical and Solid-State Letters*, vol. **10**, pp. H20-H21, 2007.

[16] N. Chaix, S. Landis, D. Hermelin, T. Leveder, C. Perret, V. Delaye, and C. Gourgon, “Influence of mold depth on capillary bridges in nanoimprint lithography”, *Journal of Vacuum Science and Technology B: Microelectronics and Nanometer Structures*, vol. **24**, pp. 3011-3015, 2006.

[17] F. B. Segerink, "How to make *.str files.", University of Twente, Enschede, 2005.

[18] FEI, "NOVA NanoLab Training Course, Part 2".

[19] PreFib, version **2.0**, by W. C. L. Hopman, "\\udsel02\GroupLow\IOMS\Software IOMS".

3.2 FIB processing for nanosmooth photonic crystals

Abstract—We report the design and fabrication of small photonic crystal structures which are combined with conventional dielectric ridge waveguides. We describe in detail the fabrication of both rough and smooth membranes, which are used as host for photonic crystals. Two focused ion beam milling experiments are highlighted: the first one shows how photonic crystals can be fast and accurately milled into a Si membrane, whereas the second experiment demonstrates how focused ion beam milling can turn a rough surface into a well-patterned nanosmooth surface. The previously ultra rough surface showed no detectable roughness after milling due to the nanopolishing effect of the focused ion beam milling.

This section has been published:
W. C. L. Hopman, R. M. De Ridder, S. Selvaraja, C. G. Bostan, V. J. Gadgil, L. Kuipers and A. Driessen, "Realization of 2-dimensional air-bridge silicon photonic crystals by focused ion beam, milling and nanopolishing," Proceedings of SPIE - The International Society for Optical Engineering (Strasbourg), Proc. 6182, (2006).

3.2.1 Introduction

Photonic crystals are structures with a periodic dielectric function, which may result in the prohibition of the propagation of electromagnetic waves for certain frequencies in all crystal directions: the photonic bandgap. In this paper we investigate a 2-dimensional triangular pattern of hexagonal holes in a high index silicon membrane. When introducing 'defects' in photonic crystal slabs (PCS) in a controlled manner, this arrangement becomes suitable for design and implantation of passive and active building blocks (e.g. filters [1], sensors [2], lasers [3]). The size of the bandgap of the uniform crystal area not only depends on the refractive index contrast but also on the air filling factor of the photonic crystal, which is determined by the size of the holes compared to the lattice constant *a*. It is well known from the literature [4] that a complete bandgap, i.e. a stopband for all polarizations and directions, can be maximized by creating a crystal having small islands of high-index dielectric, which are interconnected through narrow veins. Previously we calculated [5] that using hexagonal holes rotated by 9 degrees with respect to the lattice can result in an optimized complete bandgap. This means that for a typical design with lattice parameter ~ 500 nm the width of the veins (i.e. the thickness of the sidewalls separating adjacent holes), can be as small as ~ 50 nm or even less. This calls for fabrication with nanometer precision, which is not easily achieved with most lithographic techniques. Using a focused ion beam milling machine (dual beam Nova 600) with a spot size of ~ 12 nm and an address grid resolution of 3.1 nm we were able to fabricate these structures.

Focused ion beam (FIB) processing is a well-established technique with the unique capabilities to locally sputter etch, ion implant, and deposit metals and insulators with a feature size in the order of nanometers, without the need of a mask [6]. In optoelectronics, FIB has been applied for defining the end facet mirrors of conventional semiconductor lasers [7,8]. It also has been applied for bulk micromachining of macro-porous silicon in order to fabricate 3-D Yablonovite-like photonic crystals [9], and recently for fabricating 2-D periodic structures in III-V compounds [10]. Another recent application of FIB has been the fabrication of quasi-1-D photonic crystals by milling 1-D gratings into freestanding multilayer membranes [11]. An advantage of FIB milling, compared to direct e-beam writing and deep-UV lithography, is that it does not need proximity correction if used on conducting surfaces. Moreover, it provides direct definition of a pattern either directly into the target layer or into an etch resistant mask, and it can be integrated with optical lithography. Finally, similar to its use with electronic circuits, FIB can be used for repairing or trimming optical waveguides and resonator structures.

For photonic (crystal) structures which require the definition of submicron features in high-index contrast material systems, a particularly attractive property of FIB is the nanopolishing effect that we observed, resulting in smooth structures which are hard to obtain with other etching methods (e.g. reactive ion etching – RIE). The nanopolishing effect is a complex process of ion-implantation, amorphization, and re-deposition of nanocrystalline silicon [12]. Although promising photonic crystal structures have been FIB-fabricated in thin slabs, and especially in free-standing membranes, it is still a challenge for FIB to obtain deep holes with extremely high aspect ratios. Other issues important for photonic devices are charge-related proximity effects on insulating substrates, amorphization and implantation of Ga+ ions [12,13] which deserves attention by optical investigation. It should be noted that these FIB induced effects can be minimized by merely using the FIB as lithography tool, as is outlined by Figure 3.2-1.

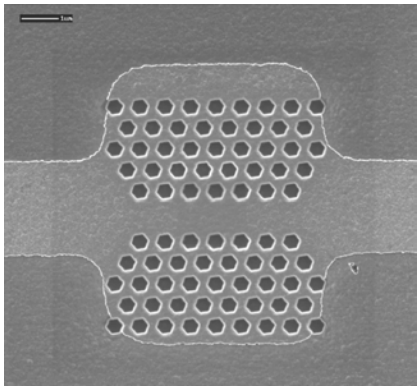

Figure 3.2-1: FIB-milled hexagon-type photonic crystal chromium pattern on silicon using a Nova 200 single beam FIB (FEI Company).

FIB machines can resolve a limited number of "pixels", so that a compromise must be found between resolution and the accessible area for processing (field-of-view, FoV). The processed area can always be extended by mechanical specimen translation, but this requires additional alignment procedures and may introduce stitching errors. There are several photonic structures of interest that fit entirely within the high-resolution FoV of a few tens of microns square. For larger structures the most promising application of FIB is the combination with large-area lithographic techniques e.g. mask-based deep-UV, where substructures may be FIB-defined. This type of fast prototyping allows for testing of many variations on a prefabricated generic photonic crystal "breadboard", avoiding the typical long turn-around times for mask-based lithography. It can also be used for trimming/tuning existing structures, e.g. resonators and their coupling coefficients, and critical waveguide junctions/facets. In this paper we will first present the design and fabrication scheme of the host structures: the crystalline silicon membranes from silicon-on-insulator (SOI) wafers. Furthermore we will discuss two fabrication methods for removing the SiO_2 that result in either smooth or extremely rough surfaces in section 3.2.2. Also a detailed description of the important parameters for the milling experiments will be given. The fabrication result of a photonic crystal lattice milled into the membrane is presented in section 3.2.3. A demonstration of the FIB induced nanopolishing effect will be also be given. Finally we will present the main conclusions.

3.2.2 Fabrication

In this section we will first briefly describe the design and fabrication of the photonic host structures needed for the FIB milling process. Secondly we will describe the FIB milling process and its relevant parameters.

3.2.2.1 Host structure definition

As a host structure for FIB milling we focused on symmetric air-bridge type PCS [14] in silicon (Si) membranes that are fabricated from commercially available SOI wafers [15] with a Si device top-layer etched back to ~300 nm on top of a 3.3 µm SiO_2 layer. The fabrication of a membrane starts with (UV) optical lithography for defining the etch windows, and the alignment markers. Next RIE is used to etch the top Si layer. The PCS area (host-area) and the waveguides are defined by a second lithography step. Another dry-etching step is used to etch the pattern into the silicon, see Figure 3.2-2.

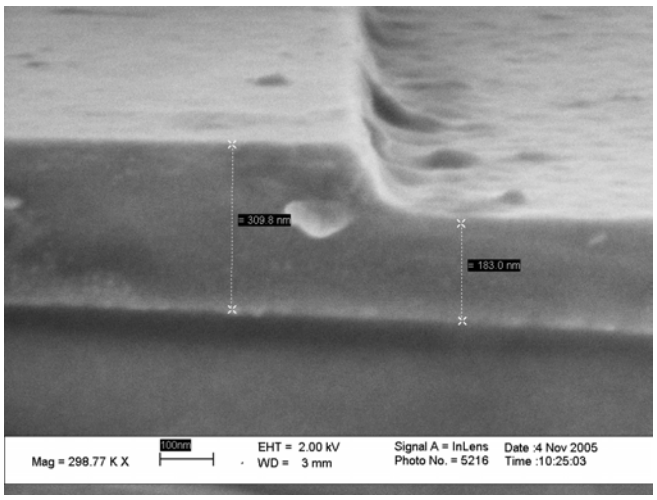

Figure 3.2-2: A cross-section of the fabricated ridge waveguide in SOI, showing relatively large sidewall roughness. This particular waveguide has a ridge height of ~ 120 nm.

We have chosen to use low-lateral-contrast access waveguides which can be single-moded at a width larger than 1 μm, thus avoiding the need for expensive e-beam generated masks. Therefore, fabrication of our design called for a relatively slow RIE process in order to produce the needed shallow (~20 nm) ridge with sufficient accuracy. However, our laser-beam generated mask provided poor edge definition, which induced large side-wall roughness, although the overall loss parameter of the waveguides is still low, because the side-wall area is very small compared to the case of photonic wires. To obtain both smooth and highly roughened (porous [16]) surfaces we have fabricated the membranes in two different ways. The former is obtained by applying a third lithography step to protect the top silicon during the buffered HF etch of the bottom sacrificial SiO_2 layer in a dark environment to form the final membranes. The roughened sample is fabricated by BHF etch without protecting layer and by exposure of light to porosify the Si surface of the membranes (see the SEM in Figure 3.2-5). The sample shows pores (roughness) with an average diameter around 100 nm. For integrated optics such a roughness is clearly unwanted. In this research we will show that after processing, the target area becomes smooth with an average roughness of less than 5 nm.

3.2.2.2 FIB milling of Si membranes

A recently introduced dual-beam FIB machine, the dual beam FEI Nova 600, was used for the FIB processing of our structures. It has both an ion and e-beam column, which can be used simultaneously, e.g. for charge neutralization, or separately for milling followed by a destruction free inspection using the e-beam. For the experiments presented in this paper the magnification was set to 10000 (10kX), which gives a pixel allocation size of 3.1 nm. The total field that could be written without stitching errors (FoV) was about 12.7 μm x 12.7 μm. The acceleration voltage was fixed as well as the dwell time (time that the beam is stationary at a certain pixel) to respectively 30 kV and 100 μs. For definition of submicron structures it is important to use low milling currents to minimize charging and re-deposition effects; also a lower current gives a smaller 1/*e* spot size. The downside to a small etch current is that the total etch time becomes longer and consequently the milling process will be more sensitive for distortion by drift. In our experiment the etch times were typically about 5 minutes per prototype. We used two different ion-beam current values which provide a good compromise between milling speed and accuracy, viz. 28 pA resulting in a spot size (1/*e* beam diameter) of ~15.5 nm, and 9.7 pA which gives a spot size of 11.9 nm. For nanostructures the (pixel) sequence of milling may become important, i.e. the temporarily local geometry affects the final result. In this investigation we have fixed the milling

direction of the ion beam by writing the design in horizontal lines, thus avoiding an additional degree of complexity.

3.2.3 FIB milling results

In section 3.2.3.1 we present a PCS that has been designed for characterization of the complete bandgap of rotated hexagonal holes in a triangular lattice. The milling experiment, performed at 28 pA, shows that the FIB is a valuable tool for easy and fast definition of integrated photonic functions, especially suited for photonic crystals in high-index-contrast systems, since they only require small writing areas. Another interesting phenomenon, the observed nanopolishing effect is discussed in section 3.2.3.2. We will show a clear example for this nanopolishing effect.

3.2.3.1 Planar photonic crystal for optical characterization

For optical transmission experiments we have fabricated a lateral multimodal waveguide of ~10 μm width having a wider region (~12 μm) exactly in the middle of the membrane. The ridge waveguide gives a lateral mode spread (about 6 modes) over a small index difference, which may be preferred for accurate detection of the band edges.

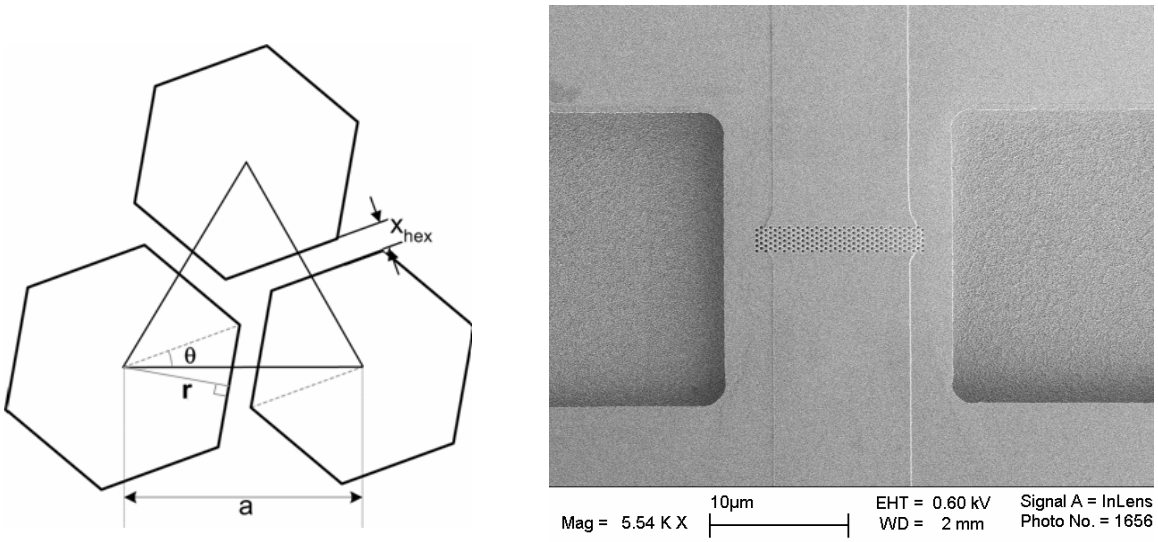

(a) **(b)**

Figure 3.2-3: (a) Schematic drawing of the triangular lattice with hexagonal holes rotated over an angle θ. (b) Top view of a 5-periods photonic crystal structure, designed for transmission measurements

The lattice constant *a* used for this design was 380 nm and the radius *r* was designed as $r/a = 0.25$, using the definition of the unit cell as shown in Figure 3.2-3a. A top view image of the milled planar photonic crystal (PhC) region plus waveguide section and etch windows (used for bottom oxide removal) is shown in Figure 3.2-3b. SEM photo's with higher magnifications of the PhC area are shown in Figure 3.2-4.

A 5-periods long and 37 "layers" wide ΓK oriented crystal was chosen. After analyzing the SEM photo's, we find a value of 380 nm ± 10 nm for *a*, and an average r/a of the holes of $r/a \approx 0.24 \pm 0.2$. The fabricated structures match well with the design. However some variations are found in hole size in the region outside the ridge waveguide, see Figure 3.2-4a. This is caused by the smaller silicon thickness outside the ridge region which requires a smaller milling time. Since changing the current locally is not an option (loss of focus), a possible solution is to vary either the dwell times of the individual holes or simply modify the total number of pixels representing the hole area. The latter approach may lead to a decrease of the definition accuracy. The 28 pA milling

current used for this design (spot size 15.5 nm) causes some rounding of the hexagons, due to beam overlap. A further decrease of the beam current to 9.7 pA will sharpen the hexagons, but the milling time will also triple to ~15 minutes.

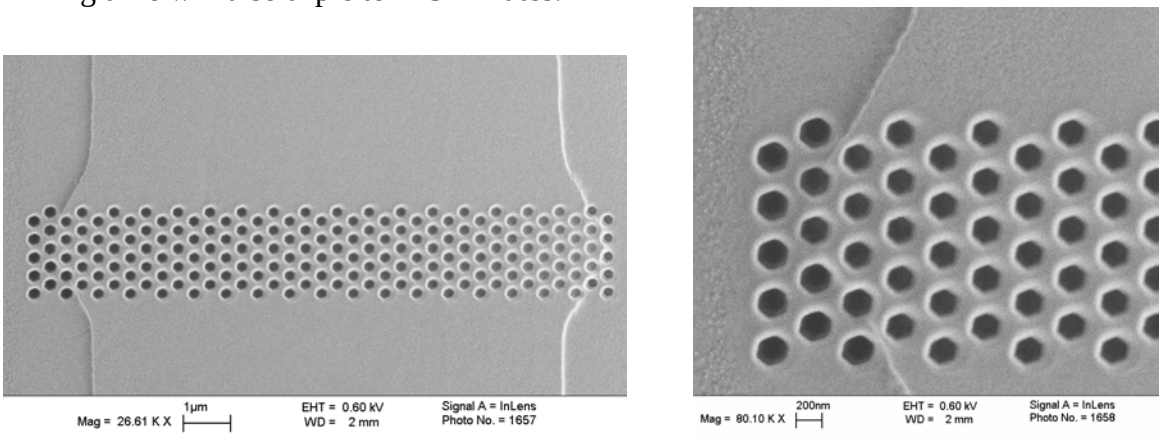

(a) **(b)**

Figure 3.2-4: (a) A zoomed-in top view of the photonic crystal section shown in Figure 3.2-4b. (b) A (further zoom in) top view of the photonic crystal section shown in the left graph.

3.2.3.2 Nanopolishing effect

In 3.2.2.1 we have described the method to realize roughened membranes. The result is presented in Figure 3.2-5, which shows the porosification of the top silicon layer. For clearness we have chosen to use a large air-filling fraction and a larger lattice constant, respectively $r/a \sim 0.4$, $a = 950$ nm. Using graphical analysis: edge detection and a Fourier technique on the porous area of the SEM graph, we observe an average pore size of about 100 nm. After etching for ~ 2.5 minutes at a low current of 9.7 pA we obtain a PhC structure which has not yet been etched through the membrane. It is interesting that the previously rough area has been transformed into a smooth (patterned) surface.

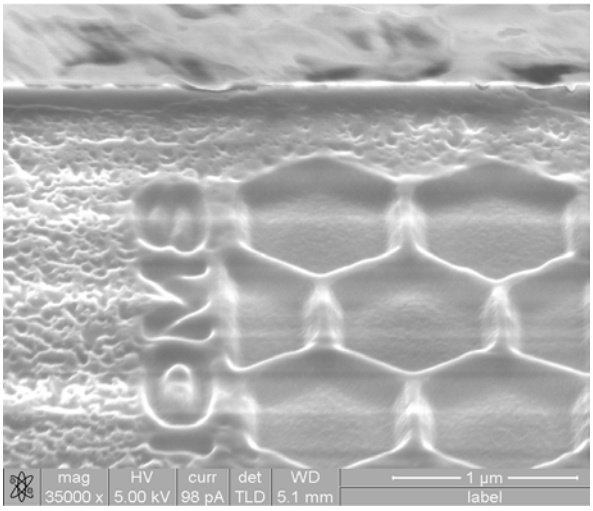

Figure 3.2-5: A milled hexagonal structure which shows the nanopolishing effect in and around the holes.

In fact, the roughness inside the hole has dropped below the accuracy of the (Dual) FIB-SEM. An AFM measurement method could be used to more exactly quantify the roughness. An interesting idea would to combine both the rough surface (having an extremely large surface) with a photonic crystal structure for sensing purposes. The actual implementation is still to be designed.

We anticipate that the observed nanopolishing is an important property of the FIB, which can be exploited for the realization of nanosmooth photonic crystals. We will report on the impact of FIB-related effects like smoothening, amorphization, and implantation, on the optical properties of a PCS in a different paper.

3.2.4 Conclusions

We have shown successful fabrication of low-ridge SOI waveguide structures. The air-bridge structure could be obtained either by protective etching of the SiO_2 buffer layer in a dark environment to achieve smooth surfaces or they could be obtained by etching in an unprotected environment, which gives ultra-rough surfaces. The smooth membranes could be used to host photonic crystal prototype structures, in our case a uniform lattice. On the other hand, the membranes having a porous layer could be used to prove the nanopolishing capabilities of the FIB in photonic structures. The hybrid structure having a porous region and a nanosmooth PhC region may also be useful in optical sensing applications. Though the nanopolishing effect has not been optically characterized at the moment, we are convinced of its important role in nanofabrication of high index-contrast photonic devices, where extremely low roughness is required.

3.2.5 Acknowledgments

We thank Bert Otter, Eddy Ruiter and Mark Smithers for taking the SEM pictures. Further we would like to thank Frans Segerink for his technical advice on FIB milling. This research is supported by NanoNed, a national nanotechnology program coordinated by the Dutch ministry of Economic Affairs. This research was also supported by the Dutch Technology Foundation STW and the MESA+ Scientific Research Orientation on “Advanced Photonic Structures”.

3.2.6 References

[1] P. R. Villeneuve, S. Fan and J. Joannopoulos, “Microcavities in photonic crystals: Mode symmetry, tunability, and coupling efficiency”, *Physical Review B*, vol. **54**, pp. 7837-7842, 1996.

[2] W. C. L. Hopman, P. Pottier, D. Yudistira, J. van Lith, P. V. Lambeck, R. M. De La Rue, A. Driessen, H. J. W. M. Hoekstra and R. M. de Ridder, “Quasi-one-dimensional photonic crystal as a compact building-block for refractometric optical sensors”, *IEEE Journal Of Selected Topics In Quantum Electronics*, vol. **11**, pp. 11-16, 2005.

[3] S. Noda, M. Yokoyama, M. Imada, A. Chutinan and M. Mochizuki, “Polarization mode control of two-dimensional photonic crystal laser by unit cell structure design”, *Science*, vol. **293**, pp. 1123-1125, 2001.

[4] J. D. Joannopoulos, R. D. Meade and J. N. Winn, "Photonic crystals: Molding the flow of light", ISBN: 0-691-03744-2, Princeton University Press, 1995.

[5] C. G. Bostan & R. M. de Ridder, “Design of photonic crystal slab structures with absolute gaps in guided modes”, *Journal of Optoelectronics and Advanced Materials*, vol. **4**, pp. 921-928, 2002.

[6] S. Reyntjens & R. Puers, “A review of focused ion beam applications in microsystem technology”, *Journal of Micromechanics and Microengineering*, vol. **11**, pp. 287-300, 2001.

[7] Q. Ren, B. Zhang, J. Xu, Z. S. Zhang, Y. B. Jin, Y. Qian and D. P. Yu, “Etched facet and semiconductor/air DBR facet of a AlGaInP laser diode prepared by focused ion beam milling”, *Solid State Communications*, vol. **130**, pp. 433-436, 2004.

[8] T. Ito, H. Ishikawa, T. Egawa, T. Jimbo and M. Umeno, “Fabrication of flat end mirror etched by focused ion beam for GaN-based blue-green laser diode”, *Japanese Journal of Applied Physics Part 1*, vol. **36**, pp. 7710-7711, 1997.

[9] A. Chelnokov, K. Wang, S. Rowson, P. Garoche and J. M. Lourtioz, “Near-infrared Yablonovite-like photonic crystals by focused-ion-beam etching of macroporous silicon”, *Applied Physics Letters*, vol. **77**, pp. 2943-2945, 2000.

[10] M. J. Cryan, M. Hill, D. C. Sanz, P. S. Ivanov, P. J. Heard, L. Tian, S. Y. Yu and J. M. Rorison, “Focused ion beam-based fabrication of nanostructured photonic devices”, *IEEE Journal Of Selected Topics In Quantum Electronics*, vol. **11**, pp. 1266-1277, 2005.

[11] Y. Fu, N. K. A. Bryan, O. N. Shing and H. N. P. Wyan, "Influence analysis of dwell time on focused ion beam micromachining in silicon", *Sensors and Actuators*, A: Physical, vol. **79**, pp. 230-234, 2000.

[12] T. L. Matteson, S. W. Schwarz, E. C. Houge, B. W. Kempshall and L. A. Giannuzzi, "Electron backscattering diffraction investigation of focused ion beam surfaces", *Journal of Electronic Materials*, vol. **31**, pp. 33-39, 2002.

[13] B. I. Prenitzer, C. A. Urbanik-Shannon, L. A. Giannuzzi, S. R. Brown, R. B. Irwin, T. L. Shofner and F. A. Stevie, "The correlation between ion beam/material interactions and practical FIB specimen preparation", *Microscopy and Microanalysis*, vol. **9**, pp. 216-236, 2003.

[14] M. Loncar, T. Doll, J. Vuckovic and A. Scherer, "Design and fabrication of silicon photonic crystal optical waveguides", *Journal of Lightwave Technology*, vol. **18**, pp. 1402-1411, 2000.

[15] S.O.I. TEC, Silicon on Insulator technologies, http://www.soitec.com.

[16] V. Lehmann & U. Gosele, "Porous Silicon Formation - a Quantum Wire Effect", *Applied Physics Letters*, vol. **58**, pp. 856-858, 1991.

3.3 FIB milling routine and parameter optimizations

Abstract– Focused ion beam (FIB) milling is receiving increasing attention for nanostructuring in silicon (Si). These structures can for example be used for photonic crystal structures in a silicon-on-insulator (SOI) configuration or for moulds which can have various applications in combination with imprint technologies. However, FIB-fabrication of submicrometre holes having perfectly vertical sidewalls is still challenging due to the redeposition effect in Si. In this study we show how the scan routine of the ion beam can be used as sidewall optimization parameter. The experiments have been performed in Si and SOI. Furthermore, we show that sidewall angles as small as 1.5 degrees are possible in Si membranes using a spiral scan method. We investigate the effect of the dose, loop number and dwell time on the sidewall angle, interhole milling and total milling depth by studying the milling of single and multiple holes into a crystal. We show that the sidewall angles can be as small as 5 degrees in (bulk) Si and SOI when applying a larger dose. Finally we found that a relatively large dwell time of 1 ms and a small loop number is favorable for obtaining vertical sidewalls. By comparing the results with those obtained by others, we conclude that the number of loops at a fixed dose per hole is the parameter that determines the sidewall angle and not the dwell time by itself.

This section has been accepted for publication:
W. C. L. Hopman, F. Ay, W. Hu, V. J. Gadgil, L. Kuipers, M. Pollnau and R. M. de Ridder, "Focused ion beam scan routine, dwell time and dose optimizations for submicrometre period planar photonic crystal components and stamps in silicon", Accepted for publication in nanotechnology, 2007.

3.3.1 Introduction

The ultimate goal of integrated optics is to achieve full control of light propagation. Functional devices based on classical planar optical waveguiding in low to moderate refractive index contrast systems are reaching the limits of achievable complexity due to the necessarily large bend radii [1]. One possible route towards increasing integration density by several orders of magnitude is using so-called 'photonic crystal slabs' (PCS), which have recently received much attention. By introducing 'defects' in a PCS in a controlled manner, one is able to implement passive and active building blocks (e.g. filters [2], sensors [3], lasers [4]). Important breakthroughs have been reported on nanocavities having Q-factors [5] exceeding 10^5 [6] and their applications as filter and even as all-optical transistor [7]. Also the reduction of the group velocity in PCS structures by several orders of magnitude [8] and its application as a tunable time delay has been reported [9]. A typical PCS structure consists in a high-refractive-index layer (e.g. Si, GaAs) perforated with a 2-D periodic lattice of air holes and having a diameter of approximately half the lattice period. The layer is stacked between two semi-infinite claddings that can be either patterned or homogeneous. There are two coexisting confinement mechanisms of light in PCS: in-plane confinement by the photonic bandgap effect [10] and vertical confinement by refractive-index-guiding realized by an index contrast between the PCS and its claddings. The basic functional PCS-based building blocks (resonators, waveguides, filters, switches, etc.) are relatively small structures (10-40 μm) which can be combined to form more complex large-scale architectures. Desired milling depths for photonic operation and moulds are between 100 and 200 nm [11] and the typical hole size is about 200-300 nm in diameter arranged in a lattice with a periodicity around 0.5 μm [5,7,8,12-14].

Focused ion beam (FIB) milling can be used to define these PCS structures in, for example, silicon, which can be used as a mould for nanoimprint lithography, or in a silicon on insulator (SOI) layer configuration suitable for photonic applications [14]. An important challenge for nanophotonics is its interfacing to the outside world. For guided-wave applications, it is often necessary to use relatively large-sized access waveguides that are usually defined using conventional lithography and etching methods. On the other hand, we have the small photonic crystal elements with features requiring sub-10 nm resolution, which should be accurately aligned with respect to the larger structures. Due to its inherent imaging and high-accuracy alignment properties, FIB is a promising tool for fabricating nanophotonic structures on substrates containing predefined microscopic and macroscopic waveguiding structures.

In opto-electronics, FIB has been applied for fabrication of microoptical components with low surface roughness [15] and for defining the end facet mirrors for conventional semiconductor lasers [16]. It has also been applied for bulk micromachining of macroporous silicon in order to fabricate 3-D Yablonovite-like photonic crystals [17], and for fabricating 2-D periodic, metal nanostructures [18] of which the shape of the primitive unit cell can be varied [19]. Another application of FIB has been the fabrication of quasi-2-D photonic crystals by milling 1-D gratings into freestanding multilayer membranes [20]. Direct FIB milling in silicon is still in an early state of maturity, the losses by modifications of the crystalline Si [21-23] induced by ion bombardment and implantation of, for example, gallium ions within the sample [24], are still too high [25] to realize high-quality PCS devices. However, some recent results have been achieved in lowering the losses by either using etch-assisting gasses [25,26] or heat-treatments (out-diffusion of ions) [27,28], which may lead to breakthroughs on this subject. The damaged Si at the Si-air interface may be removed by wet chemical etching [29]. On the other hand, FIB processing is and ideal candidate for fabrication of moulds, where the previously mentioned disadvantages of the ion milling process do not apply [11,30,31]. The smoothening effect of FIB processing [32] can, for example, be exploited for creating nanosmooth moulds and replicas.

Perfectly vertical sidewalls are, in principle, required for photonic applications to guarantee low-loss propagation; sidewall angles of 5 degrees can already induce a 8 dB/mm propagation loss [33]. Fabricating submicron holes in silicon with perfectly vertical sidewalls by FIB milling is

challenging due to the redeposition effect [23,34-36]: sputtered Si atoms or clusters can be redeposited locally. This effect is less pronounced in the milling of slits (or trenches), which can result in sidewall angles up to a few degree for low currents [37]. For similar structures as studied in this paper, sidewall angles of ~ 9 degrees have been reported obtained using a multi-pass type raster scan [38]. The redeposition effect becomes more dominant when the size of the holes is decreased. A straightforward solution for lowering the effects of redeposition by using a repetitive pass system was published in 1984 by Yamaguchi et al. [39]. That work forms the basis for investigations on the milling properties that can by manipulated by varying the dwell time [40-42] (the time the beam is stationary at a fixed point), which may influence the number of repetition loops. However, dwell-times cannot be made arbitrarily small, because FIB does not provide infinite contrast between written and non-written areas. This is because a structure is defined using, for example, a raster scan while modulating the ion beam current. The ion beam cannot be completely turned off when moving sequentially from one pixel to the next, leading to unwanted milling of the nominally unwritten area. However, the contrast can be increased choosing an appropriate milling strategy, as we will show in this paper. Besides the contrast, the scan path of the ion beam can also influence the geometry of the milled structure. The most common scan routines are: serpentine, raster, annulus and radial (or spiral) which are described in [35,43]. The main method for analyzing the geometry is cross-sectioning of the holes and subsequent inspection by scanning electron microscopy (SEM). The SEM photos are then further analyzed to find the milling depths, sidewall angles and average hole diameters. The exact cross-sectioning method is presented first in detail in section 3.3.2.2, because we found that some cross-sectioning methods might influence the originally milled geometry leading to incorrect interpretations. In section 3.3.3, we compare the hole geometry obtained for two routines for bulk Si, SOI and Si membranes namely raster and spiral scanning. The remainder of this paper refers to results obtained by using the spiral-scan routine. To optimize the sidewall angles of the submicrometre holes needed for photonic operation further, we investigated in section 3.3.4 the impact of a range of doses on the milling depth and sidewall angle for both individual holes and holes within a triangular-lattice crystal at 48 pA. Furthermore, in section 3.3.5 we present the effects of varying the combination of dwell time and number of loops for a milling current of 48 pA, while keeping the total dose constant. Finally, the main conclusions are presented in section 3.3.6.

3.3.2 FIB processing

3.3.2.1 Machine properties and general settings

A dual-beam FIB machine, the Nova 600 from FEI Company, was used for processing our structures. This machine has the advantage that it contains both an ion beam and an e-beam column. This powerful combination allows for both charge-neutralization in the case of milling insulating materials, and non-destructive characterization by SEM. The ion beam is generated from a gallium liquid metal source. The Field of View (FoV) of this FIB machine is divided into 4096 x 4096 pixels. The actual size of this grid depends on the magnification set prior to the milling. We used a magnification (in a view mode termed Quad-view) of 5000 (5 kX), resulting in a field of view of about 25 x 25 μm^2, and a minimum inter-pixel distance of 6.2 nm. For the experiments reported in this section the dwell time was predefined without optimizing at a value of 0.1 ms, which in our case resulted in a loop time of 6.0 s. All pixels are sequentially specified by their coordinates and dwell time. The 1/*e* ion beam spot size was maintained at approximately 1.5 times the inter-pixel distance. This spot size is mainly determined by the FIB milling current, which can be set in discrete steps by selecting an aperture size. Although the spot size grows with the milling current, the lowest current (1.5 pA, spot size = 7.5 nm) is not the optimum for practical reasons like the total milling-time and the feasible accuracy of focusing of the beam. In previous experiments we found that milling at 48 pA, which gives a spot size about 18 nm, provides for this FoV a good balance between milling time and accuracy. Switching between currents would be

ideal for larger structures; the boundaries of the hole could then be defined at a low current (small spot size). However, switching between currents and thus apertures is not an option in the FIB used in this research, because each aperture has a different focus and beam offset which can (in our current machine) not be programmed.

3.3.2.2 Cross-sectioning

In this work, cross-sections need to be realized in order to study how geometries of submicrometre-sized holes in several material systems are affected by the milling parameters. We tried several cross-sectioning techniques, namely milling of a hole with a sloped milling depth, line by line polishing, and combinations of these. In Figure 3.3-1a, a combination of both methods is used, first a big hole is milled at a current of 48 pA having a sloped bottom with the largest depth found at the cross-section interface, secondly a line by line milling strategy is applied at a lower current of 28 pA to achieve a smooth surface. Figure 3.3-1 shows that redeposited material fills up the holes and possibly modifies the shape of the hole. One of the effects of redeposition is a very low contrast between the original un-milled Si and the milled holes. The shape may be partially resolved by using low acceleration voltages and a high resolution SEM machine to minimize the influence of the observed charging effect. However a better method, which is used for the Si and SOI milling experiments presented in this paper, is first locally depositing a layer of platinum (Pt) using the FIB and a precursor gas (methylcyclopentadienyl)trimethyl-platinum. Secondly, a hole is milled with a sloped bottom to avoid long milling times. Finally, a line by line scan (termed cleaning cross-section) is applied at a lower current (28 pA) to establish a high-contrast high-resolution image, see Figure 3.3-1b.

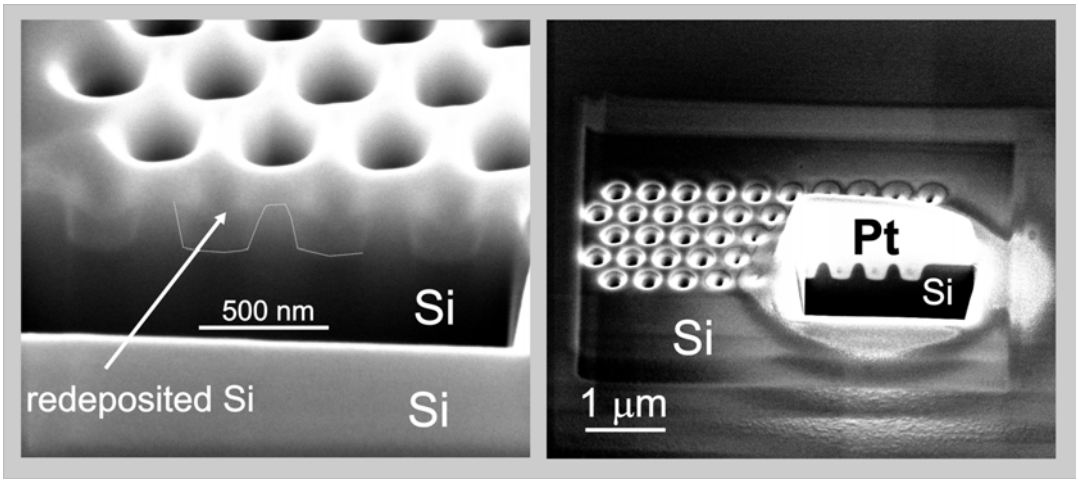

(a) (b)

Figure 3.3-1: Different methods for cross-sectioning. (a) Direct milling of a rectangular hole into the Si crystal; details can be found in the main text. (b) Cross-section milling after local metal (Pt) deposition.

Since the electron beam and the ion beam are arranged at a fixed angle of 52°, SEM photos at an angle can be made of the cross-section without rotating the stage. Small angles can be used for visualizing the cross-sections of deep holes to minimize the size and consequently the milling times of the large hole for cross-sectioning. Since the SEM photos are taken under an angle, the horizontal scale bar cannot be applied to the vertical direction. The length of the image in vertical direction has to be scaled by 1/sin(*angle*).

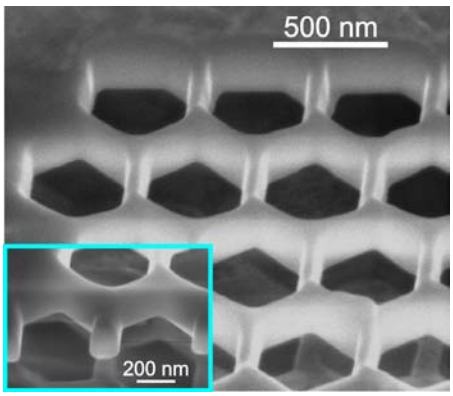

Figure 3.3-2: An example of a well defined FIB-milled planar PCS in a Si membrane (viewed at 52°). The hexagons shown here were rotated by 9° with respect to the photonic crystal lattice, in order to obtain an enlarged photonic bandgap [13]. Through the structure a "shadow pattern" can be seen in the bottom silicon due to milling of the ion beam into the substrate. A cross-section (viewed at 35°) of the same structure made by milling a slit into the air-bridge PCS is shown in the inset. The structure was milled at 9.7 pA using a dwell time of 0.01 ms.

The membrane structures were cross-sectioned by milling a slit into the membrane using a current of 48 pA and fine-polishing using a line by line milling strategy at a current of 9.7 pA. Although redeposition on the sidewall can not be completely avoided when using this procedure, we observed little difference when comparing the cross-sectioned membrane with the angled top view SEM images; an example is shown in Figure 3.3-2.

3.3.3 Spiral scanning versus raster scanning

The standard scanning method used in most FIB applications is the raster scan, which is schematically shown in Figure 3.3-3a. The ion beam scans from one side to the other, while it mills for a specified dwell time at the pixel positions provided in the pattern definition file (here termed stream file). Since the beam is not switched off between the holes, the scan routine causes interhole milling, which leads to the top surface in the entire FoV to be lowered with respect to the surrounding surface. We refer to this effect as the structure being "sunk" into the substrate.

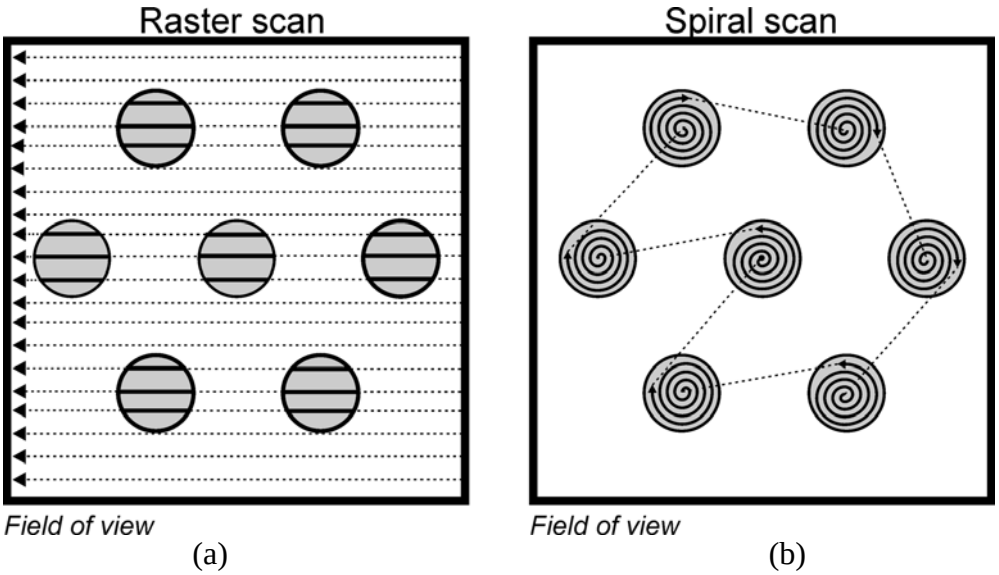

Figure 3.3-3: (a) Raster scanning. (b) Spiral scanning.

A better method for milling arrays of holes is spiral scanning. A schematic drawing of the spiral scan is also shown in Figure 3.3-3b. The spiral scan significantly reduces the amount of interhole

milling, as will be shown experimentally in the next section. This method is expected to produce more vertical sidewalls, because locally redeposited material is immediately milled away to a large extent. The method is tested on circular holes for reasons of obvious symmetry; however the spiral scan method is also expected to yield results with respect to the decrease in interhole milling and the sidewall angle for non-circular holes. The spiral scan method may also be beneficial for holes having sharp corners; however this has not been investigated in this research.
In section 3.3.3.1 we will compare the two scan routines, applied to "bulk" Si for 2 doses. In section 3.3.3.2 the same experiment is repeated for SOI, and in section 3.3.3.3 the scan routines are evaluated on Si membranes.

3.3.3.1 Silicon

For the experiments reported here we mounted a piece of p-type Silicon <100> on a chuck using silver-paint for providing a conducting path between the sample and the grounded holder. The electrical contact when using the paint is much better than for example is obtained using double-sided carbon tape. However, in some cases we noticed that the paint had a non-uniform layer thickness resulting in specimens that were slightly tilted up to 2 degrees, which may lead to asymmetrical holes. We designed two stream files defining 50 holes with 250 nm diameter and 440 nm periodicity. The raster scan file defined 64689 pixels, whereas the spiral scan file comprised 59900 pixels. The difference, which is caused by the spiral pattern filling the circular hole shape more efficiently, leads to small differences in the dose per hole. The 2 writing patterns were compared for 12 and 36 repetitions (loops), resulting in milling depths of about 250 and 900 nm, respectively. The ratio between the number of loops and the milling depth is not linear due to the redeposition effect, as we will show in section 3.3.4. The spread in milling depth will reveal both the best method for fabricating holes suitable for photonic application (12 loops) and it can show the geometry differences when subjected to a high level of redeposition (36 loops).

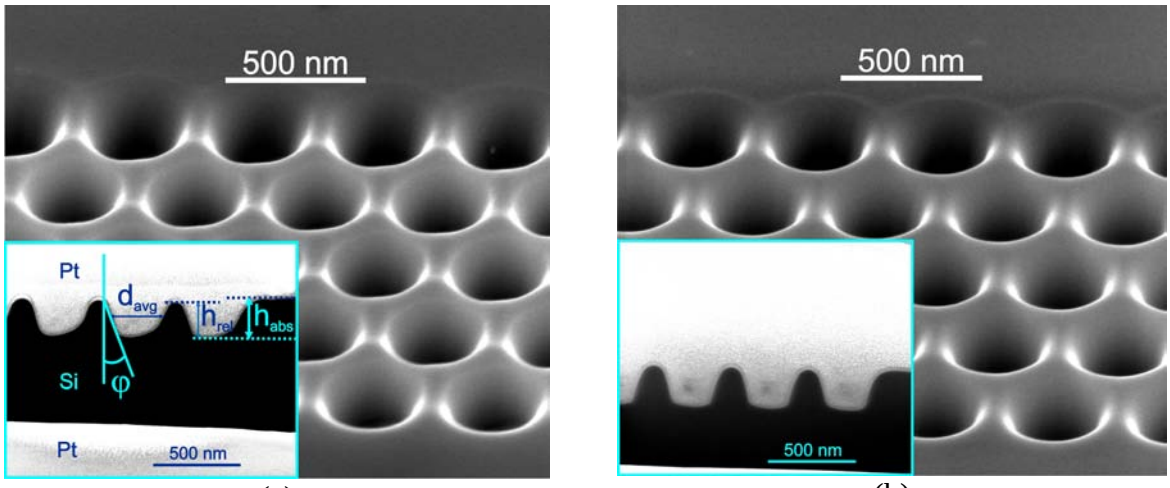

(a) (b)

Figure 3.3-4: Patterns milled at 48 pA using 12 loops and 0.1 ms dwell time per pixel. All SEM images were taken at a 52° angle. The insets show the cross-sections. (a) Raster scan (b) Spiral scan.

Figure 3.3-4a shows the result of a 12-loop raster scan. The overview SEM and the cross-section were taken at an angle of 52 degrees. Due to the angle, the scale bar in the vertical direction has to be multiplied by sin(52°) to match the scale bar displayed for the horizontal direction, as mentioned in section 3.3.2.2. Because the structure of holes is sunk into the host material, we define 2 milling depths, shown in the inset of Figure 3.3-4a. The first one is the total ("absolute") height h_{abs} from the bottom of the hole to the surface of the silicon (just outside the exposed area around the holes which might be subject to swelling [44,45]). The second one, the relative height

h_{rel} is defined as the height difference between the bottom of the hole and the interhole sidewall. Furthermore the average hole diameter is defined from the side view as the hole diameter at 0.5 h_{rel}. The sidewall angle φ is defined as the angle between the surface normal and the sloped sidewall, estimated around 0.5 h_{rel}. In some cases, for either scanning routine, the holes may show different angles at both sidewalls, which may be due to drift, sample-tilt or other mechanisms. Therefore, we took φ as the average angle of both visible sidewalls. Figure 3.3-4b shows the results of the spiral scan. Without detailed graphical analysis it can be seen that the spiral scan gives better-defined features; the sidewall angles are much smaller. This can be explained from the scanning routines shown in Figure 3.3-3; the raster scan passes over the Si sidewalls many more times than is the case for the spiral scan. Nevertheless, we always find rounding at the top and bottom of the hole, which cannot be avoided by mask-less milling. A hard mask on top like Al_2O_3 [26] may reduce the rounding effect at the top. Another difference between the scan patterns that is apparent from Figure 3.3-4 (see also Figure 3.3-3), is the difference between h_{abs} and h_{rel} for both methods. Careful examination of the hole cross-sections reveals for the case of raster scanning a systematic difference between the sidewall angles, measured at the right and the left hand side. A possible explanation will be given in the next section. The detailed analysis for comparison can be found in Table 3.3-1.

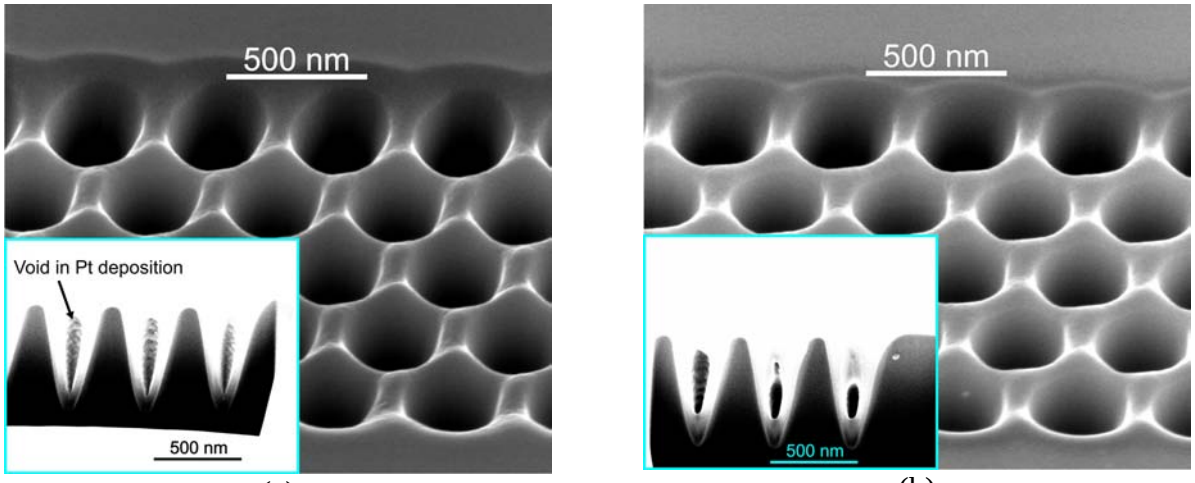

(a) (b)

Figure 3.3-5: Patterns milled at 48 pA in Si using 36 loops and 0.1 ms dwell time per pixel. The top view SEM images were taken at a 52 ° angle, and the cross-sections shown in the insets were taken at 45 °. (a) Raster scan (b) Spiral scan.

Increasing the number of loops to 36 led to "V" shaped holes. Figure 3.3-5 shows the results of both scan methods. Voids within the Pt are observed in the cross-section. The pattern obtained by the raster scan has sunk deeper into the Si host material, and when carefully examined, the spiral scan results show a slightly better sidewall angle (8° versus 9°). Despite the 10 % lower dose for the spiral scan, the milling depth is only a 1 % (11 nm) less. This may be partially explained by the non-linear relationship between dose and depth, which will be discussed in more detail in section 3.3.4. However, the difference may also be partly attributed to the difference in scanning method, indicating that the spiral scanning method is more efficient in sputtering the material out of the hole.

Table 3.3-1: Comparison of raster and spiral milling in Si, SOI and Si membranes (Si-m).

Scan routine	Material	Pixels per hole	Loop-number	Dose/ hole[a], D (pC)	Absolute depth, h_{abs}± 3 % (nm)	Relative depth, h_{rel} ± 3 % (nm)	Average diameter, d_{avg} ± 5% (nm)	sidewall angle ± 10 % (°)
Raster	Si	1293	12	75	253	214	299	19
Spiral	Si	1198	12	69	300	282	276	13
Raster	Si	1293	36	224	906	855	249	9
Spiral	Si	1198	36	207	917	885	232	8
Raster	SOI	1293	12	75	364	345	330	11
Spiral	SOI	1198	12	69	355	355	262	7
Raster	Si-m	1293	13	81	-	338	350	5
Spiral	Si-m	1198	13	75	-	339	380	5
Raster	Si-m	1293	20	115	-	470	366	<1.5

[a] The current and dwell times are fixed to 48 pA and 0.1 ms, respectively.

3.3.3.2 Silicon on insulator (SOI)

Photonic crystal slabs require that a core layer with a high refractive index, containing the periodic structure, is enclosed between two lower index cladding layers, in order to confine the light by effective index guiding. Moreover, for obtaining a photonic bandgap the refractive index difference between core and cladding layers should be as large as possible. A high index contrast can be established using SOI (silicon on top of silicon dioxide) for infrared wavelengths, where Si forms the guiding layer. Since the Si top layer is stacked on top of an insulator, the milling performance may be quite different from that of bulk Si because the charge distributions are influenced. Applying a conductive metal layer first is not preferred, because the milling process may cause implantation of metal particles that will give rise to increased optical loss. Therefore, the FIB milling was performed on an unmodified SOI layer stack with a Si layer thickness of 340 nm and a buried oxide thickness of 1 μm.

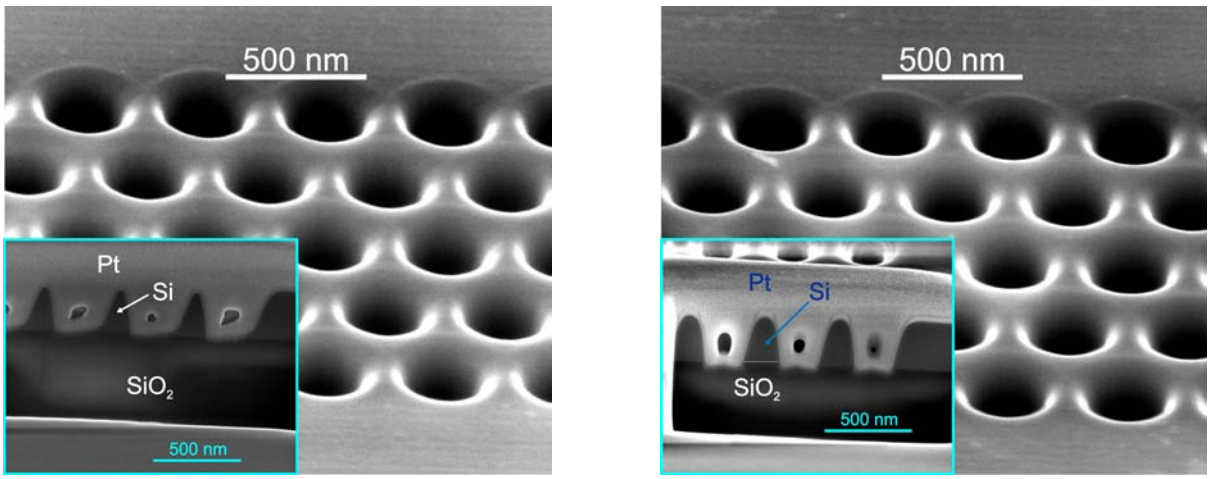

(a) (b)

Figure 3.3-6: Hole arrays milled at 48 pA in SOI using 12 loops and 0.1 ms dwell time per pixel. The SEM images were taken at a 52° angle, leading to a vertical scaling factor of 1.27. (a) Raster scan (b) Spiral scan.

The SOI milling results are depicted in Figure 3.3-6. Although the angled top view SEM images suggest that the hole shape does not strongly depend on the choice of scanning scheme, the cross-sections reveal a considerable difference. Raster scanning gives thinner interhole sidewalls and the angles are on average worse than for spiral scanning. In section 3.3.3.1 it was already observed that the raster method produces non-symmetrical shapes. This is a systematic effect originating from the scanning method, as can be seen in Figure 3.3-4a, Figure 3.3-5a and Figure 3.3-6a.

Because in the raster scan method the ion beam moves in vertical lines from right to left, the right part of the hole is milled earlier than the left part. Consequently the material milled from the left part may re-deposit on the right part, resulting in non-symmetric holes. The same explanation can be applied to the spiral method, which scans from the inside to the outside in concentric circles. As can be seen in Figure 3.3-6b, the inside of the hole is at lower depth than the outer part. Nevertheless, the hole is quite symmetric. This effect can be reduced by slightly decreasing the dwell time, i.e., using a higher number of passes. To do this without generating a larger amount of interhole milling, each hole has to be repeated several times in the stream file before jumping to the next hole. The major restriction for this method is the maximum allowed number of coordinates within the stream file, which is presently 10^6 for the used Nova 600 dual FIB. A further quantification of the geometries can be found in Table 3.3-1.

3.3.3.3 Silicon membranes

Silicon membranes are important material hosts for photonic structures [9,10], as they form a symmetric layer stack (Air-Si-Air) and maximize the index contrast (1-3.4-1 @ λ_0 = 1550 nm). Membrane-type PCS, often termed air-bridge photonic crystals, are better suited for FIB milling than SOI-based PCS because the redeposition effect is less severe in membranes. Two main reasons contribute to this effect. First of all, the sputtered material can escape in two directions as soon as the bottom of the membrane has been reached. Secondly, by slightly overetching (milling) the holes, the redeposited material can be selectively removed, resulting typically in a "shadow-pattern" milled into the bottom substrate, see Figure 3.3-2 and Figure 3.3-7.

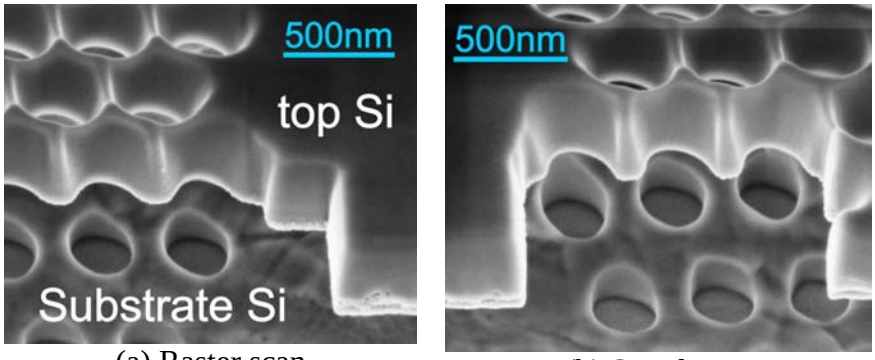

(a) Raster scan (b) Spiral scan

Figure 3.3-7: SOI membranes (the SiO2 has been selectively removed) milled at 48 pA and 0.1 ms pixel dwell time. Both SEM pictures were taken at a 60° angle. The cross-section was made using a line by line milling method to reduce deposition. (a) Raster scan. (b) Spiral scan.

By comparing the realized hole diameters (350-380 nm) in Figure 3.3-7 with the designed value (250 nm), we observed that holes milled through a membrane were larger than designed. This is caused by both the intentional over-milling and the more efficient milling process, due to the easier transport of milled material from the forming hole. This increase of hole size can be easily compensated for in the design of the structure. From Figure 3.3-7, we further find that both milling routines give similar average sidewall angles, see Table 3.3-1. Increasing the over-milling-time results in even better sidewall angles, see Figure 3.3-8. We report a sidewall angle better than *1.5 degree*, which can compete with the combination of direct e-beam lithography and reactive ion etching [46,47].

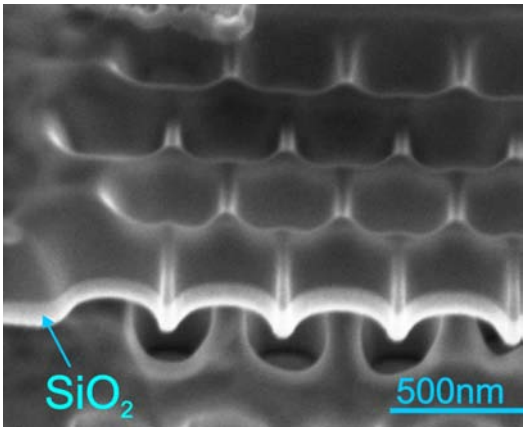

Figure 3.3-8: Milling result on a SOI membrane at 48 pA and 0.1 ms pixel dwell time. The pattern shows that with FIB a sidewall angle of less than 1.5 degree can be achieved. The SEM photo is taken at a 30° angle.

3.3.4 Milling depth and sidewall angle versus dose in silicon

A linear relationship between the milling depth and dose can often be assumed for large d_{avg}/h_{abs} ratios. The local redeposition effect is not dominant in this regime, because the sputtered silicon can escape easily into the vacuum. The following relation has been found experimentally,

$$T = \frac{V}{I\,B}, \tag{1}$$

with I the milling current, T the milling time, V the sputtered volume and B the material-dependent sputter rate. The sputter rate for Si is 0.27 $\mu m^3\ nC^{-1}$ at 30 kV. To find the milling depth as function of the dose, we can rewrite (1) using dose $D = I\,T$ and $V = 0.25\,\pi\,d_{avg}^2 h_{abs}$ as,

$$h_{abs} = D\frac{4\,B}{\pi\,d_{avg}^2}. \tag{2}$$

The function shows a linear relation between the dose and the milling depth. However, in our case the ratio d_{avg}/h_{abs} is close to unity making the redeposition more prominently observable. Therefore, the total volume that has to be milled is higher than the designed hole volume. Also the sputter efficiency B can change because the ions impinge on a slanted surface (resulting in higher milling rates [48]), therefore (2) transforms into a nonlinear relation for small hole sizes. In this section, the milling depth and the sidewall angle is studied as a function of the applied dose. We distinguish two situations, a single milled hole and a hole within a crystal (an array of holes) to investigate the proximity effects.

3.3.4.1 Single hole

In the "single hole" experiment, the same 250 nm hole diameter was used as in the experiments mentioned in the previous sections. The hole was milled using the spiral scan strategy and the current and dwell time were fixed at 48 pA and 0.1ms, respectively. The dose was varied by changing the loop number in discrete steps from 3 to 200, resulting in a dose variation between 17 and 1150 pC. The holes were cross-sectioned by the method described in section 3.3.2.2 and the SEM images were analyzed to quantify the hole geometry. The data obtained from the SEM images are shown in Figure 3.3-9. The graphs shown in Figure 3.3-9 can be used as calibration curves for milling individual 250 nm or 300 nm diameter holes. As expected, the figure shows that that the milling efficiency decreases with increasing milling depth. Moreover, we observe a strong decrease in sidewall angle at higher doses. In principle, this effect could be exploited for the fabrication of photonic components by designing the waveguiding layer to be at a depth where the sidewall angle and hole diameter have the desired values or using, for example, a sacrificial etch

layer, but having the structures at the surface is for obvious reasons the most convenient choice. The observed large sidewall angles at low doses are caused by the rounding effect. Therefore, it is unlikely that the sidewall angle at the top can be lowered by increasing the dose. However, as previously mentioned, a hard mask could lower the rounding at the top of the hole. It can also be seen that the diameter defined at half the hole depth is approaching the designed value for higher doses. For comparison, we also milled a sequence of 300 nm diameter holes in Si using the FIB built-in spiral scan routine (not convenient for defining an array for holes) with the standard dwell time of 0.1 μs. Since the hole diameter is larger, the sputtered material can escape more easily, which results in higher milling depth for the dose range between 200 pC and 1000 pC. A collage of the SEM images can be found in appendix A, Figure 3.3-12. The data belonging to the curves in Figure 3.3-9 can be found in Appendix A in Table 3.3-3 for the 250 nm hole and in Table 3.3-4 for the 300 nm hole.

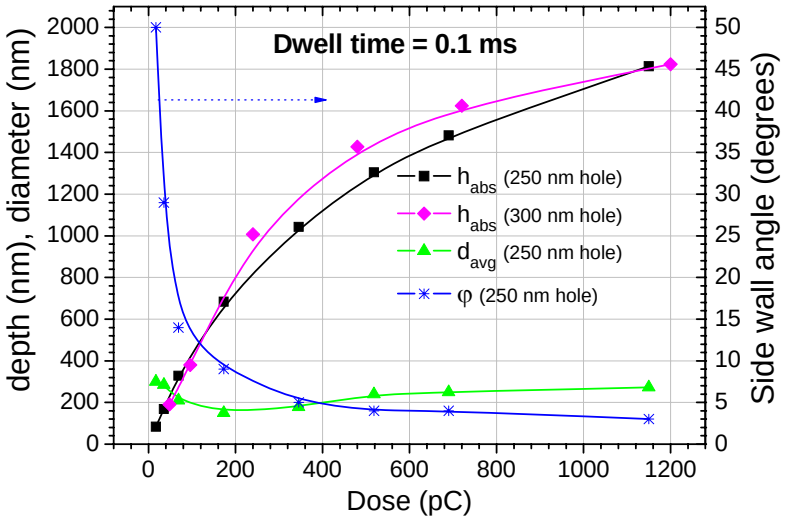

Figure 3.3-9: Milling results in bulk Si for a single hole as a function of dose. The designed hole diameter was 250 nm and the current and dwell time were fixed at 48 pA and 0.1 ms, respectively.

3.3.4.2 Hole as element of an array

In the previous section we showed the single hole milling results, however for PCS many holes arranged within, for example, a triangular or square lattice have to be milled. The geometry evolution at increasing dose is likely to differ from the single hole experiment due to proximity effects: milling of 1 hole interferes with the milling process of the surrounding holes in the array, resulting in different geometries. Another important effect for PCS is the interhole milling which manifests itself by the difference h_{abs}-h_{rel}. We studied the milling of holes in a triangular lattice having a 440 nm lattice constant. The dwell time was again fixed at 0.1 ms and the current at 48 pA. In Figure 3.3-10 we observe similar results for the milling of PCS holes as for single holes. However, an important difference is that in this case the milling depths are larger for the dose range studied here. As expected, the relative milling depth is smaller than the absolute milling depth. The figure suggests that the difference h_{abs}-h_{rel} evolves to a constant value. The data can be found in Appendix B, Table 3.3-5.

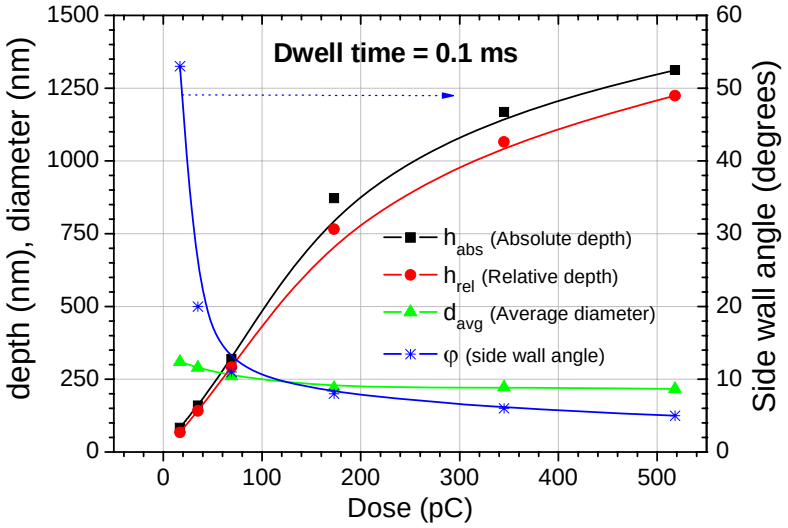

Figure 3.3-10: Milling results for holes in an array. The designed hole diameter was 250 nm and the current and dwell time were fixed to 0.1 ms and 48 pA, respectively.

3.3.5 Dwell time and loop number variation

Besides optimizing the hole geometry by choosing an appropriate scan strategy, the geometry can also be favorably influenced by the dwell time [39,41]. Varying the pixel dwell time implies a variation in dose, which makes the effect of the dwell time value less visible, see Figure 3.3-9 and Figure 3.3-10. Therefore, the dose was kept constant at 69 pC per hole while varying the combination loop number and dwell time. The loop number was varied from 2 to 200 and the dwell time from 6 µs to 0.6 ms.

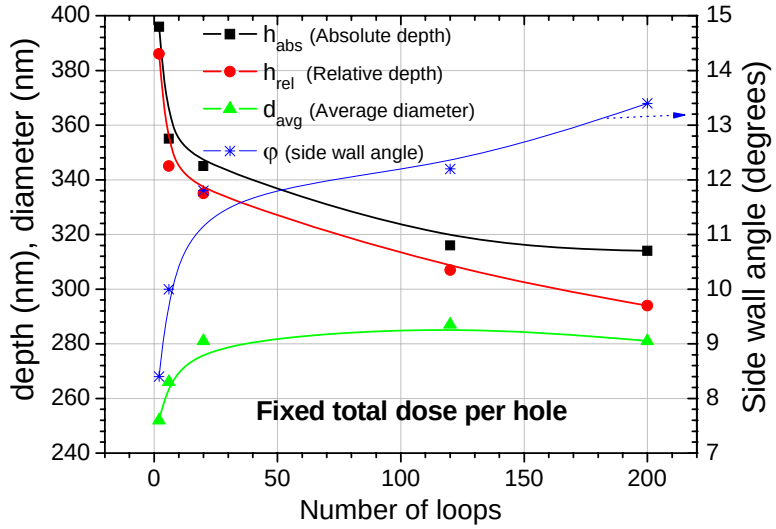

Figure 3.3-11: Milling results for a hole in an array, at a constant dose of 69 pC per hole. The designed hole diameter was 250 nm and the current was fixed at 48 pA.

The results of the experiments are displayed by the graphs in Figure 3.3-11. They show that the most favorable conditions for milling are at low loop numbers and, consequently, at large dwell times around 1 ms for the studied dose. However in [41] it was reported that extremely large dwell times should be avoided. The figure also shows that the milling efficiency decreases for an increasing number of loops. Regarding the sidewall angle it is obviously not desired to have a high number of loops for a dose of 69 pC. A high loop number also increases the interhole milling drastically. These findings confirm the assumption that the dwell time is not the parameter that

should be optimized but the dose per pixel per loop, or in other terms optimizing the number of loops while keeping the total dose per hole constant. In [49] it was suggested that smaller dwell times lead to better sidewall angles, however the authors used a large current (> 2.8 nA), which may explain their findings. The data from which the graphs in Figure 3.3-11 have been constructed can be found in Appendix B, Table 3.3-6.
Similar experiments were conducted on SOI for two currents; the results are shown in Table 3.3-2. The values show a close resemblance with the value obtained from the Si milling experiment at 48 pA. Based on these results, we conclude that lowering the current does not lead to a significant reduction in sidewall angle at a dose around 60 pC. This seems to contradict the observation published in [48]. However the difference may be explained by the fact that the authors also modify the dose per pixel when varying the current. Other differences may be explained by the difference in dose and hole diameter.

Table 3.3-2: Loop number variation of a hole within an array in SOI.

Current I (pA)	Loops	Dwell time (ms)	Dose per hole (pC)	Relative depth, h_{rel} ± 3 % (nm)	Average diameter, d_{avg} ± 5 % (nm)	sidewall angle ± 5 % (°)
48	2	1	61	286	282	7
9.7	6	1	59	320	258	7
9.7	62	0.1	66	349	255	11
9.7	617	0.01	66	301	210	20

3.3.6 Conclusions

We have shown that it is necessary to deposit a metal (here platinum) before making cross-sections to avoid perturbation of submicrometre milled holes through redeposition, and to achieve a large contrast. The large contrast was needed to determine parameters such as the sidewall angle, milling depth and hole diameter with high precision. Two different routines for scanning the beam over the sample were compared for milling in silicon, SOI and silicon membranes: raster scanning and spiral scanning. The spiral method has the advantage that the amount of structure lowering (sinking of the structure within the substrate) and interhole milling can be reduced significantly. We also found a slight increase in verticality of the sidewall angles and an increase in symmetry of the hole for the spiral scan routine applied to silicon and SOI. The study on the silicon membranes showed that, using the spiral method, it is possible to achieve sidewall angles as small as 1.5 degrees, which is comparable to state of the art dry etching achievements in silicon.

Further optimizations were explored by varying the dose applied to a single hole and to a hole as part of an array, while fixing the dwell time at 0.1 ms. We found that the sidewall angle at half the hole depth can be decreased to values of about 5 degrees in Si. Furthermore, we experimentally showed the non-linear relationship between the depth and dose for submicrometre holes. We found that due to the proximity effects presented here, we obtain a slightly higher milling rate for the holes in an array than for single holes. In the studied dose range we observed also a constant difference between the absolute depth h_{abs} and the relative depth h_{rel}. The impact of the combination dwell time and loop number was investigated by fixing the dose at 69 pC and varying the number of loops between 2 and 200 and the dwell time between 0.6 ms and 6 µs in Si. The most favorable combination with respect to the hole geometry was found to be a small loop number in combination with a relatively high dwell time of 1 ms. The results seem to contradict with other findings in which smaller dwell times are recommended. Therefore, we assume that the number of loops at a fixed dose per hole is the best optimization parameter with respect to the sidewall angles (redeposition) and not necessarily only the dwell time. In SOI we found a similar result for the combination of dwell time and loop number for beam currents of 9.7 and 48 pA.

3.3.7 Acknowledgments

This research was supported by NanoNed, a national nanotechnology program coordinated by the Dutch ministry of Economic Affairs, and was also supported by the European Network of Excellence ePIXnet. Laurens Kuipers would like to acknowledge the 'Stichting voor Fundamenteel Onderzoek der Materie (FOM)', which is financially supported by the 'Nederlandse Organisatie voor Wetenschappelijk Onderzoek (NWO)'.

3.3.8 References

[1] A. Melloni, P. Monguzzi, R. Costa and M. Martinelli, "Design of curved waveguides: the matched bend", *Journal Of The Optical Society Of America A-Optics Image Science And Vision*, vol. **20**, pp. 130-137, 2003.

[2] P. R. Villeneuve, S. Fan and J. Joannopoulos, "Microcavities in photonic crystals: Mode symmetry, tunability, and coupling efficiency", *Physical Review B*, vol. **54**, pp. 7837-7842, 1996.

[3] S. Chakravarty, J. Topol'ancik, P. Bhattacharya, S. Chakrabarti, Y. Kang and M. E. Meyerhoff, "Ion detection with photonic crystal microcavities", *Optics Letters*, vol. **30**, pp. 2578-2580, 2005.

[4] S. Noda, M. Yokoyama, M. Imada, A. Chutinan and M. Mochizuki, "Polarization mode control of two-dimensional photonic crystal laser by unit cell structure design", *Science*, vol. **293**, pp. 1123-1125, 2001.

[5] Y. Akahane, T. Asano, B. S. Song and S. Noda, "High-Q photonic nanocavity in a two-dimensional photonic crystal", *Nature*, vol. **425**, pp. 944-947, 2003.

[6] E. Kuramochi, M. Notomi, S. Mitsugi, A. Shinya, T. Tanabe and T. Watanabe, "Ultrahigh-Q photonic crystal nanocavities realized by the local width modulation of a line defect", *Applied Physics Letters*, vol. **88**, pp. 041112/1-3, 2006.

[7] M. Notomi, A. Shinya, S. Mitsugi, G. Kira, E. Kuramochi and T. Tanabe, "Optical bistable switching action of Si high-Q photonic-crystal nanocavities", *Optics Express*, vol. **13**, pp. 2678-2687, 2005.

[8] H. Gersen, T. J. Karle, R. J. P. Engelen, W. Bogaerts, J. P. Korterik, N. F. van Hulst, T. F. Krauss and L. Kuipers, "Direct observation of Bloch harmonics and negative phase velocity in photonic crystal waveguides", *Physical Review Letters*, vol. **94**, pp. 123901/1-4, 2005.

[9] Y. A. Vlasov, M. O'Boyle, H. F. Hamann and S. J. McNab, "Active control of slow light on a chip with photonic crystal waveguides", *Nature*, vol. **438**, pp. 65-69, 2005.

[10] S. G. Johnson, S. H. Fan, P. R. Villeneuve, J. D. Joannopoulos and L. A. Kolodziejski, "Guided modes in photonic crystal slabs", *Physical Review B*, vol. **60**, pp. 5751-5758, 1999.

[11] S. Y. Chou, P. R. Krauss and P. J. Renstrom, "Nanoimprint lithography", *Journal of Vacuum Science and Technology B: Microelectronics and Nanometer Structures*, vol. **14**, pp. 4129-4133, 1996.

[12] W. C. L. Hopman, K. O. Van Der Werf, A. J. F. Hollink, W. Bogaerts, V. Subramaniam and R. M. De Ridder, "Nanomechanical tuning and imaging of a photonic crystal microcavity resonance", *Optics Express*, vol. **14**, pp. 8745-8752, 2006.

[13] C. G. Bostan & R. M. de Ridder, "Design of photonic crystal slab structures with absolute gaps in guided modes", *Journal of Optoelectronics and Advanced Materials*, vol. **4**, pp. 921-928, 2002.

[14] C. G. Bostan, R. M. De Ridder, V. J. Gadgil, H. Kelderman, L. Kuipers and A. Driessen, "Design and fabrication of line-defect waveguides in hexagon-type SOI photonic crystal slabs," Photonics Europe (Strasbourg), Proc. **5450**, pp. 323-332 (2004).

[15] Y. Fu & N. K. A. Bryan, "Experimental study of microcylindrical lenses fabricated using focused-ion-beam technology", *Journal of Vacuum Science & Technology B*, vol. **19**, pp. 1259-1263, 2001.

[16] T. Ito, H. Ishikawa, T. Egawa, T. Jimbo and M. Umeno, "Fabrication of flat end mirror etched by focused ion beam for GaN-based blue-green laser diode", *Japanese Journal of Applied Physics Part 1*, vol. **36**, pp. 7710-7711, 1997.

[17] A. Chelnokov, K. Wang, S. Rowson, P. Garoche and J. M. Lourtioz, "Near-infrared Yablonovite-like photonic crystals by focused-ion-beam etching of macroporous silicon", *Applied Physics Letters*, vol. **77**, pp. 2943-2945, 2000.

[18] H. J. Lezec & T. Thio, "Diffracted evanescent wave model for enhanced and suppressed optical transmission through subwavelength hole arrays", *Optics Express*, vol. **12**, pp. 3629-3651, 2004.

[19] K. J. K. Klein Koerkamp, S. Enoch, F. B. Segerink, N. F. van Hulst and L. Kuipers, "Strong influence of hole shape on extraordinary transmission through periodic arrays of subwavelength holes", *Physical Review Letters*, vol. **92**, pp. 183901/1-4, 2004.

[20] K. Wang, P. Filloux, N. Paraire and P. Roca i CabarrocasBulkin, "Two-dimensional photonic crystals by focused-ion-beam etching of multilayer membranes", *Journal of Vacuum Science & Technology B*, vol. **21**, pp. 966-969, 2003.

[21] W. Brezna, H. Wanzenböck, A. Lugstein, E. Bertagnolli, E. Gornik and J. Smoliner, "Scanning capacitance microscopy investigations of focused ion beam damage in silicon", *Physica E-Low-Dimensional Systems & Nanostructures*, vol. **19**, pp. 178-182, 2003.

[22] J. G. Pellerin, G. M. Shedd, D. P. Griffis and P. E. Russell, "Characterization of Focused Ion-Beam Micromachined Features", *Journal of Vacuum Science & Technology B*, vol. **7**, pp. 1810-1812, 1989.

[23] Y. K. Kim, A. J. Danner, J. J. Raftery and K. D. Choquette, "Focused ion beam nanopatterning for optoelectronic device fabrication", *IEEE Journal on Selected Topics in Quantum Electronics*, vol. **11**, pp. 1292-1298, 2005.

[24] A. P. Knights & G. E. Hopper, "Effect of ion implantation induced defects on optical attenuation in silicon waveguides", *Electronics Letters*, vol. **39**, pp. 1648-1649, 2003.

[25] M. J. Cryan, M. Hill, D. C. Sanz, P. S. Ivanov, P. J. Heard, L. Tian, S. Y. Yu and J. M. Rorison, "Focused ion beam-based fabrication of nanostructured photonic devices", *IEEE Journal on Selected Topics in Quantum Electronics*, vol. **11**, pp. 1266-1277, 2005.

[26] J. Schrauwen, D. Van Thourhout and R. Baets, "Focused-ion-beam fabricated vertical fiber couplers on silicon-on-insulator waveguides", *Applied Physics Letters*, vol. **89**, pp. 141102/1-3, 2006.

[27] I. Chyr, B. Lee, L. C. Chao and A. J. Steckl, "Damage generation and removal in the Ga+ focused ion beam micromachining of GaN for photonic applications", *Journal of Vacuum Science & Technology B*, vol. **17**, pp. 3063-3067, 1999.

[28] Y. Tanaka, M. Tymczenko, T. Asano and S. Noda, "Fabrication of two-dimensional photonic crystal slab point-defect cavity employing local three-dimensional structures", *Japanese Journal of Applied Physics Part 1-Regular Papers Brief Communications & Review Papers*, vol. **45**, pp. 6096-7002, 2006.

[29] C. Lehrer, L. Frey, S. Petersen, H. Ryssel, M. Schafer and T. Sulzbach, "Integration of field emitters into scanning probe microscopy sensors using focused ion and electron beams", *Journal of Vacuum Science & Technology B: Microelectronics and Nanometer Structures*, vol. **22**, pp. 1402-06, 2004.

[30] N. Chaix, S. Landis, D. Hermelin, T. Leveder, C. Perret, V. Delaye and C. Gourgon, "Influence of mold depth on capillary bridges in nanoimprint lithography", *Journal of Vacuum Science and Technology B: Microelectronics and Nanometer Structures*, vol. **24**, pp. 3011-3015, 2006.

[31] H. W. Li, D. J. Kang, M. G. Blamire and W. T. S. Huck, "Focused ion beam fabrication of silicon print masters", *Nanotechnology*, vol. **14**, pp. 220-223, 2003.

[32] W. C. L. Hopman, R. M. De Ridder, S. Selvaraja, C. G. Bostan, V. J. Gadgil, L. Kuipers and A. Driessen, "Realization of 2-dimensional air-bridge silicon photonic crystals by focused ion beam, milling and nanopolishing," Photonics Europe (Strasbourg), Proc. **6182**, pp. 167-173 (2006).

[33] Y. Tanaka, T. Asano, Y. Akahane, B. S. Song and S. Noda, "Theoretical investigation of a two-dimensional photonic crystal slab with truncated cone air holes", *Applied Physics Letters*, vol. **82**, pp. 1661-1663, 2003.

[34] B. I. Prenitzer, C. A. Urbanik-Shannon, L. A. Giannuzzi, S. R. Brown, R. B. Irwin, T. L. Shofner and F. A. Stevie, "The correlation between ion beam/material interactions and practical FIB specimen preparation", *Microscopy and Microanalysis*, vol. **9**, pp. 216-236, 2003.

[35] Y. Fu, N. K. A. Bryan, O. N. Shing and N. P. Hung, "Influence of the redeposition effect for focused ion beam 3D micromachining in silicon", *International Journal of Advanced Manufacturing Technology*, vol. **16**, pp. 877-880, 2000.

[36] L. Frey, C. Lehrer and H. Ryssel, "Nanoscale effects in focused ion beam processing", *Applied Physics a-Materials Science & Processing*, vol. **76**, pp. 1017-1023, 2003.

[37] S. Lipp, L. Frey, C. Lehrer, B. Frank, E. Demm and H. Ryssel, "Investigations on the topology of structures milled and etched by focused ion beams", *Journal of Vacuum Science and Technology B: Microelectronics and Nanometer Structures*, vol. **14**, pp. 3996-3999, 1996.

[38] K. Balasubramanian, P. J. Heard and M. J. Cryan, "Focused ion beam fabrication of two dimensional photonic crystals in silicon-on-insulator", *Journal of Vacuum Science and Technology B: Microelectronics and Nanometer Structures*, vol. **24**, pp. 2533-2537, 2006.

[39] H. Yamaguchi, A. Shimase, S. Haraichi and T. Miyauchi, "Characteristics of silicon removal by fine focused gallium ion beam", *Journal of Vacuum Science & Technology B: Microelectronics Processing and Phenomena*, vol. **3**, pp. 71-74, 1984.

[40] Y. Fu, N. K. A. Bryan, O. N. Shing and H. N. P. Wyan, "Influence analysis of dwell time on focused ion beam micromachining in silicon", *Sensors and Actuators, A: Physical*, vol. **79**, pp. 230-234, 2000.

[41] D. P. Adams & M. J. Vasile, "Accurate focused ion beam sculpting of silicon using a variable pixel dwell time approach", *Journal of Vacuum Science & Technology B*, vol. **24**, pp. 836-44, 2006.
[42] P. M. Nellen, V. Callegari and R. Brönnimann, "FIB-milling of photonic structures and sputtering simulation", *Microelectronic Engineering*, vol. **83**, pp. 1805-1808, 2006.
[43] A. A. Tseng, "Recent developments in micromilling using focused ion beam technology", *Journal of Micromechanics and Microengineering*, vol. **14**, pp. R15-R34, 2004.
[44] A. Lugstein, B. Basnar, J. Smoliner and E. Bertagnolli, "FIB processing of silicon in the nanoscale regime", *Applied Physics A: Materials Science and Processing*, vol. **76**, pp. 545-548, 2003.
[45] L. Bischoff, J. Teichert and V. Heera, "Focused ion beam sputtering investigations on SiC", *Applied Surface Science*, vol. **184**, pp. 372-376, 2001.
[46] S. J. McNab, N. Moll and Y. A. Vlasov, "Ultra-low loss photonic integrated circuit with membrane-type photonic crystal waveguides", *Optics Express*, vol. **11**, pp. 2927-2939, 2003.
[47] M. Settle, M. Salib, A. Michaeli and T. F. Krauss, "Low loss silicon on insulator photonic crystal waveguides made by 193nm optical lithography", *Optics Express*, vol. **14**, pp. 2440-2445, 2006.
[48] C. Lehrer, L. Frey, S. Petersen and H. Ryssel, "Limitations of focused ion beam nanomachining", *Journal of Vacuum Science & Technology B*, vol. **19**, pp. 2533-2538, 2001.
[49] O. Wilhelmi, S. Reyntjens, D. Wall, R. Geurts, C. Jiao and L. Roussel. in Micro- and NanoEngineering (Barcelona, 2006).

Appendix A

Table 3.3-3: Values obtained from milling a single 250 nm diameter hole in Si.

Loops	Dose per hole[a] D (pC)	Absolute depth, h_{abs} ± 3 % (nm)	Average diameter, d_{avg} ± 5 % (nm)	sidewall angle ± 10 % (°)
3	17	84	300	50
6	35	169	285	29
12	69	328	210	14
30	173	683	150	9
60	345	1043	178	5
90	518	1305	240	4
120	690	1481	250	4
200	1150	1814	273	3

[a] Milled at 48 pA using a 0.1 ms dwell time

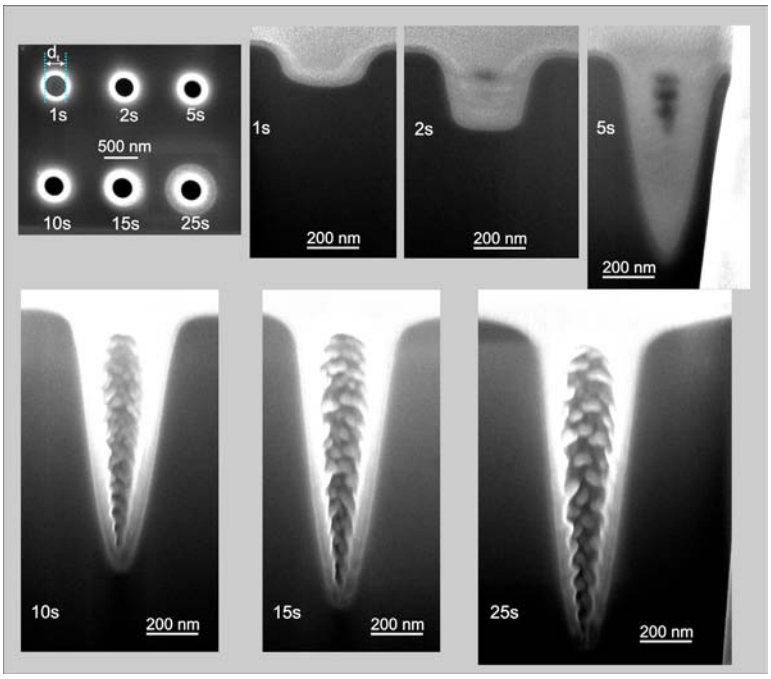

Figure 3.3-12: The effect of the dose on the geometry. The top left image shows a top view of all holes. The SEM images of the cross-sections in the top row are taken at a 52 degree angle, and the bottom row at 45 degrees. The holes were designed using the FIB built-in procedure to average diameter of 300 nm and the current and dwell time were fixed at 48 pA and 0.1 μs, respectively.

Table 3.3-4: Values obtained from milling a single 300 nm diameter hole in Si.

Milling time, T (s)	Dose/ hole[a] D (pC)	Absolute depth, h_{abs} ± 3 % (nm)	Average diameter, d_{avg} ± 5 % (nm)	sidewall angle φ ± 10 % (°)
1	48	191	349	27
2	96	380	322	9
5	240	1007	280	8
10	480	1428	283	6
15	720	1624	305	5
25	1200	1823	291	4

[a] Milled at 48 pA using a 0.1 μs dwell time

Appendix B

Table 3.3-5: Values obtained from milling an array[a] of holes in silicon.

Loop-number	Dose per hole[b] D (pC)	Absolute depth, h_{abs} ± 3 % (nm)	Relative depth, h_{rel} ± 3 % (nm)	Average diameter, d_{avg} ± 10% (nm)	sidewall angle ± 10 % (°)
3	17	83	68	310	53
6	35	160	141	290	20
12	69	320	292	261	11
30	173	872	766	220	8
60	345	1168	1065	222	6
90	518	1312	1224	217	5

[a] lattice constant 440 nm, hole diameter 250 nm
[b] Milled at 48 pA using a 0.1 ms dwell time

Table 3.3-6: Effect of dose[a]-loop number variation in an array[b] of holes.

Loops	Dwell time (ms)	Absolute depth, h_{abs} ± 3 % (nm)	Relative depth, h_{rel} ± 3 % (nm)	Average diameter, d_{avg} ± 5 % (nm)	sidewall angle ± 5 % (°)
2	0.6	396	386	252	8.4
6	0.2	355	345	266	10.0
20	0.06	345	335	281	11.8
120	0.001	316	307	287	12.2
200	0.006	314	294	281	13.4

[a] The dose was fixed at 69 pC
[b] lattice constant 440 nm, hole diameter 250 nm

3.4 Fabrication of high quality waveguide gratings.

Abstract—A method is presented for fabricating high quality ridge waveguide gratings by combining conventional mask lithography with laser interference lithography. The method, which allows for apodization functions modulating both amplitude and phase of the grating is demonstrated by fabricating a grating that is chirped by width-variation of the grated ridge waveguide. The structure was optically characterized using both an end-fire and an infrared camera setup to measure the transmission and to map and quantify the power scattered out of the grating, respectively. For a uniform grating we found a Q value of ~ 8000 for the resonance peak near the lower wavelength band edge, which was almost completely suppressed after apodization.

This section has been published:
W. C. L. Hopman, R. Dekker, D. Yudistira, W. F. A. Engbers, H. Hoekstra and R. M. de Ridder, "Fabrication and characterization of high-quality uniform and apodized Si_3N_4 waveguide gratings using laser interference lithography," IEEE Photonics Technology Letters, vol. 18, pp. 1855-1857, 2006.

3.4.1 Introduction

Waveguide gratings (WGG's) have shown their value for many years in filters and mirrors [1], sensors [2], lasers [3], second harmonic generation [4], tunable time-delays [5], and many more applications and theoretical studies. In a WGG a guided mode is manipulated through a 1-dimensional periodic variation of the dielectric constant along the propagation direction. An important property of finite uniform periodic structures in lossless media is the occurrence of fringes in the transmission and reflection spectra near the stop-band edges. It is well known that these oscillations in the transfer function (near the edges outside the stopband) of a uniform grating are due to Fabry-Perot resonance modes of the grating Bloch modes [6]. These fringes which are undesired for many applications, e.g. wavelength filtering, can be strongly reduced by apodization, i.e. making gradual transitions between the grating region and the unperturbed waveguide [7]. The optimum shape of the apodization function depends on the application and the grating parameters, and in general requires numerical optimization [8-10]. In this paper we propose a fabrication scheme which provides a straightforward way of implementing two types of apodization: (I) chirping through varying the width of the ridge-WGG [11,12], and (II) strength modulation by varying the width or location of the grating [12]. The main difference of our approach compared to most other approaches known from literature, e.g. [9,10,13], is that we first pattern the waveguides and the apodization function using conventional UV lithography, and then use laser interference lithography [14] in combination with an image reversal bake for defining the grating with the desired shape. In this paper we will show that these relatively strong low-loss WGG's can have a high quality factor for a first order longitudinal Fabry-Perot resonance in the case of no apodization. We demonstrate the potential of our fabrication method only for the chirp-based apodization method, because of its larger misalignment tolerance. We did not attempt to optimize the apodization function, but just chose to linearly taper the waveguide width to chirp the effective index. This led to an evident reduction of the modulation depth of the fringes near the lower wavelength side of the stop band edge. This is shown by both transmission and scatter measurements using an end-fire and an infrared-camera setup [15], respectively.

3.4.2 Realization

The fabrication of the grated ridge waveguide structures consisted of a three-step etching process performed on a Si_3N_4 guiding layer. First, a 275 nm thick stoichiometric Si_3N_4 (n = 1.981) slab was deposited on an 8 μm thermally grown SiO_2 (n = 1.445) buffer, using low pressure chemical vapor deposition. The first mask (dark field) contained text comments and alignment markers to assist further processing and characterization. This pattern was etched completely through the guiding film using a reactive ion etching (RIE) process. A second mask (bright field) defining both waveguide and taper structures was used for patterning the ridge waveguides. Our waveguide design for single-moded operation called for a 5 nm ridge step, which was achieved (Figure 3.4-1), after exposing the Si_3N_4 slab to buffered HF for 7 minutes. The gratings were defined using laser interference lithography (LIL), a technique that typically exposes a much larger area (several cm^2) than needed for the gratings. In order to confine the gratings and to define the apodization functions, a positive image reversal resist (Ti04-TX from MicroChemicals) was used with a double exposure technique. The first exposure for 5.5 s through a third (bright-field) mask defined the grating areas. After an image reversal bake, all areas where no grating was desired became insoluble and insensitive to further exposure, while the photosensitivity of the future grating areas was preserved (Figure 3.4-1b). The second exposure was made using a Lloyd's mirror LIL setup [14] employing a laser wave-length of 266 nm to realize Λ = 460 nm period gratings having a duty cycle of 20 % (Figure 3.4-1c). Finally, the gratings were transferred to the Si_3N_4-layer using RIE (Figure 3.4-1d). An etch depth of 60 nm was estimated using both profilometry and fitting of

optical measurement data using a mode expansion technique. Finally, a polymer top cladding (n ≈ 1.5) was applied to the grating regions for ensuring single-mode behavior.

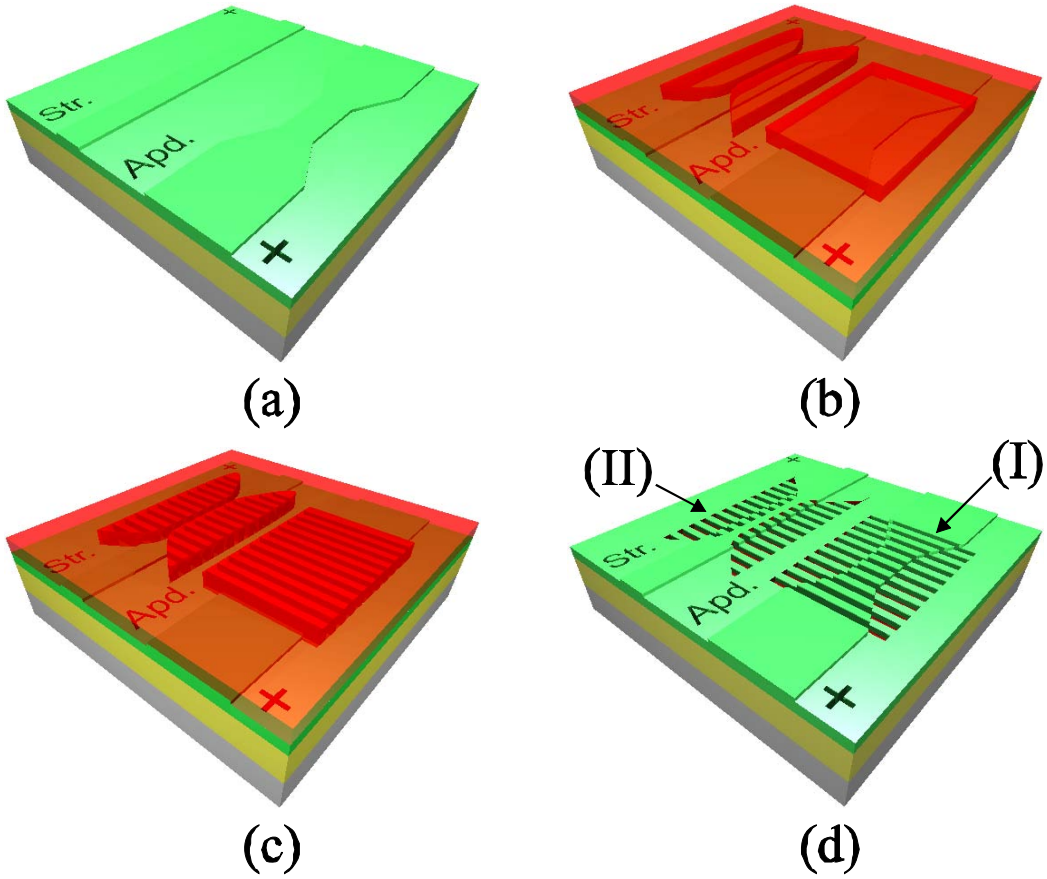

Figure 3.4-1: Schematic representation of the triple step lithographic fabrication process of the grated ridge waveguides.

3.4.3 Realization of apodization functions

As mentioned in the introduction two types of apodization can be achieved using our scheme, i.e. chirping (I) and strength modulation (II). The first method uses a variation of the waveguide width to obtain a corresponding position-dependent variation of the modal propagation constant (I in (Figure 3.4-1d). Thus, the mode has a position-dependent tuning with respect to the grating constant $2\pi/\Lambda$, having an effect equivalent to a period-chirped grating. Since this chirping function is determined by the local waveguide width, its realization process is essentially self-aligned and the definition of the grating areas only requires coarse alignment. The second method varies the effective grating strength by varying the overlap of the grating with the waveguide modal field. By positioning the lateral grating edge in the evanescent modal field tail (II in (Figure 3.4-1d), the effective grating strength can be gradually increased, starting from zero without the need for high resolution lithography, allowing, e.g. the realization of the well-known raised cosine function [12]. The methods could be combined in order to modulate both the phase and the amplitude of the grating.

We chose to use only method (I) with a 3-section linearly tapered waveguide (section 1: 7 µm to 2 µm over 225 periods; section 2: 50 periods at 2 µm width; section 3: inverse of section 1), which certainly does not result in an optimum apodization function, but which serves our purpose of demonstrating the technology. Modeling results showed that this type of apodization resulted in a reduction of the group delay (resonances) at the short-wavelength side of the stop band [6], which is experimentally verified in section 3.4.5

3.4.4 Experimental setup

Both an end-fire setup and an infrared (IR) sensitive camera were used for characterizing the WGG's. The IR-camera was positioned to collect the scattered photons from a selected area of the grating (see the dotted rectangle in Figure 3.4-2B). For the analyses we assume that the Rayleigh scattering is proportional to the local intensity. The available 12-bits IR-camera produced images of 320 x 240 pixels, each pixel representing a 0.8 μm x 0.8 μm chip area. The WGG's show a relatively small amount of scattering (compared to the peak value at resonance) at wavelengths outside the stop band, except for the transitions at the beginning and end of the grating. This low amount of scattering gives a clear indication of a high quality (e.g. low roughness) of the fabricated device and also leads to a fully exploited dynamic range of the IR-camera indicated by the graphs in Figure 3.4-2A.
For the end-fire transmission experiments we coupled light into the TE_{00} waveguide mode using a tunable laser (1470 to 1580 nm) in combination with a polarization controller. Since our photo-detector was calibrated and the transmission spectrum of the ungrated waveguides showed a flat response, we omitted further normalization.

3.4.5 Experimental results

The transmission results of WGG's, both with (solid curve) and without (dotted) apodization are shown in Figure 3.4-2A. The non-apodized structure shows sharp fringes at the left edge of the stop band, of which especially the first one is significantly reduced in the apodized case, as expected [6]. A slightly reduced stop band is observed induced by the apodization. Figure 3.4-2B shows three camera frames of the uniform grating but without cladding, taken at different wavelengths, see the labels in the left graph: in the stop band (b); at the first fringe (c); outside the stopband (d). The input and output of the grating can easily be distinguished by the relatively high scattering from these spots. The envelope of the scattering intensity of the first resonance perfectly matches the first order Fabry-Perot-like resonance of the Bloch modes in the grating [4]. The quality factor *Q*, defined as the ratio between the wavelength and the -3dB bandwidth of the resonance peak, can be obtained both from the scatter graph (Figure 3.4-2C) and the transmission spectrum (Figure 3.4-2A). For both cases we find $Q \approx 8000$. With an air cladding $Q \approx 14000$ is found. These numbers give an indication that the experienced optical loss is low. The loss is induced by for example non-uniformities in etch depth, layer thickness, waveguide width, material loss, etc.
A clear evidence of a successful reduction of the first order grating resonance is shown in panel C of Figure 3.4-2. The upper graph (I) shows the integrated collected scatter intensity for the uniform grating. Near the stop-band edges there is a huge increase in scatter intensity. It has been shown that these resonances can be used for integrated sensors [2]. However, these high-*Q* resonances, corresponding to large group delays [5], limit the bandwidth for the use in telecom applications. Furthermore, the apodized structure (II) shows an almost total disappearance of the previously mentioned resonance on the left side of the stop band, which indicates strongly reduced group delays. Further modeling suggests that an even larger side-lobe reduction can be achieved by using a slightly larger ridge height (e.g. 10 nm), though its impact on fabrication processes should be taken into account carefully.

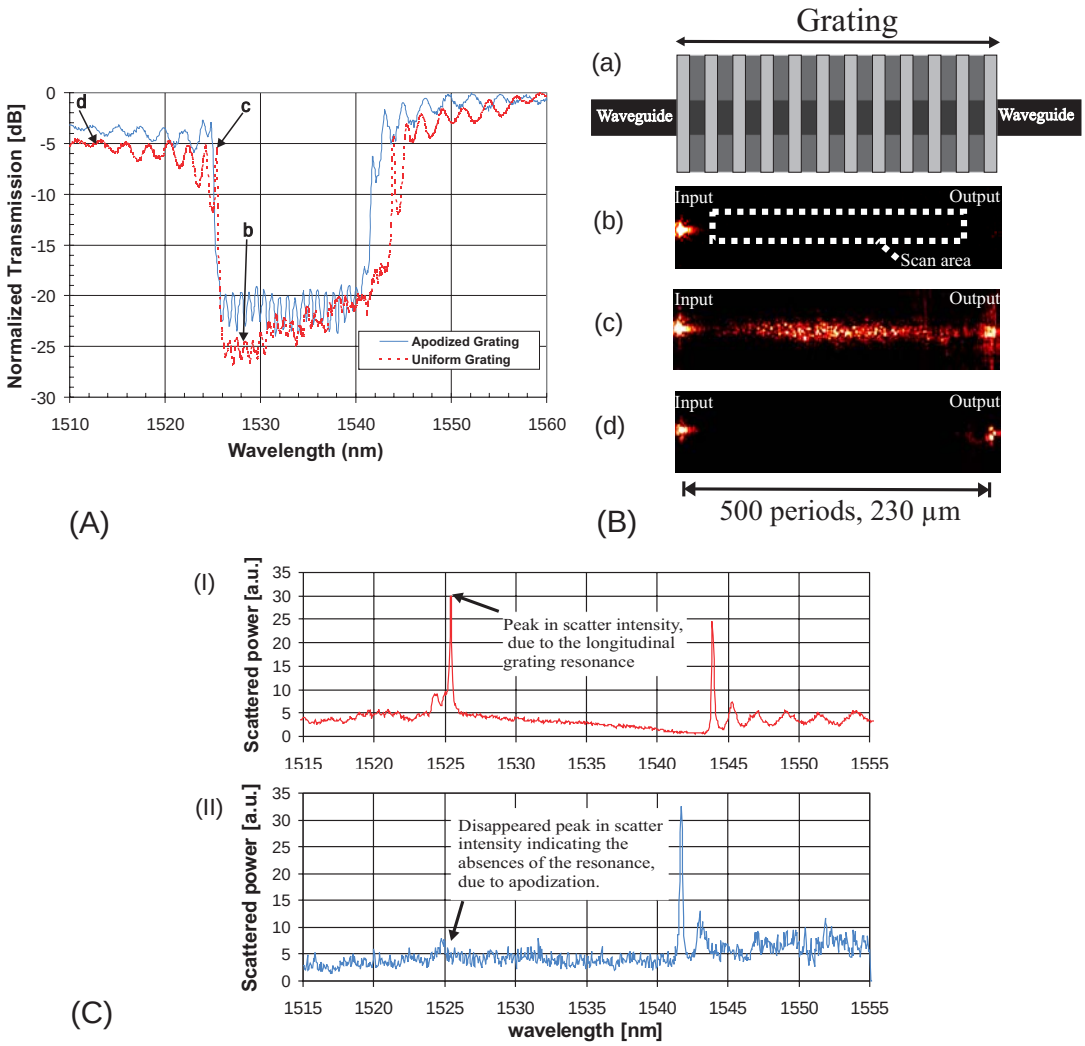

Figure 3.4-2: Optical characterization of the fabricated gratings. ***(A)*** *Measured transmission of the uniform (dashed) and apodized (solid) gratings, showing less pronounced fringes in the short-wavelength transmission band for the apodized case. The oscillations in the stopband at low transmitted power, are caused by a parasitic Fabry-Perot effect in the sample.* ***(B)*** *(uniform grating without cladding): (a) Schematic top view (grating period exaggerated); (b) no power transmission in the stop band. The dotted contour indicates the area from which scattered light was collected to produce the right-hand graphs (I) and (II); (c) full transmission at the first resonance mode (see label c in the left graph), exhibiting strongly enhanced scattering in the grated region; (d) full transmission outside the stop band, almost without increased scattering in the grating region.* ***(C)*** *Light scattered out of the grating region within the dotted contour in (b); (I) uniform grating showing two distinct peaks at the band edge positions; (II) apodized grating showing almost complete suppression of the short-wavelength peak.*

3.4.6 Conclusions

Waveguide gratings have successfully been realized in Si_3N_4 using a CMOS compatible technology by combining both conventional and laser interference lithography. A strongly increased amount of scattering was observed for a wavelength near the stop-band edge in the grating region using an IR-camera, indicating large a group delay. Quality factors of 8000 and 14000 were observed for resonances in uniform gratings with and without a polymer cladding, respectively. The reduction of some of the Fabry-Perot-like resonances outside the stopband of the grating, indicating a strong reduction of the group delay has been achieved by a width-tapering scheme, as observed from both the transmission and scatter measurement data. This demonstrates that in principle our method is suitable for implementing apodization functions.

3.4.7 References

[1] J. F. Lepage, R. Massudi, G. Anctil, S. Gilbert, M. Piche and N. McCarthy, "Apodizing holographic gratings for the modal control of semiconductor lasers", *Applied Optics*, vol. **36**, pp. 4993-4998, 1997.

[2] W. C. L. Hopman, P. Pottier, D. Yudistira, J. van Lith, P. V. Lambeck, R. M. De La Rue, A. Driessen, H. Hoekstra and R. M. de Ridder, "Quasi-one-dimensional photonic crystal as a compact building-block for refractometric optical sensors", *IEEE Journal Of Selected Topics In Quantum Electronics*, vol. **11**, pp. 11-16, 2005.

[3] P. Madasamy, G. N. Conti, P. Poyhonen, Y. Hu, M. M. Morrell, D. F. Geraghty, S. Honkanen and N. Peyghambarian, "Waveguide distributed Bragg reflector laser arrays in erbium doped glass made by dry Ag film ion exchange", *Optical Engineering*, vol. **41**, pp. 1084-1086, 2002.

[4] D. Faccio, F. Bragheri and M. Cherchi, "Optical Bloch-mode-induced quasi phase matching of quadratic interactions in one-dimensional photonic crystals", *Journal Of The Optical Society Of America B-Optical Physics*, vol. **21**, pp. 296-301, 2004.

[5] M. L. Povinelli, S. G. Johnson and J. D. Joannopoulos, "Slow-light, band-edge waveguides for tunable time delays", *Optics Express*, vol. **13**, pp. 7145-7159, 2005.

[6] J. E. Sipe, L. Poladian and C. M. de Sterke, "Propagation through non-uniform grating structures", *Journal of the Optical Society of America A (Optics and Image Science)*, vol. **11**, pp. 1307-1320, 1994.

[7] M. Matsuhara & K. O. Hill, "Optical-waveguide band-rejection filters: design", *Applied Optics*, vol. **13**, pp. 2886-2888, 1974.

[8] K. Ennser, N. Zervas and R. L. Laming, "Optimization of apodized linearly chirped fiber gratings for optical communications", *IEEE Journal of Quantum Electronics*, vol. **34**, pp. 770-778, 1998.

[9] D. Wiesmann, C. David, R. Germann, D. Emi and G. L. Bona, "Apodized surface-corrugated gratings with varying duty cycles", *IEEE Photonics Technology Letters*, vol. **12**, pp. 639-641, 2000.

[10] T. W. Mossberg, C. Greiner and D. Iazikov, "Interferometric amplitude apodization of integrated gratings", *Optics Express*, vol. **13**, pp. 2419-2426, 2005.

[11] H. Abe, S. G. Ayling, J. H. Marsh, R. M. De La Rue and J. S. Roberts, "Single-Mode Operation Of A Surface Grating Distributed-Feedback GaAs-AlGaAs Laser With Variable-Width Wave-Guide", *IEEE Photonics Technology Letters*, vol. **7**, pp. 452-454, 1995.

[12] J. T. Hastings, M. H. Lim, J. G. Goodberlet and H. I. Smith, "Optical waveguides with apodized sidewall gratings via spatial-phase-locked electron-beam lithography", *Journal of Vacuum Science & Technology B*, vol. **20**, pp. 2753-2757, 2002.

[13] C. T. Brooks, G. L. Vossler and K. A. Winick, "Integrated-optic dispersion compensator that uses chirped gratings", *Optics Letters*, vol. **20**, pp. 368-370, 1995.

[14] F. J. van Soest, H. van Wolferen, H. Hoekstra, R. M. de Ridder, K. Worhoff and P. V. Lambeck, "Laser interference lithography with highly accurate interferometric alignment", *Japanese Journal Of Applied Physics Part 1-Regular Papers Brief Communications & Review Papers*, vol. **44**, pp. 6568-6570, 2005.

[15] S. J. McNab, N. Moll and Y. A. Vlasov, "Ultra-low loss photonic integrated circuit with membrane-type photonic crystal waveguides", *Optics Express*, vol. **11**, pp. 2927-2939, 2003.

CHAPTER 4

4 CHARACTERIZATION & MODELING RESULTS

Abstract—This chapter gives first an overview of all optical characterization experiments and methods presented in this thesis. Then, a highly sensitive and compact cladding sensor is presented as a direct application of a one-dimensional photonic crystal. The next section describes far-field scattering microscopy, a novel method that can be used to map the performance of, for example, a slow-light based grating sensor. Another novel method, based on locally disturbing the optical field with a nanosized probe, e.g., an AFM tip, is presented next. It is most suitable for imaging a highly confined resonant mode in a two-dimensional photonic crystal micro-cavity, where disturbing the standing-wave pattern in the resonator strongly affects its power transmission. This nanomechano-optical effect can also be used to tune the resonance wavelength and quality factor of the microcavity, just by moving the AFM tip by a few tens of nanometers. Finally, a model is presented, describing the nanomechano-optical interaction in the case of the AFM tapping mode, which is much less likely to cause mechanical damage to both the specimen and the AFM tip.

4.1 Characterization methods and setups

Similar to the variety of fabrication methods used for realizing the devices presented in this thesis, a number of different setups have been deployed for characterizing them. Here we relate the experiments presented in this thesis to the used setups, and provide the references in which detailed descriptions of the setups can be found.

4.1.1 Summary

- End-fire: Practically all devices were characterized for their transmission using an end-fire like setup. The setup consists of the following main components: tunable laser, polarization controller, objective lenses, micrometer stages, photodiode, a computer and Labview software for automation of the wavelength scans. The objectives can easily be replaced by fibers to form a butt-end coupling setup. More detailed information can be found in [1-3].
- White light setup: A photonic-crystal-fiber-based white-light source can be interchanged with the tunable laser used in the end-fire setup. In combination with a spectrometer, this enables the measurement of transmission spectra over a wide spectral range [4]. The spectrometer can also be controlled by Labview software [5]. The white-light setup was convenient for characterizing the stopbands of the photonic crystals.
- Fluidic setup: This is a relatively rarely used setup. It has been used for the sensor measurements presented in section 4.2. The main principle of the setup is also described in that section. Further details can be found in [6].
- Phase-shift method using an Agilent 5230A network analyzer for delay measurements: In section 4.3, group delay measurements on gratings are presented. This type of measurement is useful for characterizing, for example, slow-light for time delay applications. The setup is briefly explained in section 4.3. A further description of the setup can be found in [7-9].
- IR-camera setup: When working with infrared light with wavelengths beyond 1100 nm, a sensitive IR camera (from Sensors Unlimited Inc.) is most convenient. It can help to rapidly couple light into, for example, silicon (which doesn't guide red light) and it can be used to locate the devices on a chip by illumination with an incandescent lamp. In section 4.3, another application is discussed; it can be used to map the intensity of Rayleigh scattering in a device. Besides the details mentioned in section 3.4 and section 4.3, other descriptions of the setup can be found in [1,2]. The camera images have been analyzed using Labview software [10].
- AFM setup: A scanning tip atomic force microscope was temporarily combined with the end-fire setup [11]. A description can be found in section 4.5 and 4.6. Details about the scanning tip AFM can be found in [12].

4.1.2 References

[1] C. G. Bostan, PhD thesis, "Design and fabrication of quasi-2D photonic crystal components based on silicon-on-insulator technology", ISBN: 90-365-2155-6, University of Twente, Enschede, 2005.

[2] R. Dekker, PhD thesis, "All-optical processes in integrated optical devices using materials with large third-order nonlinearities and gain", ISBN-13: 978-90-9021436-8, University of Twente, Enschede, 2006.

[3] W. C. L. Hopman, MSc thesis, "The Visible challenge of 1-D Photonic Crystals", University of Twente, Enschede, 2002.

[4] Fianium, "Optical Supercontinuum Systems: SC-450-2," http://www.fianium.com.

[5] *MeSla+*, version **3.0**, by W. C. L. Hopman, "\\udsel02\GroupLow\IOMS\Software IOMS".

[6] J. van Lith, PhD thesis, "Novel integrated optical sensing platforms for chemical and immuno-sensing", ISBN: 90-365-2117-3, Enschede, 2005.

[7] D. H. Geuzebroek, PhD thesis, "Flexible optical network components based on densely integrated microring resonators", ISBN: 90-365-2258-7, University of Twente, Enschede, 2005.

[8] C. G. H. Roeloffzen, PhD thesis, "Passband flattened binary-tree structured add-drop multiplexers using SiON waveguide technology", ISBN: 90-365-1803-2, Enschede, 2002.

[9] L. Zhuang, C. G. H. Roeloffzen, R. G. Heideman, A. Borreman, A. Meijerink and W. van Etten, "Ring resonator-based single-chip 1x8 optical beam forming network in LPCVD waveguide technology", Proc. Annual symposium of the IEEE LEOS Benelux Chapter (Eindhoven), pp. 45-48 (2006).

[10] *EliXeR*, version **5.0**, by W. C. L. Hopman, "\\udsel02\GroupLow\IOMS\Software IOMS".

[11] W. C. L. Hopman, K. O. Van Der Werf, A. J. F. Hollink, W. Bogaerts, V. Subramaniam and R. M. De Ridder, "Nano-mechanical tuning and imaging of a photonic crystal micro-cavity resonance", *Optics Express*, vol. **14**, pp. 8745-8752, 2006.

[12] K. O. van der Werf, C. A. J. Putman, B. G. De Grooth, F. B. Segerink, E. H. Schipper, N. F. van Hulst and J. Greve, "Compact stand-alone atomic-force microscope", *Review of Scientific Instruments*, vol. **64**, pp. 2892-2897, 1993.

4.2 Strong waveguide gratings as compact refractometric optical sensors

Abstract— We report the fabrication and the characterization of the refractometric and thermo-optical properties of a quasi-one-dimensional waveguide photonic crystal - a strong, 76-micrometer-long Bragg grating. The transmission spectra (around 660 nm) of the structure have been measured as a function of both the cladding refractive index and the temperature. The transmission stopband was found to shift by 0.8 nm wavelength for either a cladding refractive index change of 0.05 or a temperature change of 120 K. The steep stopband edges provide a sensitive detection method for this band shift, by monitoring the transmitted output power.

This section has been published:
Hopman W. C. L., Pottier P., Yudistira D., van Lith J., Lambeck P. V., De La Rue R. M., Driessen A., Hoekstra H. J. W. M. and de Ridder R. M., "Quasi-one-dimensional photonic crystal as a compact building-block for refractometric optical sensors" IEEE Journal Of Selected Topics In Quantum Electronics 11, 11-16, 2005.

4.2.1 Introduction

A structure having a periodic index modulation in one dimension is known as a one-dimensional photonic crystal. If the structure has nonperiodic features in the other two dimensions, it is denoted as a quasi-one-dimensional photonic crystal. We consider a wide ridge-type channel waveguide of silicon nitride with a grating etched into the core layer.

Besides their use in theoretical studies for computationally efficient modeling of selected properties of quasi-two-dimensional photonic crystals (also known as photonic crystal slabs), e.g., [1,2], such grating structures have found direct application as distributed Bragg reflectors and the like in semiconductor lasers, and fiber Bragg gratings, especially for optical wavelength filtering and dispersion compensation in optical communication networks [3,4]. They have also been used as sensing structures, both in fiber devices [5] and in planar integrated optics [6]. In many of these Bragg grating applications, one is interested in obtaining a narrow reflection peak and low transmission losses outside the peak in order to obtain a selective and efficient optical wavelength filter. Such characteristics require a relatively long grating with a weak index modulation.

A Bragg grating with a strong index modulation shows a typical property of photonic crystals: an extended transmission stopband. Although such a structure does not possess a full photonic bandgap (i.e., overlapping stopbands for all propagation directions and polarizations), it can still have a useful transmission stopband, since the channel waveguide strongly limits the angular spectrum of incident waves. The width of this stopband and the steepness of its edges increase with the strength of the refractive index modulation.

For optical sensing purposes, we propose to exploit the steep edges of the stopband of a strong grating. The central wavelength and the edges of the stopband shift towards longer wavelengths with increasing average index of the structure. A small wavelength shift of such an edge can cause a large change in the transmitted power from a source having an appropriate wavelength. The Bloch modes of a strong grating can have a large overlap with the cladding material, providing an efficient mechanism for detecting index changes of, e.g., a fluid cladding. Although the losses at the long wavelength stopband edge can reach low levels [1], strong gratings are often considered less suitable for practical applications due to out-of-plane diffraction loss. In fact this may be of key importance considering telecom devices, contrary to most sensor applications, where this property can well be the measuring principle [7]. For example, it is sometimes immaterial whether a transmission minimum is caused by back reflection or out-of-plane scattering.

A key advantage of the proposed device is that the sensing elements can be very compact (in this work 76 μm long, compared to typically 4 cm for a Mach-Zehnder interferometer, as in [8], or a few mm for surface plasmon resonance sensors, e.g., [9]), opening the possibility of integrating an array of sensors, each for detecting a different measurand or covering a different range (e.g., of concentrations). The small measurand volume needed and the resolution obtained are similar to those of a recently demonstrated microring resonator based sensor [10].

It has been demonstrated that the bandgap of a photonic crystal that is infiltrated with a liquid crystal can be widely tuned due to the thermally induced refractive index change of the liquid crystal [11]. Also, thermal tuning of resonance frequencies of cavities in semiconductor photonic crystals has been shown [12]. We show that the much smaller thermo-optic effect of Si_3N_4 and SiO_2 can be used for tuning the stopband over a small range, which is, however, easily detectable by observing the optical transmission near a band edge. This effect may be used for tuning the structure into its optimum operating point (with respect to the source wavelength) or for optical switching. Although we used bulk heating of the entire structure for measuring the thermo-optic actuation, like [12], it has recently been demonstrated that in spite of their strongly nonplanar surface, photonic crystal structures can be thermally tuned using small local heaters [13,14].

4.2.2 Experimental

4.2.2.1 Device fabrication

A schematic cross-section of the investigated device, which is based on the structure that was modeled in [1], is shown in Figure 4.2-1. The optical part of the structure is a three-layer waveguiding-system with a 212-nm-thick Si_3N_4 guiding layer (n_g = 2.01), grown on top of a 9-μm-thick SiO_2 buffer layer (n_s = 1.46) on silicon. The top cladding (refractive index $n_{cladding}$) is either air, or a fluid of which the index could be varied. A shallow, 2-μm-wide ridge with a 2-nm step height, forming a single-mode waveguide at $\lambda > 450$ nm, was etched into the Si_3N_4 layer using conventional photolithography and wet chemical etching. The grating period was chosen to be Λ = 190 nm, leading to a stopband located in the red visible spectrum. It has 401 periods, resulting in an overall length of 76.19 μm. The width of the grating is 80 μm to ensure full overlap with the evanescent field tails in the slab region next to the ridge. The grating was defined with its grooves perpendicular to the axis of the ridge waveguide using direct e-beam writing, and etched into the Si_3N_4 guiding layer using an intermediate titanium mask and reactive ion etching. After etching, an atomic force microscope (AFM) was used for measuring the filling factor (groove width 60 % of Λ) and the etch depth (22 nm, i.e., approximately 10 % of the guiding layer thickness). A small cuvette was placed over the photonic crystal area, and sealed with silicone paste, so that the top cladding of the structure could be replaced by a fluid.

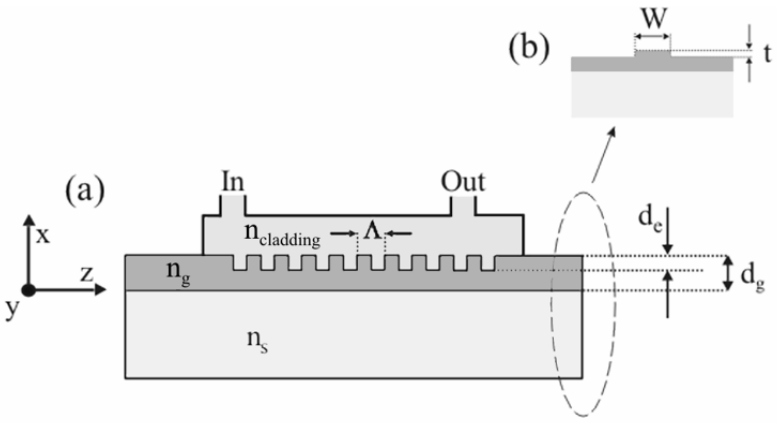

Figure 4.2-1: (a) Cross-section of the refractive-index sensor. The sensing element is a quasi-one-dimensional photonic crystal, a strong grating in a Si_3N_4 shallow ridge-type waveguide. The top cladding over the grating is formed by a fluid (the measurand) contained in a cuvette that is sealed to the sensor chip. d_e = 22 nm, d_g = 212 nm, n_g = 2.01, n_s = 1.46, the value of $n_{cladding}$ is varied, Λ = 190nm. (b) A schematic side view of the ridge waveguide, t = 2 nm, W = 2 μm.

4.2.2.2.A. Refractive index measurements

The sensitivity of the sensor for changes in the cladding index could be measured by feeding different fluids with known refractive indices through the cuvette, using the setup shown schematically in Figure 4.2-2. A continuous change in refractive index could be realized by slowly mixing together two fluids of different refractive indices. At the start of the measurement, the closed vessel N2 contained pure ethanol (refractive index n = 1.36). Vessel N1 contained a benzyl-alcohol with a refractive index of 1.54, which is 13 % higher than that of ethanol. Pump 1 slowly added benzyl alcohol to the fluid in vessel N2 which was stirred; both fluids are well mixable. After feeding the mixture through a relatively small volume cuvette the fluid was collected in a third vessel. During the measurements, calibration data were collected by monitoring the refractive index in vessel N2 using an Abbe refractometer at a wavelength of 632.8 nm. The flow system illustrated in Figure 4.2-2 is characterized by a set of simple differential equations. Using the calibration data, the parameters that were originally known with insufficient accuracy, could be

determined using a fitting procedure. After calibration, the index at each moment in time was known with an accuracy of approximately 5×10^{-4}.

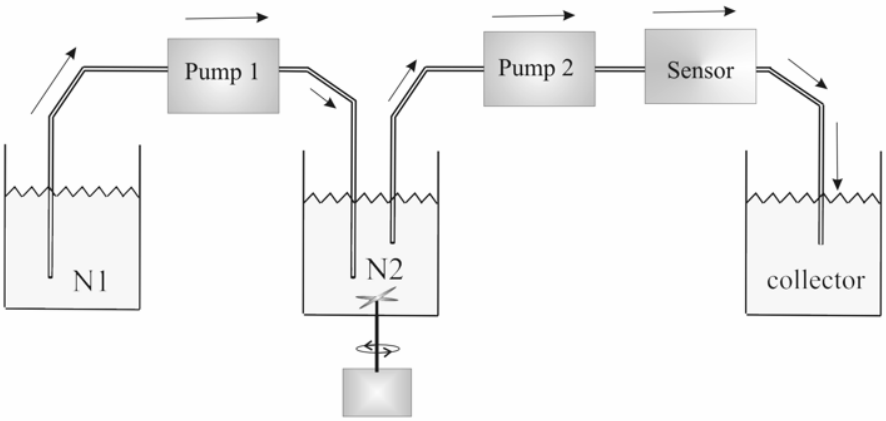

Figure 4.2-2: Setup for characterizing the refractometer. At the start of a measurement, vessels N1 and N2 contain different, mixable fluids. Pump 1 slowly adds fluid from vessel N1 to the stirred vessel N2, producing a mixture of which the change of refractive index with time can be calibrated. Pump 2, having the same flow rate as pump 1, feeds the mixture through the cuvette, so that the refractive-index sensitivity of the sensor can be determined by measuring the light transmission versus time.

4.2.2.2 Measurement setup

The sensor is characterized by measuring transmission spectra as a function of a measurand. This is carried out by using a tunable dye laser (620-700 nm) and a simple photodetector. In all cases, TE-polarized light was used, which was coupled into the structure using the commonly used end-fire setup, consisting of a half-wave plate, polarizer, and two × 40 microscope objectives for input and output coupling.

4.2.2.2.B. Temperature measurements

The temperature of the sensor was adjusted by heating the entire chip. The temperature was measured using a thermocouple. Due to the bulk heating procedure, the optical alignment of the setup tended to drift after adjusting the temperature. A period of approximately 30 minutes after an adjustment had been made, was needed for stabilization.

4.2.3 Measurement results

The transmission spectra that were measured at the start and at the end of a refractive index scan using the setup of Figure 4.2-2 are presented in Figure 4.2-3. The first spectrum was measured with pure ethanol (n = 1.36), the second one with a mixture (n = 1.528) of ethanol and benzyl-alcohol. A wavelength shift (shift of edge *B*) of about 4 nm was found for a cladding index change of 0.168.

The following variation of the measurement method exploits the steep edges of the transmission stopband. By choosing a measurement wavelength to be approximately halfway the slope of the band edge (the wavelengths λ_1 and λ_2 are chosen outside the slope region so that the edges A and B respectively could be characterized completely, see Figure 4.2-3), a change in the cladding index can be very accurately determined by monitoring the transmitted power. A small change in cladding index will shift the stopband to higher or lower wavelength, depending on the sign of the index change. This shift causes a corresponding large change in output power due to the steep slope of the band edge. Setting λ_1 = 660.5 nm and λ_2 = 662.5 nm, the results shown in Figure 4.2-4

were obtained. The figure shows that the maximum sensitivity is found at an index change of 0.024 for curve 2. In order to arrive at a numerical value for obtained sensitivity, we use, however, a conservative estimate based on the more gradual slope of curve 1.

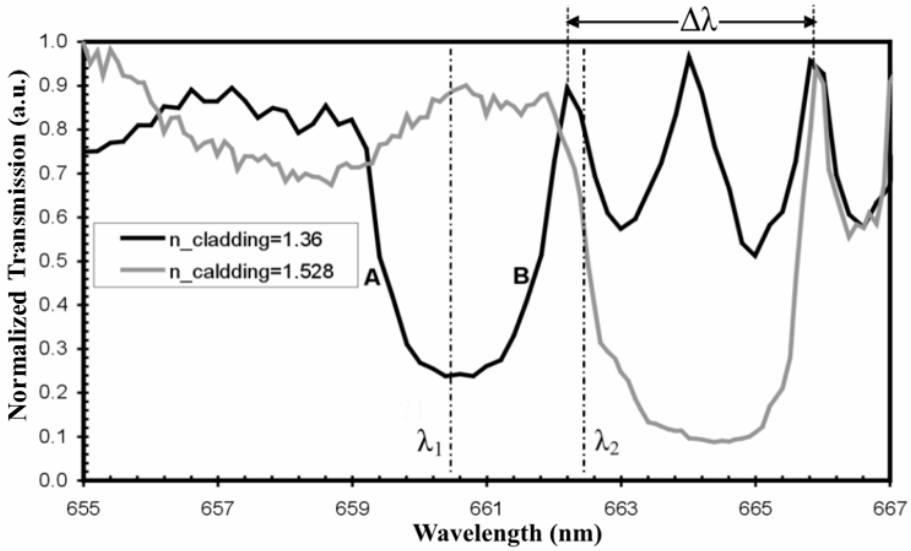

Figure 4.2-3: The normalized transmission spectra for two different cladding indices ($n_{\_cladding}$). The air band edge and the dielectric band edge are labeled with the letters A and B, respectively. Wavelengths λ_1 and λ_2 are fixed for probing edges A and B, respectively, leading to the characteristics shown in Figure 4.2-4.

It is clear that both band edges show a marked output power change with a change of cladding index. We define the sensitivity *S* of the sensor as:

$$S = \frac{1}{P}\frac{\partial P}{\partial n}. \tag{1}$$

The values of the transmitted power *P* and its derivative with respect to the cladding refractive index $\partial P/\partial n$ can be determined from Figure 4.2-4, leading to a conservative estimate of $S \cong 24$ (based on the average slope of curve 1).

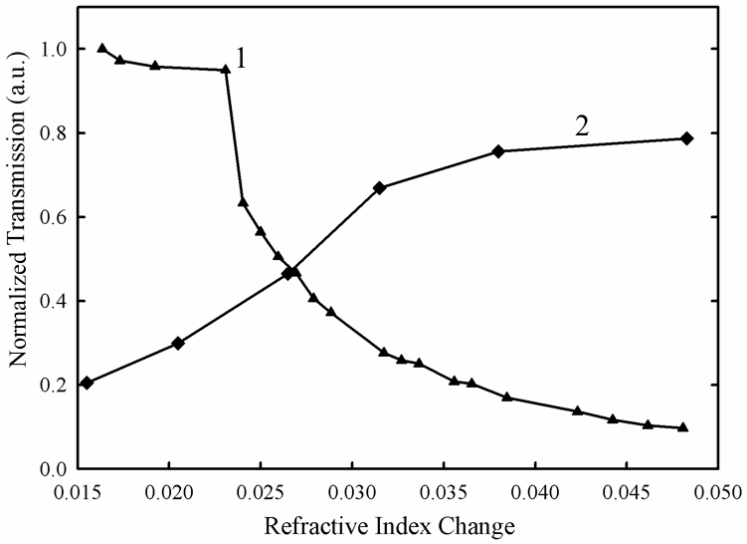

Figure 4.2-4: The normalized transmission versus the change in cladding index. Curve 1 (scanning edge A) is measured at λ_1 and curve 2 (edge B) is measured at λ_2 (c.f. Figure 4.2-3). Both curves are normalized to the maximum transmitted power, for curve 1 and 2 respectively 360 nW and 635 nW.

With the simple photodetector setup we used, a resolution η of 1 % of the maximum transmitted power could be obtained. The minimum detectable cladding index change Δn is:

$$\Delta n = \frac{\eta}{S}, \tag{2}$$

for this sensor evaluating to a value $\Delta n \cong 4\times10^{-4}$. Approximately the same value can be found directly from Figure 4.2-3 by estimating S from the spectral shift of the stopband for the given index change, and the slope of the band edge.

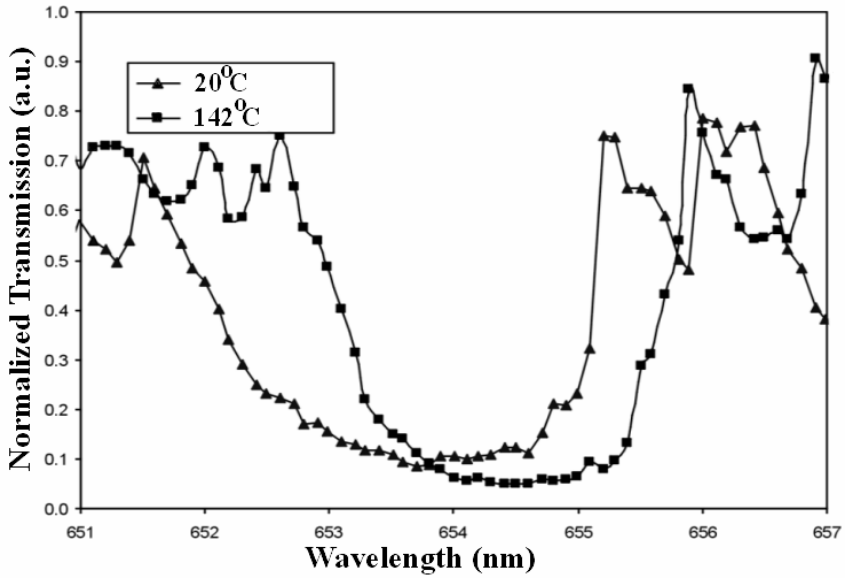

Figure 4.2-5: The normalized transmission spectra for two different temperatures

The thermal tunability of the photonic crystal is demonstrated by the normalized transmission spectra for two different temperatures shown in Figure 4.2-5. A 0.8 nm shift of the center stopband wavelength is observed for a 122 K temperature change, corresponding to a thermal tuning coefficient $\partial\lambda/\partial T \cong 7 \pm 1$ pm/K. As mentioned in section 4.2.2.2.B, the measurement setup suffered from drift of the in-coupling conditions. Since the measurement of a single spectrum took several minutes, the distortion of the transmission spectrum may be partly attributed to this effect.

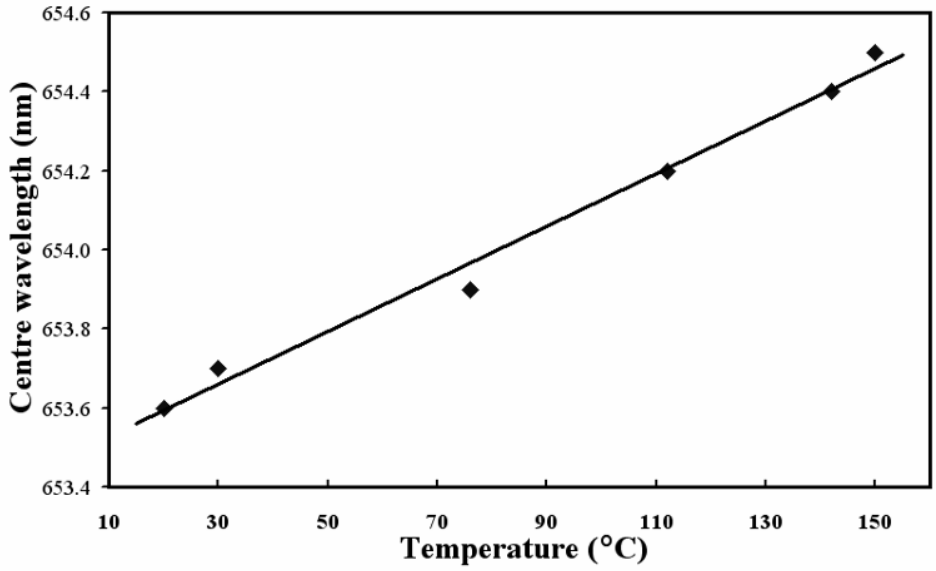

Figure 4.2-6: The center wavelength (i.e., the wavelength exactly in the middle of the stopband defined by the -3dB point of the stopband edges) versus temperature.

Figure 4.2-6 shows the center wavelength versus temperature. Between measurement points, we allowed the setup to stabilize for at least 30 minutes. As should be expected, a linear relation was found. The average thermal tuning coefficient found from this more accurate measurement was $\partial\lambda/\partial T \cong 6.7$ pm/K.

A calculation with a 2-dimensional bidirectional eigenmode propagation method using the known thermo-optic coefficients of Si_3N_4 and SiO_2 (both approximately 1×10^{-5}), and the geometric parameters of the structure, results in a value of $\partial\lambda/\partial T = 4$ pm/K. The discrepancy may be attributed to the effect of thermal expansion of the bulk silicon substrate and the elasto-optic effect, which the model did not account for.

4.2.4 Discussion

The photonic crystal structure used in the measurements was not optimized for sensing purposes, therefore a further detailed investigation is needed to determine the maximum achievable improvement of the sensitivity. As expected, a wavelength shift of the photonic band edges was observed on changing the cladding index. The results prove that this photonic crystal device can be used as a sensitive integrated device for determining the cladding index. Expanding (1), we obtain

$$S = \frac{1}{P}\frac{\partial P}{\partial n} = \frac{1}{P}\frac{\partial P}{\partial \lambda}\frac{\partial \lambda}{\partial n}, \tag{3}$$

clearly showing that the sensitivity can be enhanced by increasing the slope of the band edge, $\partial P/\partial\lambda$. One way to do this is by increasing the number of periods of the grating. Figure 4.2-7 shows the results from a 1-D photonic crystal model for the maximum slope (at the band edge) versus the number of periods (length of the grating). The model is based on an effective index approximation and a plane wave expansion. This figure indicates that the sensitivity of this device is increasing stronger than linear with the number of periods in the computed range. Since, in the actual 3-dimensional device, loss increases with increasing number of periods, an optimum number of periods may exist. Further study and more computational resources are needed to validate this behavior outside the computed region. From Figure 4.2-7 we can conclude that increasing the etch depth and thus increasing the contrast will also strongly enhance the slope $\partial P/\partial\lambda$.

The optical insertion loss of the device can be significantly reduced by using an optimized fiber-chip coupling (e.g., [8]). Clever signal processing, e.g., by simultaneously using both band edges in a push-pull way (requiring two light sources at different wavelengths) will increase the sensitivity. The resolution η can be increased by a factor of 10, from 1 % to 0.1 %, by using a more sophisticated photo-detection setup.

The resulting increase in sensitivity of at least two orders of magnitude will make this photonic crystal sensor an interesting building-block for densely integrated optic sensor arrays. The stability problems and slow response time observed with bulk thermal actuation can both be considerably reduced by using a local heater as in [13,14]. Using an integrated fiber-chip coupling will also be very beneficial for increasing stability.

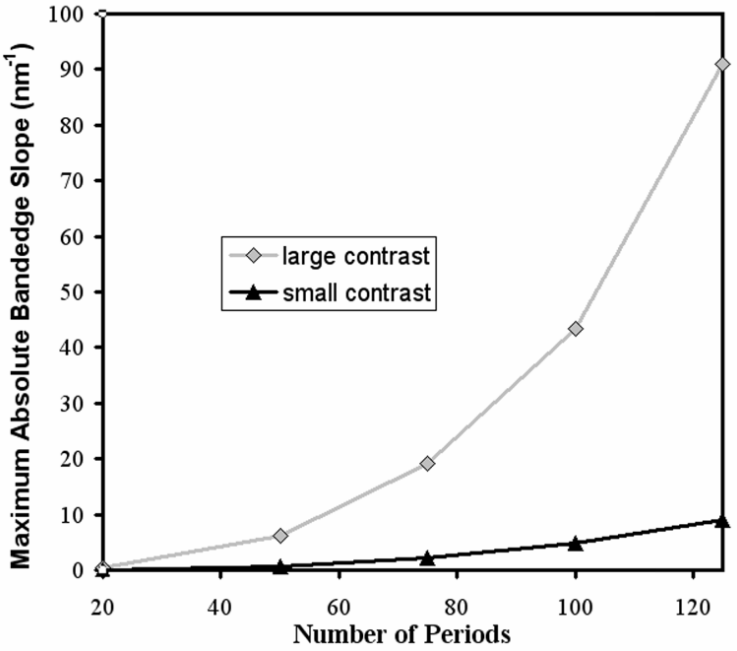

Figure 4.2-7: The maximum slope of the band edge, $\partial P/\partial\lambda$, versus the number of grating periods. Increasing the contrast in this 1-D model corresponds to increasing the etching depth of the grating. The "small contrast" approximately represents the fabricated structure; a contrast of 0.2. An refractive index contrast of 0.8 was taken for the "large contrast".

4.2.5 Summary

We have demonstrated a very compact refractometer sensor based on a short deeply etched grating. An increase of the cladding refractive index causes a shift of the transmission spectrum of the grating towards longer wavelengths of approximately 23 nm per unit index change. The steep slopes of the photonic band edges (in our case especially, the dielectric band edge at the long-wavelength side of the gap) can be used for increasing the sensitivity of the device. With a simple photodetector, a variation of 4×10^{-4} in the cladding index could be detected. A thermally induced spectral shift of approximately 7 pm/K was observed.

Besides an improvement of resolution by two orders of magnitude by changing the detection equipment alone, we believe that also the optical design of devices based on this sensing principle can be further optimized. Although Mach-Zehnder interferometers will probably remain the devices of choice if the ultimate in sensitivity is to be attained, the deep grating device presented in this paper may offer a good compromise between size and sensitivity that is required for the present and future large scale integrated sensor arrays.

4.2.6 Acknowledgments

We would like to thank Edwin Klein for fruitful discussions and for help with the temperature characterization.

4.2.7 References

[1] W. Bogaerts, P. Bienstman, D. Taillaert, R. Baets and D. De Zutter, "Out-of-plane scattering in 1-D photonic crystal slabs", *Optical and Quantum Electronics*, vol. **34**, pp. 195-203, 2002.

[2] J. Ctyroky, S. Helfert, R. Pregla, P. Bienstman, R. Baets, R. De Ridder, R. Stoffer, G. Klaasse, J. Petracek, P. Lalanne, J. P. Hugonin and R. M. De La Rue, "Bragg waveguide grating as a 1D photonic band gap structure: COST 268 modelling task", *Optical and Quantum Electronics*, vol. **34**, pp. 455-470, 2002.

[3] D. Gauden, E. Goyat, A. Mugnier, P. Lesueur, P. Yvernault and D. Pureur, "A tunable four-channel fiber Bragg grating dispersion compensator", *IEEE Photonics Technology Letters*, vol. **15**, pp. 1387-1388, 2003.

[4] L. G. Sheu, K. P. Chuang and Y. Lai, "Fiber Bragg grating dispersion compensator by single-period overlap-step-scan exposure", *IEEE Photonics Technology Letters*, vol. **15**, pp. 939-941, 2003.

[5] W. Jin, Y. Zhou, P. K. C. Chan and H. G. Xu, "Fibre-optic grating sensor for the study of flow-induced vibrations", *Sensors and Actuators A*, vol. **79**, pp. 36-45, 2000.

[6] G. J. Veldhuis, J. H. Berends, R. G. Heideman and P. V. Lambeck, "Integrated optical Bragg-reflector used as a chemo-optical sensor", *Pure and applied optics*, vol. **7**, pp. L23-L26, 1998.

[7] J. van Lith, P. V. Lambeck, H. J. W. M. Hoekstra and R. G. Heideman, "The segmented waveguide sensor: principle and experiments", European Conference on Integrated Optics Proc. **11**, 277-280 (2003).

[8] P. V. Lambeck, "Remote opto-chemical sensing with extreme sensitivity: Design, fabrication and performance of a pigtailed integrated optical phase-modulated Mach-Zehnder interferometer system", *Sensors and Actuators, B: Chemical*, vol. **61**, pp. 100-127, 1999.

[9] A. K. Sheridan, R. D. Harris, P. N. Bartlett and J. S. Wilkinson, "Phase interrogation of an integrated optical SPR sensor", *Sensors and Actuators, B: Chemical*, vol. **97**, pp. 114-121, 2004.

[10] E. Krioukov, D. J. W. Klunder, A. Driessen, J. Greve and C. Otto, "Sensor based on an integrated optical microcavity", *Optics Letters*, vol. **27**, pp. 512-514, 2002.

[11] S. W. Leonard, J. P. Mondia, H. M. van Driel, O. Toader, S. John, K. Busch, A. Birner, U. Gosele and V. Lehmann, "Tunable two-dimensional photonic crystals using liquid-crystal infiltration", *Physical Review B*, vol. **61**, pp. R2389-R2392, 2000.

[12] B. Wild, R. Ferrini, R. Houdre, M. Mulot, S. Anand and C. J. M. Smith, "Temperature tuning of the optical properties of planar photonic crystal microcavities", *Applied Physics Letters*, vol. **84**, pp. 846-848, 2004.

[13] E. A. Camargo, H. M. H. Chong and R. M. De La Rue, "2D Photonic crystal thermo-optic switch based on AlGaAs/GaAs epitaxial structure", *Optics Express*, vol. **12**, pp. 588-592, 2004.

[14] H. M. H. Chong & R. M. De La Rue, "Tuning of photonic crystal waveguide microcavity by thermooptic effect", *IEEE Photonics Technology Letters*, vol. **16**, pp. 1528-1530, 2004.

4.3 Far-field scattering microscopy and grating resonances

Abstract— A novel method is presented for determining the group index, intensity enhancement and delay times for waveguide gratings, based on (Rayleigh) scattering observations. This far-field scattering microscopy (FScM) method is compared with the phase shift method and a method that uses the transmission spectrum to quantify the slow wave properties. We find a minimum group velocity of 0.04c and a maximum intensity enhancement of ~14.5 for a 1000-period grating and a maximum group delay of ~80 ps for a 2000-period grating. Furthermore, we show that the FScM method can be used for both displaying the intensity distribution of the Bloch resonances and for investigating out-of-plane losses. Finally, an application is discussed for the slow-wave grating as index sensor able to detect a minimum cladding index change of 10^{-8}, assuming a transmission detection limit of 10^{-4}.

This section has been published:
W. C. L. Hopman, H. J. W. M. Hoekstra, R. Dekker, L. Zhuang and R. M. de Ridder, "Far-field scattering microscopy applied to analysis of slow light, power enhancement, and delay times in uniform Bragg waveguide gratings", Optics Express, vol. 15, pp. 1851-1870, 2007.

4.3.1 Introduction

Bragg waveguide gratings can be used in many integrated optical architectures to achieve a broad range of functionalities. For many years, they have, for example, shown their value in filters and mirrors [1], sensors [2], lasers [3], pulse compression [4], second harmonic generation [5,6] and many more applications and theoretical studies. A waveguide grating (WGG) can be formed by periodic variation of the dielectric constant along the propagation direction. A straightforward method to achieve this modulation is by etching slits into a waveguide. The waveguide is needed for vertical and lateral confinement. WGGs having a strong modulation in dielectric constant, are often referred to as one-dimensional (1-D) photonic crystals [7].

The 1-D periodicity induces a gap in guided modes, the so-called photonic stopband. The corresponding dispersion curves of such a system reveal a slowdown of the group velocity near the band edges of the "semi-infinite" photonic crystal (PhC) [8]. In principle, the theory shows that the group velocity approaches to zero at the band edges. This phenomenon is referred to as slow light in this paper; however, the phase velocity still is in the order of the speed of light in vacuum, *c*. A slow lightwave has a longer interaction time with the material it is traveling through. This effect can be exploited, for example, for sensors [2], nonlinear optical devices [9] and enhanced effective gain or low-threshold lasing [10]. However, a slow wave, or in the extreme a standing wave, can occur only over a very limited frequency range [11] which makes it unsuitable for high bandwidth-demanding telecom applications.

In finite periodic structures, the limited length causes characteristic fringes in the transmission and reflection spectra of WGGs, occurring near the band edge [12,13] due to Fabry-Perot resonances of the grating Bloch modes [6]. The Fabry-Perot effect and the slow-wave effect are inseparable in such structures [12]. A maximum in the density of modes is found at the first resonant fringe [14] and not at the corresponding stopband-edge positions of the equivalent infinite structure. The reflected power of Fabry-Perot-like resonators is generally minimum at the resonance wavelength [7]. However, a fabricated structure may show increased loss at the resonance wavelength(s) because of out-of-plane scattering (OPS) and linear absorption, which are proportional to the field intensity. The scattering is caused by nonuniformities of the material and surface roughness due to etching processes.

Several measurement and analyzing methods have been proposed and applied for determining the group velocity or the group delay of a slow lightwave in micrometer-sized devices. Examples are photon scanning tunneling microscopy (PSTM) [15], time of flight measurement [16-19], integrated Mach-Zehnder interferometers (MZI) [20], and spectral analysis of Fabry-Perot-like transmission phenomena [21,22]. The major disadvantage of the present methods is that they are complex and time-consuming (time of flight and PSTM) or may demand special extra design complexity, as, for example, in the MZI-type measurements. The analysis of the Fabry-Perot-like transmission phenomena is based on fitting calculated fringe locations (based on the Fabry-Perot free spectral range formula) to the measured spectrum, to obtain the group velocity as a fitting parameter. The approach uses a linear approximation of the dispersion, which results in the substitution of the phase index by the group index. This, however, affects the accuracy, because near the stopband edge the dispersion curve shows a strong curvature [12], resulting in a strong change in effective and group index near the stopband edge as we will show experimentally.

In this paper we introduce an alternative method –the far-field scattering (FScM) method– for estimating the power enhancement factor within the resonator, the group delay, and the resulting group index. The major advantage of our method, compared to the previously mentioned ones, is that analyzing the scattering intensity by infrared camera is an easy and straightforward technique for determining the group velocity at different wavelengths. We will demonstrate the quality of this method, by comparing its results to reference delay measurements using an interferometric setup, and by rigorous modeling. The only requirement for the method to work is that the device should show detectable randomly distributed scattering, which usually is not a problem.

We will first briefly present the design and fabrication of the characterized structures; a more detailed description of the fabrication method can be found elsewhere [13]. The scattering measurement setup is discussed in detail in section 4.3.3. A brief description of the setup used for reference delay measurements will also be given. In section 4.3.4 we present both the theory and simulations describing the resonance properties of the WGGs, and the experimental results obtained from the fabricated structures. In subsection 4.3.4.1 we will derive a relation for the group delay using the quality factor Q and also using the far-field scattering microscopy method. The modeling of the WGGs is presented in subsection 4.3.4.2 for verification of experimental results presented in subsection 4.3.4.3. In this subsection we will present our main experimental results, demonstrating Q factors up to 10^5, and showing how the "scatter-intensity" approach can be applied to slow-wave structures for estimating the corresponding group velocity. The results are verified with those obtained using the well-known RF phase shift method [17,23-25]. In section 4.3.5 we will demonstrate how our method can be used to determine and study the OPS loss [26,27]. In section 4.3.6 we discuss the application of slow light in WGGs for refractometric sensors, and the maximum sensitivity that can be achieved with such devices (10^{-8}). Finally we will present the main conclusions of this research in section 4.3.7.

4.3.2 Design and fabrication

A schematic 3-D drawing of the WGG design is shown in Figure 4.3-1a, a SEM photo zoomed in on the grating, is shown in Figure 4.3-1b. The WGG was fabricated using a three-step etching process performed on a Si_3N_4 guiding layer with refractive index n = 1.981 and initial thickness d_g= 275 nm, which was LPCVD-deposited on top of a 9-micrometer-thick SiO_2 (n = 1.445) buffer layer.

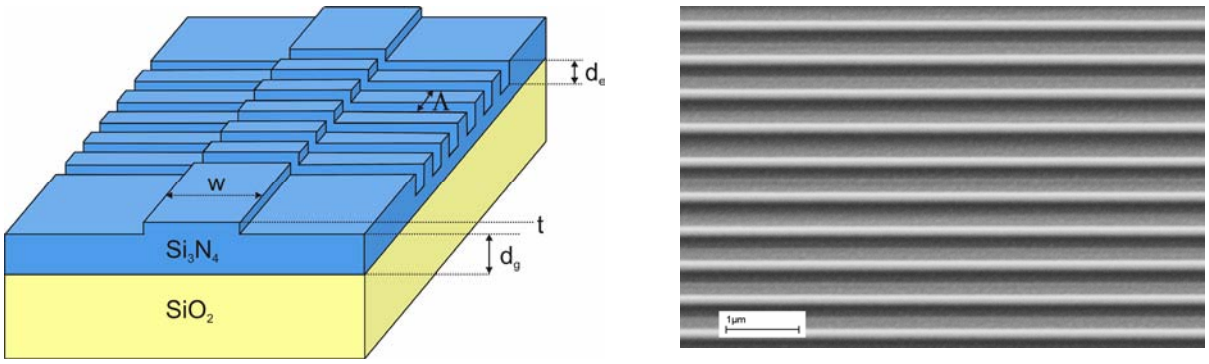

(a) (b)

Figure 4.3-1: (a) Schematic 3-D drawing of the WGG. (b) Top view SEM image of a zoomed in view of the 500-Period WGG, the small ridge of only 5 nm is not observed in the image.

A small ridge-step t = 5 nm was chosen for lateral confinement. The advantage of the resulting small lateral effective index contrast is that a 2-D model provides sufficient accuracy for designing the grating and simulating its optical properties [7]. Because of this contrast, a relatively large width w = 7 μm could be chosen for the ridge waveguide to be still single moded. In order to have a stopband in the 1.5-μm-wavelength region, we chose the period of the WGGs to be Λ = 0.47 μm. The gratings were defined using laser interference lithography. After reactive ion etching of the grating mask the etch depth was estimated to be d_e = 50 nm (i.e., ~19 % of the core-thickness), using both profilometry and fitting of the measurement data using a mode expansion technique in 2-D. The gratings were characterized with both an air cladding (n = 1) and a polymer cladding ($n \cong$ 1.5) on top. In this paper we consider three different lengths of the WGGs, determined by the number of periods: 500, 1000 and 2000 periods. Further details of the fabrication process of similar WGGs can be found in [13].

4.3.3 Measurement setup

The WGGs were characterized using an end-fire setup, suitable for simultaneously obtaining the transmission spectrum and near infrared (NIR) scattered power images. This type of setup has proven its value in other applications such as determining the loss in a photonic crystal waveguide [28], characterization of apodized gratings [13], Bloch mode detection in photonic crystal waveguides [29], and mapping of the intracavity power of a microring resonator [30]. A schematic drawing of the setup is depicted in Figure 4.3-2. The highly linear and sensitive NIR-CCD-camera was positioned to collect scattered photons from the selected area, indicated by the (white) dotted area in Figure 4.3-2. The camera produces 320 x 240 pixel images with a 12-bits pixel depth, where at the highest magnification each pixel represents the scattering from a 0.8 μm x 0.8 μm chip area.

By tuning the wavelength of the laser (λ_s), we obtain "scatter images" for each selected wavelength. The wavelength dependent scattering intensities of the selected area (region of interest: ROI) could be obtained by image processing of the scatter data. A tunable laser (HP 8186c) in combination with a polarization controller was used to couple light into the TE_{00} waveguide mode. The light source provided a wavelength range of 1470 nm to 1600 nm with a resolution of 1 pm. The transmission spectra of the waveguide gratings were normalized with respect to that of a reference waveguide without a grating, in order to cancel out any other wavelength dependencies in the optical path. In principle, all fabricated devices scatter due to inhomogenities in the waveguide structures. The scatterers obtained in our fabrication process have a random distribution, so that no coherent interference effects are to be expected. The size of the scatterers is on average smaller than 50 nm (determined from the SEM images), well in the Rayleigh scattering regime for the considered wavelength range. For sufficiently low power, nonlinear effects can be neglected and the scattered intensity is directly proportional to the local light intensity in the structure. In practice our method is dependent on the (inevitable) fabrication errors in the device, the minimum detection level of the linear camera, and the materials used for realizing the waveguide gratings (WGGs). We estimate guiding losses due to imperfections of <8 dB/cm for the WGGs (at the reference wavelength), which is relatively low considering the strong corrugation. For the feeding waveguides we estimate a guiding loss of <1 dB/cm.

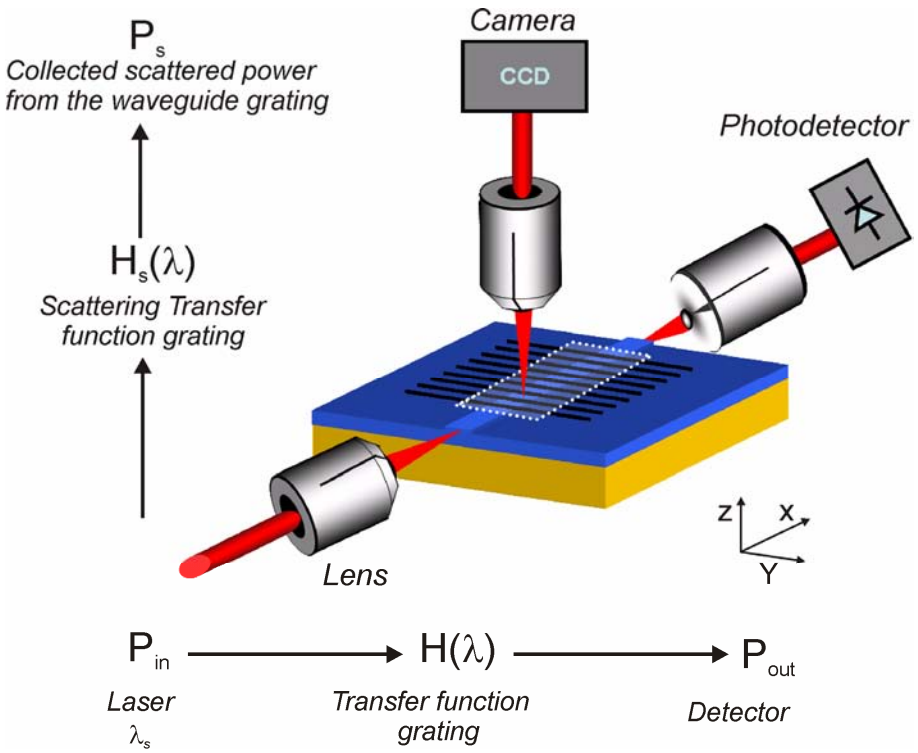

Figure 4.3-2: Schematic drawing of the dual-setup: NIR CCD-camera + end-fire detection.

Nevertheless, the method is expected to work for even smoother WGGs (with lower loss) as well. We used a relatively low input power of 0.2 mW to avoid overexposure of the NIR camera. The input power can easily be increased by a factor of 10 if needed. Another increase in power of at least 10 can be achieved by optimizing the input and output coupling, i.e., replacing the objectives by, for example, small-core fibers and/or carefully optimizing the fiber-chip coupling in the design. Furthermore, the signal to noise level can also be increased by averaging multiple frames. We expect that by applying the aforementioned optimizations our method will also work for imperfection levels at least 100 times lower than in our WGG. Therefore, the method may yield accurate results for gratings with propagation losses due to scattering as small as 0.08 dB/cm.
The reference delay measurements were performed using an RF vector network analyzer (VNA) [31]. The phase of a 2 GHz RF modulation of the optical wave was measured with the VNA. From this phase shift the group delay, and hence the group velocity of the optical signal could be deduced. One erbium-doped fiber amplifier (+20 dB) was placed after the RF modulator and the another one was placed before the RF detector to amplify the power coupled into the device under test in order to obtain an as high as possible signal to noise ratio, while taking care not to excite nonlinear effects in the device.

4.3.4 Resonances in waveguide gratings

As already mentioned, the resonances in finite WGGs give rise to fringes in the transmission spectrum near the stopband edges. These alternating transmission maxima and minima are often unwanted, because they limit the available bandwidth, making the devices less suitable for high speed telecom optics. Reduction of these fringes through apodization has therefore been the subject of many investigations [13,32-35]. The presence of the fringes in the transmission spectrum can be explained by longitudinal resonances which occur due to interference of the Bloch harmonics in the structure [6,11,12], with each maximum corresponding to a specific intensity distribution along the WGG. This phenomenon is studied here numerically and experimentally. This section is divided into two main parts. A theory subsection introduces the important quantities like group index N_g, Q and field enhancement factor η. These quantities are then used to derive expressions for the group delay experienced in the investigated WGGs. In the section 4.3.4.2 we calculate numerically a relation between the length of the grating and the quantities mentioned above. The simulations also demonstrate that the fringes in the transmission spectrum are related to resonances in the grating. In the experimental section 4.3.4.3 we will present the measured transmission and scatter data from a 500, 1000 and 2000 period WGG. The maximum values of Q, η, and N_g are obtained from these measurements. The delay times derived from the equations given in the theory section are compared with the group delays measured using the phase shift method.

4.3.4.1 Theory

In this section we will present the expressions that relate the group index to four different parameters of a resonator that can be directly measured: the Q factor, the scattered power, the free spectral range (FSR), and the group delay. In order to compare the methods experimentally, the first three parameters will be written as three separate expressions fro the delay times.
In general the group velocity describes the velocity at which envelope of a modulated optical signal is traveling. The modal group velocity can be calculated from the dispersion curve of an optical mode for an infinitely long grating using the following relation:

$$v_g(\omega) = \frac{d\omega}{dk}, \tag{1}$$

with ω as the angular frequency and k defined as the wave vector ($2\pi/\lambda$) of the optical wave. The group index is defined as $N_g = c/v_g$. A resonance can be described by its quality factor Q defined as,

$$Q = \omega_0 \frac{U}{dU/dt}, \tag{2}$$

where U is the time averaged energy stored in a resonator at the resonant angular frequency ω_0, and (T_0 dU/dt) is the energy loss in one period T_0 ($=2\pi/\omega_0$) of this frequency. Assuming an exponential decay of the resonator with decay time $\tau_c = U/(dU/dt)$, it follows,

$$Q = \omega_0 \, \tau_c. \tag{3}$$

A practical method for determining Q is by measuring the spectral transmission response of a resonator. The Q factor can than be obtained using the expression:

$$Q = \frac{\lambda_0}{\Delta\lambda_{-3\mathrm{dB}}}, \tag{4}$$

with $\Delta\lambda_{-3\mathrm{dB}}$ as the full width at half maximum of the Lorentzian shaped spectral response of the resonator and with λ_0 as the resonance wavelength.
In order to relate Q to the group velocity and to measurable scattered light, we will evaluate (2) using a power balance as illustrated by Figure 4.3-3. To find a relation between the intensity at resonance and Q and v_g we first write the energy stored in the resonator as the product of the energy density W_r with the modal volume of the resonator V.

$$U = W_r \, V = W_r \, A_r \, L. \tag{5}$$

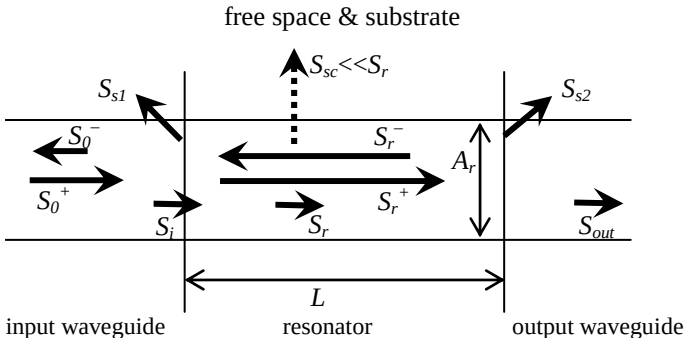

Figure 4.3-3: Power balance of the resonator (effective length L, effective cross-section A_r) with input and output waveguides, and radiative coupling to free space (and substrate). The right traveling energy flux density S_0^+ in the input waveguide is partly back reflected (S_0^-) and couples in part to the resonator (flux density S_i) and in part to radiation modes S_{s1} due to modal mismatch between waveguide mode and resonator mode. Inside the resonator, the net flux density S_r, which is composed of a right traveling flux density S_r^+ and a left traveling one S_r^- is assumed to be constant along the cavity (neglecting S_{sc}). At the interface to the output waveguide, an output flux density S_{out} remains after subtracting radiation loss S_{s2} due to modal mismatch.

The volume of the resonator is formally written as the product of an assumed modal cross-sectional area A_r and the cavity length L. In a stationary state, the outgoing energy loss per period at the right hand side (S_{out}) is exactly equal to the energy flux fed to the resonator [36] (neglecting S_{sc}). Therefore the time derivative of U can be written as,

$$\frac{dU}{dt} = S_i \, A_r. \tag{6}$$

Here, S_i is the net energy flux density (power density) that is transferred to the resonator. We assume the scattering loss from the cavity to be relatively small, so that the scatter flux S_{sc} is small compared to the net intensity flux inside the resonator S_r. Then S_r will be approximately constant and equal to S_i, and its relation to v_g is given by [11],

$$S_i \approx S_r = W_r \, v_g. \tag{7}$$

Next, we can write Q as a function of v_g at the resonance wavelength, by using (2), (5), (6) and (7),

$$Q = \omega_0 \frac{W_r V}{S_r A_r} = \omega_0 \frac{S_r}{S_i} \frac{L}{v_g} = \omega_0 \frac{L}{v_g}. \tag{8}$$

Equation (8) can be rewritten as,

$$Q = 2\pi \frac{L N_g}{\lambda_0}. \tag{9}$$

The group index can be related to the group delay t_d of a resonator, which can be measured, for example, as done in this paper, by using the phase shift method. This relationship is given by:

$$t_d(\lambda) = \frac{L}{c} N_g(\lambda). \tag{10}$$

An important observation can now be made by comparing (9) and (10), and using (3): the group delay t_d of the resonator is equal to its cavity decay time τ_c, which was also derived in [36]. This relation can be understood from the fact that the group delay is determined by the response of the resonator (filter) within this exponential decay time. A group delay larger than the decay time would be unlikely, because the power has leaked away, leaving no power to support the signal further. Using (3) we define the delay (decay) time t_q derived from the measured Q (see (4)) at the resonance wavelength as:

$$t_q = \tau_c = \frac{Q \lambda_0}{2\pi c}. \tag{11}$$

From (7) we can see that at a constant input power density S_i, a lower group velocity implies a higher energy density W_r. The ratio η between the average energy in the cavity at two different wavelengths λ and λ_{ref}, hence different group indices N_g and $N_{g,ref}$, can than be written as:

$$\eta(\lambda) = \frac{U}{U_{ref}} = \frac{W_r(\lambda) V}{W_{ref}(\lambda_{ref}) V} = \frac{S(\lambda)\ v_{g,ref}(\lambda_{ref})}{S_{ref}(\lambda_{ref})\ v_g(\lambda)} = \frac{N_g(\lambda)}{N_{g,ref}(\lambda_{ref})}. \tag{12}$$

This equation allows us to calculate N_g at a specific wavelength λ, if both $N_{g,ref}$ is known, and η is known at wavelength λ. With the FScM approach we present a method for estimating the reference group index $N_{g,ref}$ in order to measure N_g at wavelengths near the band edge. The scattered power $I_{sc}(\lambda)$ is proportional to the probability that a photon is scattered, which is proportional to the number of photons in the resonator, hence to the total energy. This is true if the considered wavelength range is small (to limit the influence of the λ^{-4} dependency of Rayleigh scattering), the number of scatterers is high and the distribution is random, which is the case in our WGGs as can be observed further in this paper, in Figure 4.3-9b. We assume that in the wavelength region of interest, the scatter efficiency is not strongly wavelength dependent. By measuring a reference scatter intensity $I_{sc,ref}(\lambda_{ref})$ at a wavelength where a value for N_g is known (a method will be explained in section 4.3.4.2), an estimate for $N_g(\lambda)$ can be found:

$$\eta(\lambda) = \frac{N_g(\lambda)}{N_{g,ref}(\lambda_{ref})} \approx \frac{I_{sc}(\lambda)}{I_{sc,ref}(\lambda_{ref})}. \tag{13}$$

An equivalent group delay t_{sc} can be calculated from the measured scatter ratio η by substituting (13) into (10):

$$t_{sc}(\lambda) = \frac{L}{c} \eta(\lambda)\, N_{g,ref}(\lambda_{ref}). \tag{14}$$

It is also possible to calculate Q from the scatter ratio (or visa versa) at the resonance wavelength λ_0, by substituting t_{sc} from (14) for t_q in(11):

$$Q(\lambda_0) = \eta(\lambda_0)\frac{2\pi\ L\ N_{g,ref}(\lambda_{ref})}{\lambda_0}. \tag{15}$$

In the derivations above, we assumed the equivalence of (group) delays that are measured or calculated in different ways at the resonance wavelength: directly measured, calculated from Q, and calculated from measured scatter enhancement η: $t_d \approx t_q \approx t_{sc}$.
A method, based on the Fabry-Perot free spectral range (FSR) equation, is sometimes applied [21,22] to derive the group index from the transmission spectrum.

$$\Delta\lambda_{FSR} = \frac{{\lambda_0}^2}{2N_g\ L}. \tag{16}$$

Again using (10), one more equivalent group delay t_{FSR} can be found.

$$t_{FSR} = \frac{{\lambda_0}^2}{2c\ \Delta\lambda_{FSR}}. \tag{17}$$

Without further evaluating this expression, we will test this FSR-method for its validity by comparing its results with the other methods.
Finally we will derive a value for the group velocity applicable over the whole spectrum from the modeled complex transfer function to get more insight into the dispersion behavior of the WGG. It is well known that periodic structures can have a flat angular frequency vs. wave number (ω–k) dispersion curve for a small wavelength range close to the photonic band edge. For finite structures, however, this curve never becomes completely flat, i.e., the group velocity will not approach to zero. The minimum vg can be calculated using the complex optical transfer function $t(\omega)$ of the WGG [14]:

$$t(\omega) \equiv x(\omega) + \mathrm{j}\ y(\omega). \tag{18}$$

The group velocity of a propagating mode in the WGG can be determined by calculating $\mathrm{d}\omega/\mathrm{d}\varphi$, with φ defined as the total phase kL, with L the device length which equals the number of periods N times the period Λ. Using $\varphi = \tan^{-1}(y/x)$, the group velocity can be calculated from the (computed) real and imaginary parts of the transfer function, as follows [14]:

$$v_g = \frac{d\omega}{dk} = L\frac{x^2 + y^2}{x\frac{dy}{d\omega} - y\frac{dx}{d\omega}}. \tag{19}$$

4.3.4.2 Method & simulations

To study the properties of the WGGs grating resonances we used a bi-directional eigenmodes propagation method (BEP) [37] with 128 basis functions (eigenmodes) to calculate the complex transfer function $T(\omega)$ for TE polarization. The group index was derived as a function of the wavelength using (19), and the transmission of the WGG (T_g) is derived from the absolute value of the complex transfer function, see Figure 4.3-4. We chose a WGG having a total number of periods of 350 instead of the fabricated 500 or more, for computing time/resources convenience. The group index shows two major peaks near the stopband edges of almost equal height/value. A maximum value for N_g = 7.3 at the smaller wavelength band edge is derived for this grating. Moving away from the band edge, the group index rapidly decreases to a value of ~1.86 (at 1560 nm) approximately equal to the N_g of the unperturbed ridge waveguide. This effect is used to define the reference group index ($N_{g,ref}$). At a wavelength around, for example, 1560 or 1510 nm, we can determine the scatter intensity, which we then relate to the reference scattering intensity $I_{sc,ref}$. However, this approach is not used in this paper; we take the average of the oscillation present around these reference wavelengths. A value for the group index of the WGG can then be calculated using (13).

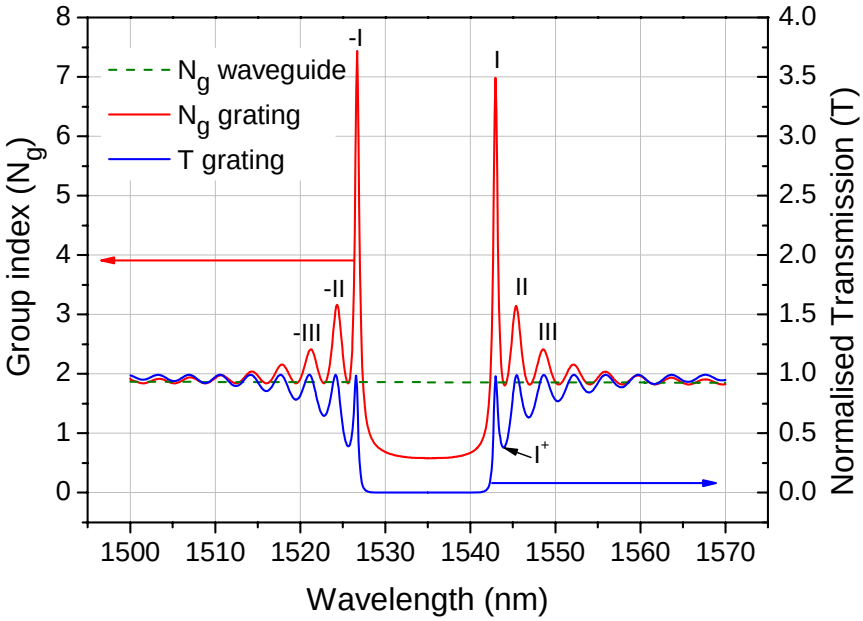

Figure 4.3-4: The group index of a reference waveguide (dashed) and the normalized transmission T (blue) and group index (red) of a 350-period WGG obtained using a BEP method and (19).

For the weak or moderate grating strengths as in the modeled WGG displayed in Figure 4.3-4, we observe approximately symmetric $T(\lambda)$ and $N_g(\lambda)$ curves [7]. A small difference can be seen between the group index curve shapes near the lower and upper wavelength edges. This is due to numerical errors in calculating the derivatives in (19); a larger number of simulation points will yield a more accurate result.

We note that the simulated WGG was modeled without optical loss due to absorption by the material or scattering, caused by inevitable errors in the fabrication processes. Consequently, the fringes in the fabricated WGGs (in Figure 4.3-9) will be less narrow than in the simulated gratings. Imperfections such as variations of layer thickness and etch depth, will compromise the geometrical coherence of the structure, which will cause serious deviations from the calculated response for longer gratings. For larger fabrication errors or larger L the grating may act as an apodized grating. We found in our measurements (section 4.3.4.3) that for a maximum number of periods of 2000 (L ~ 1 mm), the WGG still showed the clearly separated fringes as seen in the simulations.

Besides the maximum N_g of a WGG, we can also find the longitudinal intra-cavity grating resonance patterns using the BEP method by modeling the cross-section of a WGG, see Figure 4.3-5. These resonances are also verified experimentally in section 4.3.4.3. At the maximum of each fringe we can find a sinusoidal field distribution along the length of the grating, with nodes at its beginning and end; a simple mathematical derivation for this phenomenon can, for example, be found in [11]. The first resonance near the dielectric band edge, labeled as 'Resonance I' in Figure 4.3-4, shows a single maximum exactly in the middle of the grating (Figure 4.3-5a). The top image shows the H-field distribution in the cross-section of the WGG. The lower plot shows the field distribution exactly in the middle of the Si_3N_4 slab. In the feeding waveguide (left) we see a small ripple indicating a small residual reflection. At the first minimum in the transmission curve, denoted by 'Resonance I^+' (Figure 4.3-5b), a strong reflection is evidenced by the large amplitude of the standing wave in the input waveguide. At the start of the grating, we now find a maximum and inside the grating we find both a minimum and a maximum. On the output of the grating (right) we observe a lowered value of the transmitted field, which is consistent with the calculated transmission shown in Figure 4.3-4. Increasing the wavelength further, away from the stopband, we find the higher order resonances. Figure 4.3-5c and Figure 4.3-5d show the higher order resonances II and III. The maximum H-field amplitude decreases with the resonance order, which

is expected from Figure 4.3-4, which shows equivalently a decrease in group index. This decrease in modal-amplitude can be explained by the decrease in reflectivity from the grating for wavelengths further away from the Bragg condition.

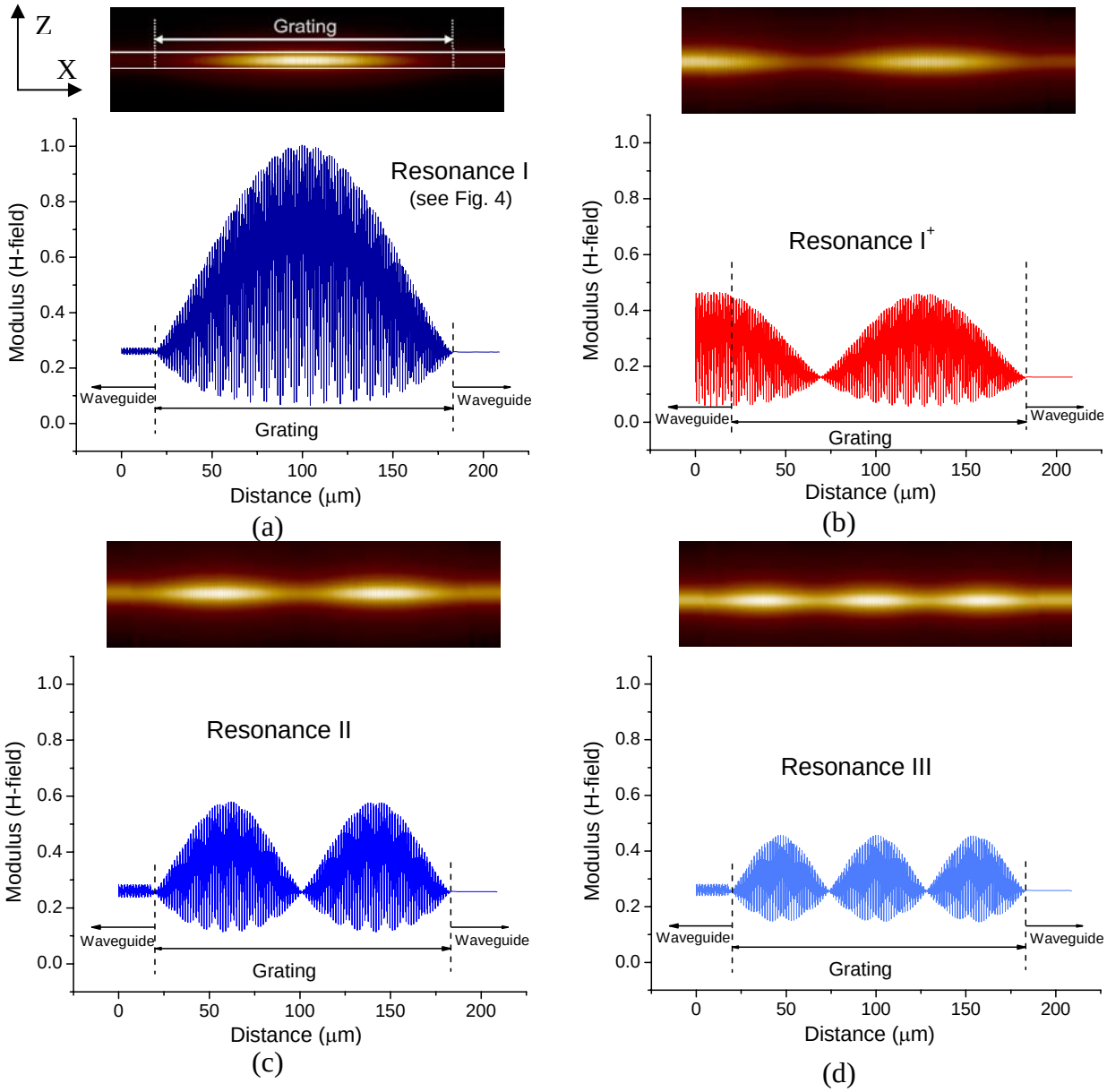

Figure 4.3-5: Intra-cavity grating resonance modes in the dielectric band obtained via BEP Simulations. (a)-(d) The top image shows the H-field amplitude in the cross-section of the WGG for the resonance wavelengths shown in Figure 4.3-4. The x- and z-coordinates are defined in Figure 4.3-2. The bottom graphs show the H-field amplitude along the center-line of the guiding layer.

In Figure 4.3-6, we have plotted both resonances near the band edge of the WGG in black and in red corresponding to Resonance I and –I (Figure 4.3-4), respectively, for a 100-period WGG. For a slow wave at the airband edge it is expected that the light is mainly concentrated in the low-index regions of the periodic medium [8]: the grooves of the grating, and for the dielectric band edge in the high-index regions: the teeth of the WGG. These assumptions are based on an infinite structure using periodic (Bloch) boundary conditions. Figure 4.3-6 shows that for a finite structure, this is indeed the case for a region around the center of the periodic medium (the location of the field has been checked with the modeled WGG). However, moving outwards, we find both field intensity distributions coinciding. The region where the field maxima are shifted by half a grating period

can be increased by choosing a longer or stronger grating. The above phenomena can be explained, using the theory outlined in reference [12], in terms of the interference between the two counter propagating intra-cavity modes, for the wavelength regions above and below the band gap.

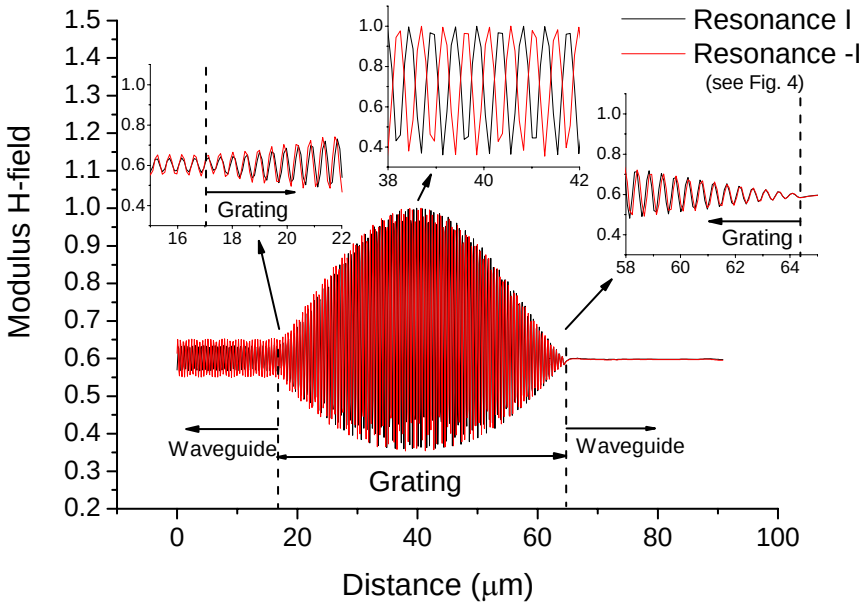

Figure 4.3-6: Field amplitude (H-field) of the grating resonances at both band edges (resonances I and -I) of a 100-period WGG. In the middle section of the periodic medium (the grating) we see the well known phenomena [8] (studied by overlaying the grating structure with the field-distributions): the field for the first resonance in the air band is concentrated in the grooves (low-index) and for the dielectric band in the teeth (high-index). There is a shift between both field distributions of half a period. At the transition between the grating and the waveguide we observe the same (in phase) field distribution.

It has already been shown that the maximum field enhancement factor is linear with the length of the grating [38]. This is also verified by the modeling results presented in Figure 4.3-7. Panel (a) shows the maximum relative field enhancement η found at the first resonance fringe (resonance I in Figure 4.3-4) versus the number of periods, calculated using BEP modeling. The figure clearly shows the expected linear relationship. Besides the field enhancement, we also calculated the group index as a function of the number of periods. The curve for the maximum N_g (at resonance I) is quadratically related to the number of periods as expected, since N_g is proportional to the maximum (relative) intensity, which is proportional to the square of the electric field. The fringes are narrow near the stopband and thus have a high Q (= $\lambda/\Delta\lambda_{\text{-3dB}}$). Further away from the band edge the Q of each fringe declines (Figure 4.3-4) until it can not be defined anymore (less than 3dB difference between the maximum and adjacent minimum).

A third-order relationship between Q and the grating length has been found using coupled mode equations for a waveguide grating suitable for second harmonic generation [5]. Moreover, this relation can also be deduced from (9) by using the quadratic relation between N_g and L. We have also verified this relation by rigorous BEP modeling (Figure 4.3-7b). For gratings shorter than 200-periods, we have estimated the Q from the left half side of the resonance I, taking $\Delta\lambda_{\text{3dB}}$ as 2 times the value found left from the resonance wavelength at the -3dB point.

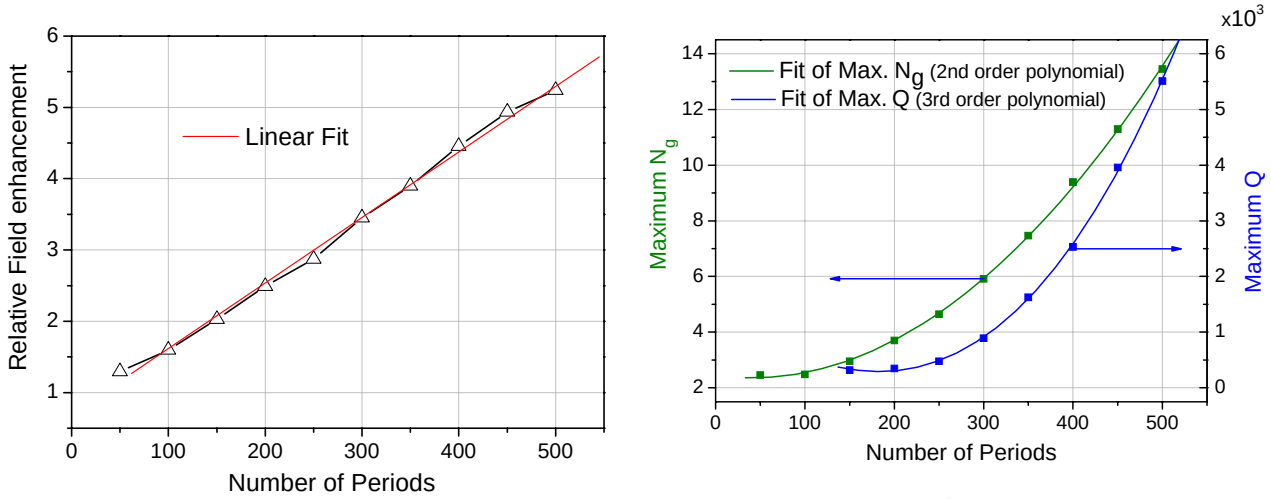

Figure 4.3-7: (a) Maximum field strength as function of the number of periods. (b) Maximum group index (N_g) and Q versus the number of periods.

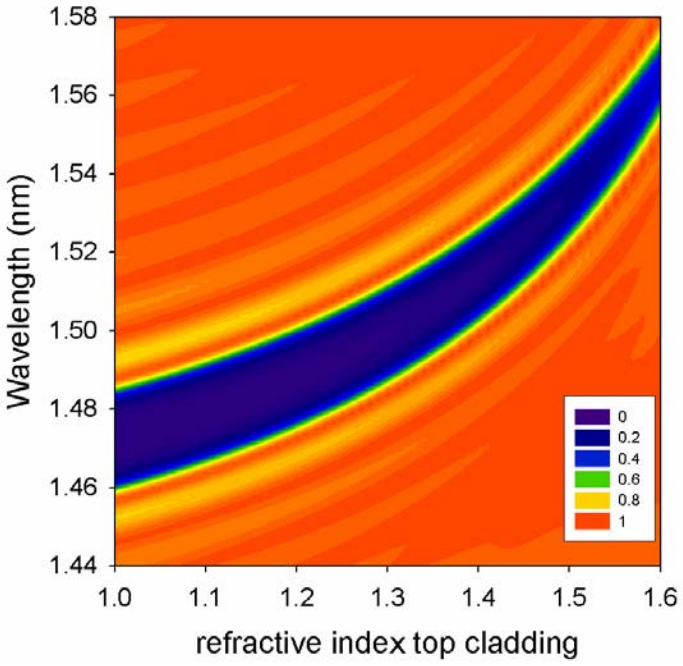

Figure 4.3-8: Normalized transmission versus cladding index and wavelength for a 200-period WGG.

In the measurements presented in this paper, we have characterized WGGs with and without polymer cladding. Due to the higher contrast for the WGGs without cladding a higher maximum N_g is expected for the same device length. In Figure 4.3-8 we have plotted the transmission as a function of the refractive index of the cladding and the wavelength for a 200-period WGG. The figure clearly shows how the stopband shifts with cladding index. As expected the stopband shifts to larger wavelengths when the refractive index of the cladding is increased.

4.3.4.3 Experimental

The transmission of the 500-period grating was measured after applying a polymer cladding with refractive index 1.5 onto the structure shown in Figure 4.3-1a, see Figure 4.3-8 for location of the stopband as a function of the cladding index. Next to the stopband, we find the predicted narrow

fringes, see Figure 4.3-9a. The *Q*s of resonances I and –I (Figure 4.3-4) are ~8500 and 6000, respectively.

To obtain clear images of the intensity distributions of the grating resonances we also captured the scattered light without the use of a polymer cladding. Due to the difference in cladding index, the spectra of the air-clad device were down-shifted by approximately 70 nm compared to the polymer-clad devices. This scaling has been taken into account for locating the labels A-D in Figure 4.3-9a and Figure 4.3-9b.

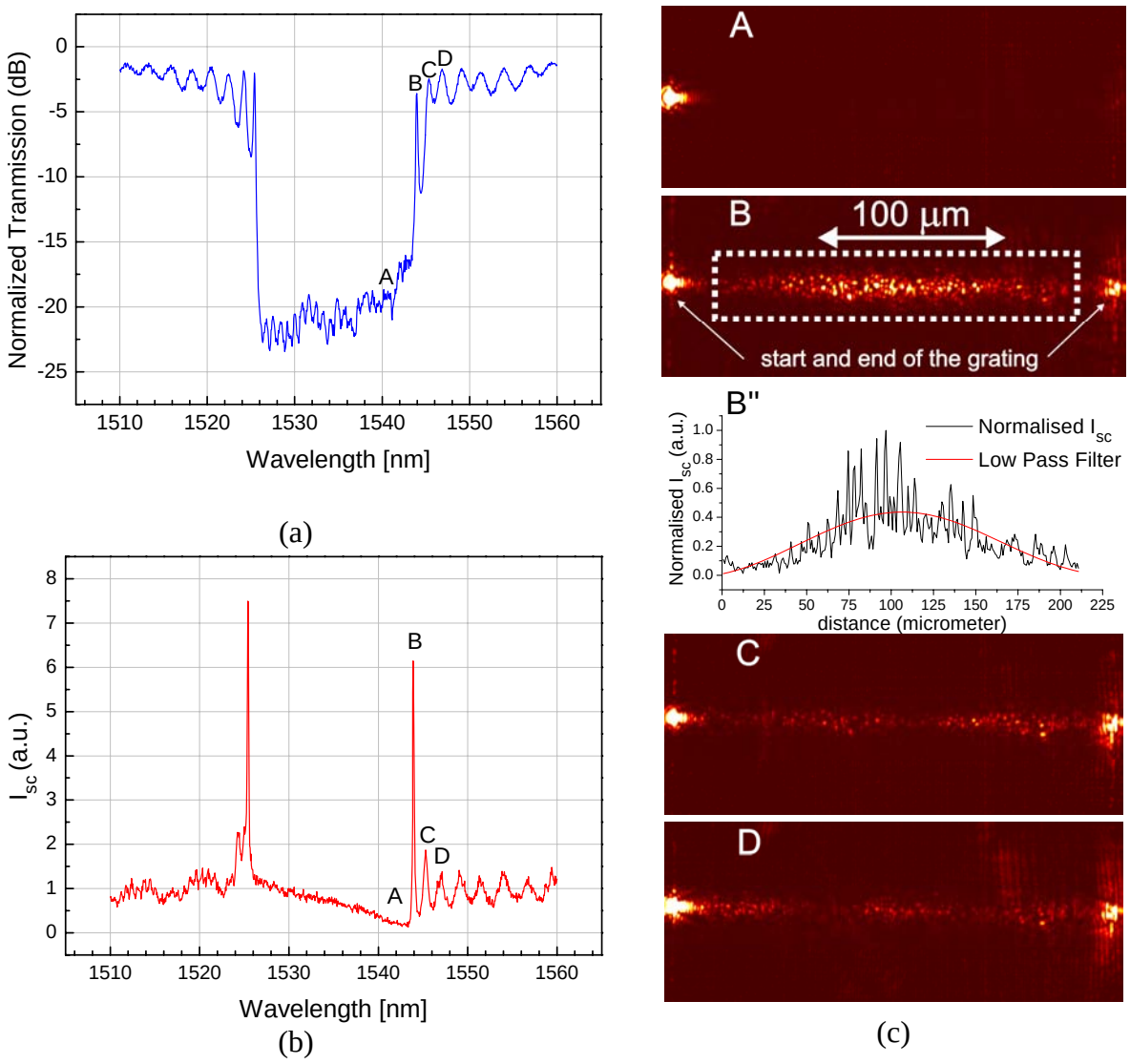

Figure 4.3-9: Measurements on the 500-period waveguide grating. (a) Transmission spectrum of the WGG. (b) The scatter intensity (I_{sc}) collected using the NIR camera. (c) Scatter image A is taken from the grating region without cladding at the wavelength in the stopband labeled A in the transmission and scatter graphs (panels (a) and (b), respectively). A wavelength scaling factor has been used to account for the difference in cladding index, as explained further in the text. Only scattering from the input spot is observed for this wavelength. Image B is taken at the lowest-order resonance wavelength. The smoothed curve in graph B″ shows a single maximum. Images C and D show 2 and 3 intra-cavity maxima, respectively. A movie of the transmission versus an increasing wavelength (available at http://www.opticsexpress.org/).

Image A in Figure 4.3-9c shows a capture for a wavelength in the stopband (see Figure 4.3-9a or Figure 4.3-9b for the location in the spectrum). Only one bright spot is seen, which is the scattering from the transition of waveguide to WGG. Slightly increasing the wavelength to the first resonance in the dielectric band results in the single maximum intensity distribution shown in B

(resonance I, Figure 4.3-4). Graph B″ shows the scatter intensity (I_{sc}) integrated over a vertical line in the dotted box shown in B as a function of the distance (horizontal in the box). Although the camera images cannot resolve the sub-wavelength details of the field distribution in the grating area, they clearly show the envelope of the intensity distribution of the Fabry-Perot-like resonances of the Bloch modes in the WGG. By integrating I_{sc} over the area enclosed by the dotted box, it is possible to derive the I_{sc} spectrum shown in Figure 4.3-9b.

The maximum intensity enhancement (η) we obtain is about 7.4 taking the scattered intensity at 1514 nm as a reference. Using (13) and taking the reference index $N_{g,ref}$ equal to the group index of the undisturbed ridge waveguide ($N_{g,ref} \approx 1.9$) a value of $N_g \approx 7.4 \times N_{g,ref} = 14$ can be calculated. This corresponds to a group velocity of ~0.07 c. The estimated value of N_g using (9) with a Q of 8500 is about 8.8. The deviation between both numbers could be explained from the definition of Q given in (9). The shape of the fringes near the stopband is not strictly Lorentzian, because the reflectance changes rapidly with wavelength. Therefore, Q derived from the spectrum may be different from the actual Q value defined by (2) at the resonance wavelength.

In the experiments performed on the longer gratings, which will be discussed next, we notice that the deviation between both methods for obtaining the group index is smaller which may indicate that the Qs are more accurately determined using (9) for the longer gratings. Also other factors may contribute to small differences, for example, the presence of slab-light and/or noise by the input and output spot of the WGG (see Figure 4.3-9c image D), to which the FScM-method is sensitive. For longer WGGs the influence of both contributions is lower, which results in a better signal-to-noise ratio and a better agreement between both methods as we will show. The group delay can now also be calculated using (11) and (14), resulting in values $t_q \approx 7$ ps and $t_s \approx 11$ ps.

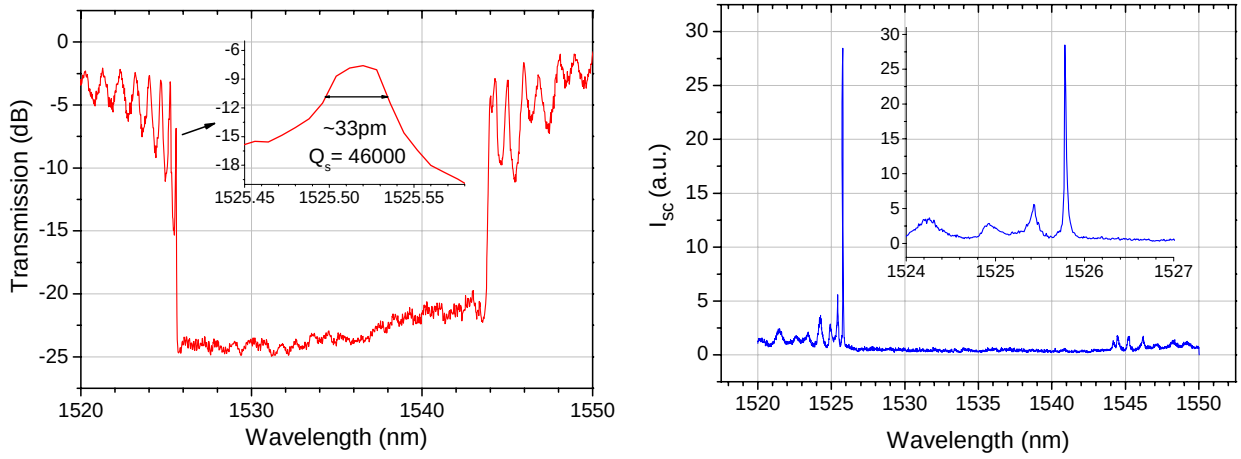

(a) (b)

Figure 4.3-10: Measurements on the 1000-period grating. (a) Transmission spectrum of the WGG, showing a very sharp fringe with a FWHM of only 33 pm in the airband, which corresponds to a Q of 46000. (b) The scatter intensity (I_{sc}) spectrum collected using the NIR camera.

A larger value for N_g can be expected when the length of the selected WGG is increased (Figure 4.3-7b) to 1000 periods. The measured transmission curve of this grating is shown in Figure 4.3-10a. The fringes in the airband are separately observable, whereas the fringes in the dielectric band show overlap near the edge, which is caused by fabrication errors inducing apodization, see [13] and the references therein. The first order resonance (resonance –I) shows a FWHM of only ~33 pm, which corresponds to a Q of 46000. Figure 4.3-10b shows the corresponding spectrum of the scattered intensity, from which a large $N_g \approx 24$ is deduced indeed at this high Q resonance, using (9). The noise level (due to slab light) in this particular grating was higher than in the other 2 gratings; therefore the background noise was subtracted from the scattered intensity collected from the grating area by selecting an equal-sized area as reference next to the ridge waveguide at

approximately 20 micrometer below the waveguide. From this scatter intensity enhancement we estimate η to be about 12. Using (13) we then find $N_g \approx 27$, corresponding to a group velocity of 0.04 c. For the corresponding group delays at the resonance wavelength (λ = 1525.52 nm) calculated using the measured Q and η, we find $t_q \approx 38$ ps and $t_{sc} \approx 42$ ps, respectively. Both methods agree quite well on the group index and consequently on the group delay at resonance –I (see Figure 4.3-4).

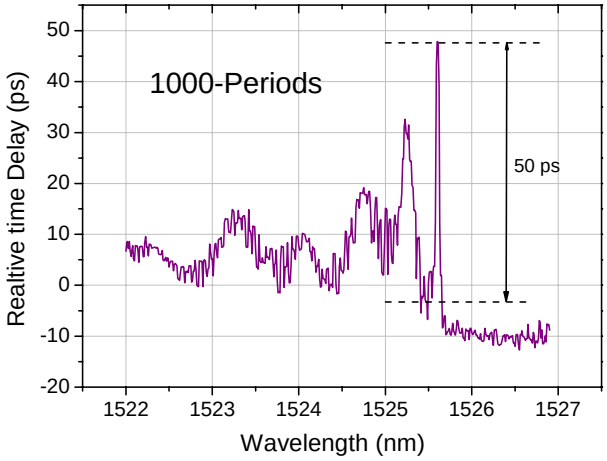

Figure 4.3-11: Relative group delay as a function of wavelength, directly measured using the phase shift method for the 1000-periods long grating.

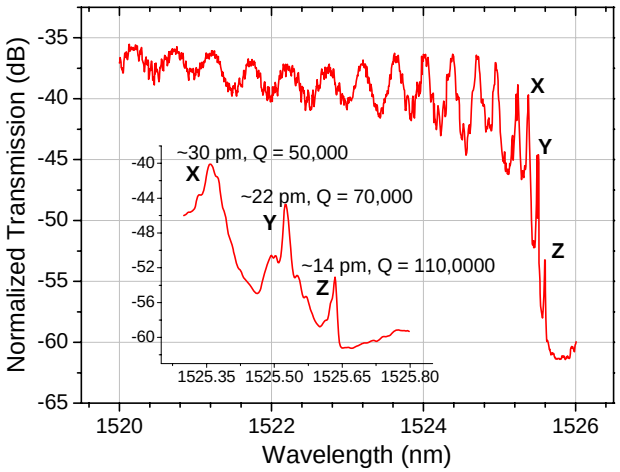

Figure 4.3-12: Transmission spectrum obtained from the 2000-periods grating, zoomed in on the left edge.

However, with a reference measurement using the phase shift method to directly determine the group delay, a maximum $t_d \approx 50$ ps is found, see Figure 4.3-11. The difference between t_q, t_{sc} and t_d can be explained from the inaccuracy in each method.

To compare the FScM method even further experimentally with the other methods, we doubled the number of periods again to 2000 resulting in a device length of 940 μm. The corresponding transmission spectrum is shown in Figure 4.3-12, which is zoomed in on the air band region. For the resonances labeled *X*, *Y* and *Z*, *Q*-values of approximately 50 000, 70 000 and 110 000 respectively were found. With increasing *Q* the transmission drops due to the longer lifetime of the resonant photons, which causes a larger fraction of the light to scatter out of the WGG. The spectrum of the scattered intensity is shown in Figure 4.3-13a. We find a maximum $N_g \approx 25$ using (13), which results in a maximum group delay of $t_{sc} \approx 78$ ps (see (14)). For the maximum group delay calculated using the maximum Q of 110 000, a maximum $t_q \approx 88$ ps is found. The estimated group delays using both indirect methods match within 13 %.

The group delay calculated using the phase shift method is shown in Figure 4.3-13b. For resonance –I a maximum delay $t_d \approx 75$ ps is found. Although a larger N_g should be expected from a longer grating, the maximum N_g was found for the 1000-period grating, rather than for one with 2000 periods. Inaccuracies in the fabrication process limit the maximum achievable spatial coherence in the grating, which puts a limit on the maximum achievable Q.

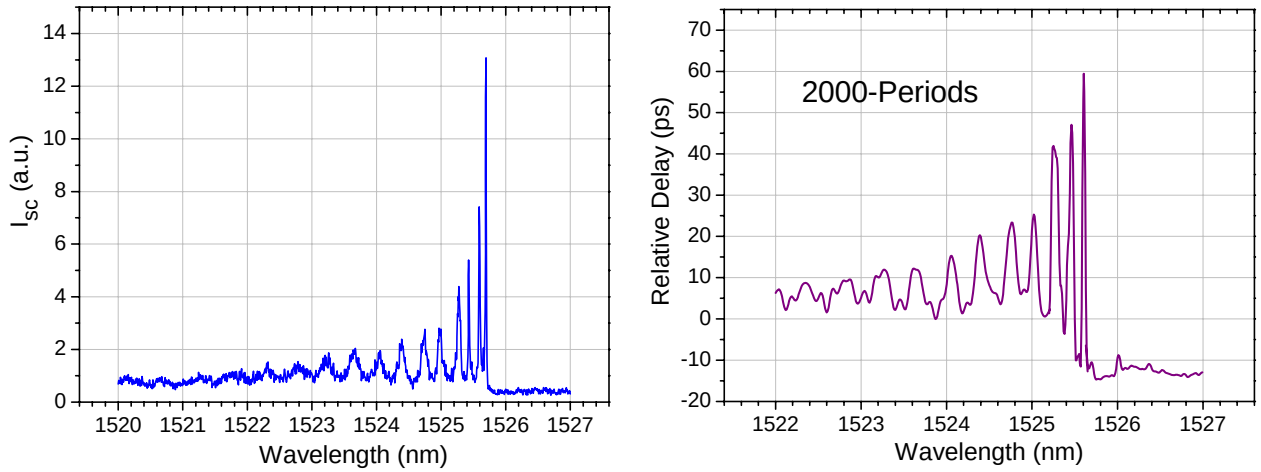

Figure 4.3-13: Measurements on the 2000-periods long grating. (a) The scatter intensity spectrum. (b) Relative group delay, directly measured using the phase shift method.

In the previous part we have focused only on the zero-order resonance in the airband (resonance – I); however, the approach should also be valid for higher order resonances. To verify this we have determined several *Q*-values and plotted them as a function of η, see Figure 4.3-14a. The graph shows a linear relationship which agrees with (15).

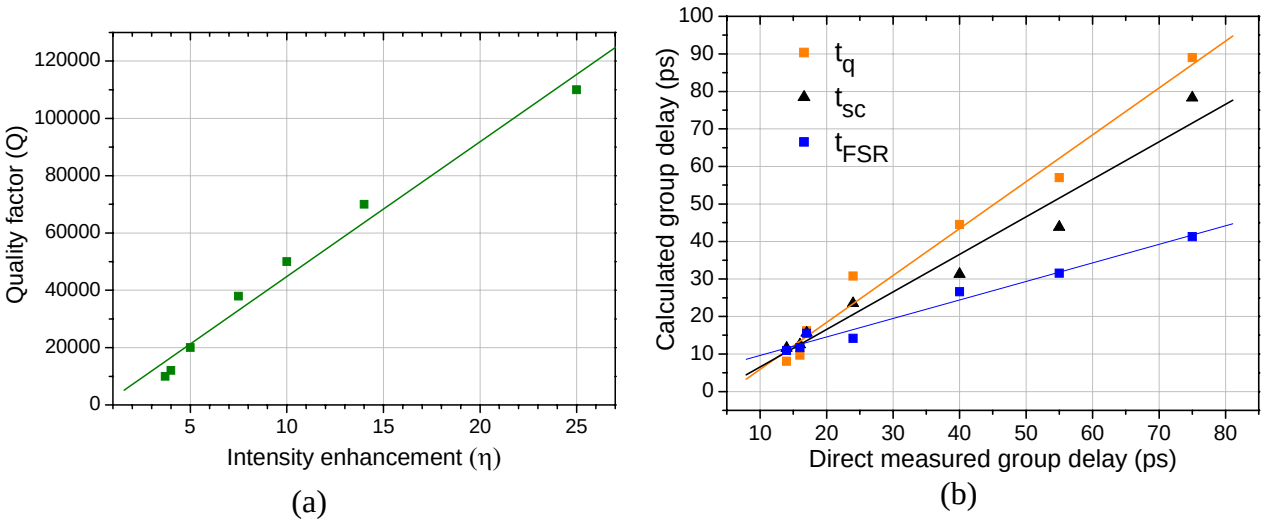

Figure 4.3-14: (a) Experimentally derived relationship between η and Q. (b) Group delays calculated using various methods versus the directly measured group delay (t_d).

Figure 4.3-14b shows the indirectly derived group delays as a function of the directly measured time-delay. In this plot we also included the delay calculated from (17), using the FSR between the peaks. We observe that the group delays calculated from *Q* and η show a fairly good agreement with the directly measured group delay. From these results we can conclude that both indirect methods can be used to determine the group delay taking into account the accuracy of the methods. Both methods are somewhat complementary; for example, a transmission spectrum, obtained using a high resolution tunable laser having a small spectral linewidth, can be used for calibrating the FScM method. In this way N_g can be determined easily over a broad spectrum, by cancelling the noise contribution by slab light in the scatter experiments. On the other hand, the FScM method provides N_g also for wavelengths out of resonance. Figure 4.3-14b clearly shows that the FSR method (using (17)) shows the strongest deviations from the values measured using the phase shift method, especially close to the band edge (at a t_d of 75 ps we find a t_{FSR} of ~40 ps). A possible

explanation is the invalidity of the assumption of linear dispersion that is made to derive this equation (linear Taylor expansion), whereas in reality the dispersion curve is approximately quadratic near the stopband edge (ω versus β).

4.3.5 Out-of-plane scattering

The coupling of periodic dielectric structures to input and output waveguides, mostly leads to an important source of loss in slab type designs, due to out-of-plane scattering (OPS). In order to optimize these transitions, this loss needs to be analyzed. In section 4.3.5.1 we will briefly describe the origin and nature of the OPS, using BEP modeling. In section 4.3.5.2, we will show that the NIR camera allows us to determine the wavelength dependency of the OPS losses.

4.3.5.1 Simulations

The two main sources for out-of-plane scattering in the WGGs discussed in this paper are the scattering at the transition from waveguide to WGG and at the transition from WGG to waveguide, denoted as input and output spot respectively (see the images in Figure 4.3-9). The scattering at the transition is caused by a modal mismatch between waveguide mode and the grating Bloch mode. Some adiabatic converters have been suggested for this transition [39,40], but these tapers have the disadvantage of modifying the phase of the grating, which can lead to an apodized spectrum, which is clearly unwanted in this study.

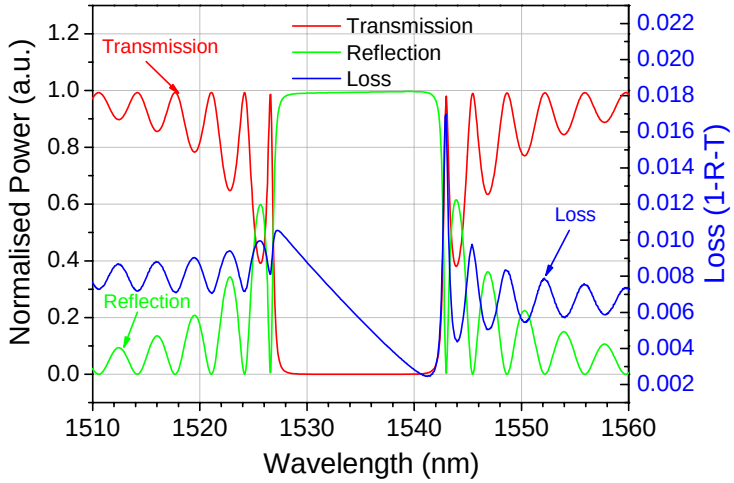

Figure 4.3-15: A BEP [37] simulation of the transmission (T), reflection (R) and loss of a 350 period WGG. The out-of-plane loss is calculated using the relation OPS = 1 – R – T.

The result of a BEP simulation on a 350 period WGG is shown in Figure 4.3-15. The same grating model as used for the results shown in Figure 4.3-4 was chosen. The figure shows the transmission (T), reflection (R) and loss curves. The out-of-plane loss is calculated for each wavelength using the relation OPS = 1 – T – R. The loss-curve shows interesting behavior. It has a global minimum near the dielectric band edge, where the reflection reaches its maximum; for shorter wavelengths (in the bandgap) the loss increases and reaches a global maximum close to the air band edge. The loss maxima coincide with the transmission maxima in the dielectric band, whereas in the airband they coincide with the reflection maxima; a possible explanation will be given in the section below.

4.3.5.2 Experimental

In this paper we propose to quantify the out-of-plane loss by measuring the scattered light at the input and output of the grating. A figure for the OPS losses can be obtained by integrating the scatter data from the NIR camera over the input and output spot areas. Although our camera objective had a high NA (0.65), the OPS measured here may differ slightly from the actual OPS,

because the scattering does not necessarily show a uniform distribution over all angles and over the complete spectrum analyzed here. However, it may provide relative information about the OPS. The scattering at both transitions can, for example, be compared. The sum of the OPS at both transitions may give a good figure for the behavior of the total OPS.

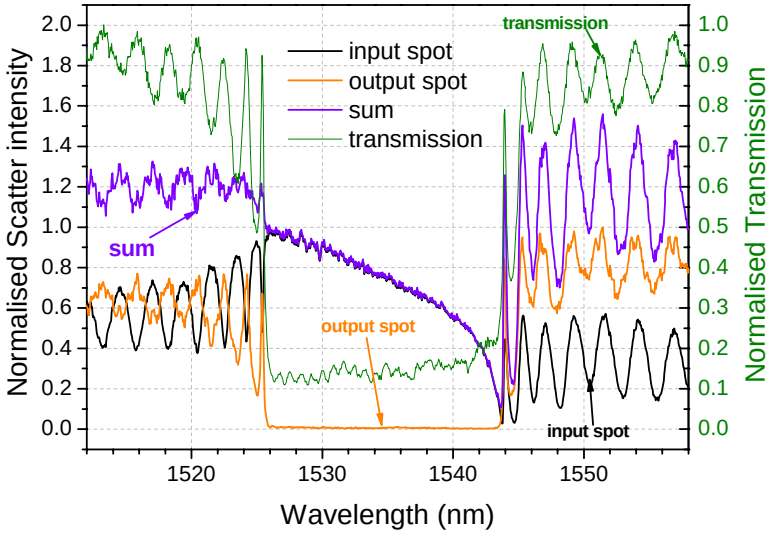

Figure 4.3-16: Measurement of the scattering observed at the input and output spots of the grating. A sum of both gives a figure for the total OPS.

The OPS measurement results are presented in Figure 4.3-16, which contains three curves, viz., the measured (integrated) OPS from the input and output spot and the sum of both curves. We find that the OPS observed at the output spot is approximately proportional to the measured transmission of our structures. Some of the differences can be explained from the temperature drift (in the coupling conditions) in the two measurements, which were not performed at the same time. Comparing the measured total OPS (the sum curve) with the OPS calculated using BEP simulation (Figure 4.3-15) leads to the conclusion that both show resemblance. They both show a minimum in losses just before the first resonance in the dielectric band. Another agreement is found in the dielectric band and the airband, where in both cases the OPS loss has either coinciding maxima with the transmission curve (or output spot) or with the reflection (input spot). At wavelengths below the band edge the maxima in transmittance, and so in intra-cavity power, coincide with minima in the calculated loss curve (Figure 4.3-15) and also with minima in the power scattered from a region near the input spot. This can be explained by assuming that, at the corresponding WG-WGG interface, light scattered by the two incoming modes (from left and right) is out of phase, leading to a cancellation of scattered power. This picture is supported by the observation from Figure 4.3-16, that for wavelengths below the band edge, the dips in the power scattered at the input spot have approximately the same shape as the peaks in the transmittance. However, some differences in shape and magnitude are observable apart from the high frequency ripples on the “sum” graph, for example, in the stopband the shape differs from the simulated shape, most probably caused by fabrication inaccuracies. Nevertheless, we conclude that the NIR is also a powerful tool for investigating the relative OPS losses.

4.3.6 Sensor application

In this section we will discuss briefly an application for the high-*Q* gratings presented in this paper. Among many other applications, the relatively small, simple and easy to fabricate WGGs are suited for integration into sensor arrays. Their relatively small dimensions compared to linear phase based sensors, such as Mach-Zehnder interferometers [41], allows for compact design while maintaining a high sensitivity [2]. The sensitivity can be calculated assuming a precision in

minimum detectable change of transmission power of $\Delta T_0 = 10^{-4}$ (determined by the quality peripheral equipment and the number of samples taken) and the following approximation:

$$\Delta n_{cladding} \approx \frac{\partial n}{\partial \lambda} \frac{\partial \lambda}{\partial T} \Delta T_0 \tag{20}$$

A value of $\sim 15\times10^{-12}$ can be estimated for $\partial\lambda/\partial T$ using the transmission curve in Figure 4.3-12 (the 2000-period WGG, resonance *Z*). For $\partial n/\partial\lambda$ a value of 7.8×10^{6} m^{-1} (0.5/64 nm) is derived from the stopband shift with and polymer cladding, see also Figure 4.3-8. Inserting these numbers in (20), we find a minimum detectable cladding index change $\Delta n_{cladding} \sim 1\times10^{-8}$. Such a grating sensor performs well compared to the state of the art MZI sensors ($\Delta n_{cladding} \sim 10^{-8}$) [41], especially when the size and simplicity are considered, (for attaining the quoted sensitivity, the MZI sensor needs an advanced detection system). In conclusion we find that WGG gratings shown here are good candidates for all sorts of cladding sensors, for example, without a cladding, for gases, or with a water-based cladding for dissolved chemicals.

4.3.7 Conclusions

We have experimentally shown the existence of intensity resonance patterns in gratings which correspond well to the distributions found in the simulations of the waveguide grating. We have presented a novel and straightforward method for determining the group index and intensity enhancement over a wide wavelength range using the scatter intensity method. The far-field scattering microscopy method (FScM) was compared with two other methods and showed reasonable good agreement verifying the model presented in this paper. For the 500-period waveguide grating we found a minimum group velocity of 0.07 *c*. The 1000-period WGG showed a v_g as low as 0.04 *c*. For the 2000-period grating we measured a maximum *Q* of 110.000 and a maximum delay of 75 ps. The minimum v_g for this grating was estimated to be approximately equal to the value found for the 1000-period WGG: 0.04 *c*. The reason for this is the errors in fabrication.

In general we found that, the method estimating the group index (or delay) using the free-spectral-range formula (17) shows a significant deviation from the other methods, especially for the peaks at the stopband edge. In section 4.3.5 it was shown that the scatter data can also be used to analyze the out-of-plane scattering at the grating/waveguide transitions, which can be helpful for designing low insertion loss devices, for example. Finally we presented an application for the "high *Q*" WGG as compact sensor, and the minimum detectable change in cladding index of 1×10^{-8}.

4.3.8 Acknowledgements

We thank Henry Kelderman, Henk van Wolferen their help with the laser interference lithography and Marco Gnan and Chris Roeloffzen for discussions. This work was supported by NanoNed, a national nanotechnology program coordinated by the Dutch ministry of Economic Affairs.

4.3.9 References

[1] J. F. Lepage, R. Massudi, G. Anctil, S. Gilbert, M. Piche and N. McCarthy, "Apodizing holographic gratings for the modal control of semiconductor lasers", *Applied Optics*, vol. **36**, pp. 4993-4998, 1997.

[2] W. C. L. Hopman, P. Pottier, D. Yudistira, J. van Lith, P. V. Lambeck, R. M. De La Rue, A. Driessen, H. J. W. M. Hoekstra and R. M. de Ridder, "Quasi-one-dimensional photonic crystal as a compact building-block for refractometric optical sensors", *IEEE Journal Of Selected Topics In Quantum Electronics*, vol. **11**, pp. 11-16, 2005.

[3] P. Madasamy, G. N. Conti, P. Poyhonen, Y. Hu, M. M. Morrell, D. F. Geraghty, S. Honkanen and N. Peyghambarian, "Waveguide distributed Bragg reflector laser arrays in erbium doped glass made by dry Ag film ion exchange", *Optical Engineering*, vol. **41**, pp. 1084-1086, 2002.

[4] H. C. Wu, Z. M. Sheng and J. Zhang, "Chirped pulse compression in nonuniform plasma Bragg gratings", *Applied Physics Letters*, vol. **87**, pp. 201502/1-3, 2005.

[5] D. Pezzetta, C. Sibilia, M. Bertolotti, J. W. Haus, M. Scalora, M. J. Bloemer and C. M. Bowden, "Photonic-bandgap structures in planar nonlinear waveguides: application to second-harmonic generation", *Journal of the Optical Society of America B-Optical Physics*, vol. **18**, pp. 1326-1333, 2001.

[6] D. Faccio, F. Bragheri and M. Cherchi, "Optical Bloch-mode-induced quasi phase matching of quadratic interactions in one-dimensional photonic crystals", *Journal of the Optical Society of America B-Optical Physics*, vol. **21**, pp. 296-301, 2004.

[7] J. Ctyroky, S. Helfert, R. Pregla, P. Bienstman, R. Baets, R. De Ridder, R. Stoffer, G. Klaasse, J. Petracek, P. Lalanne, J. P. Hugonin and R. M. De La Rue, "Bragg waveguide grating as a 1D photonic band gap structure: COST 268 modelling task", *Optical and Quantum Electronics*, vol. **34**, pp. 455-470, 2002.

[8] J. D. Joannopoulos, R. D. Meade and J. N. Winn, "Photonic crystals: Molding the flow of light", Princeton University Press, 1995.

[9] M. Soljacic & J. D. Joannopoulos, "Enhancement of nonlinear effects using photonic crystals", *Nature Materials*, vol. **3**, pp. 211-219, 2004.

[10] V. I. Kopp, B. Fan, H. K. M. Vithana and A. Z. Genack, "Low-threshold lasing at the edge of a photonic stop band in cholesteric liquid crystals", *Optics Letters*, vol. **23**, pp. 1707-1709, 1998.

[11] A. Figotin & I. Vitebskiy, "Slow light in photonic crystals", *Waves in Random and Complex Media*, vol. **16**, pp. 293-382, 2006.

[12] H. J. W. M. Hoekstra, W. C. L. Hopman, J. Kautz, R. Dekker, and R. M. de Ridder, "A simple coupled mode model for near band-edge phenomena in grated waveguides", *Optical and Quantum Electronics*, vol. **38**, pp. 799-813, 2006.

[13] W. C. L. Hopman, R. Dekker, D. Yudistira, W. F. A. Engbers, H. J. W. M. Hoekstra and R. M. de Ridder, "Fabrication and Characterization of High-Quality Uniform and Apodized Si_3N_4 Waveguide Gratings Using Laser Interference Lithography", *IEEE Photonics Technology Letters*, vol. **18**, pp. 1855-1857, 2006.

[14] J. M. Bendickson, J. P. Dowling and M. Scalora, "Analytic expressions for the electromagnetic mode density in finite, one-dimensional, photonic band-gap structures", *Physical Review E - Statistical Physics, Plasmas, Fluids, and Related Interdisciplinary Topics*, vol. **53**, pp. 4107-4121, 1996.

[15] H. Gersen, T. J. Karle, R. J. P. Engelen, W. Bogaerts, J. P. Korterik, N. F. van Hulst, T. F. Krauss and L. Kuipers, "Real-space observation of ultraslow light in photonic crystal waveguides", *Physical Review Letters*, vol. **94**, pp. 073903/1-4, 2005.

[16] C. E. Finlayson, F. Cattaneo, N. M. B. Perney, J. J. Baumberg, M. C. Netti, M. E. Zoorob, M. D. B. Charlton and G. J. Parker, "Slow light and chromatic temporal dispersion in photonic crystal waveguides using femtosecond time of flight", *Physical Review E*, vol. **73**, pp. 016619/1-10, 2006.

[17] R. S. Jacobsen, A. V. Lavrinenko, L. H. Frandsen, C. Peucheret, B. Zsigri, G. Moulin, J. Fage-Pedersen and P. I. Borel, "Direct experimental and numerical determination of extremely high group indices in photonic crystal waveguides", *Optics Express*, vol. **13**, pp. 7861-7871, 2005.

[18] M. C. Netti, C. E. Finlayson, J. J. Baumberg, M. D. B. Charlton, M. E. Zoorob, J. S. Wilkinson and G. J. Parker, "Separation of photonic crystal waveguides modes using femtosecond time-of-flight", *Applied Physics Letters*, vol. **81**, pp. 3927-3929, 2002.

[19] Y. A. Vlasov, S. Petit, G. Klein, B. Honerlage and C. Hirlimann, "Femtosecond measurements of the time of flight of photons in a three-dimensional photonic crystal", *Physical Review E - Statistical Physics, Plasmas, Fluids, and Related Interdisciplinary Topics*, vol. **60**, pp. 1030-1035, 1999.

[20] Y. A. Vlasov, M. O'Boyle, H. F. Hamann and S. J. McNab, "Active control of slow light on a chip with photonic crystal waveguides", *Nature*, vol. **438**, pp. 65-69, 2005.

[21] M. Notomi, K. Yamada, A. Shinya, J. Takahashi, C. Takahashi and I. Yokohama, "Extremely large group-velocity dispersion of line-defect waveguides in photonic crystal slabs", *Physical Review Letters*, vol. **87**, pp. 253902/1-4, 2001.

[22] X. Letartre, C. Seassal, C. Grillet, P. Rojo-Romeo, P. Viktorovitch, M. Le Vassor D'Yerville, D. Cassagne and C. Jouanin, "Group velocity and propagation losses measurement in a single-line photonic-crystal waveguide on InP membranes", *Applied Physics Letters*, vol. **79**, pp. 2312-2314, 2001.

[23] K. Daikoku & A. Sugimura, "Direct measurement of wavelength dispersion in optical fibres-difference method", *Electronics Letters*, vol. **14**, pp. 149-151, 1978.

[24] K. Hosomi, T. Fukamachi, T. Katsuyama and Y. Arakawa, "Group delay of a coupled-defect waveguide in a photonic crystal", *Optical Review*, vol. **11**, pp. 300-302, 2004.

[25] S. Ryu, Y. Horiuchi and K. Mochizuki, "Novel chromatic dispersion measurement method over continuous Gigahertz tuning range", *Journal of Lightwave Technology*, vol. **7**, pp. 1177-1180, 1989.

[26] W. Bogaerts, P. Bienstman, D. Taillaert, R. Baets and D. De Zutter, "Out-of-plane scattering in 1-D photonic crystal slabs", *Optical and Quantum Electronics*, vol. **34**, pp. 195-203, 2002.

[27] R. Ferrini, R. Houdre, H. Benisty, M. Qiu and J. Moosburger, "Radiation losses in planar photonic crystals: two-dimensional representation of hole depth and shape by an imaginary dielectric constant", *Journal of the Optical Society of America B-Optical Physics*, vol. **20**, pp. 469-478, 2003.

[28] S. J. McNab, N. Moll and Y. A. Vlasov, "Ultra-low loss photonic integrated circuit with membrane-type photonic crystal waveguides", *Optics Express*, vol. **11**, pp. 2927-2939 2003.

[29] M. Loncar, D. Nedeljkovic, T. P. Pearsall, J. Vuckovic, A. Scherer, S. Kuchinsky and D. C. Allan, "Experimental and theoretical confirmation of Bloch-mode light propagation in planar photonic crystal waveguides", *Applied Physics Letters*, vol. **80**, pp. 1689-1691, 2002.

[30] D. J. W. Klunder, F. S. Tan, T. Van der Veen, H. F. Bulthuis, G. Sengo, B. Docter, H. J. W. M. Hoekstra and A. Driessen, "Experimental and numerical study of SiON microresonators with air and polymer cladding", *Journal of Lightwave Technology*, vol. **21**, pp. 1099-1110, 2003.

[31] D. B. Hunter, M. E. Parker and J. L. Dexter, "Demonstration of a continuously variable true-time delay beamformer using a multichannel chirped fiber grating", *IEEE Transactions on Microwave Theory and Techniques*, vol. **54**, pp. 861-867, 2006.

[32] J. T. Hastings, M. H. Lim, J. G. Goodberlet and H. I. Smith, "Optical waveguides with apodized sidewall gratings via spatial-phase-locked electron-beam lithography", *Journal of Vacuum Science & Technology B*, vol. **20**, pp. 2753-2757, 2002.

[33] J. F. Lepage & N. McCarthy, "Analysis of the diffractional properties of dual-period apodizing gratings: theoretical and experimental results", *Applied Optics*, vol. **43**, pp. 3504-3512, 2004.

[34] D. Wiesmann, C. David, R. Germann, D. Emi and G. L. Bona, "Apodized surface-corrugated gratings with varying duty cycles", *IEEE Photonics Technology Letters*, vol. **12**, pp. 639-641, 2000.

[35] L. Xuhui, C. Xiangfei, Y. Yuzhe and X. Shizhong, "A novel apodization technique of variable duty cycle for sampled grating", *Optics Communications*, vol. **225**, pp. 301-305, 2003.

[36] H. G. Winful, "The meaning of group delay in barrier tunnelling: A re-examination of superluminal group velocities", *New Journal of Physics*, vol. **8**, pp. 101/1-16, 2006.

[37] Olympios, "OlympIOs Integrated Optics Software," C2V, http://www.c2v.nl/software/.

[38] C. De Angelis, F. Gringoli, M. Midrio, D. Modotto, J. S. Aitchison and G. F. Nalesso, "Conversion efficiency for second-harmonic generation in photonic crystals", *Journal of the Optical Society of America B-Optical Physics*, vol. **18**, pp. 348-351, 2001.

[39] M. L. Povinelli, S. G. Johnson and J. D. Joannopoulos, "Slow-light, band-edge waveguides for tunable time delays", *Optics Express*, vol. **13**, pp. 7145-7159, 2005.

[40] D. Yudistira, H. Hoekstra, M. Hammer and D. Marpaung, "Slow light excitation in tapered 1D photonic crystals: Theory", *Optical and Quantum Electronics*, vol. **38**, pp. 161-176, 2006.

[41] P. V. Lambeck, "Integrated optical sensors for the chemical domain", *Measurement Science & Technology*, vol. **17**, pp. R93-R116, 2006.

4.4 Transmission scanning near-field optical microscopy for resonance probing

Abstract— In order to model transmission scanning near-field microscopy (T-SNOM) experiments, we study the interaction between a nanosized AFM-type probe and the optical field in a microcavity at or near resonance. Using a 2-dimensional cross-sectional model of an experimentally studied photonic crystal (PhC) microcavity (MC) we have simulated the T-SNOM method by scanning a probe over the surface while monitoring the transmitted and reflected power. The simulations were performed for two probe-materials: silicon and silicon-nitride. From the probe-induced change in the transmission and reflection spectra, a wavelength shift was extracted. A shift almost proportional to the local field intensity was found if the resonator was excited just below a resonance wavelength. However, at the spots of highest interaction, we observed besides the desired resonance wavelength shift, an increase in scattering. Furthermore, by moving the probe at such a spot in the vertical direction to a height of approximately 0.5 μm, a 5 % increase in transmission can be established because the anti-resonant condition is satisfied. Finally, a 2-dimensional top view simulation is presented of the experimentally studied T-SNOM method, which shows a remarkably good correspondence in intensity profile, except for the exact location of the high interaction spots.

This section has been accepted for publication:
W. C. L. Hopman, R. Stoffer and R. M. de Ridder, "High resolution measurement of resonant wave patterns by perturbing the evanescent field using a nanosized probe in a transmission scanning near-field optical microscopy configuration", Accepted for publication in IEEE journal of lightwave technology, April 2007.

4.4.1 Introduction

Scanning near-field optical microscopy (SNOM) has contributed substantially to the understanding of the effect of local geometrical features on the properties of integrated optical devices. Before, the only available method was to study a device by its reflection, transmission or scattered power. If some unexpected behavior was observed, only simulations and a great deal of experience could be used to find an explanation for the observed phenomena. With the introduction of SNOM and all it variants it became possible to visualize the nature of the optical modes in some photonic structures. An overview on the existing SNOM related methods can, for example, be found in [1-2] and the references therein. In present silicon-based photonics, the dimensions of optical structures have shrunk down to the micrometer regime, i.e., sub-micrometer features are used. One of the SNOM methods to visualize light in these devices is photon scanning tunneling microscopy (PSTM) also sometimes referred to as near-field scanning optical microscopy (NSOM). This method has been exploited successfully on silicon on insulator (SOI) photonic crystal structures [3-5], which in principle are designed with periodicities around 0.5 μm and hole sizes around 0.25 μm. For example, the method has recently been used to show slow light in W3 waveguides (i.e., 3 holes left out), dispersion characteristics of photonic crystals, and whispering gallery modes in microring resonators [4-6]. The disadvantage of this method and most other SNOM methods is that they cannot be used to map the resonance wave pattern in a high quality factor (Q) cavity. The reason for this is that the probe interferes too strongly with the cavity resonance; its contribution to the transfer function cannot easily be extracted from the measured signal. Both apertureless SNOM (a-SNOM, see, for example, [7]) and PSTM have this limitation because the aperture of the PSTM fiber tip has to be large enough in order to tunnel light into the probe, and for apertureless SNOM the size of the probe should be large enough to be able to detect the scattered light. Another type of SNOM has recently been introduced [8] to map out the wave-pattern inside a photonic crystal (PhC) microcavity (MC). This method uses the change in the transmitted optical power due to a local perturbation by a dielectric nanosized atomic force microscopy (AFM) probe, for mapping out the wave pattern inside a PhC MC. The method was later [9] termed transmission-based SNOM (or TraNSOM), but will be referred to as simply transmission-SNOM (T-SNOM) in this article. It has been shown that PhC MC resonances can be very sensitive to perturbations by nanoprobes [8], [10], [11]. In [8] it was suggested that the patterns found by the T-SNOM method performed on a PhC MC were related to the local intensity of the PhC resonance. It was assumed that the dielectric tips mainly induced a shift in resonance wavelength. However, at the spots where the highest interaction was observed, also a change in Q was observed, which could be explained from the extra out-of-plane scattering that is locally induced by the probe. In this paper, we present a cross-sectional model, i.e., a waveguide grating modeled in longitudinal cross-section, to verify these assumptions. After a brief description of the PhC MC and the primary measurement results in section 4.4.2, we present in section 4.4.3.1 the main model and the modeling method used in this paper. The model deals with a thin (50 nm) silicon nitride (Si_3N_4) or silicon (Si) tip that is scanned over the surface of the grating, while the transmitted, reflected and scattered powers are monitored simultaneously for each tip position. The analyses of these results are also presented in section 4.4.3.1, and the quality and practical use of the T-SNOM method will be briefly discussed. In section 4.4.3.2 we will show that besides imaging, the tip can also have the effect of suppressing the out-of-plane scattering, resulting in higher transmitted powers. The T-SNOM method as presented here is found to rely mainly on a shift in resonance wavelength. This is verified by modeling the probe as a local increase in refractive index in a 2-dimensional top view simulation performed on the PhC MC, as presented in section 4.4.3.3. The main conclusions are finally summarized in section 4.4.4.

4.4.2 Device and measurements

The experiments reported in this section were performed on a MC integrated in a slab-type 2-dimensional PhC in SOI (220 nm device layer thickness on 1 μm of buried oxide, see Figure 4.4-1a) with hole diameters of 270 nm arranged in a triangular lattice with 440 nm period. A Fabry-Perot-like cavity having a length of about 2 μm was formed by placing two holes on each side of the cavity in a PhC waveguide.

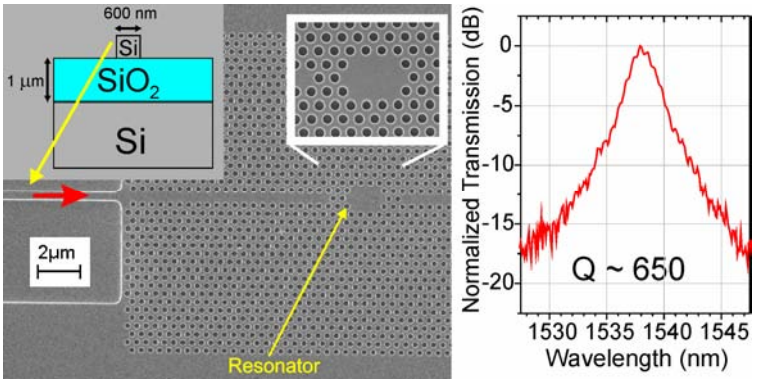

(a) (b)

Figure 4.4-1: (a) A SEM photo of the fabricated photonic crystal microcavity showing the magnification of the resonator and a schematic drawing of the layer stack in the insets. (b) The measured transmission spectrum of the PhC MC.

W1 waveguides were used (i.e., one row of holes left out) as input and output waveguides for the resonator. The W1 PhC waveguides were connected with photonic wires having a width of 600 nm for single TE-mode operation for wavelengths around 1550 nm. The structure as shown in the SEM photo in Figure 4.4-1a, was fabricated (at IMEC, Belgium) using a process [12] involving deep UV lithography (λ = 248 nm) and reactive ion etching. A resonance wavelength of approximately 1.538 μm, see Figure 4.4-1b, was measured for this PhC MC. This high-finesse cavity has a Q of about 650.

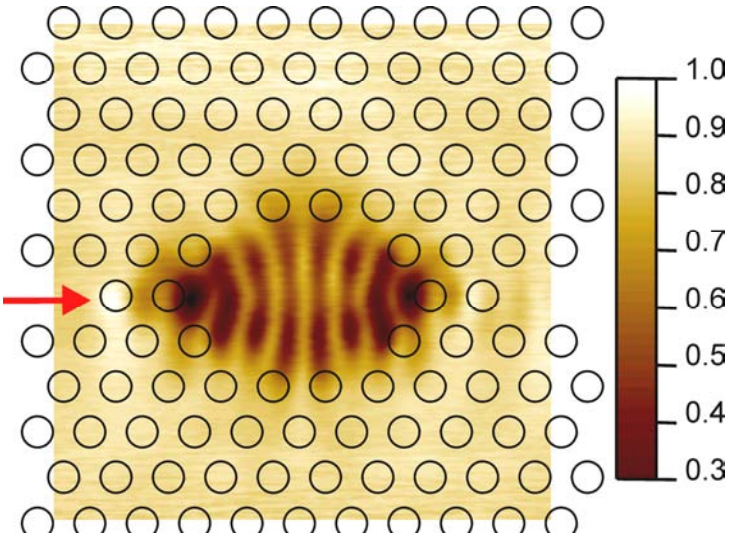

Figure 4.4-2: A demonstration of the T-SNOM technique. The measurement was performed in contact mode (at the resonance wavelength) using a scanning probe AFM with a Si_3N_4-probe. The red arrow indicates the propagation direction of the incident wave. The holes have been overlaid according to the position and sizes obtained from the AFM topography signal.

Using the T-SNOM technique with a nanosized dielectric AFM-probe, the location of the interaction pattern can be found by plotting the measured transmission versus the (2-D) tip position within the topography obtained from the cavity region. The result of the T-SNOM experiment performed at the resonance wavelength is shown in Figure 4.4-2. A mask has been overlaid with sizes and positions according to the data obtained from the AFM height signal. To obtain this well-defined map we used a sharpened Si_3N_4 tip. Eight maxima can be observed with two distinct darker spots at the start and end of the cavity; the first most pronounced location (at the entrance of the cavity) is called the "hot spot" here. The measurement shows clearly that the high-interaction spots are located inside the cavity, right next to the terminating holes. A more detailed description of the measurement setup and mapping results can be found in [8].

4.4.3 Modeling methods

To establish a better interpretation of the experiments described above, two-dimensional simulations have been performed. In section 4.4.3.1, the side view of a comparable cross-section is studied; in section 4.4.3.3, the top view is considered instead. When a silicon nitride or silicon tip is brought in close proximity to a defect-cavity within a grating, i.e., perturbing the resonator with a probe, the transmission and reflection of the resonator change. The interaction may lead to a shift in resonance wavelength and an increase or even decrease in scattering, depending on the height of the probe above a field-maximum in the cavity, as will be shown in section 4.4.3.2. The amount of perturbation caused by the probe is expected to be related to the local field intensity of the unperturbed resonator; the following subsections will show simulations to clarify this point.

4.4.3.1 Cross-sectional model

The structure simulated in this section is a resonator formed by a defect in a two-dimensional waveguide grating, using the same material stack as the measured device discussed in the previous section. The grating periods and pitches were chosen to obtain a resonance near the resonance wavelength of the measured structure. The model is shown in Figure 4.4-3.

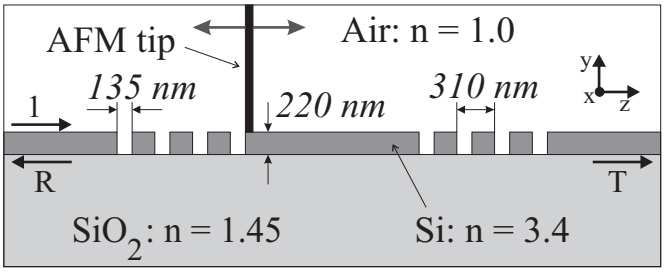

Figure 4.4-3: Structure used in side view simulations. The black tip is either a silicon or silicon nitride tip that is scanned across the surface of the defect grating. The length of the central defect is 1.515 μm.

The simulation method used is the quadridirectional eigenmode propagator (or QUEP) [13]. It divides the structure into vertical slices and horizontal layers, and connects slab modes of these slices and layers such that the four boundaries of the computational window are transparent for outgoing radiation, while still allowing influx of light through the waveguides. It is a method that is fast for single-wavelength calculations; however, to calculate a spectrum one needs to do calculations for each wavelength of interest.

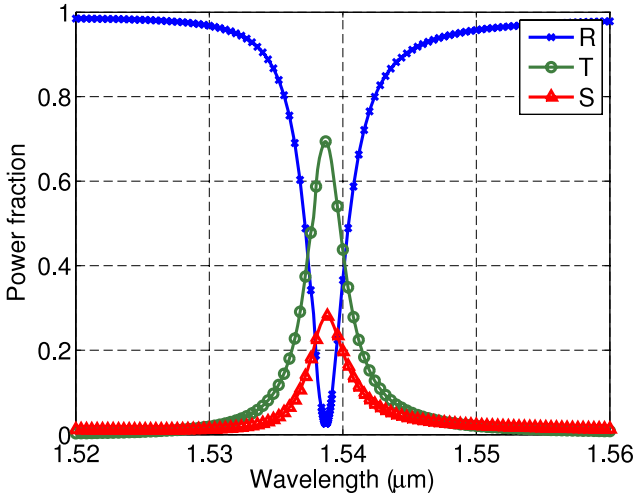

Figure 4.4-4: Simulated spectrum of unperturbed resonator showing about 70 % transmission (T), 3 % reflection (R) and 27 % scattering (S = 1 – T – R) at the resonance wavelength (λ_r = 1.5388 μm).

The spectral response of the unperturbed resonator for TE polarization is shown in Figure 4.4-4. It shows a pronounced Lorentzian-shaped resonance near λ_r = 1.5388 μm, where the transmission rises to about 70 % and the reflection drops to about 3 % and the remainder goes into scattering. For the experiments discussed next, we tune the wavelength either to resonance (λ_r) or slightly off-resonance at λ_s = 1.5376 μm. Performing the T-SNOM measurements slightly off-resonance (preferably half-way the slope of the response curve) has the advantage of higher sensitivity to the presence of the AFM tip because the wavelength-derivative of the transfer function is approximately at a maximum there. Furthermore, as will become clear later in this subsection, the good linear approximation to this steep slope that holds around λ_s turns out to be convenient for calculating the intensity profile in the resonator from the T-SNOM data.

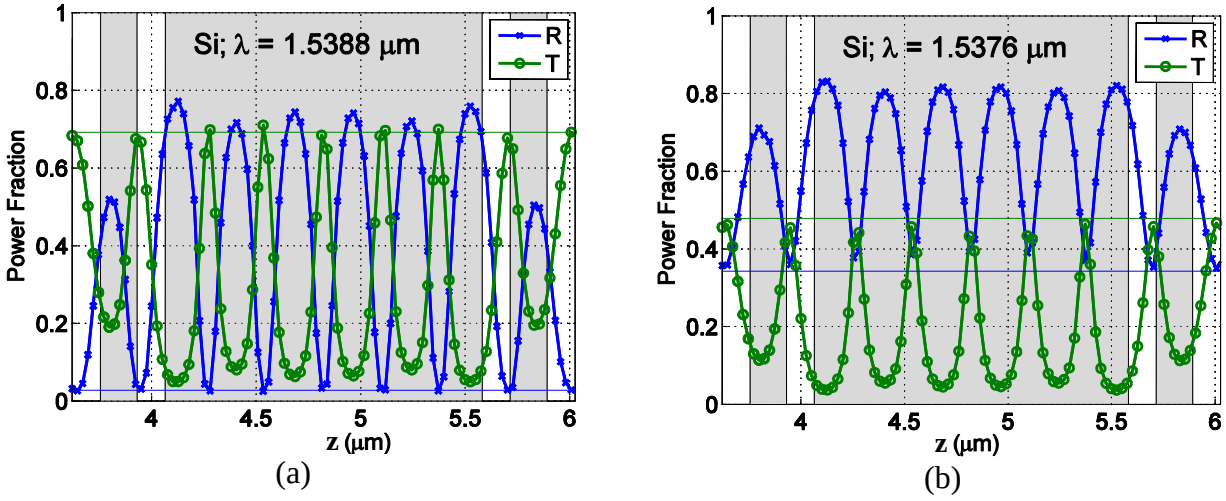

Figure 4.4-5: Simulated power transmission and reflection for a 50-nm-wide semi-infinitely long silicon tip (probe) scanned over the cavity. The vertical white bands at both sides of the cavity indicate the positions of the holes, c.f. Figure 4.4-3. (a) At the resonance wavelength, λ_r. (b) Slightly off resonance, λ_s.

A long, rectangular-shaped silicon (Si, n = 3.4) or silicon nitride (Si_3N_4, n = 2.0) tip having a width of 50 nm is scanned across the surface of the structure. The scan-path of the tip is chosen exactly parallel to the waveguide surface; it is in contact with the top of the waveguide, but it does not drop into the air holes. Figure 4.4-5 shows the reflection and transmission for a silicon tip, at the two wavelengths λ_r and λ_s. At λ_r we find a maximum modulation in the transmission of about 11

dB, and for λ_s = 1.5376 μm we find a maximum modulation of about 10 dB. If the only effect of the perturbation by the dielectric probes would be a shift of the spectrum, the changes in reflection and transmission could be directly related to a shift of the resonance wavelength by correlating them with the spectrum in Figure 4.4-4, as was suggested in [8]. The estimated wavelength shift derived from the transmission curve in Figure 4.4-4 is shown in Figure 4.4-6.

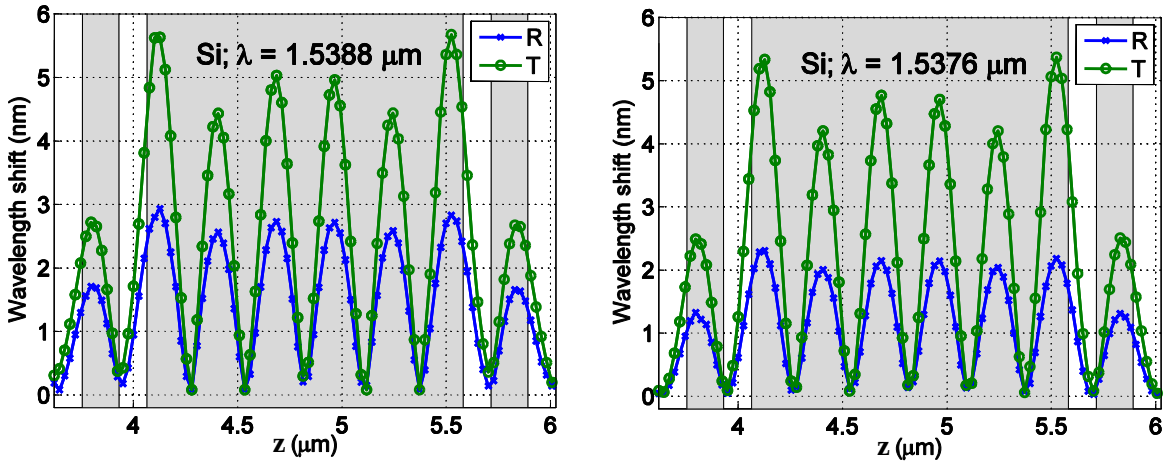

(a) (b)

Figure 4.4-6: Estimated wavelength shift as a function of silicon tip position, calculated by correlating either the transmission T or the reflection R to the unperturbed spectrum in Figure 4.4-4. (a) Wavelength tuned on-resonance (λ_r). (b) Wavelength tuned off-resonance (λ_s).

Figure 4.4-6 shows that the silicon tip perturbs the spectrum in a slightly different way than just a wavelength shift: if the spectrum would only experience a fixed shift without additional scattering, both curves, calculated using reflection and using transmission would yield the same wavelength shift. As an example, in Figure 4.4-7 we show the spectrum with the tip at the top of the highest disturbance (z = 4.12 μm): the "hot spot".

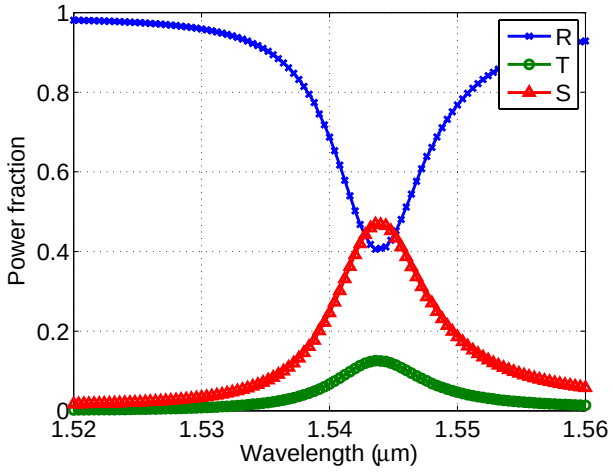

Figure 4.4-7: The spectrum of the grating perturbed by a Si tip at the position of strongest interaction (z = 4.12 μm): "the hot spot". An increased amount of scattering (c.f. Figure 4.4-4) is observed with the tip at the hot spot, which agrees with the result found in [11] and [14].

Even though the spectrum is strongly perturbed by the presence of the tip at the hot spot (compare Figure 4.4-4 and Figure 4.4-7), the wavelength shifts, calculated from transmission and reflection spectra still show the same behavior. Their magnitude is different, but the shape is almost exactly equal and the locations of maxima and minima match very well. The results for simulations at λ_r

and λ_s only show a small difference in the magnitude of the calculated wavelength shift. From Figure 4.4-8 it can be seen that this shape correlates with the unperturbed intensity of the resonance at the surface of the resonator. Both Figure 4.4-8a and Figure 4.4-8b show the estimated wavelength shift and the intensity ($|E|^2$) at the tip location, where the intensity is scaled such that the curves overlap well. These figures show that the estimated wavelength shift (calculated from the transmission curve) and the local intensity of the unperturbed resonator do indeed correlate well. Moreover, these simulations reproduce the experimentally observed feature (Figure 4.4-2), that the hot spots are located inside the cavity and not inside the cavity terminating holes.

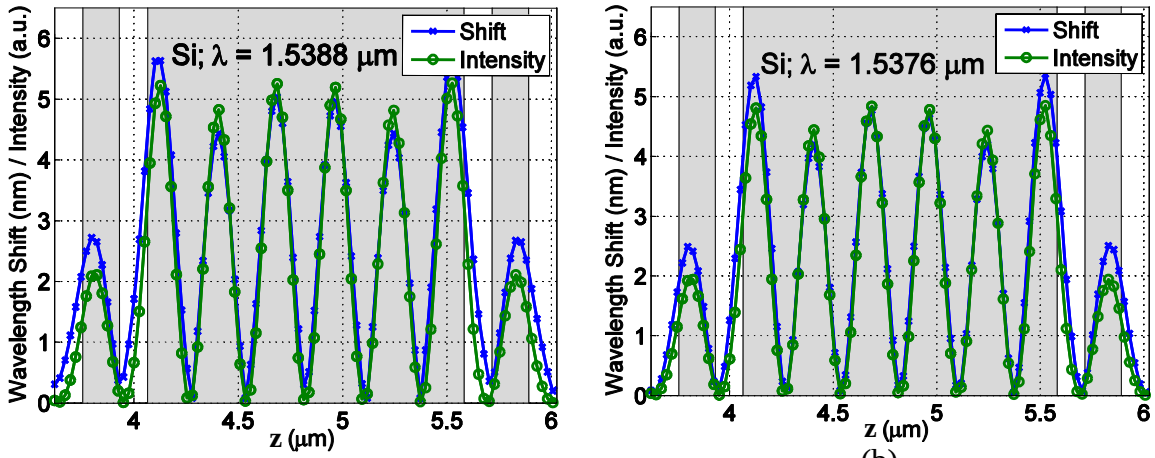

Figure 4.4-8: Estimated wavelength shift from transmission calculation and (on the same axis) local unperturbed intensity at the silicon tip position. The intensity (at the surface) is scaled to yield good visual correspondence between the curves. Some differences are observed only at the first and last field-maximum in the resonator and the maximum outside the resonator, caused by probe-induced scattering. (a) λ_r = 1.5388 μm. (b) λ_s = 1.5376 μm.

For the silicon nitride tip, the same procedure can be followed. The perturbance is smaller and thus also the wavelength shift of the resonator; moreover, the spectrum is not deformed as strongly. The unperturbed intensity (at the surface) and the apparent wavelength shift for both wavelengths are shown in Figure 4.4-9. A similar correlation is found for λ_s = 1.5376 μm as for the Si probe presented in Figure 4.4-8a and Figure 4.4-8b. However, for the wavelength tuned to the resonance wavelength (λ_r = 1.5388 μm) we observe a larger difference between the wavelength shift and the local intensity. This is because the spectrum is flat at the top of the curve, so the calculated wavelength shift could not be accurately determined. The optimum T-SNOM operating point is found at the wavelength where the second order derivative is equal to zero. Obviously, when a probe with a medium or low refractive index is used, as, for example, the Si_3N_4 probe, the choice for the operation wavelength becomes more important.

The good resemblance between the observed wavelength shifts and the intensity can be explained from the well-known [15] variation theorem, which relates a small change in dielectric constant (ε) to a small change in the effective index (N_{eff}). For a dielectric waveguide at a given wavelength, it can be written as:

$$\Delta N_{eff} = \frac{c}{P} \iint_{\infty} \Delta\varepsilon(x,y)\mathbf{E}(x,y)\cdot\mathbf{E}^{*}(x,y)dxdy, \qquad (1)$$

where c is the speed of light in vacuum, E is the modal field, and P is the power carried by the mode. Equation (1) shows that the strongest effect on N_{eff} can be expected at the locations of modal field maxima. In this form the theorem holds only for waveguides with a constant cross-section, so it may be safely applied only to the cavity region (not in the holes). A further condition

for validity is a small probe size and/or a small $\Delta\varepsilon$ (hence small Δn). It is questionable whether other probes like the metallic ones used in [9] satisfy this criterion.

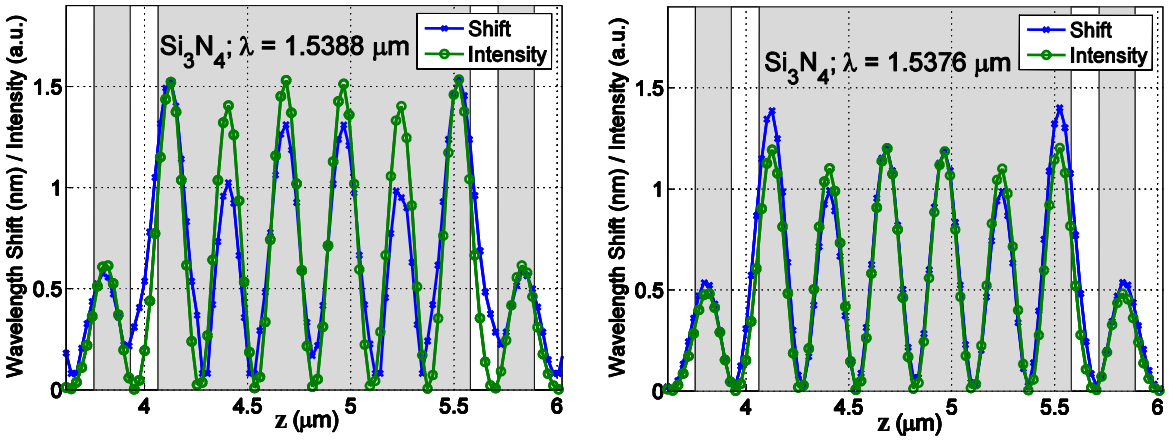

Figure 4.4-9: Estimated wavelength shift from transmission calculation and local unperturbed intensity at the silicon nitride tip position. (a) λ_r = 1.5388 μm. (b) λ_s = 1.5376 μm.

In conclusion, these 2-D side-view simulations indicate that the T-SNOM method can be exploited for mapping of the local intensity of the grating-resonator by looking up the wavelength shifts from the transmission spectrum of the unperturbed resonator. The method only requires measuring the transmission spectrum of the unperturbed system and recording the reflected or transmitted signal while a nanosized (AFM) tip is scanned across the surface of the resonator-cavity.

4.4.3.2 Height scan

A decrease in the magnitude of the perturbation can be obtained by placing the silicon tip at the hot spot of the resonator in resonance, at z = 4.12 μm, and moving it in the upward direction y. The result of this simulation is given in Figure 4.4-10. Besides this decrease in interaction, we also observe oscillations on the transmission graph. Moreover, at approximately a tip height y = 0.5 μm a maximum in transmission is found which is larger than the maximum transmission without tip, i.e., the transmission is now about 75 % instead of the 70 % found without the presence of a tip. Since the oscillations are of periodic nature as can be seen in the figure, the extra cavity between the resonator and the tip gives rise to this oscillation.

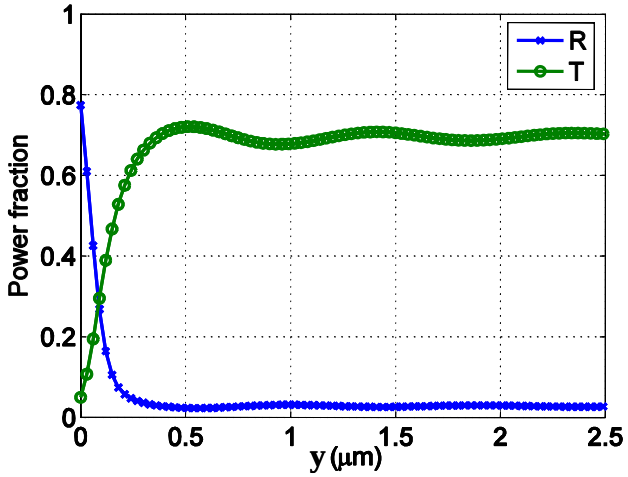

Figure 4.4-10: As the tip is placed at the hot spot (z = 4.12 μm) and the wavelength is set to λ_r = 1.5388 μm, the transmission and reflection are calculated as the tip is moved vertically. At approximately a tip height y = 0.5 μm the first maximum in transmission is found which is larger than the maximum transmission without tip.

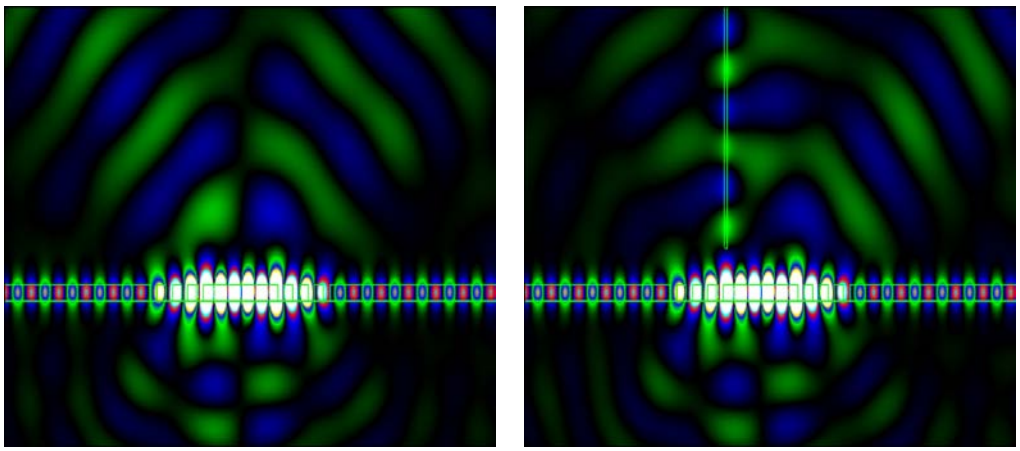

(a) (b)

Figure 4.4-11: (a) Modeled field distribution at the resonance wavelength λ_r. From the figure we derive an angle θ between the normal to the surface and the radiated beam of about 35 degrees. (b) With the tip at y = 0.5 μm above the surface, the disturbed field pattern shows partial suppression of the out-of-plane scattering.

Two characteristic field distributions are shown in Figure 4.4-11. Without the presence of the probe (Figure 4.4-11a), we find two radiation directions above the grating (in air), having an angle θ of about +35 and –35 degrees with respect to the normal of the waveguide plane. With the probe at height y = 0.5 μm, the radiation is partially suppressed (Figure 4.4-11b). If the scattered light is reflected at the probe and coupled into the guiding layer again, the following relation has to be satisfied for the anti-resonance (Bragg) condition,

$$y = \frac{\lambda(1+2m)}{4\cos(\theta)}, \qquad m \in \mathbb{N}. \tag{2}$$

Using this relation, we find the first maximum at $y \approx 0.5$ μm and the second one at $y \approx 1.4$ μm, in good agreement with the values found in Figure 4.4-10. These scattering suppression results are based on the same principle as is applied in hollow core waveguides [16] or 2.5 dimensional photonic crystals [17] where the periodicity in the third dimension can, for example, be formed by omni-directional Bragg-mirrors. Our results show that with a small nanosized probe located at the hot spot, the transmission can be increased by 5 %. Even larger values can be achieved when the size of the material on top (here the probe) is increased or when a multilayer is added to avoid the apparent leakage of light through the probe, see Figure 4.4-11b.

4.4.3.3 2-D top view model

In 4.4.3.1, we showed that the intensity distribution inside a resonator could be measured indirectly by perturbation of the electric field by a dielectric probe. We found that the predominant effect of the probe is to cause a shift of the resonance wavelength, and that only at the hot spot an increase in scattering was observed when the probe is in contact. This suggests the possibility of a kind of effective-index approximation of the PhC MC shown in Figure 4.4-2, where the influence of "a probe" is modeled by a local increase of the refractive index. In this case we have defined a square of 120 by 120 nm that simulates the probe by a local increase of the refractive index. A grid size of 40 nm was chosen to speed up the calculations that were performed using a finite difference time domain (FDTD) code. The refractive index values to be used in the 2-D approximation of a PhC slab have been chosen in such a way that the wavelength of the calculated standing-wave pattern matches the experimental observation, leading to n_{slab} = 2.9 and n_{hole} = 1. The top view simulations were performed such that the *E*-field was in the plane of the simulation (top view, see Figure 4.4-12), and *H*-field was perpendicular to it. In a standing wave situation, the major *E*-field component has an antinode where the major *H*-field component has a node. Figure 4.4-12 shows

the intensity $|E|^2$ in the unperturbed structure for a wavelength at resonance, excited from the left. The major difference apparent from this graph, with the measurement that was presented in Figure 4.4-2, is in the locations of the hot spots; in the measurements we found these locations to be right next to the two terminating holes and not inside them. This difference can possibly be attributed to the restriction enforced by the 2-D nature of the calculations. The use of a full 3-D model, like in [18], is needed to reach a better agreement in wave-patterns.

As mentioned above, we modeled the probe by an area in which the refractive index is increased by a fraction of the original index. To find the amount of refractive index units (RIU) to add to this square of 120 by 120 nm, we first obtained the resonance with a *Q* of about 350 by tuning of the hole radius and refractive indices. The *Q* value is important for the speed of the numerical experiment, since a large *Q* would require a large simulation time for each probe position. Next, the needed increase in RIU was determined by positioning the rectangle on the hotspot found in Figure 4.4-12, and by varying the index increase of the probe-square to obtain a similar resonance wavelength shift as observed in the measurements. We found that an index increase in this square region of 0.2 RIU was sufficient. Finally, we conducted a 2-D parameter scan, moving the square over the region outlined by the dashed box in Figure 4.4-13, while mapping the transmitted power. We find a remarkably good agreement between the pattern obtained from the scan and the resonance field distribution from Figure 4.4-12. However, some minor differences are visible, especially at the hole locations. From these modeling results, we conclude that the scanning probe can be modeled well in 2-D (top view) by a region with slightly increased index superimposed on the original structure.

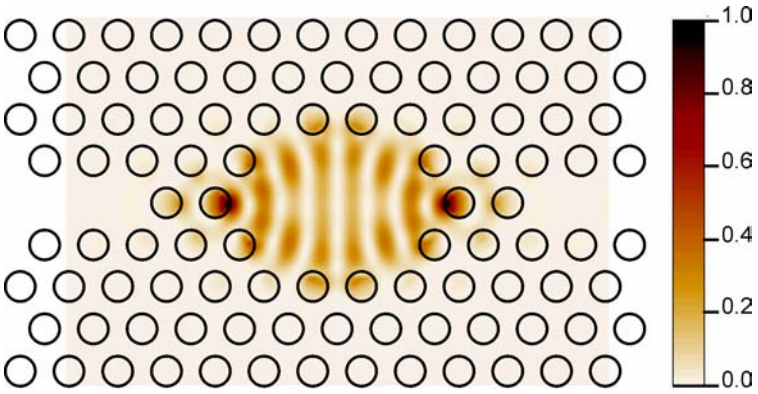

Figure 4.4-12: The standing wave pattern in the unperturbed PhC MC, obtained using a 2-D FDTD simulation method displaying the square of the transverse electrical field $|E|^2$ at the resonance.

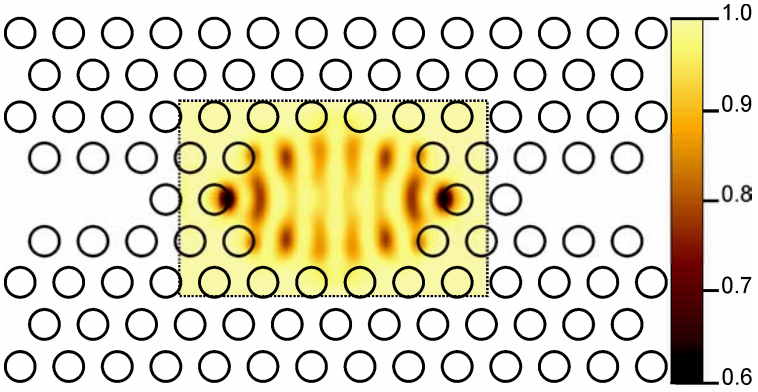

Figure 4.4-13: The 2-D plot of the transmission obtained from a raster scan of a square region with a local refractive index increase of 0.2 RIU over the structure. The size of the square region was 120 by 120 nm, and the simulation grid had a size of 40 nm.

4.4.4 Conclusion

The modeling results as presented in this paper demonstrate that the T-SNOM imaging method can be used to estimate the intra-cavity intensity distribution of the standing wave at the surface of the cavity. Using a 2-D cross-sectional model, calculated using the QUEP method, we found a good agreement between the local field intensity and the simulated T-SNOM values for an operation wavelength just below the resonance wavelength, for both a silicon and a silicon-nitride probe. We also observed that the probe could be used to decrease the out-of-plane scattering by moving it in the vertical direction to a height of about 0.5 μm above the top surface of the structure in our case.

We also used a top-view model for calculating the intensity distribution of the standing wave in the PhC MC using a 2-D FDTD method. We found that this calculated intensity distribution corresponds well to the pattern obtained from the measurements. However, at the hot spots we observed a difference; the simulation suggests that we can find the highest-interaction spots in the cavity-terminating holes, whereas the measurements show that these spots are located right next to these holes. Nevertheless, the simulation results obtained from the cross-sectional model agree with the experimental results that these maxima are located within the cavity and not in the cavity terminating holes.

Furthermore, we have simulated the T-SNOM method also using the top-view model of the PhC MC. The influence of the probe was calculated using a local increase in refractive index. These T-SNOM modeling results also show a good agreement with the original intensity distribution, which confirms the idea that no big error is made by neglecting the probe-induced scattering and assuming the local intensity to be proportional to the probe-induced detuning which is the main effect determining the transmission through the structure. Therefore, we anticipate that the T-SNOM method will be a valuable tool for near-field analyses of air-clad resonators, like, for example, microring resonators, gratings and photonic crystal microcavities.

4.4.5 References

[1] L. Novotny & S. J. Stranick, "Near-field optical microscopy and spectroscopy with pointed probes", *Annual Review of Physical Chemistry*, vol. **57**, pp. 303-331, 2006.

[2] S. F. Wu, "Review of near-field optical microscopy", *Frontiers of Physics in China*, vol. **1**, pp. 263-274, 2006.

[3] M. L. M. Balistreri, J. P. Korterik, G. J. Veldhuis, L. Kuipers and N. F. Van Hulst, "Quantitative photon tunneling and shear-force microscopy of planar waveguide splitters and mixers", *Journal of Applied Physics*, vol. **89**, pp. 3307-3314, 2001.

[4] R. J. P. Engelen, T. J. Karle, H. Gersen, J. P. Korterik, T. F. Krauss, L. Kuipers and N. F. Van Hulst, "Local probing of Bloch mode dispersion in a photonic crystal waveguide", *Optics Express*, vol. **13**, pp. 4457-4464, 2005.

[5] D. J. W. Klunder, M. L. M. Balistreri, F. C. Blom, H. J. W. M. Hoekstra, A. Driessen, L. Kuipers and N. F. Van Hulst, "Detailed analysis of the intracavity phenomena inside a cylindrical microresonator", *Journal of Lightwave Technology*, vol. **20**, pp. 519-529, 2002.

[6] H. Gersen, J. P. Korterik, N. F. van Hulst and L. Kuipers, "Tracking ultrashort pulses through dispersive media: Experiment and theory", *Physical Review E*, vol. **68**, pp. 026604/1-10, 2003.

[7] I. Stefanen, S. Blaize, A. Bruyant, S. Aubert, G. Lerondel, R. Bachelot and P. Royer, "Heterodyne detection of guided waves using a scattering-type Scanning Near-field Optical Microscope", *Optics Express*, vol. **13**, pp. 5553-5564, 2005.

[8] W. C. L. Hopman, K. O. Van Der Werf, A. J. F. Hollink, W. Bogaerts, V. Subramaniam and R. M. De Ridder, "Nano-mechanical tuning and imaging of a photonic crystal micro-cavity resonance", *Optics Express*, vol. **14**, pp. 8745-8752, 2006.

[9] J. T. Robinson, S. F. Preble and M. Lipson, "Imaging highly confined modes in sub-micron scale silicon waveguides using transmission-based near-field scanning optical microscopy", *Optics Express*, vol. **14**, pp. 10588-10595, 2006.

[10] I. Märki, M. Salt and H. P. Herzig, "Tuning the resonance of a photonic crystal microcavity with an AFM probe", *Optics Express*, vol. **14**, pp. 2969-2978, 2006.

[11] M. Hammer & R. Stoffer, "PSTM/NSOM modeling by 2-D quadridirectional eigenmode expansion", *Journal of Lightwave Technology*, vol. **23**, pp. 1956-1966, 2005.

[12] W. Bogaerts, R. Baets, P. Dumon, V. Wiaux, S. Beckx, D. Taillaert, B. Luyssaert, J. Van Campenhout, P. Bienstman and D. Van Thourhout, "Nanophotonic waveguides in silicon-on-insulator fabricated with CMOS technology", *Journal of Lightwave Technology*, vol. **23**, pp. 401-412, 2005.

[13] M. Hammer, "Quadridirectional eigenmode expansion scheme for 2-D modeling of wave propagation in integrated optics", *Optics Communications*, vol. **235**, pp. 285-303, 2004.

[14] E. Flück, M. Hammer, A. M. Otter, J. P. Korterik, L. Kuipers and N. F. Van Hulst, "Amplitude and phase evolution of optical fields inside periodic photonic structures", *Journal of Lightwave Technology*, vol. **21**, pp. 1384-1393, 2003.

[15] H. Kogelnik, "Theory of optical waveguides", *in Guided-wave optoelectronics*, 2nd ed., T. Tamir Ed. Berlin, Germany: Springer-Verlag, 1990, p. 31.

[16] H. P. Uranus, H. J. W. M. Hoekstra and E. Van Groesen, "Considerations on material composition for low-loss hollow-core integrated optical waveguides", *Optics Communications*, vol. **260**, pp. 577-582, 2006.[17] B. Ben Bakir, C. Seassal, X. Letartre, P. Regreny, M. Gendry, P. Viktorovitch, M. Zussy, L. Di Cioccio and J. M. Fedeli, "Room-temperature InAs/InP Quantum Dots laser operation based on heterogeneous "2.5 D" Photonic Crystal", *Optics Express*, vol. **14**, pp. 9269-9276, 2006.

[18] A. F. Koenderink, R. Wuest, B. C. Buchler, S. Richter, P. Strasser, M. Kafesaki, A. Rogach, R. B. Wehrspohn, C. M. Soukoulis, D. Erni, F. Robin, H. Jackel and V. Sandoghdar, "Near-field optics and control of photonic crystals", *Photonics and Nanostructures-Fundamentals and Applications*, vol. **3**, pp. 63-74, 2005.

4.5 Nanomechanical interaction with a photonic crystal microcavity

Abstract— We show that nanomechanical interaction using atomic force microscopy (AFM) can be used to map out mode-patterns of an optical microresonator with high spatial accuracy. Furthermore we demonstrate how the Q-factor and center wavelength of such resonances can be sensitively modified by both horizontal and vertical displacement of an AFM tip consisting of either Si_3N_4 or Si material. With a silicon tip we are able to tune the resonance wavelength by 2.3 nm, and to set Q between values of 615 and zero, by expedient positioning of the AFM tip. We find full on/off switching for less than 100 nm vertical, and for 500 nm lateral displacement at the strongest resonance antinode locations.

This section has been published:
W. C. L. Hopman, K. O. Van Der Werf, A. J. F. Hollink, W. Bogaerts, V. Subramaniam and R. M. De Ridder, "Nano-mechanical tuning and imaging of a photonic crystal micro-cavity resonance", Optics Express, vol. 14, pp. 8745-8752, 2006.

4.5.1 Introduction

Nanomechanical interactions with the evanescent field of photonic crystal (PhC) microcavities (MCs) enable tuning of important resonator properties such as quality-factor (Q) and resonance wavelength. The fabrication of high-Q silicon-on-insulator (SOI) based PhCs demands sophisticated nanometer-scale-precision [1-3], and has driven the search for alternative resonator tuning strategies. These include using heaters to achieve thermo-optic tuning [4,5], and pore infiltration by liquids [6], polymers [7] or liquid crystals [8] to achieve a broad tuning range. The progress in micrometer-scale integrated optics has led to an increase in attention for mechanical tuning [9-12]. Mechano-optical interactions have been utilized in, for example, sensor [13] and actuator [14] applications to modulate the evanescent field. Two types of interaction can be effected, namely, changing the modal amplitude through the attenuation constant (leaking or scattering of light, which can been used for scanning near-field microscopy [15]), or changing its phase through the phase constant (changing the effective refractive index). In traditional mechano-optical approaches, the size of the object placed in the evanescent field is much larger than the optical wavelength [14] to obtain a sufficiently large phase shift while avoiding strong attenuation. In this case, boundary effects causing out-of-plane scattering can be neglected. However, if we use a resonant cavity that provides a strongly enhanced field in a small volume (that is, a high quality factor to modal volume ratio Q/V [16]), then an object as small as 10 nm in close proximity to the resonator can strongly affect the transfer properties [17,18]. Although the analysis of nanomechano-optical transduction is more involved than that of the classical configuration, we demonstrate that it also offers many more opportunities for manipulation of light. We explore this manipulation experimentally in great detail using a high Q/V microcavity in a photonic crystal slab.

4.5.2 Design and realization

For the experiments reported here, we designed a PhC MC in SOI (220 nm device layer thickness on 1 μm buried oxide) with a triangular lattice of periodicity a = 440 nm and a hole radius r = 270 nm. We chose a relatively large cavity, designed to have a resonance near 1550 nm wavelength, and a medium Q-factor of 650 with a high finesse to have a good wavelength separation of adjacent resonances. In principle, the MC could be made smaller and optimized for high Q [19], but this is not needed due to the strong interaction of the probe with the cavity resonance. The Fabry-Pérot-type cavity is defined in a W1 line-defect waveguide (1 row left out), providing optical access for transmission measurements. We calculated the resonant field distribution using a finite-difference time-domain method. Although accurate modeling requires full 3-D calculations [20] and consequently high computer resources, we relied on (fast) 2-D calculations, which have been qualitatively validated by a 3-D calculation. The pattern shows 8 fringes with two distinct major peaks in the field amplitude within the resonator, close to the entrance and exit of the cavity (see Figure 4.5-1a). One may expect that a disturbance at these two peaks will have the largest effect on two essential resonance properties: central resonance wavelength and Q.

The structure as shown in the SEM photo in Figure 4.5-1b, was fabricated (at IMEC, Belgium) using a process [21] involving deep UV lithography (λ = 248 nm) and reactive ion etching. The resonance wavelength $\lambda_{r,0}$ of the fabricated cavity was measured to be 1539.25 nm.

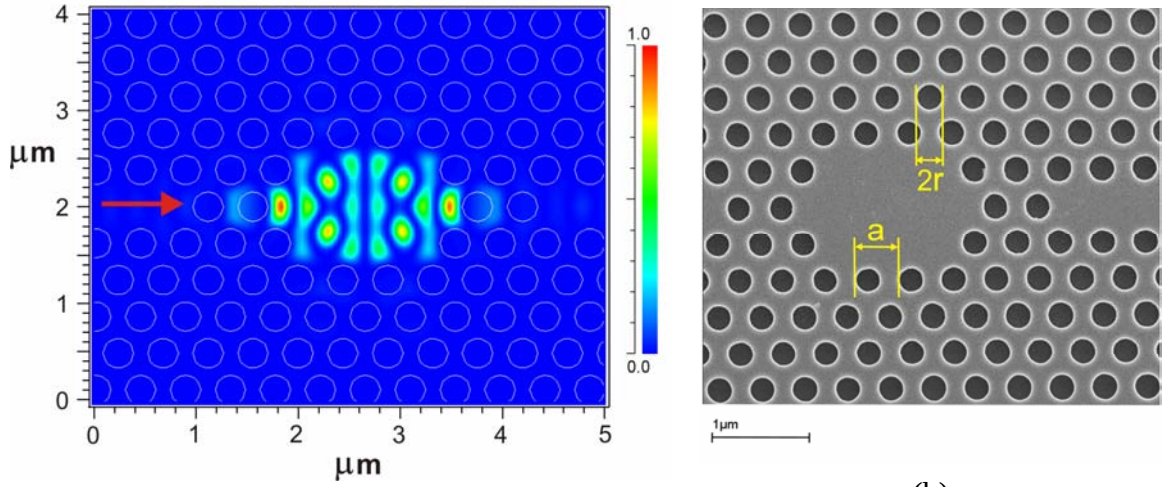

(a) (b)

Figure 4.5-1: Photonic crystal microcavity. (a) Computed optical field intensity of the resonant mode pattern. The arrow indicates the launching direction of light exciting the resonator. (b) SEM image of the microcavity. The period and hole radius are denoted with a and r respectively.

4.5.3 Measurement principle and imaging results

To bring a nanosized object in the field of the resonator in a controlled way, we combined a typical optical end-fire transmission setup with a stand-alone scanning tip AFM stage [22] (Figure 4.5-2a). For our first experiments we selected an AFM tip that is expected to have a relatively small impact on optical loss, by choosing a small size (minimum radius 10 nm) and a low-loss material Si_3N_4, with a refractive index (n_{Si3N4} ~ 2) lower than the effective index of the guided mode in the photonic crystal waveguide (n_{eff} ~ 2.9). By raster scanning the AFM probe over the sample in contact mode and closed loop operation, we obtained both geometrical and optical transfer information from the AFM deflection data (Figure 4.5-2b) and the power recorded by the photodetector (Figure 4.5-2c) simultaneously. The scanning speed was kept sufficiently low to prevent artifacts caused by the limited photodetector response time. Acquisition of a typical 256 x 256-pixels image revealing all important details took about 45 s. We chose a 20 nm interpixel grid distance, resulting in a scanning window size of 5.2 x 5.2 micrometers. However, grid sizes as small as 1 nm or less can be selected when needed. By combining both the deflection and optical transmission data, the exact locations of strong interaction of the probe with the optical field in the cavity can be visualized, as shown in Figure 4.5-2d, where the topographic data has been enhanced in order to improve the visibility of the holes. The figure shows how the transmitted optical power is affected by the tip through both detuning the cavity and causing scattering loss [17]. A simple intuitive model, taking into account only the tuning effect, predicts a decrease in transmitted optical power if the source wavelength λ_s is set to a value smaller than the undisturbed resonance wavelength $\lambda_{r,0}$, because the resonance wavelength λ_r is shifted further away from λ_s (to longer wavelengths). Conversely, if λ_s is longer than $\lambda_{r,0}$, an increase in transmitted power will be detected (moving up the transmission-wavelength curve of the resonance). Note, however, that this model is rather simplified (see section 4.4), an issue addressed experimentally below.

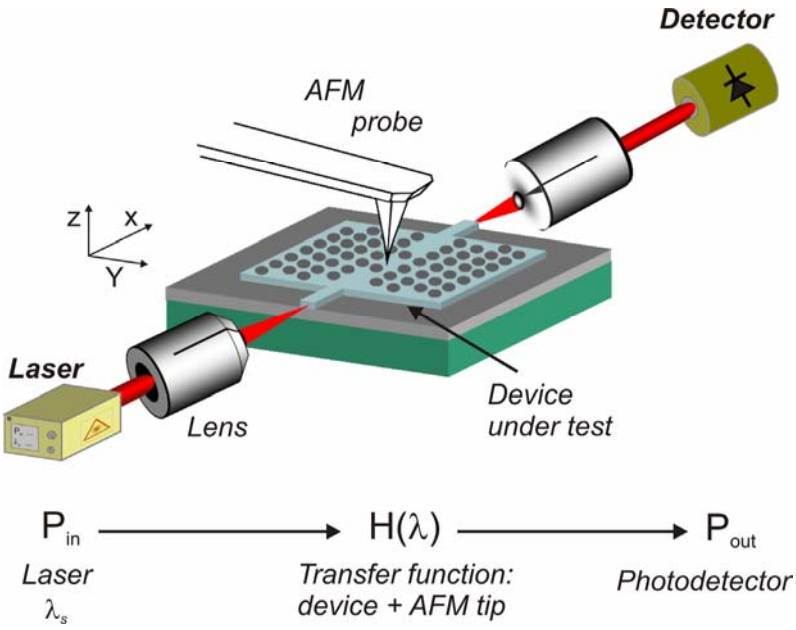

(a)

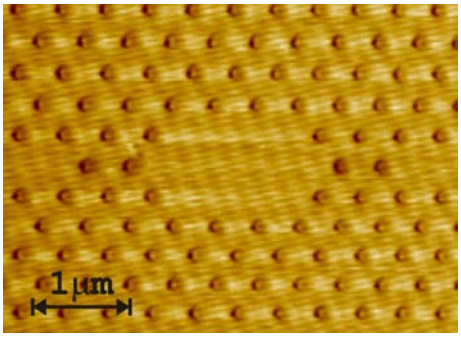

(b)

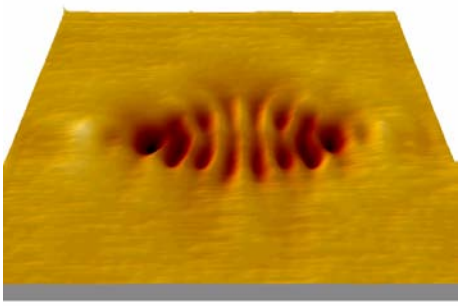

(c)

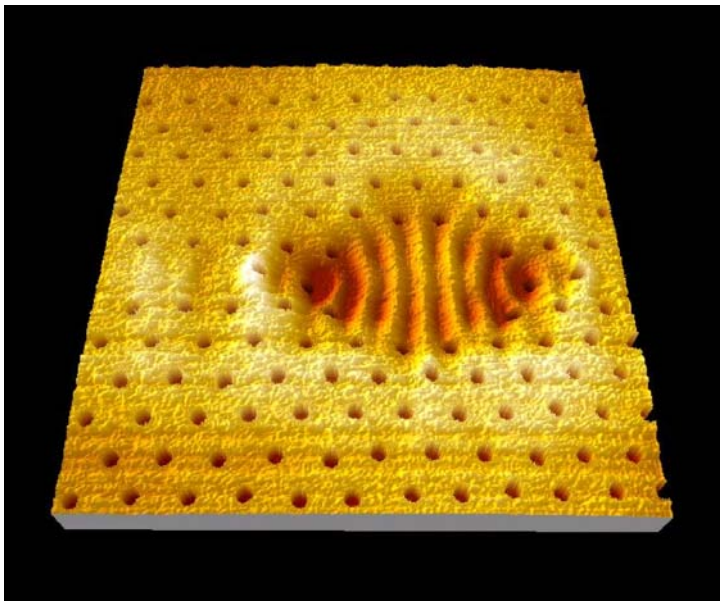

(d)

Figure 4.5-2: Setup and optical field mapping using AFM. (a) Schematic drawing of the setup. (b) Geometry of the photonic crystal microcavity + input waveguide as obtained by conventional AFM probing in a raster scan. (c) Transmitted optical power recorded for each (grid) position of the scanning AFM tip. (d) Enhanced AFM image overlaying the optical detector data resulting in a precise map of the locations of maximum probe-field interaction, corresponding to amplitude peaks of the resonance pattern within the cavity.

Comparison of Figure 4.5-2d and Figure 4.5-1a shows that that the method can be used to find the maximum field locations of a cavity resonance. Moreover it proves that these locations are indeed the “hottest spots” for tuning [17,18] as predicted by the simulations (Figure 4.5-1a).
We have further used this innovative method of visualizing the resonator properties to study the wavelength dependent cavity disturbance. Figure 4.5-3a shows the transmission result for $\lambda_s = \lambda_{r,0}$ which confirms the expected decrease in power transmission at the locations of field maxima in the cavity.

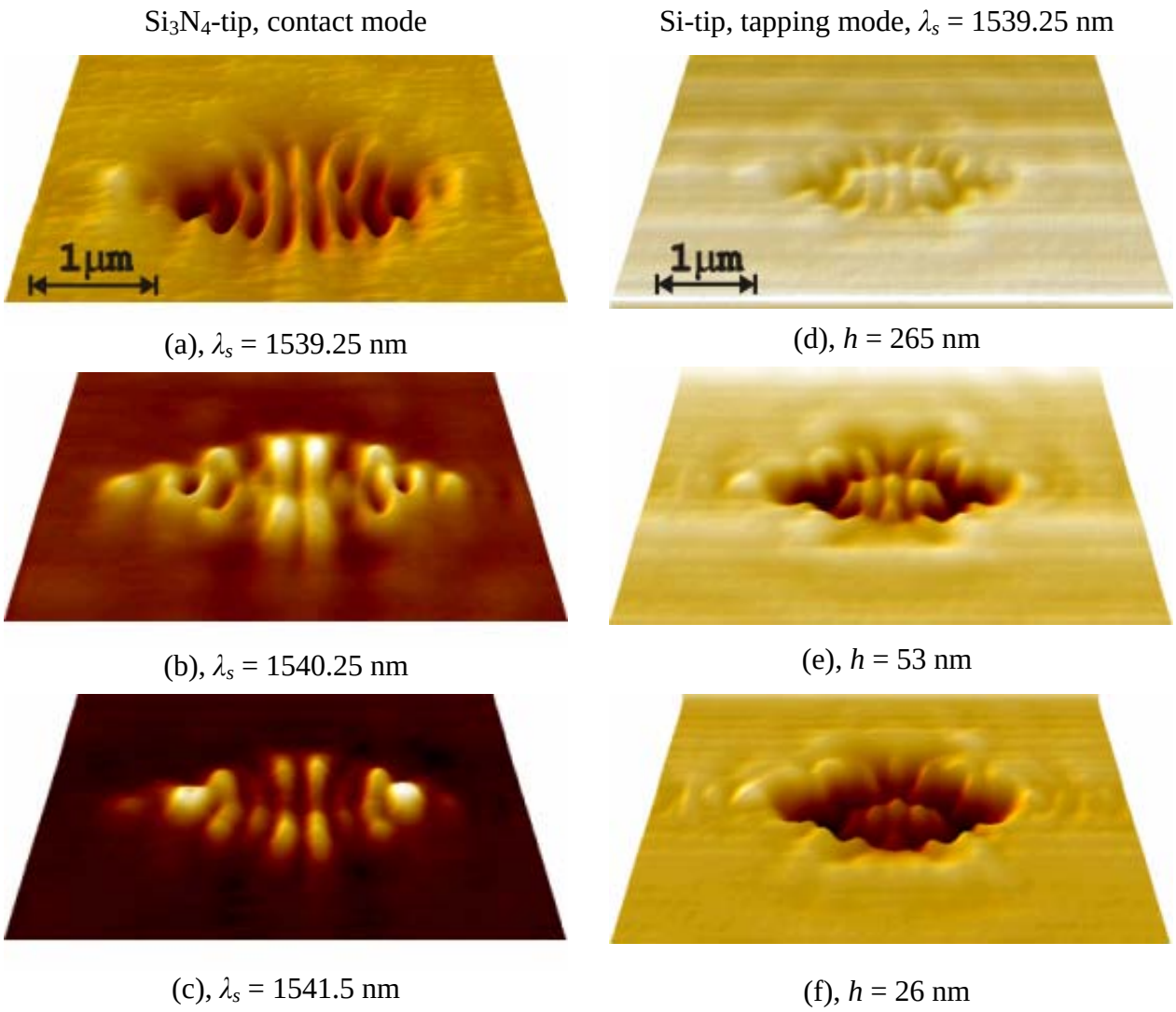

Figure 4.5-3: Quasi-3-D representations of the position dependent probe effect on the transmission. Figs. 3(a)-3(c): Si_3N_4 probe in contact mode at different wavelengths λ_s; Figs. 3(d)-3(f): Si tip in tapping mode with different tapping amplitudes resulting in different average probe heights (h). (a) At resonance (λ_s =1539.25 nm ~ $\lambda_{r,0}$), showing lower transmission (dark regions) near antinodes of the optical field. (b) λ_s slightly larger than $\lambda_{r,0}$. (c) λ_s ~ $\lambda_{r,0}$, showing the inverse pattern of figure 3a. (d) Si tip, tapping mode, large average height has small optical effect. (e), (f) Smaller average heights give larger optical effects.

For λ_s slightly larger than $\lambda_{r,0}$ we find an interesting complex pattern, shown in Figure 4.5-3b, with reduced transmission at some probe locations and increased transmission at others. This complex pattern can be explained by the wavelength dependence of each extreme in the MC on the resonance wavelength shift and induced loss. Increasing λ_s further to a value larger than $\lambda_{r,0}$, we find the inverse image of Figure 4.5-3a, as shown in Figure 4.5-3c.

4.5.4 Cavity tuning method and results

A stronger response can be expected when the Si_3N_4 tip is replaced by a Si one, due to its much larger refractive index (n_{Si} ~ 3.45). We used a Si tip with minimum radius of only 7.5 nm. In order to explore the height dependence of the mechano-optical interaction, we used the AFM in tapping mode. By adjusting the tapping amplitude we obtained control of the average height (in time) above the surface. The very high sensitivity of transmission to the average tip height is shown in Figure 4.5-3d-Figure 4.5-3f. Another advantage of tapping mode is that the tip wears out at a much lower pace compared to contact mode.

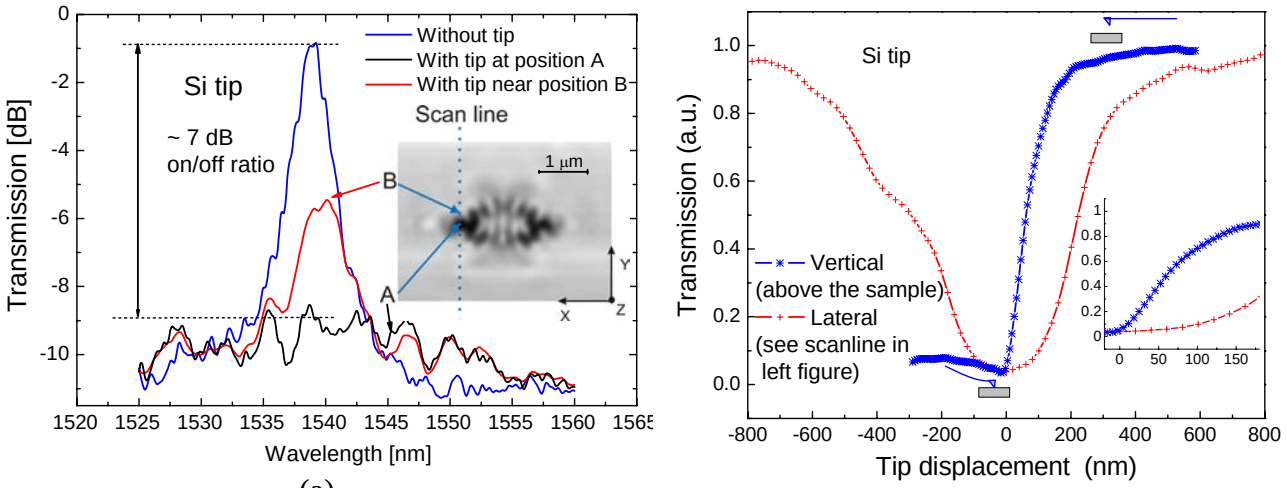

Figure 4.5-4: Nanomechanical interaction. (a) Transmission spectra for the situation without probe, and with a Si probe positioned at the antinode labeled A, and at a location B close to A, as indicated in the inset. (b) Transmission versus Si tip displacement in the z and y direction, see the dotted "scan line" in the inset of the left figure, $\lambda_s = \lambda_{r,0}$ (note: the figure has been corrected, because there was an error in "vertical" curve: a factor of 2).

After locating the field maxima at resonance in tapping mode, we placed the tip exactly in the middle of the largest maximum at the input side (labeled A in the inset of Figure 4.5-4a), switched to contact mode, and measured the spectrum (Figure 4.5-4a). We found a full drop of about 7 dB in the transmitted power (black curve) for this cavity. After moving the tip to point B, we measured the spectrum again. The new spectrum (red), compared to the undisturbed one (blue) shows a shift in λ_r of about 2 nm and a reduction of Q by a factor of about 2, while the transmission has dropped by ~ 4 dB. To find the exact lateral dependence of the transmitted power (in the y-direction as shown by the dotted line in the inset of Figure 4.5-4a for a wavelength at $\lambda_{r,0}$, we plotted the transmitted power versus vertical tip displacement, see Figure 4.5-4b). The graph shows that the cavity resonance is highly sensitive to tip displacement and can be switched on and off by a lateral tip displacement of about 500 nm.

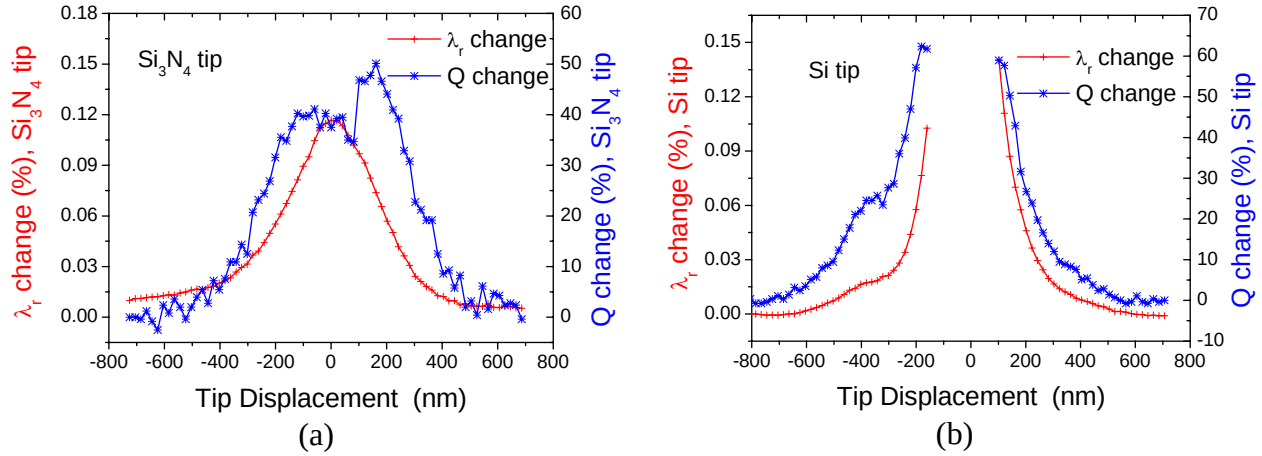

Figure 4.5-5: Nanomechanical tuning. (a) Change of Q and resonance wavelength detuning for a Si_3N_4 probe versus y-displacement along the scan line shown in Figure 4.5-4a. (b) The same but now for a Si tip. In close proximity to the field maximum no data could be obtained because the transmission had dropped below the noise level.

An even stronger effect can be obtained by vertical movement (z-direction) of the probe, as was indicated by the tapping mode experiments shown in Figure 4.5-3d-Figure 4.5-3f. Full on/off

switching can be achieved in only ~200 nm vertical displacement (blue curve in Figure 4.5-4b). The wavelength dependency of each point in the resonator could be found by performing 2-D scans in the XY plane for wavelengths ranging from 1538 nm to 1544 nm with a step of 0.25 nm, using both a Si_3N_4 and a Si tip in contact mode. Using these results, fitted to the expected Lorentzian response, we mapped the shift of the resonance wavelength and the change in *Q* as a function of the displacement from the center position of the antinode. The results for the Si_3N_4 tip are shown in Figure 4.5-5a. A maximum detuning of λ_r by 1.8 nm (0.12 % of λ_s) is found together with a maximum *Q* change of 50 %. The shape of the *Q*-factor curve is less smooth due to the larger uncertainty in the width parameter found by applying the fitting procedure. The experiments with the Si tip show that a further detuning is possible (Figure 4.5-5b). However, for tip positions too close to the field maximum, it was not possible to fit the data because the power had dropped below the noise level, as is also shown by the black curve in Figure 4.5-4a. We found a maximum detuning of λ_r by ~ 2.3 nm (0.15 % of λ_s) and a maximum change of *Q* by 65 %.

4.5.5 Conclusion

In conclusion, we have shown experimentally that an AFM probe can be used to map out the resonance pattern of a PhC MC with, to our knowledge, the highest resolution reported so far. The results show the exciting complex behavior that follows from the interaction of a nanotip with the resonator mode, which is an interesting subject for future theoretical and experimental studies. Furthermore we have shown that the two important parameters (*Q*-factor and resonance wavelength) of a PhC MC can be nanomechanically tuned over a considerable range. The results strongly motivate further exploitation of the tip-resonator mode interaction, which may be used for designing many new complex optical structures, such as a mechano-optically integrated reconfigurable PhC add-drop multiplexer. Another implication of our study is that near-field probing on high *Q* (or bandwidth limited ultra slow light [23]) structures cannot be performed without appreciably changing the optical properties of the device under study (while maintaining the same spatial resolution). Finally we mention that the strong advantage of this tuning is the ability to compensate for inevitable small fabrication errors, i.e., shifting the resonance wavelengths or changing the *Q*-value to the desired values.

4.5.6 Acknowledgements

We thank Edwin Klein, Ronald Dekker and Frans Segerink for discussions and help. This work was supported by NanoNed, a national nanotechnology program coordinated by the Dutch ministry of Economic Affairs, and was also supported by the European Network of Excellence (ePIXnet).

4.5.7 References

[1] D. Gerace & L. C. Andreani, "Effects of disorder on propagation losses and cavity Q-factors in photonic crystal slabs", *Photonics and Nanostructures-Fundamentals and Applications*, vol. **3**, pp. 120-128, 2005.

[2] R. Ferrini, D. Leuenberger, R. Houdre, H. Benisty, M. Kamp and A. Forchel, "Disorder-induced losses in planar photonic crystals", *Optics Letters*, vol. **31**, pp. 1426-1428, 2006.

[3] M. Settle, M. Salib, A. Michaeli and T. F. Krauss, "Low loss silicon on insulator photonic crystal waveguides made by 193nm optical lithography", *Optics Express*, vol. **14**, pp. 2440-2445, 2006.

[4] H. M. H. Chong & R. M. De La Rue, "Tuning of photonic crystal waveguide microcavity by thermooptic effect", *IEEE Photonics Technology Letters*, vol. **16**, pp. 1528-1530, 2004.

[5] Y. A. Vlasov, M. O'Boyle, H. F. Hamann and S. J. McNab, "Active control of slow light on a chip with photonic crystal waveguides", *Nature*, vol. **438**, pp. 65-69, 2005.

[6] W. C. L. Hopman, P. Pottier, D. Yudistira, J. van Lith, P. V. Lambeck, R. M. De La Rue, A. Driessen, H. Hoekstra and R. M. de Ridder, "Quasi-one-dimensional photonic crystal as a compact building-block for refracttometric optical sensors", *IEEE Journal Of Selected Topics In Quantum Electronics*, vol. **11**, pp. 11-16, 2005.

[7] R. van der Heijden, C. F. Carlstrom, J. A. P. Snijders, R. W. van der Heijden, F. Karouta, R. Notzel, H. W. M. Salemink, B. K. C. Kjellander, C. W. M. Bastiaansen, D. J. Broer and E. van der Drift, "InP-based two-dimensional photonic crystals filled with polymers", *Applied Physics Letters*, vol. **88**, pp. 161112/1-3, 2006.

[8] S. F. Mingaleev, M. Schillinger, D. Hermann and K. Busch, "Tunable photonic crystal circuits: concepts and designs based on single-pore infiltration", *Optics Letters*, vol. **29**, pp. 2858-2860, 2004.

[9] A. F. Koenderink, R. Wuest, B. C. Buchler, S. Richter, P. Strasser, M. Kafesaki, A. Rogach, R. B. Wehrspohn, C. M. Soukoulis, D. Erni, F. Robin, H. Jackel and V. Sandoghdar, "Near-field optics and control of photonic crystals", *Photonics and Nanostructures-Fundamentals and Applications*, vol. **3**, pp. 63-74, 2005.

[10] I. Marki, M. Salt and H. P. Herzig, "Tuning the resonance of a photonic crystal microcavity with an AFM probe", *Optics Express*, vol. **14**, pp. 2969-2978, 2006.

[11] T. Takahata, K. Hoshino, K. Matsumoto and I. Shimoyama, "Transmittance tuning of photonic crystal reflectors using an AFM cantilever", *Sensors and Actuators A (Physical)*, vol. **128**, pp. 197-201, 2006.

[12] P. T. Rakich, M. A. Popovic, M. R. Watts, T. Barwicz, H. I. Smith and E. P. Ippen, "Ultrawide tuning of photonic microcavities via evanescent field perturbation", *Optics Letters*, vol. **31**, pp. 1241-1243, 2006.

[13] S. Wonjoo, O. Solgaard and F. Shanhui, "Displacement sensing using evanescent tunneling between guided resonances in photonic crystal slabs", *Journal of Applied Physics*, vol. **98**, pp. 33102/1-4, 2005.

[14] G. N. Nielson, D. Seneviratne, F. Lopez-Royo, P. T. Rakich, Y. Avrahami, M. R. Watts, H. A. Haus, H. L. Tuller and G. Barbastathis, "Integrated wavelength-selective optical MEMS switching using ring resonator filters", *IEEE Photonics Technology Letters*, vol. **17**, pp. 1190-1220, 2005.

[15] I. Stefanon, S. Blaize, A. Bruyant, S. Aubert, G. Lerondel, R. Bachelot and P. Royer, "Heterodyne detection of guided waves using a scattering-type Scanning Near-Field Optical Microscope", *Optics Express*, vol. **13**, pp. 5553-5564, 2005.

[16] M. Notomi, A. Shinya, S. Mitsugi, G. Kira, E. Kuramochi and T. Tanabe, "Optical bistable switching action of Si high-Q photonic-crystal nanocavities", *Optics Express*, vol. **13**, pp. 2678-2687, 2005.

[17] A. F. Koenderink, M. Kafesaki, B. C. Buchler and V. Sandoghdar, "Controlling the resonance of a photonic crystal microcavity by a near-field probe", *Physical Review Letters*, vol. **95**, pp. 153904/1-4, 2005.

[18] M. Hammer & R. Stoffer, "PSTM/NSOM modeling by 2-D quadridirectional eigenmode expansion", *Journal of Lightwave Technology*, vol. **23**, pp. 1956-1966, 2005.

[19] Y. Akahane, T. Asano, B. S. Song and S. Noda, "High-Q photonic nanocavity in a two-dimensional photonic crystal", *Nature*, vol. **425**, pp. 944-947, 2003.

[20] M. Gnan, G. Bellanca, H. Chong, P. Bassi and R. De La Rue, "Modelling of photonic wire Bragg gratings", *Optical and Quantum Electronics*, vol. **38**, pp. 133-148, 2006.

[21] W. Bogaerts, R. Baets, P. Dumon, V. Wiaux, S. Beckx, D. Taillaert, B. Luyssaert, J. Van Campenhout, P. Bienstman and D. Van Thourhout, "Nanophotonic waveguides in silicon-on-insulator fabricated with CMOS technology", *Journal of Lightwave Technology*, vol. **23**, pp. 401-412, 2005.

[22] K. O. Vanderwerf, C. A. J. Putman, B. G. Degrooth, F. B. Segerink, E. H. Schipper, N. F. Vanhulst and J. Greve, "Compact stand-alone atomic-force microscope", *Review of Scientific Instruments*, vol. **64**, pp. 2892-2897, 1993.

[23] H. Gersen, T. J. Karle, R. J. P. Engelen, W. Bogaerts, J. P. Korterik, N. F. van Hulst, T. F. Krauss and L. Kuipers, "Real-space observation of ultraslow light in photonic crystal waveguides", *Physical Review Letters*, vol. **94**, pp. 073903/1-4, 2005.

4.6 AFM tapping mode interaction model verified using a photonic crystal microcavity

Abstract— We present a simple transmission model for estimating the AFM tapping height influences on a photonic crystal microcavity. This model uses a fit of the measured tip-height dependent transmission above the "hot spot" in the microcavity. The prediction for the average tapping height dependent transmission shows good agreement with the values obtained from tapping mode experiments. Furthermore, we show that the transmission can be tuned between 0.32 to 0.8 by varying the average tapping height from 26 to 265 nm. Moreover, when the tip is placed before the holes that terminate the cavity we observe an increase in transmitted power compared to the situation in the absence of the tip.

This section has been submitted for publication:
W. C. L. Hopman, K. O. Van Der Werf, A. J. F. Hollink, W. Bogaerts, V. Subramaniam and R. M. De Ridder, "Experimental verification of a simple transmission model for predicting the interaction of an AFM-probe with a photonic crystal microcavity in tapping mode operation", 2007.

4.6.1 Introduction

Photonic crystal (PhC) microcavities (MC) are key components in sensor, lasing or nonlinear switching applications. More complex device functionalities can be achieved by modeling the photonic crystal design by using, for example, a 3-D finite difference time domain FDTD method to predict its optical response characteristics. Besides the transmission and reflection of a PhC structure, a map of the field inside the PhC can be helpful in experimental studies of device dynamics. Such field maps have been generated by scanning near field optical microscopy (SNOM) [1]. However, for higher quality factor (*Q*) PhC MC, SNOM is less suitable since it interferes with the field inside the cavity. We have recently proposed a novel method to map the influence of nanomechanical interactions with the field within the PhC [2]. The method is based on mapping of the optical transmission while scanning an AFM-probe in contact over a PhC MC. The results show a close agreement with the calculated optical standing wave pattern. The disadvantage of contact mode operation is that the tip (especially when using a Si tip on a Si PhC device) may wear off at a fast rate. To preserve the integrity of fragile (for example, polymer) PhC devices, operating the AFM in the well-known tapping mode [3] would be preferable. However, the response of a PhC MC scanned in tapping mode is more complicated, because the height of the tip is varied in time over the sample, usually at a resonance frequency (in our case 63 KHz) of the cantilever plus tip which is much higher than the scan frequency (around 10 pixels per second). In this paper we show how the response of a PhC MC can be predicted as a function of the tapping amplitude using a simple model and a fit of the measured approach curve (height sensitivity curve). We consider a Fabry-Perot-like MC in a photonic crystal waveguide, as shown in Figure 4.6-1a, and study the manipulation of an optical resonance using a dielectric tip located at a position in close proximity to the MC where the interaction has a maximum [2], the “hot spot”. We first discuss the design and the straight-forward transmission measurement. Next the approach curve is determined experimentally [4]. This result is then fit using an exponentially decaying function and inserted in the model presented here to predict the transmission influenced by a probe in tapping mode. Because we use a slow but sensitive photodetector (HP 8153A) to monitor the transmitted power in our experiments, we focus on the time-averaged transmission (the signal varies with the cantilever frequency of 63 kHz). Finally the predicted transmission as a function of the tapping mode amplitude is compared with the values obtained by choosing 4 different average tapping heights *h*. A good agreement is found between the derived curve and the transmission measured at different tapping amplitudes.

4.6.2 Photonic crystal design & setup

The device used for the experiments is a PhC MC design in SOI (220 nm device layer thickness on 1 μm buried oxide) in a triangular lattice with 440 nm period and 270 nm hole radius. For practical purposes we designed a relatively large Fabry-Perot-like cavity (~ 2 μm) terminated by two holes at each side in a PhC waveguide (see Figure 4.6-1a). This high-finesse cavity has a $Q \sim 650$. This *Q* value was sufficient for our purpose, showing already a strong interaction of the probe with the cavity resonance, although much higher *Q*s and thus interaction can be attained, if needed, by optimizing the cavity design [5].

For feeding the PhC cavity we simply used W1 waveguides (i.e., one row of holes left out). The connecting photonic wires had a width of 600 nm, which ensures single TE-mode operation for wavelengths around 1550 nm. The structure shown in Figure 4.6-1a was fabricated (at IMEC, Belgium) using a process [6] involving deep UV lithography (λ = 248 nm) and reactive ion etching. The resonance wavelength was measured to be 1539.25 nm (Figure 4.6-1b).

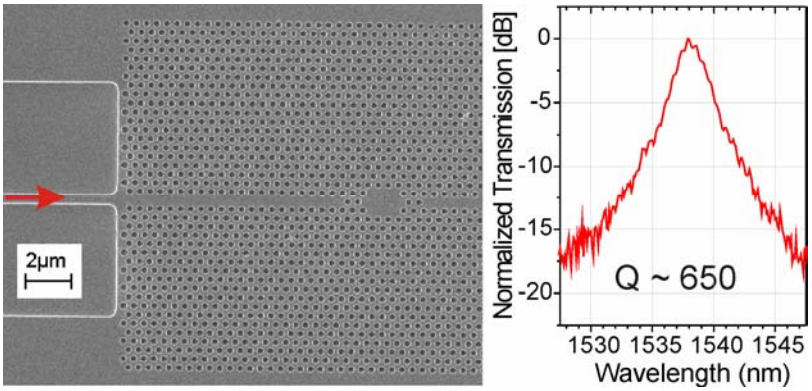

(a) (b)

Figure 4.6-1: (a) A SEM picture of the PhC MC. (b) The corresponding normalized transmission.

The measurement setup was formed by combining a scanning cantilever AFM [7] with a standard end-fire transmission setup for performing the nanomechano-optical experiments. A schematic representation of the setup is shown in Figure 4.6-2.

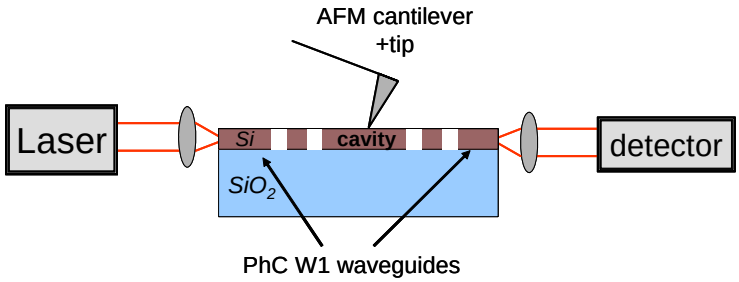

Figure 4.6-2: A schematic representation of the dual-measurement setup.

The AFM could be operated both in contact mode (dragging the tip over the sample) and in tapping mode. The cantilever was driven at its resonance frequency (~ 63 kHz) for tapping mode operation. A raster scan (256 x 256 points) was conducted by scanning the tip over the grid. The height (obtained from the AFM height piezo at constant tapping amplitude) and the optical transmission could be synchronously determined at each raster point. By experiments [2] and modeling it was found that a small silicon nitride probe having a relatively low refractive index n (Si_3N_4, $n \approx 2.0$) can be used to map out the standing wave pattern in a PhC resonator. This can be explained by the local phase shift induced by the probe, which results in a shift of the resonance to higher wavelengths. Because of this shift, a drop in transmitted power can be observed if the laser wavelength remains constant (at the initial resonance wavelength). A silicon (Si, $n \approx 3.5$) probe tip yields an even stronger interaction with the MC, and was also used for the tapping experiments presented here.

4.6.3 Probe height sensitivity & interaction model

First the transmission as a function of the tip height above the sample was determined. This was not conducted in tapping mode, but by lifting the tip and cantilever assembly up and down over a scan line (shown later in Figure 4.6-5) using a saw tooth-shaped vertical movement. The period of the saw tooth signal was chosen to be slightly larger than the time needed to measure a single scan line of 256 points. By repeating the measurement over this scan line for 256 times, we could determine the transmission at the resonance wavelength as a function of the tip height. The difference in periods should be small enough to shift one period over the 256 scanned lines to obtain the full approach curve, i.e., a value for the transmission for a tip height between 0 and ~ 1 μm.

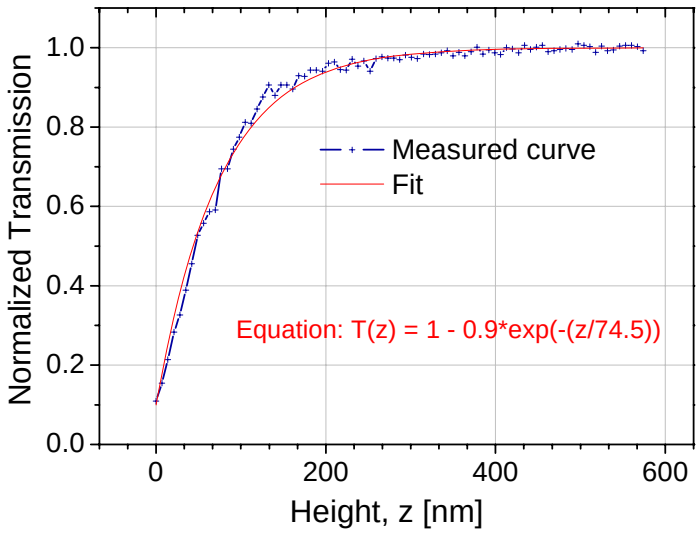

Figure 4.6-3: Measured and fit transmission curve versus the height z of the tip above the sample

The result of this experiment is displayed by the blue (interrupted) curve in Figure 4.6-3. Since the evanescent field decays exponentially outside the resonator, we have chosen to fit the transmission (interaction) curve with a simple exponential decaying function. This fit, characterized by the equation in Figure 4.6-3, is represented by the red (solid) curve. The motion of the tip in tapping mode can be described by a cosine function which gives the tip height z as function of time t and average tip height h:

$$z = h + h\cos(\omega t). \tag{1}$$

This function can be substituted in the fit for the height and time dependent transmission function (approach curve) shown in Figure 4.6-3 to yield

$$T(h,t) = B - A\exp(-(h + h\cos(\omega t)/y)), \tag{2}$$

where A, B and y are constants. The time averaged signal can be calculated as follows,

$$T_{avg}(h) = \frac{1}{T_0}\int_0^{T_0} B - A\cdot\exp(-(h + h\cdot\cos(\omega t)/y))\,dt. \tag{3}$$

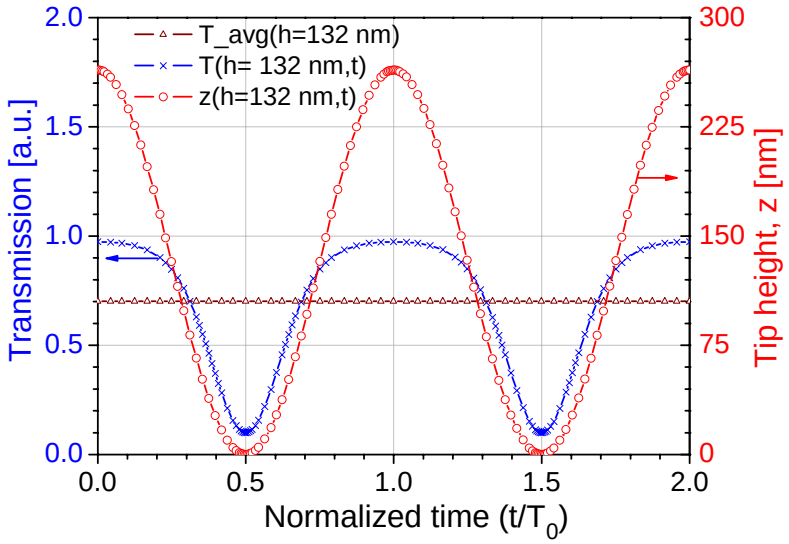

Figure 4.6-4: Results obtained from the model. Blue curve (-x-): transmitted power as a function of the time (t) normalized by the oscillation period (T_0). Red curve (-o-): sinusoidal movement of the tip (y-axis is the height above the sample). Brown (constant) curve (-Δ-): Average transmitted power.

The period of one oscillation of the cantilever plus tip ensemble is denoted by T_0. Since the photodetector used in the measurement is a relatively slow detector having a time constant in the order of milliseconds, $T_{avg}(h)$ was automatically averaged over approximately 100 cycles.
In Figure 4.6-4 we have shown the results obtained using the fit and (1) and (3). As expected for a wavelength at resonance [2], the time-dependent transmission shows a minimum when the tip is in contact with the sample and a maximum when the tip is at its largest distance from the sample. The minimum value was obtained using a contact mode scan.

4.6.4 Verification of the interaction model

A typical image of a tapping-mode experiment at the cavity resonance wavelength is shown in Figure 4.6-5. The dark areas in this two dimensional representation of the transmitted power represent the places where the transmission drops due to the interaction with the tip [2]. For an average tapping height of 53 nm, we find a maximum drop in transmission of ~ 3.5 dB, and for an average tapping amplitude of 26 nm ~ 5 dB (see Figure 4.6-6).

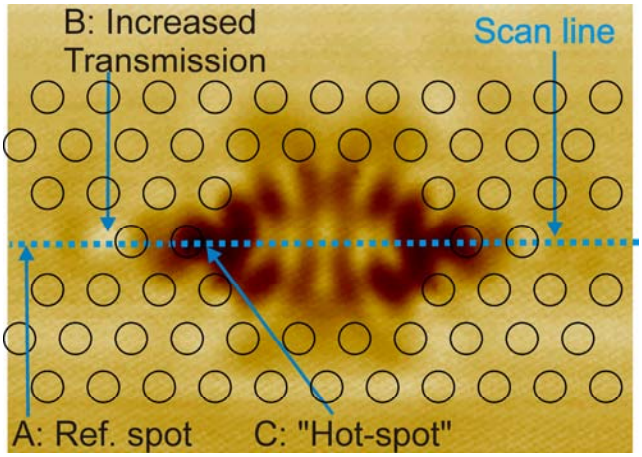

Figure 4.6-5: A 2-D representation of the transmission for h = 53 nm. The mask-layout (black circles) has been overlaid according to the measured AFM height data. The dark spots indicate a drop in transmission, i.e., the cavity is slightly off-resonance for an AFM-tip at the dark spots [14]. The scan line corresponds to the distance axis in Figure 4.6-6.

The scan line used for the tapping experiments presented in Figure 4.6-6 is displayed as the dashed (blue) line in Figure 4.6-5. Four different average tapping heights (1/2 the tapping amplitude) from 26 nm to 265 nm were chosen for verification of the presented model. The transmission was normalized to the transmission at a reference position exhibiting minimum interaction, indicated by *A* in Figure 4.6-5. The transmission in this point was found equal (see Figure 4.6-5) to the transmission found for the tip further outside the cavity and the waveguide. By reading the values at position C (the hot spot), we find the relative transmission for verification with the model at the 4 average tapping heights.
We observe another interesting phenomenon in Figure 4.6-6; just outside the cavity (before the two cavity-terminating holes, at spot *B*), we see an increase in transmission of up to 8 % above the transmission at the low-interaction reference position A. In preliminary simulations we find that two mechanisms may contribute to this effect: more light is coupled into the resonator by better matching of the wave-vector components in the W1 waveguide and the resonator, and/or the probe suppresses out-of-plane scattering at this spot. Further investigations of this effect and additional simulations are shown in section 4.4.

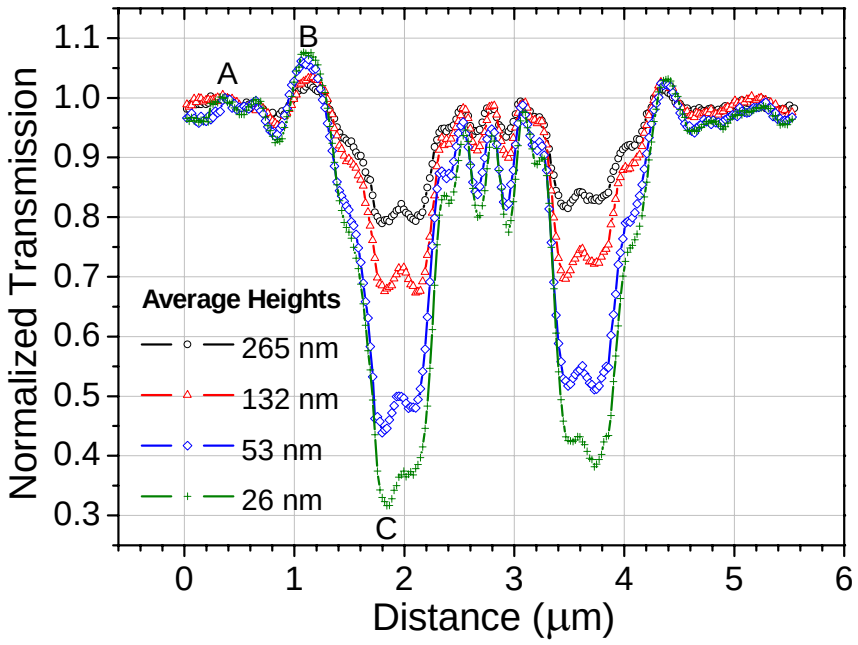

Figure 4.6-6: The measured transmission on the scan line (see Figure 4.6-5), normalized to the value at position A, for 4 different tapping heights.

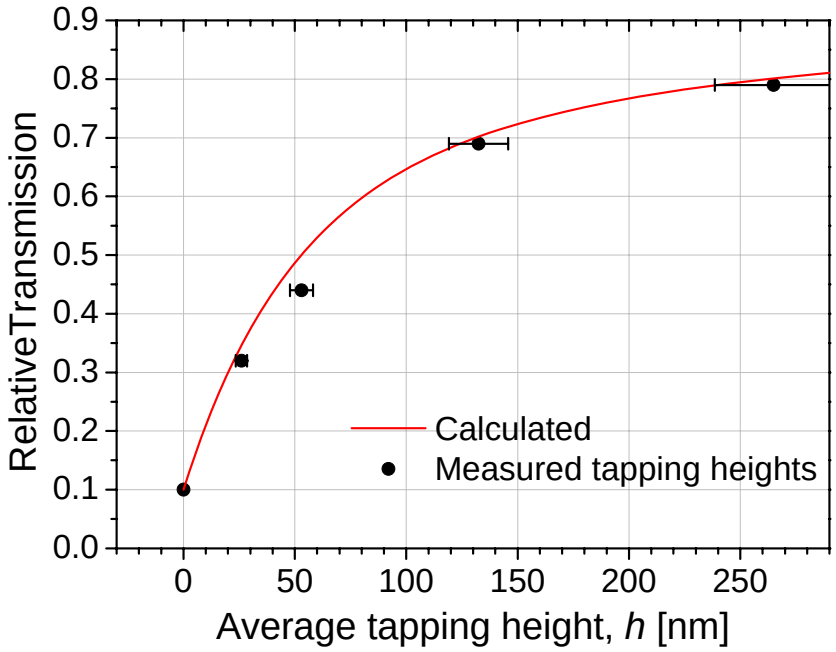

Figure 4.6-7: Comparison between the calculated average tapping-height-dependent transmission curve and the values measured at 5 different tapping amplitudes, obtained from Figure 4.6-6.

In Figure 4.6-7, we show both the results of the calculations and the measurements performed at 4 tapping amplitudes. The calculated curve was obtained from the model by calculating the average transmission as a function of *h* by using the measured approach curve (Figure 4.6-3). We see that the transmission as a function of the average tapping height can well be approximated by the method presented in this paper. The small deviations could be explained by the uncertainty in the initial tapping amplitude of about 10 %, or by the exponential fit, which may not be sophisticated enough for the actual *T(z)* curve, see also reference [8] for a simulated approach curve.

4.6.5 Conclusions

In conclusion we have shown that placing the AFM tip at the spot before the start of the cavity can increase the transmitted power above the level for the resonator without the presence of the AFM tip. Furthermore we have shown a simple and fast way to determine the transmission as a function of the tapping amplitude using a simple model and an approach curve.

4.6.6 Acknowledgements

This work was supported by NanoNed, a national nanotechnology program coordinated by the Dutch ministry of Economic Affairs, and was also supported by the European Network of Excellence (ePIXnet).

4.6.7 References

[1] R. J. P. Engelen, T. J. Karle, H. Gersen, J. P. Korterik, T. F. Krauss, L. Kuipers and N. F. van Hulst, "Local probing of Bloch mode dispersion in a photonic crystal waveguide", *Optics Express*, vol. **13**, pp. 4457-4464, 2005.

[2] W. C. L. Hopman, K. O. Van Der Werf, A. J. F. Hollink, W. Bogaerts, V. Subramaniam and R. M. De Ridder, "Nano-mechanical tuning and imaging of a photonic crystal micro-cavity resonance", *Optics Express*, vol. **14**, pp. 8745-8752, 2006.

[3] I. Märki, M. Salt and H. P. Herzig, "Tuning the resonance of a photonic crystal microcavity with an AFM probe", *Optics Express*, vol. **14**, pp. 2969-2978, 2006.

[4] N. A. Burnham, O. P. Behrend, F. Oulevey, G. Gremaud, P. J. Gallo, D. Gourdon, E. Dupas, A. J. Kulik, H. M. Pollock and G. A. D. Briggs, "How does a tip tap?" *Nanotechnology*, vol. **8**, pp. 67-75, 1997.

[5] Y. Akahane, T. Asano, B. S. Song and S. Noda, "High-Q photonic nanocavity in a two-dimensional photonic crystal", *Nature*, vol. **425**, pp. 944-947, 2003.

[6] W. Bogaerts, R. Baets, P. Dumon, V. Wiaux, S. Beckx, D. Taillaert, B. Luyssaert, J. Van Campenhout, P. Bienstman and D. Van Thourhout, "Nanophotonic waveguides in silicon-on-insulator fabricated with CMOS technology", *Journal Of Lightwave Technology*, vol. **23**, pp. 401-412, 2005.

[7] K. O. Van Der Werf, C. A. J. Putman, B. G. De Grooth, F. B. Segerink, E. H. Schipper, N. F. Van Hulst and J. Greve, "Compact stand-alone atomic-force microscope", *Review of Scientific Instruments*, vol. **64**, pp. 2892-2897, 1993.

[8] A. F. Koenderink, M. Kafesaki, B. C. Buchler and V. Sandoghdar, "Controlling the resonance of a photonic crystal microcavity by a near-field probe", *Physical Review Letters*, vol. **95**, pp. 153904/1-4, 2005.

CHAPTER 5

5 OUTLOOK

Abstract—This chapter provides a selection of the on-going research related to the topics described in this thesis. Some preliminary results on slow light and loss reduction after focused ion beam milling are also included.

5.1 Introduction

A number of fabrication and characterization methods for photonic crystals (PhCs) have been explored in this thesis, they are summarized in chapter 6. Many of the results obtained in this research induced new ideas and or insights. A selection of these research topics are briefly described in the following sections.

5.2 Challenges of focused ion beam processing

As described in chapter 3, focused ion beam (FIB) milling is a versatile tool that can add many useful aspects to the development of PhCs. In contrast to the advantages of focused ion beam milling (see section 3.2 and 3.3), there is also a big challenge in applying FIB milling, namely, to realize low-loss PhCs in Si, because milling causes implantation of Gallium [1]. The implantation of Ga causes huge losses (expressed in dB/μm), due to amorphization and the sharp increase of free charge carriers [2]: Ga+ ions can take sites forming a highly doped semiconductor; the percentage of charge carriers depends on the annealing temperatures [3].
Currently, this subject is being investigated in a joint research activity of the University of Ghent and the University of Twente (ePIXnet, FIB-JRA). After a literature study and some preliminary tests, we found out that the high difference in diffusivity between Ga in Si and Ga in SiO_2 can be exploited for reducing the Ga concentration in the Si core-material [3-6](in a SOI configuration). Annealing at, for example, 800 degrees for an hour can result in a strong decrease in loss [7], which may be attributed to Ga evaporation/diffusion out of the Si core, and repair of the crystal lattice.

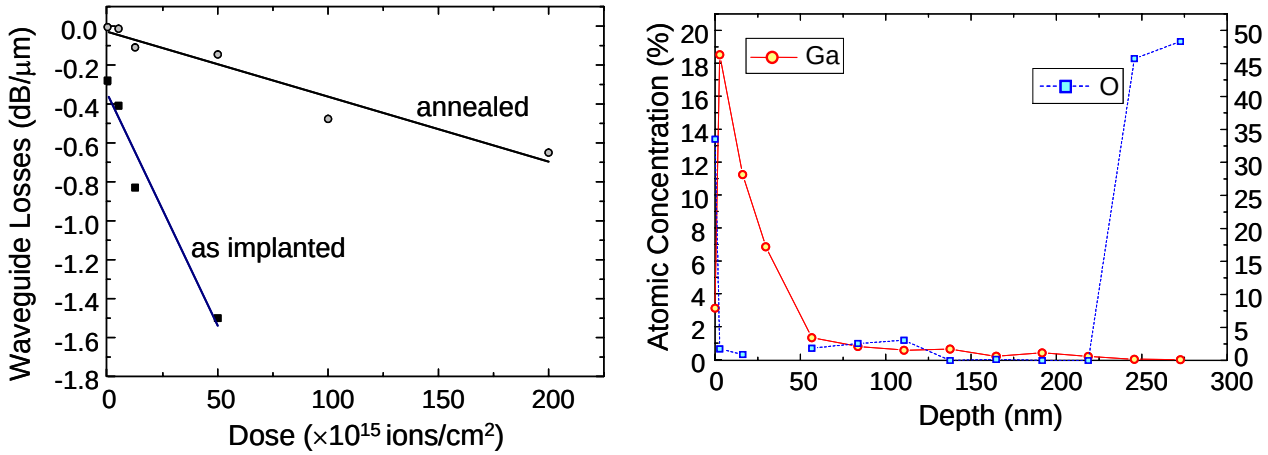

Figure 5.2-1: (a) The measured waveguide loss versus the Ga ion implantation dose for both as-implanted and annealed SOI waveguides. (b) Depth variation of Ga and oxygen atomic concentrations through SOI measured by XPS. The applied dose was 10^{17} ions/cm^2.

Preliminary measurement results show that the optical propagation loss decreases by at least one order of magnitude, see Figure 5.2-1a, which agrees with the results reported in [7]. To find the optimum recipe for lowering the Ga-implantation-related losses, we plan to do simulations of the diffusion process. In parallel we have planned a number of experiments in which we vary the temperature, time, and environment of the annealing process. The implantation profiles before and after annealing are studied using X-ray Photoelectron Spectroscopy (XPS) in Twente, see Figure

5.2-1b for another preliminary result, and Secondary Ion Mass Spectrometry (SIMS) in Ghent. A similar study is also being performed on a ceramic material Al_2O_3, which may help to estimate the ratio between the amorphization and free charge carrier concentration induced losses. Finally, the optimum recipe will be applied to the realization of a relatively low-loss photonic device.

Other promising alternatives for low-loss FIB processing are:

- FIB lithography, i.e. defining a hard mask using FIB milling in combination with existing dry etching methods. To prevent damage to the core layer, an extra sacrificial buffer has to be included, for example a 50 nm Si_3N_4 layer. Figure 5.2-2 shows a top view scattering image obtained from a NIR camera. In the FIB-processed area we don't observe more scattering than in the feeding DUV defined photonic wires. The feeding, DUV defined waveguides, however, were of low quality (some parts of the "output" waveguide were completely destroyed further on the sample), so further characterization by transmission experiments was impossible.
- As mentioned in section 3.3, FIB can well be exploited for the rapid generation of molding templates, which, in combination with imprint technologies [8], can be used to realize low-loss photonic devices.

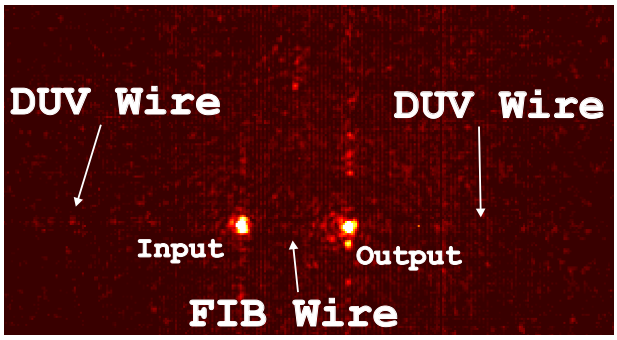

Figure 5.2-2: A top view NIR image of a photonic wire in SOI, defined using "FIB lithography" and RIE milling. An Si_3N_4 sacrificial buffer was used to prevent implantation of Ga into the Si device layer. The wire width and core thickness were 600 nm and 220 nm, respectively.

5.3 Grating sensors

In section 4.3.6, we have claimed that the studied waveguide gratings (WGGs) can be used to detect cladding index changes as small as 10^{-8}, assuming a detection limit of 10^{-4}. The length of the WGGs can be smaller than 1 mm, which makes them suitable for a dense integration (compared to current MZI type sensors) on an optical chip. As shown in section 4.2, the sharp stopband edge can be used for detection.
The next task is to apply, for example, a chemically active mono-layer suitable for detection of, for example, antibodies [9,10]. Furthermore, additional research is needed to integrate WGGs into an array to facilitate multi-sensing purposes.

5.4 Far-field scattering method

The novel far-field scattering method (FScM) presented in section 4.3, was successfully applied to estimate the group indices of a WGG over a relatively large part of the spectrum of interest. It would be interesting to use the FScM also to characterize slow light in (PhC) waveguides. We have preliminary results showing the signs of slow light near the lower frequency edge (see

chapter 2, Figure 2.3-4b). Figure 5.4-1 shows the near infrared (NIR) camera top view images of a 10 micron long W1 PhC waveguides (periodicity 0.5 μm). For a wavelength of 1509 nm, where the transmission sharply declines, we find increased scatter intensity in the W1 waveguides region. Increasing the wavelength to 1560 nm leads to high transmission and almost no scattering in this region, see Figure 5.4-1b. Similar to the slow-light studies described in section 4.3, we can perform a wavelength scan; the scatter intensity as function of wavelength is shown in Figure 5.4-1c. For a slow-light mode, we expect high energy densities within the waveguide, and, as a result, we expect a sharp increase of Rayleigh scattering (due to fabrication inhomogenities). Therefore, the increased scatter intensity may indicate the presence of slow light. However, we should note that the confinement of the W1 mode changes with wavelength. For a less confined mode, a larger part of the optical power may "feel" the fabrication errors. Therefore the analyses of these experiments are more involved than the experiments on the WGGs presented in section 4.3. Another drawback of the PhC W1 waveguides compared to the WGG is the relatively small length, which makes high quality analysis using the NIR camera difficult. Possibly, a PSTM-type measurement could help to resolve the phenomenon with high enough spatial resolution [11,12].

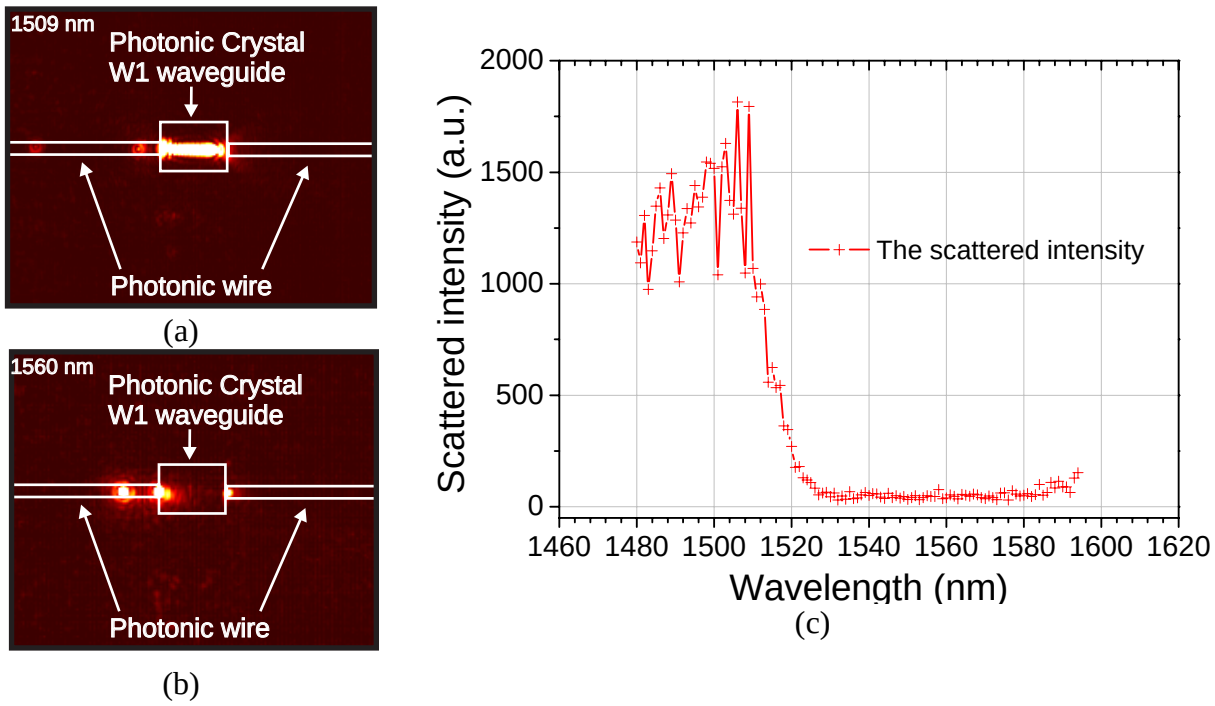

Figure 5.4-1: Measurements performed on a W1 waveguide in a 0.5 μm period 2-D PhC. (a) A top view NIR image for λ = 1509 nm showing a high scatter intensity at the W1 region. (b) A NIR image for λ = 1560 nm. (c) The spectrum of the scatter intensity from the W1 waveguide, collected from a 10-μm-long region, defined between the input and output of the W1 waveguide (these transitions, that generate a high amount of scattering, are excluded from the measurement).

5.5 Transmission-SNOM

In section 4.4 it was shown that the T-SNOM method can be used to image highly confined standing waves within an optical resonator. The measurement presented in section 4.5 showed that the transmission is highly sensitive to the exact location of a nano-sized tip near a "hot-spot" (a field maximum). This relation might be exploited for height or displacement sensing purposes.

The results presented in this thesis on the T-SNOM method and the manipulation of light using nano-probes opens up a whole new area of research. We anticipate that the research on this topic will be continued also by other research groups.

Contact mode T-SNOM should be exploited with care, because it can slightly modify the device under study. Therefore, the study on tapping mode T-SNOM could be important for non-destructive characterization.
At this moment it is not completely clear to which resonator configurations our method can be applied without problems. However, we expect that our method in its present form may yield ambiguous results for degenerate resonators, i.e. resonators with two resonances almost or completely at the same resonance wavelength.

5.6 Transmission-SNOM on a Si microring resonator

In section 4.5 we have shown the result of T-SNOM measurements performed on a PhC microcavity. Similar experiments have been conducted on Si microring resonators (MRRs). The design of the microring resonators is presented in section 2.5. The here discussed MRR has a quality factor of 20.000 at a resonance wavelength of 1573.56 nm which was determined using transmission measurements. The ring dimensions (~ 40×40 μm) exceeded the scan range (20×20 μm) of our AFM scanning probe equipped with a Si_3N_4 tip. Therefore, only part of the microring configuration could be imaged without moving the stage. The wavelength was tuned to the resonance wavelength to obtain the 2-D optical transmission T-SNOM image shown in Figure 5.6-1a. The transmission was measured in the drop port, port IV, see Fig. 2.15. The dark regions reveal a high interaction of the probe with the field inside the microring. An on/off ration of 8 dB was measured by placing the tip in contact exactly on the centerline of the ring waveguide.

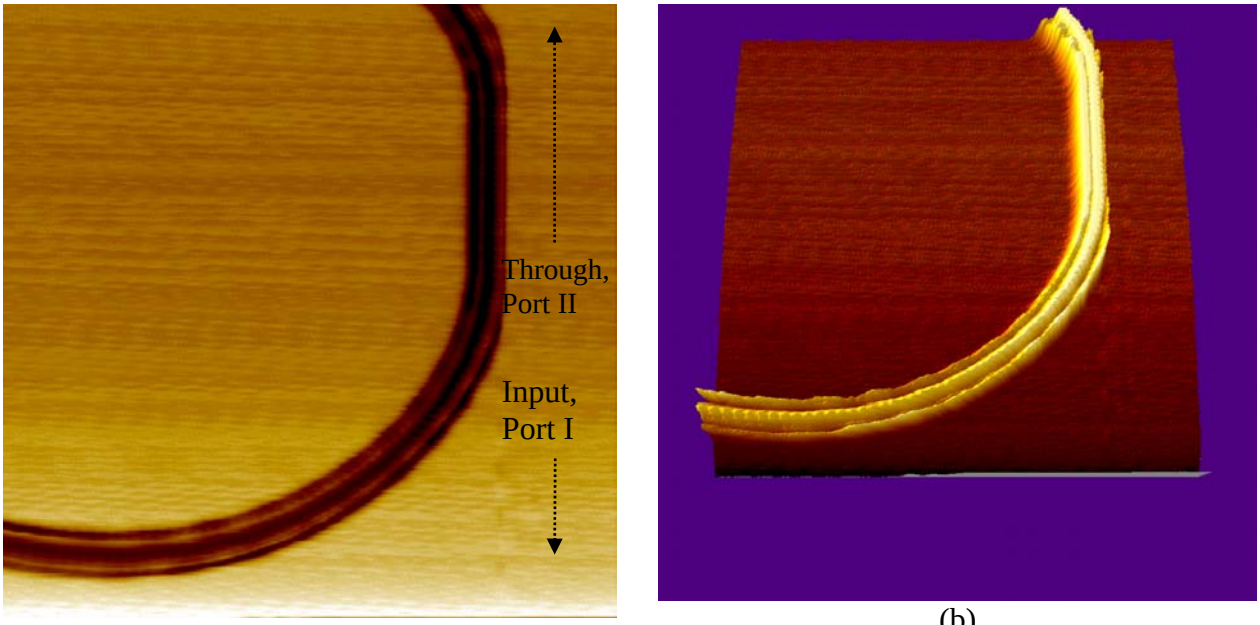

(a) (b)

Figure 5.6-1: (a) Two dimensional representation of the transmission measured in the drop at the undisturbed MRR resonance wavelength, obtained by raster scanning a Si_3N_4 AFM tip over a MRR. See Fig. 2.15 for a detailed description of the MRR configuration (b) A quasi-3-D representation of the inverted transmission data.

The inverted data is shown in quasi-3-D in Figure 5.6-1b. It clearly shows three regions of high interaction. This effect can be explained from the evanescent field strength outside the rib waveguide and the position of the AFM needle see Figure 5.6-2.

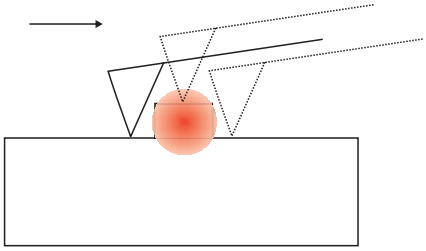

Figure 5.6-2: A schematic presentation of the rib (ring) waveguide and 3 probe positions that produce a large interaction due to the large overlap of the probe with the field.

Another interesting observation can be made from Figure 1.1-1: a beating pattern is present for a tip position in the middle of the ring waveguide. An explanation for this effect is the coupling of light to the ring that is reflected from the end-facet of the chip. This assumption is also supported by the fact that the beating pattern is exactly half the optical wavelength. The results indicate that the T-SNOM is not restricted to PhC resonators; it can also be applied to microring resonators. A further modeling study in combination with detailed analyses of the results is currently being performed.

5.7 NEMS actuated photonic crystal switches

The research presented in this thesis was part of the project “optical switching by NEMS-actuated resonator arrays”, see chapter 1. The multidisciplinary nature of the project is one its important aspects. The choice for PhCs is obvious, because they allow for a small-sized device and they receive quite some attention in the present literature, indicating that publications on the subject are interesting for a large audience.
The advantages of the switch configuration as a whole are:

- compactness
- switching speed can be higher than its thermo-optical or classical-mechanical equivalent
- near-zero energy dissipation in stationary state.

Whether the NEMS PhC switch will be a commercially attractive alternative to other integrated optical switches, depends on how the (photonics) industry evolves. The loss due to fabrication errors in (2-D) (PhCs) fabrication is still too high to develop a commercially attractive product. However, the prospective for the nano-photonic industry is favorable, since the chip-based Billion Dollar industry may solve fabrication related issues. The silicon electronics industry is using decreasing exposure wavelengths. As a consequence, the roughness due the various fabrication processes becomes increasingly important. Therefore, the photonics industry is likely to benefit from the investments made by the chip-industry, and this type of switches may be of growing interest to the market.

5.8 References

[1] J. Schrauwen, D. Van Thourhout, and R. Baets, "Focused-ion-beam fabricated vertical fiber couplers on silicon-on-insulator waveguides", *Applied Physics Letters*, vol. **89**, pp. 141102/1-3, 2006.

[2] R. A. Soref & B. R. Bennett, "Electrooptical Effects in Silicon", *IEEE Journal of Quantum Electronics*, vol. **23**, pp. 123-129, 1987.

[3] M. Tamura, S. Shukuri, M. Moniwa, and M. Default, "Focused ion beam gallium implantation into silicon", *Applied Physics A: Solids and Surfaces*, vol. **A39**, pp. 183-190, 1986.

[4] S. W. Novak, C. W. Magee, H. C. Mogul, A. J. Steckl, and M. Pawlik, "Secondary ion massspectrometry depth profiling of nanometer-scale p^+-n junctions fabricated by Ga^+ focused ion-beam implantation", *Journal of Vacuum Science Technology B*, vol. **10**, pp. 333-335, 1992.

[5] A. H. van Ommen, "Diffusion of ion-implanted Ga in SiO_2", *Journal of Applied Physics*, vol. **57**, pp. 1872-1879, 1985.

[6] K. Yokota, H. Furuta, S. Ishihara, and I. Kimura, "Background impurity dependence of redistributions of implanted gallium in silicon during annealing", *Journal of Applied Physics*, vol. **68**, pp. 5385-5387, 1990.

[7] Y. Tanaka, M. Tymczenko, T. Asano, and S. Noda, "Fabrication of two-dimensional photonic crystal slab point-defect cavity employing local three-dimensional structures", *Japanese Journal Of Applied Physics Part 1-Regular Papers Brief Communications & Review Papers*, vol. **45**, pp. 6096-7002, 2006.

[8] S. Y. Chou, P. R. Krauss, and P. J. Renstrom, "Nanoimprint lithography", *Journal of Vacuum Science and Technology B: Microelectronics and Nanometer Structures*, vol. **14**, pp. 4129-4133, 1996.

[9] E. Krioukov, J. Greve, and C. Otto, "Performance of integrated optical microcavities for refractive index and fluorescence sensing", *Sensors and Actuators, B: Chemical*, vol. **90**, pp. 58-67, 2003.

[10] P. V. Lambeck, "Integrated optical sensors for the chemical domain", *Measurement Science and Technology*, vol. **17**, pp. R93-R116, 2006.

[11] M. D. Settle, R. J. P. Engelen, M. Salib, A. Michaeli, L. Kuipers, and T. F. Krauss, "Flatband slow light in photonic crystals featuring spatial pulse compression and terahertz bandwidth", *Optics Express*, vol. **15**, pp. 219-226, 2007.

[12] R. J. P. Engelen, Y. Sugimoto, Y. Watanabe, J. P. Korterik, N. Ikeda, N. F. Van Hulst, K. Asakawa, and L. Kuipers, "The effect of higher-order dispersion on slow light propagation in photonic crystal waveguides", *Optics Express*, vol. **14**, pp. 1658-1672, 2006.

CHAPTER 6

6 SUMMARY

This thesis describes the design, fabrication and characterization of one- and two-dimensional photonic crystals (PhCs). Two novel characterization methods have been proposed, the far-field scattering method to characterize slow-light phenomena in gratings and a near-field method for mapping the standing wave patterns in a photonic crystal resonator. The fabrication and characterization methods presented are highly useful for realizing a nanomechanical PhC switch, which is the main goal of the project in which the research was carried out.

Chapter 2: Photonic crystals & resonators
A brief review of the theory of one- and two-dimensional photonic crystals and resonators is presented. Some derivations of often used relations for the group velocity, the quality factor *Q*, and the free spectral range are given. Several design choices for waveguide gratings, photonic crystal resonators and microring resonators are also addressed.

Chapter 3: Fabrication
The strengths and weaknesses of the fabrication methods, as experienced in this work, are presented. This is followed by a detailed description of an example for the preparation of a stream file, which can be adopted for milling a pattern using a focused ion beam (FIB). A focused ion beam can be exploited for turning an ultrarough surface into a nanosmooth surface. An application can be, for example, the smoothening of the end facets of an optical chip, to increase the coupling efficiency. The FIB can also be used to generate submicrometer PhC holes. However, fabrication of submicrometer holes with perfectly vertical sidewalls, needed for low-loss propagation, is non-trivial in Si due to the strong redeposition effect. The scan strategy of the ion beam can be used as a parameter for sidewall-angle optimization, i.e. aiming to mill a submicrometer hole with perfect vertical walls. The optimization is performed for both isolated holes and arrays of holes. It is shown that the sidewall angles can be as small as 5 degrees in (bulk) Si and SOI if applying a relatively large dose, i.e. milling several micrometers deep. For the Si membranes (Si suspended in air), a minimum angle of only 1.5 degrees is obtained. It is concluded that the number of loops at a fixed dose per hole is the parameter that determines the sidewall angle and not the dwell time by itself.

Another fabrication method that has been exploited for the fabrication of photonic crystals is the combination of laser interference lithography (LIL) and conventional lithography and dry etching. The fabrication method, which allows for realizing apodization functions modulating both amplitude and phase of the grating, is demonstrated by fabricating a Si_3N_4 waveguide grating chirped by width-variation of the grated ridge waveguide. The presented method is suitable for fabricating high quality Si_3N_4 waveguide gratings and it has the advantage of being CMOS-compatible.

Chapter 4: Characterization & modeling results
The setups used for the experiments presented in this thesis are briefly summarized while providing the references to their detailed descriptions.
The fabrication and characterization of the refractometric and thermo-optical properties of a quasi-one-dimensional waveguide photonic crystal –a strong, 76-μm-long Bragg waveguide grating– are reported with transmission spectra around 660 nm. It is shown that the (steep) edge of the stopband

can be used for detecting changes in the aqueous cladding refractive index of only 4×10^{-4}. A thermally induced spectral shift of approximately 7 pm/K was observed.

In section 4.3 it is experimentally shown that the fringes in the transmission spectrum near the stopband edge are associated with the occurrence of standing wave patterns in the waveguide grating. These patterns correspond well to the distributions found in the simulations of the waveguide grating. A novel and straightforward method for determining the group index and intensity enhancement over a wide wavelength range based on (Rayleigh) scattering observations is presented. This far-field scattering microscopy (FScM) method is compared with the so-called phase shift method and a method that uses the transmission spectrum to quantify the slow wave properties. The methods show a good agreement. A minimum group velocity of 0.04 *c* and a maximum intensity enhancement factor of approximately 14.5 for a 1000-period grating and a maximum group delay of about 80 ps for a 2000-period grating have been found. It is shown that the FScM method can be used for both displaying the intensity distribution of the Bloch resonances and for investigating out-of-plane losses. The gratings designed for infrared wavelengths are suggested for use as a slow-wave cladding-index sensor able to detect a minimum cladding index change of 10^{-8}, assuming a transmission detection limit of 10^{-4}.

The FScM characterization method described above can not be used to accurately map out the wave patterns in micrometer-sized resonators, because the size of the resonance is well below the diffraction limited resolution. Therefore, the remainder of chapter 4 is devoted to a novel measurement method, *transmission scanning near-field microscopy* (T-SNOM), which enables mapping out the intracavity intensity distribution of the standing wave in a cavity. It is shown by modeling of two orthogonal cross-sections of a PhC microcavity, that the resonance wavelength shift induced by a nanoprobe is approximately proportional to the local field intensity of the standing wave. In addition, the transmitted power can be used as a first approximation of the field intensity. This approximation becomes more accurate when the operation wavelength is set to the point where the slope of the Lorentzian shaped response is at maximum and the interaction levels are weak. It is concluded that a nanosized tip can be used to tune the resonance wavelength and quality factor.

The T-SNOM method was applied experimentally to characterize a silicon-on-insulator based PhC microcavity. The results showed that the standing wave patterns could be mapped out with high spatial accuracy (<100 nm) using an atomic force microscopy (AFM) tip in contact mode. Two AFM tips have been exploited for the nanomechanical interaction, a Si and Si_3N_4 tip. A detuning of the resonance wavelength by 2.3 nm was shown by expedient positioning of a Si AFM tip. With the same tip it was possible to set the *Q* between values of 615 and zero. Full on/off switching was found for displacements of less than 200 nm in the vertical direction, and for 500 nm in a lateral direction, at the strongest resonance antinode locations

In contact-mode operation, however, the tip wears out quickly. In other AFM applications, the well-known tapping mode operation has shown its value for probing delicate surfaces. This mode can also be used for the T-SNOM method. It is shown that a simple model of the tip dynamics in combination with a calibration curve is adequate to model the effect of the pre-set tapping height on the transmitted signal.

The simulations showed that the tip can efficiently reduce the out-of-plane scattering by positioning the tip in the vertical direction to a height of 0.5 μm (above a “hot-spot”) forming an anti-resonant cavity. A similar effect has been observed in the experiments where a small increase in transmission was detected when the tip was positioned before the cavity.

Chapter 5: Outlook

The on-going research related to the topics described in this thesis is presented. The challenges in FIB processing and the solutions and alternatives that are being investigated are described. It is suggested that the far-field scattering microscopy method can also be applied to slow-light PhC W1 waveguides, preliminary results are included. A preliminary result of the T-SNOM method on microring resonators is presented.

Finally, the application of the T-SNOM method and the nano-electro-mechanical system (NEMS) PhC switch is discussed.

SAMENVATTING

Dit proefschrift beschrijft het ontwerp, de fabricage and karakterisatie van één- en tweedimensionale fotonische kristallen. Twee nieuwe karakteriseringsmethoden zijn ontwikkeld: de verreveldverstrooiingsmethode om het fenomeen van het zogenoemde trage licht te onderzoeken in geïntegreerde traliestructuren en een methode om staande golven waar te nemen in een fotonischkristalresonator met behulp van beïnvloeding van het nabije veld. De fabricage- en karakteriseringsmethoden die gepresenteerd worden in dit proefschrift zijn zeer bruikbaar voor het realiseren van het hoofddoel van het project waarin dit onderzoek is uitgevoerd: de realisatie van een nanomechanische lichtschakelaar gebaseerd op fotonische kristallen.

Hoofdstuk 2: Fotonische kristallen en resonatoren
Een kort overzicht van de benodigde theorie voor één- en tweedimensionale fotonische kristallen wordt gegeven. Verscheidene relaties voor onder andere de groepssnelheid, de kwaliteitsfactor *Q* en de vrije spectrale breedte worden afgeleid. Een aantal belangrijke ontwerpkeuzes met betrekking tot tralies in golfgeleiderstructuren, fotonische kristallen en microringresonatoren worden toegelicht.

Hoofdstuk 3: Fabricatie
Er is een sterkte- en zwakteanalyse gemaakt van de fabricagemethoden die gebruikt zijn voor dit proefschrift, op basis van de ervaringen met deze technologieën. Dit wordt gevolgd door een gedetailleerde beschrijving van een voorbeeld voor het generen van een “masker”-bestand waarmee een patroon gedefinieerd kan worden met de gefocusseerde ionenbundel (FIB). Deze FIB kan onder meer gebruikt worden om een oorspronkelijk ruw oppervlak ultraglad te maken. Een toepassing hiervan kan bijvoorbeeld zijn het polijsten van de eindvlakken van de optische chip om de koppeling van licht naar de golfgeleider te vergroten. De fabricage van submicrometer gaten met perfect verticale zijwanden, die nodig zijn voor verliesvrije propagatie in (Si) fotonische kristallen, is geen standaardproces vanwege het sterk aanwezige redepositie-effect.
Het pad dat de ionenbundel aflegt tijdens het “millen” (het fysisch wegmalen van de atomen in het substraat), genaamd het scantraject, kan gebruikt worden als parameter voor het optimaliseren van de zijwandhoek, met als doel het millen van submicrometer gaten met perfect verticale zijwanden. De optimalisatie is uitgevoerd voor zowel individuele gaten als gaten in een matrixstructuur (een configuratie van een fotonisch kristal). Een waarde van ongeveer 5 graden kan bereikt worden voor de zijwandhoeken in (bulk) Si and SOI (“silicon-on-insulator”) als er een relatief grote dosis gebruikt wordt, zodat er diepe gaten ontstaan. De millingexperimenten in Si membramen laten zien dat voor deze structuren een zijwandhoek van slechts 1.5 graad bereikt kan worden. Op basis van de uitkomsten van de experimenten is de conclusie getrokken dat het aantal rondes dat de FIB aflegt bij een gegeven constante dosis per gat de beste optimalisatieparameter is en niet alleen de verblijftijd van de bundel op één plaats (de “dwell time”).

Een andere fabricagetechnologie is onderzocht en toegepast voor de realisatie van een ééndimensionaal fotonisch kristal (een tralie in een golfgeleider): de combinatie van laserinterferentielithografie met conventionele UV-lithografie en droog etsen. De fabricagemethode, die geschikt is voor de realisatie van zogenaamde apodiserende functies (met als doel oscillaties in een overdrachtsfunctie te verminderen), die zowel de fase en amplitude kunnen moduleren van het licht in de tralie, is gedemonstreerd door een tralie te fabriceren in een Si_3N_4 golfgeleider waarbij de breedte van de golfgeleider onder het tralie verloopt. Het voordeel van deze fabricagemethode waarmee kwalitatief goede tralies gemaakt kunnen worden, is dat deze compatibel is met de CMOS industriestandaarden.

Hoofdstuk 4: Karakterisering & modelleringsresultaten
Een opsomming van de opstellingen die gebruikt zijn voor de experimenten in dit proefschrift wordt eerst gegeven samen met de referenties naar uitgebreide beschrijving van deze opstellingen.

De fabricage en karakterisatie van de refractometrische en temperatuurafhankelijke eigenschappen van een quasi-ééndimensionaal fotonisch kristal, namelijk een 76 μm lang Braggtralie in een golfgeleider wordt gerapporteerd. De stopband van dit tralie met een periode van 190 nm lag rond een golflengte van 660 nm. Dit tralie kan gebruikt worden als sensor van verandering in de brekingsindex van de cladding, met een gevoeligheid in brekingsindexverandering van 4×10^{-4} en een temperatuursgevoeligheid van 7 pm/K.

In sectie 4.3 worden experimenten beschreven die aantonen dat de scherpe pieken in het transmissiespectrum vlak naast de stopband samenhangen met staandegolfpatronen in het tralie in de golfgeleider. Deze patronen komen goed overeen met de verdelingen die gevonden zijn met behulp van simulaties. Een nieuwe en eenvoudige methode wordt gepresenteerd waarmee de groepsindex en de intensiteitstoename over een grote spectrale breedte kan worden geschat. De resultaten die zijn verkregen met behulp van deze verreveldverstrooiingsmethode zijn vergeleken met de resultaten verkregen m.b.v. de zogenoemde “faseverschuivingsmethode” en met een methode die gebruik maakt van het transmissiespectrum om de eigenschappen van traag licht te onderzoeken. De resultaten van de verschillende methoden komen goed overeen. Een minimum in groepssnelheid van 0.04 *c* en een maximale intensiteitsverhogingsfactor van 14.5 zijn gevonden voor een 1000-perioden lang tralie en een maximale groepsvertraging van 80 ps is gevonden voor een 2000-perioden lang tralie. De verreveldverstrooiingsmethode kan niet alleen gebruikt worden om de intensiteitsverdelingen van de Blochresonanties waar te nemen, maar ook om de stralingsverliezen uit het vlak van de golfgeleider te bestuderen. De bovengenoemde tralies die ontworpen zijn voor het infrarode golflengtegebied (rond 1.55 μm) kunnen ook gebruikt worden als op traag licht gebaseerde sensoren van brekingsindexverschillen in de cladding. De minimale brekingsindexverandering die deze sensoren kunnen detecteren is 10^{-8}, uitgaande van een detectielimiet van 10^{-4}.

De bovenbeschreven verreveldverstrooiingsmethode kan niet gebruikt worden om nauwkeurig het staandegolfprofiel in een microresonator te bepalen aangezien het resonantiepatroon kleinere details vertoont dan de resolutie van de meetmethode, die beperkt is door diffractie. Daarom is het resterende deel van hoofdstuk 4 gewijd aan een nieuw ontwikkelde meetmethode: microscopie door aftasting van het nabije veld waarbij de optische transmissie gemeten wordt (T-SNOM). Met deze techniek is het wel mogelijk om het veldpatroon in een microresonator te bepalen. De tweedimensionale modelleringresultaten laten voor twee loodrechte doorsneden van een resonator in een fotonisch kristal zien dat de resonantiegolflengteverschuiving door de nabijheid van een nanonaaldje bij goede benadering evenredig is met de lokale intensiteitsverdeling. Een eerste benadering van deze verdeling kan verkregen worden voor een lage interactiesterkte, door een werkgolflengte te kiezen op de helling van de Lorentz-vormige responsie waar de afgeleide maximaal is. Op basis van de experimentele en numerieke resultaten is de conclusie getrokken dat een nanonaaldje gebruikt kan worden om de resonantiegolflengte nauwkeurig af te stemmen op de gewenste waarde en om de selectiviteit van de resonator, gekenmerkt door de kwaliteitsfactor *Q*, te veranderen.

De T-SNOM-methode is experimenteel toegepast om een op SOI gebaseerde microresonator in een fotonisch kristal te karakteriseren. Uit de resultaten kan geconcludeerd worden dat de staandegolfpatronen met een hoge resolutie (< 100 nm) gemeten konden worden met behulp van een microscoop op basis van atomaire krachten (AFM), waarvan de aftastnaald in contactmodus werd bedreven. Twee verschillende AFM naaldjes zijn gebruikt voor de experimenten met

nanomechanische interactie: een van Si en een andere van Si_3N_4. Een verschuiving van de resonantiegolflengte van 2.3 nm kon worden gedemonstreerd door een slimme plaatsing van een Si AFM-naaldje. Met hetzelfde naaldje was het mogelijk om de *Q* te veranderen tussen 615 en 0. Volledige aan- en uitschakeling van resonator was mogelijk met een verticale naaldverplaatsing van slechts 200 nm of met een laterale verplaatsing van 500 nm ten opzichte van de locatie met de sterkste veldintensiteit.

Omdat de naald snel kan slijten in contactmodus, is de toepassing van de zogenaamde tapping modus belangrijk. Deze techniek wordt dikwijls toegepast op delicate oppervlakken. Deze modus kan ook gebruikt worden voor de T-SNOM-methode. Het is mogelijk om met behulp van een eenvoudig model van de naaldbewegingen en met een gemeten calibratiecurve het effect van de ingestelde tappingamplitude op het transmissiesignaal te schatten.

Uit de simulatieresultaten blijkt dat een nanonaaldje gebruikt kan worden om efficiënt de uit-het-vlak-verliezen te verlagen door het naaldje op een hoogte van 0.5 μm te plaatsen boven de plaats waar de sterkste veldintensiteit heerst. Hierdoor wordt er tussen de golfgeleiderstructuur en het naaldje een antiresonante holte gevormd. Een soortgelijk effect is experimenteel waargenomen: een toename in transmissie werd gedetecteerd voor een naaldpositie net buiten de resonator.

Hoofdstuk 5: Vooruitzicht

In dit hoofdstuk worden de huidige en toekomstige onderzoeksactiviteiten genoemd die gerelateerd zijn aan het werk beschreven in dit proefschrift. De uitdagingen van het FIB-onderzoek, de mogelijke oplossingen en enkele alternatieven worden genoemd. Een eerste resultaat wordt gepresenteerd van een test van de verreveldverstrooiingsmethode op een W1 golfgeleider in een fotonisch kristal. Ook wordt een eerste resultaat gepresenteerd van een toepassingstest van de T-SNOM-methode op een microringresonator.
Tenslotte worden de toepassing van de T-SNOM-methode en een optische schakelaar gebaseerd op NEMS (nanoelectromechanical system) besproken.

Appendix A: Fabry-Perot resonator

"Lorentzian transmission function in terms of resonance frequency and quality factor"

We [1] start with equation (6.9) from the OBM lecture notes [2], for the power transmission T through a Fabry-Perot resonator:

$$T = \frac{T_0}{1 + B\sin^2\left(\frac{\varphi}{2}\right)} \tag{1}$$

with $\varphi = 2\,L\,n\,2\pi/\lambda = 2\,\omega\,L\,n/c$; L is the cavity length, n is the (effective) index of the intra-cavity medium, λ is the vacuum wavelength, c the speed of light in vacuum, ω the angular frequency, and A and T_0 are constants determined by mirror reflectivities and cavity losses.
Resonance occurs for $\varphi = m\ 2\pi$ (m = 1, 2, ...). The lowest-order resonance is for m = 1, and the corresponding angular frequency is:

$$\omega_0 = \frac{c\pi}{Ln} \tag{2}$$

which allows us to write:

$$\varphi = \frac{\omega}{\omega_0} 2\pi \tag{3}$$

Hence, we can write T (1) as a function of ω and ω_0:

$$T(\omega) = \frac{T_0}{1 + B\sin^2\left(\frac{\omega}{\omega_0}\pi\right)} \tag{4}$$

In a medium without dispersion all resonance frequencies are equally spaced by an amount ω_0, which is the free spectral range:

$$\Delta\omega_{FSR} = \omega_0 \tag{5}$$

The full width at half maximum (FWHM) refers to the interval in wavelength or (angular) frequency between two points at both sides of the same transmission peak where T is reduced to half its value at resonance. From (4) it is clear that this occurs for

$$\sin^2\left(\frac{\omega}{\omega_0}\pi\right) = \frac{1}{B} \tag{6}$$

In low-loss cavities $B >> 1$, so we may approximate the sin( ) function by its argument modulo π. In terms of the angular frequency FWHM $\Delta\omega_{FWHM}$ at the m'th order resonance (again assuming no dispersion), we find:

$$\sin^2\left(\frac{m\,\omega_0 \pm \Delta\omega_{FWHM}}{\omega_0}\pi\right) = \sin^2\left(m\pi \pm \frac{\Delta\omega_{FWHM}}{\omega_0}\pi\right) \cong \left(\frac{\Delta\omega_{FWHM}}{\omega_0}\pi\right)^2 = \frac{1}{B} \tag{7}$$

which leads to:

$$\Delta\omega_{FWHM} \cong \frac{2\omega_0}{\pi\sqrt{B}} \tag{8}$$

The finesse is defined as:

$$F = \frac{\Delta\omega_{FSR}}{\Delta\omega_{FWHM}} = \frac{\omega_0}{\Delta\omega_{FWHM}} = \frac{1}{2}\pi\sqrt{B} \tag{9}$$

A related quantity is the Q-factor for a given resonance, which can be calculated from:

$$Q = \frac{\omega_{res}}{\Delta\omega_{FWHM}} \tag{10}$$

where ω_{res} is the angular frequency of the resonance. In the dispersionless case, we have $\omega_{res} = m\ \omega_0$, so that:

$$Q = \frac{m\,\omega_0}{\Delta\omega_{FWHM}} = \frac{m}{2}\pi\sqrt{B} = m\,F \tag{11}$$

For a first-order resonance Q and F have the same value. For frequencies near resonance, (4) can be written as a Lorentzian function, in terms of the resonance frequency and the Q-factor. Near resonance, we have:

$$\omega = \omega_{res} + \Delta\omega = m\omega_0 + \Delta\omega \tag{12}$$

with $\Delta\omega << \omega_0$. Then, the sin( ) term in (4) becomes, similar to (7):

$$\sin^2\left(\frac{m\,\omega_0 + \Delta\omega}{\omega_0}\pi\right) \cong \left(\frac{\Delta\omega}{\omega_0}\pi\right)^2 = \left(\frac{\omega - \omega_{res}}{\omega_0}\pi\right)^2 \tag{13}$$

and, using (11), we write:

$$T(\omega) \cong \frac{T_0}{1 + B\left(\frac{\omega - \omega_{res}}{\omega_0}\pi\right)^2} = T_0\,\frac{\left(\frac{\omega_{res}}{2Q}\right)^2}{(\omega - \omega_{res})^2 + \left(\frac{\omega_{res}}{2Q}\right)^2} \tag{14}$$

References

[1] by R. M. de Ridder, University of Twente, Enschede, 2007.

[2] P. V. Lambeck & R. M. de Ridder, "Optical basic functions and microsystems", Integrated optical microsystems group, University of Twente, Enschede, 2006.

Appendix B: Microscope images

"Image of the photonic crystal resonator and an image of the end-facet"

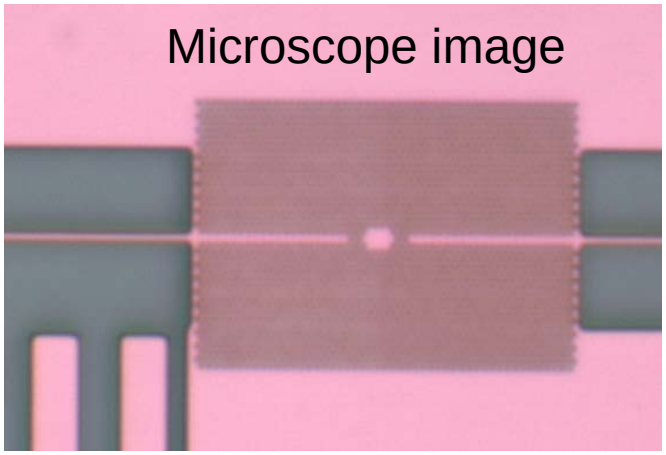

Figure B1: A microscope image of photonic crystal microcavity, showing clearly the photonic wires, the W1 waveguides and the larger than designed micro-cavity

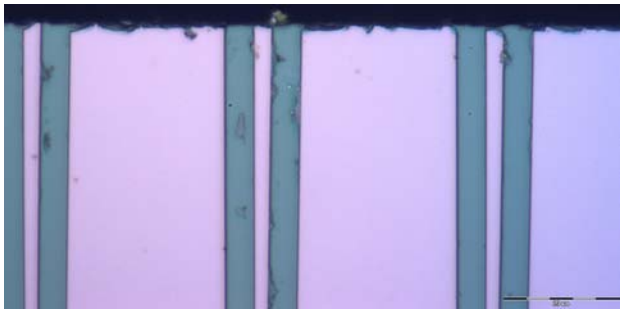

Figure B2: A microscope image of the end-facet. Dicing of the sample has roughened the end-facet, however reasonable coupling is still possible using objective lenses.

PUBLICATIONS

PEER REVIEWED JOURNALS

[1] W. C. L. Hopman, P. Pottier, D. Yudistira, J. van Lith, P. V. Lambeck, R. M. De La Rue, A. Driessen, H. J. W. M. Hoekstra, and R. M. de Ridder, "Quasi-one-dimensional photonic crystal as a compact building-block for refractometric optical sensors", *IEEE Journal Of Selected Topics In Quantum Electronics*, vol. **11**, pp. 11-16, 2005.

[2] W. C. L. Hopman, R. Dekker, D. Yudistira, W. F. A. Engbers, H. Hoekstra, and R. M. de Ridder, "Fabrication and characterization of high-quality uniform and apodized Si_3N_4 waveguide gratings using laser interference lithography", *IEEE Photonics Technology Letters*, vol. **18**, pp. 1855-1857, 2006.

[3] W. C. L. Hopman, K. O. Van Der Werf, A. J. F. Hollink, W. Bogaerts, V. Subramaniam, and R. M. De Ridder, "Nano-mechanical tuning and imaging of a photonic crystal micro-cavity resonance", *Optics Express*, vol. **14**, pp. 8745-8752, 2006.

[4] W. C. L. Hopman, H. J. W. M. Hoekstra, R. Dekker, L. Zhuang, and R. M. de Ridder, "Far-field scattering microscopy applied to analysis of slow light, power enhancement, and delay times in uniform Bragg waveguide gratings", *Optics Express*, vol. **15**, pp. 1851-1870, 2007.

[5] W. C. L. Hopman, F. Ay, W. Hu, V. J. Gadgil, L. Kuipers, M. Pollnau, and R. M. de Ridder, "Focused ion beam scan routine, dwell time and dose optimizations for submicrometre period planar photonic crystal components and stamps in silicon", *Accepted for publication*, March 2007.

[6] W. C. L. Hopman, R. Stoffer, and R. M. de Ridder, "High resolution measurement of resonant wave patterns by perturbing the evanescent field using a nano-sized probe in a transmission scanning near-field optical microscopy configuration", *Accepted for publication*, March 2007.

[7] W. C. L. Hopman, K. O. van der Werf, A. J. F. Hollink, W. Bogaerts, V. Subramaniam, and R. M. de Ridder, "Experimental verification of a simple transmission model for predicting the interaction of an AFM-probe with a photonic crystal micro-cavity in tapping mode operation", *Submitted for publication*, 2007.

[8] W. C. L. Hopman, K. O. van der Werf, A. J. F. Hollink, W. Bogaerts, V. Subramaniam, and R. M. de Ridder, "Interaction of an AFM probe with a microring resonator", *in preparation*, 2007.

[9] H. J. W. M. Hoekstra, W. C. L. Hopman, J. Kautz, R. Dekker, and R. M. de Ridder, "A simple coupled mode model for near band-edge phenomena in grated waveguides", *Optical and Quantum Electronics*, vol. **38**, pp. 799-813, 2006.

[10] P. Bienstman, S. Selleri, L. Rosa, H. P. Uranus, W. C. L. Hopman, R. Costa, A. Melloni, L. C. Andreani, J. P. Hugonin, P. Lalanne, D. Pinto, S. S. A. Obayya, M. Dems, and K. Panajotov, "Modelling leaky photonic wires: A mode solver comparison", *Optical and Quantum Electronics*, vol. **38**, pp. 731-759, 2006.

[12] M. Gnan, W. C. L. Hopman, G. Bellanca, and R. M. De La Rue, "Photonic Wire Bragg Gratings in silicon on insulator", *in preparation*, 2007.

NATIONAL JOURNALS

[1] W. C. L. Hopman, K. O. van der Werf, and R. M. de Ridder, "Licht manipuleren met een nano-naaldje", *Nederlands tijdschrift voor de natuurkunde (invited)*, vol. **73**, pp. 50-53, 2007.

BOOK CHAPTERS

[1] A. Driessen, H. J. W. M. Hoekstra, W. C. L. Hopman, H. Kelderman, P. V. Lambeck, J. Lith, D. J. W. Klunder, R. M. de Ridder, E. Krioukov, and C. Otto. in Book: Optical Chemical Sensors. NATO Science Series, Series II: Mathematics, Physics and Chemistry 224, *Ultracompact Optical Sensors based on high index-contrast Photonic Structures.*, pp. 281-295, IOS Press/Springer in conjunction with the NATO Public Diplomacy Division, Dordrecht, The Netherlands, 2006.

[2] in Book: Program and abstracts, *COST Action P11, Physics of linear, Non-linear, and Active photonic crystals*, (eds. de Ridder, R. M. & Hopman, W. C. L.), Enschede, The Netherlands, 2005.

CONFERENCE PROCEEDINGS

[1] W. C. L. Hopman, R. M. de Ridder, P. Pottier, and R. M. De La Rue, "Experimental verification of modeling results of deeply etched Bragg gratings", Poster presentation, Proc. International Workshop on Optical Waveguide Theory and Numerical Modeling (ICTON), Prague, Czech Republic, 2003.

[2] W. C. L. Hopman, P. Pottier, D. Yudistira, J. van Lith, P. V. Lambeck, R. M. De La Rue, A. Driessen, H. J. W. M. Hoekstra, and R. M. de Ridder, "Quasi 1-dimensional photonic crystals as building block for compact integrated optical sensors", Poster presentation, Proc. 6th International Conference on transparent optical networks (ICTON), Wroclaw, Poland, 0-7803-8343-5, 342-345, 2004.

[3] W. C. L. Hopman, P. Pottier, D. Yudistira, J. van Lith, P. V. Lambeck, R. M. De La Rue, A. Driessen, H. J. W. M. Hoekstra, and R. M. de Ridder, "Quasi one-dimensional photonic crystals as building block for compact integrated optical refractometric sensors", Poster presentation, Proc. Annual symposium of the IEEE LEOS Benelux Chapter, Ghent, Belgium, ISBN: 9-0765460-6-1, 223-226, 2004.

[4] W. C. L. Hopman, D. Yudistira, R. Dekker, W. F. A. Engbers, H. J. W. M. Hoekstra, and R. M. de Ridder, "Characterization of slow-light in a LIL-fabricated Si_3N_4 Waveguide grating", Poster presentation, Proc. Annual symposium of the IEEE LEOS Benelux Chapter, Mons, Belgium, ISBN: 2-9600226-4-5, 109-112, 2005.

[5] W. C. L. Hopman, R. M. De Ridder, S. Selvaraja, C. G. Bostan, V. J. Gadgil, L. Kuipers, and A. Driessen, "Realization of 2-dimensional air-bridge silicon photonic crystals by focused ion beam, milling and nanopolishing", Oral presentation, Proc. Proceedings of SPIE - The International Society for Optical Engineering, Strasbourg, ISBN-13: 9780819462381, 2006.

[6] W. C. L. Hopman, K. O. van de Werf, A. J. F. Hollink, W. Bogaerts, V. Subramaniam, and R. M. de Ridder, "Interactions with a photonic crystal micro-cavity using an AFM in contact or tapping mode operation", Proc. Annual symposium of the IEEE LEOS Benelux Chapter (Eindhoven), pp. 25-28 (2006).

[7] R. M. de Ridder, W. C. L. Hopman, and H. J. W. M. Hoekstra, "Characterisation of slow light in a waveguide grating", Oral presentation (invited), Proc. Proceedings of the 8th international conference on transparent optical networks (ICTON), Nottingham, United Kingdom, ISBN: 1-4244-0235-2, 88-90, 2006.

[8] H. J. W. M. Hoekstra, W. C. L. Hopman, J. Kautz, R. Dekker, and R. M. de Ridder, "A simple coupled mode model for near band-edge phenomena in grated waveguides", Oral presentation, Proc. Fifteenth International Workshop on Optical Waveguide Theory and Numerical Modelling (OWTNM), Varese, Italy, ISBN: 88-902405-0-4 2006.

[9] P. Bienstman, S. Selleri, H. P. Uranus, W. C. L. Hopman, A. Melloni, R. Costa, L. C. Andreani, P. Lalanne, J. P. Hugonin, D. Pinto, and S. S. A. Obayya, "Modelling lossy photonic wires: a mode solver comparison", Oral presentation, Proc. Fifteenth International Workshop on Optical Waveguide Theory and Numerical Modelling (OWTNM), Varese, Italy, ISBN: 88-902405-0-4, 2006.

[10] W. C. L. Hopman, F. Ay, W. Hu, V. J. Gadgil, L. Kuipers, M. Pollnau, and R. M. de Ridder, "Focused Ion Beam Milling Strategies of Photonic Crystal Structures in Silicon", Proc. European Conference on Integrated Optics (ECIO), Copenhagen, Denmark, Accepted for oral presentation, 2007.

[11] R. M. de Ridder, W. C. L. Hopman, R. Stoffer, and K. O. van de Werf, "Mapping the field distribution of a resonator in a photonic crystal slab, using transmission SNOM", Proc. European Conference on Integrated Optics (ECIO), Copenhagen, Denmark, Accepted for oral presentation, 2007.

PRESENTATIONS

[1] H. Gersen, W. C. L. Hopman, D. J. W. Klunder, J. P. Korterik, A. Driessen, N. F. van Hulst, and L. Kuipers, "Pulse propagation studied en route by near-field microscopy", Oral presentation, Annual symposium of the IEEE LEOS Benelux Chapter, Enschede, The Netherlands, 2003.

[2] W. C. L. Hopman, P. Pottier, D. Yudistira, J. Lith, P. V. Lambeck, R. M. De La Rue, A. Driessen, H. J. W. M. Hoekstra, and R. M. de Ridder, "Quasi 1-Dimensional Photonic Crystals as Building Block for Compact Integrated Optical Sensors", Poster presentation, MESA+ Annual Symposium, 2004.

[3] W. C. L. Hopman, R. M. de Ridder, C. G. Bostan, S. Selvaraja, V. J. Gadgil, L. Kuipers, and A. Driessen, "Design and fabrication of 2-dimensional silicon photonic crystal membranes by focused ion beam processing", Poster presentation, NanoNed-Micro Ned Symposium, Book of Abstracts, Nr. 17A, Groningen, The Netherlands, 2005.

[4] W. C. L. Hopman, R. M. de Ridder, C. G. Bostan, S. Selvaraja, V. J. Gadgil, L. Kuipers, and A. Driessen, "Design and Fabrication of 2-Dimensional Silicon Photonic Crystal Membranes by Focused Ion Beam processing", Poster presentation, ePIXnet winterschool, Pontresina Switzerland, 2006.

[5] W. C. L. Hopman, K. O. van der Werf, A. J. F. Hollink, W. Bogaerts, V. Subramaniam, and R. M. de Ridder, "Nano-mechanical tuning and imaging of a photonic crystal micro-cavity resonance", Poster presentation, ePIXnet annual meeting, Lausanne, Switzerland, 2006.

[6] K. O. van de Werf, W. C. L. Hopman, A. J. F. Hollink, W. Bogaerts, V. Subramaniam, and R. M. de Ridder, "Nano-mechanical tuning and imaging of a photonic crystal micro-cavity resonance", Poster presentation, Annual Mesa+ meeting, University of Twente, Enschede, The Netherlands, 2006.

[7] W. C. L. Hopman, K. O. van de Werf, A. J. F. Hollink, W. Bogaerts, V. Subramaniam, and R. M. de Ridder, "Nano-mechanical tuning and imaging of a photonic crystal micro-cavity resonance by AFM ", Annual Mesa+ meeting, University of Twente, Enschede, The Netherlands, 2006.

[8] W. C. L. Hopman, K. O. van de Werf, A. J. F. Hollink, W. Bogaerts, V. Subramaniam, and R. M. de Ridder, "Nano-mechanical tuning and imaging of a photonic crystal micro-cavity resonance by AFM", Oral presentation, NanoNed/MicroNed Symposium, Eindhoven, the Netherlands, 2006.

[9] W. C. L. Hopman, R. M. de Ridder, and et al., "Fabrication and Characterization of 2D Silicon-based Photonic Crystal Structures", Oral presentation (invited), Colloquium Inorganic Materials Science (IMS), Faculty of Science and Technology, University of Twente, Enschede, The Netherlands, 2006.

[10] S. M. Chakkalakkal Abdulla, W. C. L. Hopman, and G. Krijnen, "Tuning of photonic bandgap crystals by NEMS actuators", Poster presentation, ePIXnet Winterschool, Pontresina, Switzerland, 2007.

WEBSITES

[1] “Manipulating light with a tiny needle”, http://www.utwente.nl/nieuws/pers/en/cont_06-041_en.doc/.

[2] “Manipulating light with a tiny needle”, this article has been adapted by many science and technology related websites, http://www.physorg.com/news79106179.html.

OTHER

[1] "Quasi one-dimensional photonic crystal as a compact building-block for optical refractive-index sensors", Annual report, Mesa+, University of Twente, Enschede, the Netherlands, 2005.

[2] “AFM manipuleert licht in kooi”, *Technisch weekblad*, 2007.

GENERATED SOFTWARE TOOLS

[1] PreFib, version **2.0**, by W. C. L. Hopman, *Bitmap to stream file conversion and stream file viewing*, "\\udsel02\GroupLow\IOMS\Software IOMS".

[2] EliXeR, version **5.0**, by W. C. L. Hopman, *For analyzing and making movies of camera images*, "\\udsel02\GroupLow\IOMS\Software IOMS".

[3] MeSla+, version **3.0**, by W. C. L. Hopman, *For transmission measurements, broadband measurements using the spectrometer, delay measurements and camera images grabbing*, "\\udsel02\GroupLow\IOMS\Software IOMS".

DANKWOORD

Na 4 jaren arbeid, kan ik dan eindelijk mijn eigen dankwoord schrijven.
In de eerste 2 jaar van mijn promotie heb ik parttime gewerkt om te kijken of ik genoeg sporttalent had om een internationale toptriatleet te worden. Al snel kwam ik erachter dat het niveau dat ik wilde halen niet binnen mijn bereik was. Vanuit de vakgroep werd uiterst behulpzaam gereageerd op mijn verzoek in 2 stappen over te schakelen naar full time promoveren. Deze omschakeling kwam tegelijkertijd met mijn overstap naar een uitdagend NanoNed onderzoeksproject (zie hoofdstuk 1). In dit project heb ik de afgelopen 2 jaar met plezier en kunnen (samen) werken, wat ook tot uitdrukking is gekomen in de leuke onderzoeksresultaten die ik heb mogen behalen. Voor de bijdrage aan de resultaten en de zeer prettige tijd zijn er vele mensen te danken. Eerst wil ik iedereen bedanken die ik niet bij naam heb genoemd in dit dankwoord.

Vanaf mijn stage in 2001 tot half augustus 2007, ruim 6 jaar, is René de Ridder mijn begeleider in meer of mindere mate geweest. Ik heb enorme bewondering voor het geduld, de bescheidenheid, de kritische blik (de typische advocaat van de duivel houding) en literaire perfectie waarmee zijn begeleiding getypeerd werden. Ik zou graag nog een tijdje blijven samenwerken, maar enerzijds wordt het voor mij ook eens tijd om verder te kijken en anderzijds komt er ook weer een nieuwe stroom promovendi aan die nodige tijd zullen vergen. Daarom rest mij te zeggen, René bedankt!

Graag wil ik ook de andere leden van mijn commissie, naast het lezen van mijn proefschrift, bedanken voor het volgende: mijn promotor Alfred voor de interessante gesprekken die we vooral de eerste 2.5 jaar gehad hebben; mijn promotor Markus Pollnau voor de getoonde interesse en vertrouwen in mijn kwaliteiten; Kobus Kuipers, voor de leuke tijd in Wroclaw, de prikkelende gesprekken over onze PSTM resultaten en de inspirerende adviezen over de presentatie van een onderzoek al dan niet in paper vorm; Vinod Subramaniam, voor het mogelijk maken van de samenwerking tussen onze onderzoekgroepen; Hugo Hoekstra, voor de vele discussies en gesprekken al dan niet gerelateerd aan dit proefschrift; Huub Salemink, voor het deelnemen aan mijn commissie; Richard De La Rue, voor het mogelijk maken van de samenwerkingen, het geven van kritisch commentaar en de overweldigende gezelligheid tijdens de koffie/thee pauzes en kroegbezoeken. Ik zou graag een Engelse vertaling van dit dankwoord willen schrijven, maar gezien de talenvaardigheden van Richard en het plezier dat hij heeft om de tekst te ontcijferen, lijkt me dat volstrekt overbodig.

Gelukkig hebben de muren geen kleine oortjes in de Hogekamp kamer 7106, want de afgelopen 4 jaar zijn daar vele onderwerpen de revue gepasseerd. In deze inspirerende omgeving wil ik Ronald Dekker en Edwin Klein bedanken voor hun aanwezigheid en inbreng in alles. Soms had ik het idee dat met onze gezamenlijke creatieve geesten geen werk gerelateerd probleem onoplosbaar was. Misschien dat we ooit in de toekomst onze samenwerking kunnen doorzetten. Ook wil ik Didit bedanken voor de discussies, samenwerking en weetjes over de Islam.
De experimenten die ik heb gedaan zou ik nooit allemaal hebben kunnen doen zonder de hulp van Anton Hollink. Als tegenprestatie heb ik altijd met veel plezier bij allerhande

computer problemen geholpen. De vrijwel dagelijkse gesprekken bij een bakje koffie of thee over van alles en nog wat zal ik zeker missen. Verder wil mijn technoloog Gabriël Sengo bedanken voor al het moois wat hij gemaakt heeft voor me en voor de andere prettige samenwerkingen en conversaties die we hebben gehad. De adviezen van de andere techneuten die binnen onze groep werken of hebben gewerkt Meindert Dijkstra, Lucie Hilderink, Albert Borreman, Henk van Wolferen, Henry Kelderman en Robert Wijn heb ik ook zeer gewaardeerd. De altijd precieze en punctuele inbreng van Rita ter Weele-Stokkers heeft alle administratie op rolletjes laten verlopen. De interesse en hulp die ik heb gehad van de overige oud- of semistafleden, Paul Lambeck, Mart Diemeer en Kerstin Wörhoff waren zeer welkom.
In meer of mindere mate werd ik geïnspireerd door de “Aio’s” die voor mij gepromoveerd zijn, Ton Koster (ooit mijn begeleider geweest), Chris Roeloffzen (bedankt voor het helpen bij de Group delay metingen), Joris van Lith (je vloeibare opstelling was top), Dion Klunder (heeft me de beginselen van het inkoppelen bijgebracht), Freddy Tan, Geert Altena (we zwommen in hetzelfde water, ik aan het oppervlak en jij eronder…op verschillende tijden), Sami Musa (die voor mijn Aio-tijd al zeer relaxed reageerde als ik z’n gecleavde fibers verknoeit had), Cazimir Bostan (voor zijn nalatenschap, wat mij betreft hadden we meer samen kunnen werken), Arne Leinse (altijd lol), Douwe Geuzebroek (overoverbuurman en altijd in voor gezelligheid)
Ook met de nieuwe en huidige promovendi en postdocs was altijd veel plezier te beleven, Feridun Ay (samen al één mooie FIB paper geschreven), Lasse Kauppinen (mijn opvolger, succes!), Dimitri Geskus (zit nog enkele maanden opgescheept met zowel mij als Ronnie en Dekkie, maar volgens mij komt dat wel goed…), Chaitanya Dongre (het taalwonder van de groep), Muralidharan Balakrishnam, Shanmugam Aravazhi, Marcel Hoekman (labview rules the cameras), Henri Uranus (altijd net iets later aanwezig op de groepsbijeenkomsten dan ik vanwege het verschil in fietstempo), Jonathan Bradley, Gamar Hussein. De nieuwe masterstudenten, Tjeerd Pinkert en Tom Blauwendraat, wens ik veel succes toe met hun opdracht.

Dan zijn er ook nog de vele studenten die hebben bijgedragen aan de simulaties of de processing van de in dit proefschrift beschreven resultaten, jullie zullen het zwaar hebben gehad met mij als veeleisende begeleider, toch hebben jullie het volgehouden, daarom dank aan mijn afstudeerstudenten: Wouter Engbers (afwisselend, maar toch ook mooi fabricage werk), Shankar Selvaraja (inmiddels ook succesvol promovendus), Wenbin Hu (een dubbele prestatie); mijn stagiaires: Tristan Doornebosch (het automatiseren van de IR camera opstelling), Sylvain Sergent (inmiddels FEMlab goeroe en ook promovendus); en de labcursus en IOO studenten: Abhishek Kumar (het meten van vele Si PhC samples) en Jaap Kautz (de getalenteerde maar ook niet gefocusseerde student, bedankt voor de simulaties en het kratje Grolsch).

Ook wil ik de andere studenten die hun afstudeerproject hebben volbracht in onze groep bedanken voor hun samples en andere inbreng in het bijzonder, Frank van Soest, Robin Tijssen, Peter Veltman en Dorleta Oregui.

Gedurende mijn promotietijd heb ik het geluk gehad vruchtbare samenwerkingen te hebben met Kees van der Werf (buiten de gezelligheid waren zijn schat aan ervaring en oog voor artistiek detail cruciaal voor het slagen van de AFM interactie metingen), Henkjan Gersen

(Met de kennis van nu hadden we zeker een papertje of 2 uit de PSTM kunnen halen in 2003), Marco Gnan (Italiaans gezellig, onze samenwerking heeft mij aangezet de delay-metingen uit te voeren, die zeer nuttig bleken te zijn), Pierre Pottier (samen een biertje of een cidertje drinken), Remco Stoffer (bedankt voor al het Quep-werk en de hulp bij de FDTD simulaties), Peter Bienstman, Wim Bogaerts (spil binnen het SOI gedeelte van het ePIXnet, bedankt voor het DUV fabriceren van mijn samples), Jeroen Korterik (voor het helpen met het analyseren van de gigabytes aan PSTM data), Frans Segerink (voor de hulp bij het FIB millen en het delen van de triathlonpassie, hetzij over verschillende afstanden), Jonathan Schrauwen (snowboard kampioen en FIB expert), Mark Smithers (ook sportfanaat en meester SEMer), Vishwas Gadgil (voor het millen van mijn ontwerpen op de door mij aangegeven plaatsen), en alle cleanroom stafleden met name Gerard Roelofs (die geregeld had dat ik in de onderhoudsweek van de cleanroom zelfs nog de cleanroom in kon), Helmut Rathgen met wie ik onder andere een ontzettend coole submarineopstelling heb ontworpen en gebouwd.
De maandelijkse besprekingen van ons NanoNed project waren ook inspirerend, dank voor het commentaar en jullie input, Manfred Hammer, Gijs Krijnen, Shahina Abdulla, Olena Ivanova, Milan Maksimovic en eerder genoemden.

In de pauzes was ik vaak te vinden in bijvoorbeeld het zwembad, waar de badmeester Henk Siers altijd in was voor een discussie over van alles. Voor de wetenschappelijke analyses van alle water en techniek gerelateerde zaken was Bram Nauta altijd wel te interesseren, zelfs als het een beetje ten koste ging van de zwemtijd…
Op dinsdag tussen de middag werd er altijd steevast gelopen en gerekt in het bos achter de UT, waarvan ik nu alle paadjes ken. De volgende loopgenoten zorgden ervoor dat een uurtje lopen altijd veel korter leek, Jetse Scholma (ook collega “elite” triatleet), Hanneke Bodewes, Casper Smit, Andries Koers, Pieter Wolbers (thanx voor het regelen van de ASML sponsoring), Martijn Keijsers, Rina Zijgers en anderen die af en toe meeliepen.
De andere sporters die mij mede hielpen om op een hoger nivo te komen waren o.a., Dannis Brouwer, Guido Gosselink, Kees-Jan Overbeeke, Sebastiaan van den Berg, Wouter Ditters, Michel Kruiper en Mark Rankenberg.
De eerste twee jaar van mijn promotie was ik actief in de 2^{e} en 1^{e} Bundesliga samen met het SUS-Stadtlohn triathlonteam, Uwe en Michael Kappelhof, Gerrit Völker, Marcel Lücke, Jerzy Kazemier (NL) en Jan Manenschijn (NL) en alle anderen.

Op dinsdag avond na een dag ploeteren achter de pc, in het lab of in de cleanroom, kon ik altijd mijn opgekropte energie eruit trommelen in de West-Afrikaanse percussie groep van Albert Prak. We hebben heel wat groovy ritmes en breakjes gespeeld, samen met mijn mede cursisten, Jan en Ed Droog, Fred Dijkkrol, Henriëtte Schepers, Nicole Krikke, Jan en Ingrid Voogtdavina, Judith Fluitsma, Bram Zandstra (gastdocent), en alle anderen die nu misschien andere hobby’s hebben.

Op maandagavond werden mijn zangkunsten en andere muziek gerelateerde eigenschappen bijgeschaafd tijdens de inspirerende bandrepetitie van cupsized. We hebben samen heel wat leuke optredens en avondjes gehad de afgelopen jaren samen met onze ex-zangeressen Carolien Leussink, Maria Grob en Gerrie Zijgers. Mijn improvisatie drang al dan niet netjes in de maat, werd gelukkig gecompenseerd door Ruben Wassink die bij elke maat weet wie wat (niet) moet doen. De swingende basnoten en het plezier op podium met Bart

van der Wal (mede triatleet) werden niet alleen door mij gewaardeerd. Ook met de gitaristen en dinsdaghardlopers Ric Huting en Ferry Melchels, konden we nog redelijk strakke nummers neerzetten zonder een consumptie te hoeven overslaan. Met onze trompettist Thijs Brillemans en onze nieuwe bassist Thomas Schellekens is elke feest gegarandeerd een succes (of we nu spelen of niet).

Het 1e jaar van mijn promotie heb ik met veel plezier samen gewoond met Gillian Huijsse en Jessica Zoethout in een studenten appartement aan de Dr. J. van Damstraat.
Voor de nodige ontspanning in de weekenden zorgden m'n oude huisgenoten, zwemmaatjes en vrienden zo nu en dan, Stefan Oosting, Kristiaan Böhm, Jeroen Wijering en Sebastiaan Broerse.

Zonder alle namen te noemen, wil ik mijn familie en schoonfamilie (klein en groot) bedanken voor de getoonde interesse, gezelligheid en afleiding.

Mijn vriendin die ik het meest zou moeten bedanken voor haar steun, opgebrachte geduld, prettige vakantie drang, gezelligheid en nog veel meer, zou ik eigenlijk als eerste moeten noemen in mijn dankwoord. Ik kan aan jou een lang stuk tekst gaan wijden, maar ik weet dat je het leuker zal vinden als ik deze tijd gebruik om samen met jou te zijn. Renske bedankt voor alles!

Dank aan ASML voor de sponsorbijdrage voor het printen van mijn proefschrift.